AD NUMBER

AD283348

LIMITATION CHANGES

TO:

Approved for public release; distribution is unlimited.

FROM:

**Distribution authorized to U.S. Gov't. agencies and their contractors;
Administrative/Operational Use; JUL 1962. Other requests shall be referred to Directorate of Materials and Processes, Aeronautical Systems Division, Wright-Patterson AFB, OH 45433.**

AUTHORITY

AFML ltr dtd 21 Dec 1972

ASD-TDR-62-401

BIAXIAL STRESS AND STRAIN DATA ON HIGH STRENGTH ALLOYS FOR DESIGN OF PRESSURIZED COMPONENTS

TECHNICAL DOCUMENTARY REPORT NO. ASD-TDR-62-401

JULY 1962

DIRECTORATE OF MATERIALS AND PROCESSES
AERONAUTICAL SYSTEMS DIVISION
AIR FORCE SYSTEMS COMMAND
WRIGHT-PATTERSON AIR FORCE BASE, OHIO

Project No. 7381, Task No. 738103

(Prepared under Contract No. AF 33(616)-7720
by the Chance Vought Corporation, Dallas 22, Texas;
E. L. Terry and S. W. McClaren)

NOTICES

When Government drawings, specifications, or other data are used for any purpose other than in connection with a definitely related Government procurement operation, the United States Government thereby incurs no responsibility nor any obligation whatsoever; and the fact that the Government may have formulated, furnished, or in any way supplied the said drawings, specifications, or other data, is not to be regarded by implication or otherwise as in any manner licensing the holder or any other person or corporation, or conveying any rights or permission to manufacture, use, or sell any patented invention that may in any way be related thereto.

- - - - - - - - -

Qualified requesters may obtain copies of this report from the Armed Services Technical Information Agency, (ASTIA), Arlington Hall Station, Arlington 12, Virginia.

- - - - - - - - -

ASTIA release to OTS not authorized.

- - - - - - - - -

Copies of ARL Technical Documentary Reports should not be returned to Aeronautical Research Laboratory unless return is required by security considerations, contractual obligations, or notices on a specific document.

AF-WP-L-APR 62 100

FOREWORD

This report was prepared by Chance Vought Corporation, Aeronautics and Missiles Division, under USAF Contract No. AF 33(616)-7720. This contract was initiated under Project No. 7381, "Materials Application," Task No. 738103, "Data Collection and Correlation." The work was administered under the direction of the Directorate of Materials and Processes, Deputy Commander/Technology, Aeronautical Systems Division, with Major John A. Fiorillo, Mr. Sidney O. Davis, and Mr. Clayton L. Harmsworth acting as project engineers.

This report covers work conducted from January 1961 to April 1962.

Mr. E. L. Terry was the Chance Vought principal investigator. Mr. S. W. McClaren cooperated in the research and in the preparation of this report. Mr. R. O. Reade was in charge of all structural tests.

4-86C, 600, 9-24-62

ABSTRACT

A cross shaped specimen was developed for generating complete biaxial stress-strain curves under 1:1 and 2:1 biaxial tension stress ratio loading. Tests on several materials have shown that the specimen has good reliability.

The influence of strength level on the behavior of the 5CrMoV steel under biaxial loading was investigated. These tests showed that by lowering the uniaxial strength level from 280 to 260 ksi, the shattering type failure observed at the 280 ksi level ceased to exist. However, the biaxial failure strains did not increase as the strength level was decreased.

Pressure vessel tests which were conducted showed that the shattering type behavior obtained from the biaxial specimens is indicative of poor resistance to crack-like flaws. Good correlation was obtained between the failure stresses from the pressure vessels and the biaxial specimens.

Notch toughness tests were conducted to obtain a correlation between these tests and the biaxial specimen tests. No correlation could be shown between the notch toughness values and the biaxial failure strains. However, the notch toughness tests corroborated the conclusion that the shattering type failure in the biaxial test is indicative of poor resistance to crack-like flaws in the material.

The biaxial stress and strain data is presented in a form which can be used directly in the design of biaxially loaded components. In addition, the test materials are ranked according to the efficiency parameters "biaxial ductility rating," "resistance to crack-like flaws" and "biaxial strength/weight."

This technical documentary report has been reviewed and is approved.

W. P. Conrardy

W. P. CONRARDY
Materials Engineering Branch
Applications Laboratory
Directorate of Materials and Processes

TABLE OF CONTENTS

TABLE OF CONTENTS (Continued)

LIST OF TABLES

LIST OF TABLES (Cont)

LIST OF FIGURES

LIST OF FIGURES (Cont)

LIST OF FIGURES (Cont)

LIST OF FIGURE (Cont)

LIST OF FIGURES (Cont)

LIST OF FIGURES (Cont)

NOMENCLATURE, SYMBOLS AND DEFINITIONS

A, A'	instantaneous and original cross-sectional area, respectively, in^2.
C	crack length, inches
E	Young's modulus of elasticity, psi
E_s	secant modulus, psi
E_1, E_2	Young's modulus of elasticity in direction of maximum principal stress and minimum principal stress, respectively, psi
e	the base of natural logarithms ($e = 2.718 \ldots$)
e_1, e_2	principal elastic strains, in./in.
K_{cl}	fracture toughness, psi$\sqrt{\text{in.}}$
L, L'	instantaneous and original gage length, respectively, inches
N	number of specimens in a sample
n	strain hardening coefficient for uniaxial tension
P	axial load in uniaxial tension, lbs.
P_1, P_2	loading jack loads in principal stress directions, lbs.
p	internal pressure, psi
$\bar{p}$	maximum pressure, psi
R, R_i	instantaneous and initial radius, respectively, inches
R_{max}, R_{min}	maximum and minimum numerical values of stress or strain in a sample
S	standard deviation as used in statistical analysis
t, t_i	instantaneous and initial wall thickness, respectively, inches
V	dimensionless statistic normally referred to as the coefficient of variation
X	ratio of instantaneous radius to original radius (R/R_i)
$\bar{X}$	maximum radial expansion corresponding to $\bar{p}$, in./in.
Y	ratio of instantaneous thickness to original thickness (t/t_i)

$\bar{Z}$	arithmetic mean
α	stress ratio (σ_2/σ_1)
β	stress ratio (σ_3/σ_1)
$\gamma_{oct.}$	octahedral shear strain, in./in.
ϵ, ϵ'	true and nominal strain in uniaxial tension, respectively, in./in.
ϵ_e	effective strain, in./in.
$\bar{\epsilon}_e$	effective strain at maximum pressure $\bar{p}$, in./in.
$\epsilon'_{MAX.}$	nominal strain at fracture in uniaxial tension, in./in.
$\epsilon'_{pA}, \epsilon'_{pt}, \epsilon'_{pw}$	nominal plastic strain in axial direction, thickness direction, and width direction, respectively, in./in.
ϵ_u, ϵ'_u	true and nominal strain at maximum load in uniaxial tension, respectively, in./in.
$\epsilon_1, \epsilon_2, \epsilon_3$	true principal plastic strains, in./in.
$\epsilon'_1, \epsilon'_2, \epsilon'_3$	nominal principal plastic strains, in./in. (ϵ'_1 also represents test values of nominal principal plastic strains at maximum load)
μ_{E1}, μ_{E2}	elastic value of Poisson's ratio in direction of maximum principal stress and minimum principal stress, respectively
μ_E μ_p	elastic and plastic Poisson's ratio, respectively
σ, σ'	true and nominal stress in uniaxial tension, respectively, psi
σ_e	effective stress, psi
σ_o	constant fictitious value of true stress, psi
σ'_R	nominal principal stress at maximum load, psi
σ_u, σ'_u	true and nominal stress at maximum load in uniaxial tension, respectively, psi
σ_y	yield stress in uniaxial tension, psi
$\sigma_1, \sigma_2, \sigma_3$	true principal stresses, psi
$\sigma'_1, \sigma'_2, \sigma_3$	nominal principal stresses, psi
τ_{cR}	critical shear stress, psi

τ_{oct}	octahedral shear stress, psi
τ_1, τ_2, τ_3	principal shear stresses, psi
ω	surface energy per unit of area, $\frac{\text{in - lb}}{\text{in}^2}$

SECTION 1

INTRODUCTION

The behavior of metal under load has been the subject of thousands of experimental and analytical studies, and yet, even today a satisfactory explanation of the flow and fracture of engineering materials does not exist for all cases. Ever since the use of steel structures became prevalent there have been numerous reports of catastrophic failures at low nominal stress levels. Little attention was given to this matter until a large number of sudden failures occurred in welded steel merchant ships during the winters of 1942 and 1943. Airframe builders were not plagued with this problem to any great extent until the recent introduction of high strength steel and titanium alloys. In the past few years, catastrophic failures at relatively low nominal stress levels have not been uncommon, particularly in rocket motor cases fabricated from the high strength steel and titanium alloys.

The investigators who have studied these brittle fractures have carried out extensive research programs in an effort to better understand the behavior of metals under such conditions. A multitude of laboratory specimens have been devised for these studies ranging from large complicated parts to simple miniature specimens. The test data obtained from many of these specimens have permitted considerable progress in the field of fracture mechanics; however, all too often the experimental findings are qualitative rather than quantitative.

The most recent rash of catastrophic failures has occurred in rocket motor cases. The Space Age has introduced requirements for rocket motor case materials having a strength/weight ratio of 1,000,000 or more. This does not seem to be an unreasonable requirement, considering the uniaxial strength properties of the newer structural materials such as the tool steels and the titanium alloys. However, test results obtained on pressure vessels fabricated from some of these high strength materials have often been disappointing since failure has occurred at relatively low nominal stress levels. Even when extreme care is exercised in fabricating the vessel, there has been no assurance that premature failure would not occur. Based on these tests there is strong evidence that lack of ductility in the metal under biaxial loading has contributed to the catastrophic failures at low nominal stress levels. Mis-match of joining parts, discontinuity loads, dents, out-of-roundness, small flaws, etc. may require considerable plastic flow of the metal in order that high nominal stresses can be attained before failure. Numerous attempts have been made to devise a simple test specimen for evaluating the performance of materials in pressure vessels. However, in most cases the test specimens devised produce results which are qualitative rather than quantitative. Thus, there is a need for a relatively simple laboratory specimen which will give quantitative results that can be applied directly in the failure analysis of parts subjected to combined axial loading. More specifically, there is a need for a biaxial specimen in which the origin of failure can be forecasted so that it can be suitably instrumented to record strains up to the instant of fracture. Such information must be obtained experimentally since no plasticity theory has been developed which will accurately predict the plastic flow of metals.

Manuscript released by the author April 1962 for publication as a Technical Documentary Report.

The data obtained from the biaxial test specimens may be used in several ways. The most obvious use of this test is in screening materials and developing biaxial elongation requirements similar to the uniaxial elongation requirements in existence for most aircraft structural materials. Another use of this test method is in evaluating material processing procedures that are intended to improve the material performance. A third and very important application of the biaxial strain data is in the failure analysis of pressure vessels or other types of biaxially loaded components.

The purpose of this study was to gain information on the strain and fracture behavior of several high strength materials under biaxial tension stress ratio loading. A relatively simple biaxial test specimen was developed which can be suitably instrumented to record principal strains up to failure. Tests were conducted under both 1:1 and 2:1 stress ratio conditions to obtain complete biaxial stress-strain curves.

Cylindrical pressure vessels were tested to obtain a correlation between the strain and fracture behavior from the vessels and the biaxial test specimens. In addition, notch toughness tests were conducted to obtain a correlation between these tests and the biaxial specimen tests.

SECTION 2

DESCRIPTION OF TEST PROGRAM

The test program consisted of six phases as follows:

Phase I: Biaxial Stress-Strain Testing Under 1:1 Loading Conditions

Phase II: Biaxial Stress-Strain Testing Under 2:1 Loading Conditions

Phase III: The Effect of Strength Level Upon Allowable Biaxial Strain in High Strength Materials

Phase IV: The Effect of Welding Upon the Behavior of Materials Under Biaxial Load Conditions

Phase V: Cylindrical Pressure Vessel Tests

Phase VI: Notch Toughness Tests

In Phases I and II, biaxial tests were made to show that the test specimen concept was applicable for the test materials and to generate biaxial stress-strain data under 1:1 and 2:1 tension stress ratio conditions. In addition, complete uniaxial tension stress-strain curves were obtained from each material.

In Phase III 1:1 biaxial tests were conducted on one of the test materials to demonstrate the effect of strength level on allowable biaxial strain. In addition, uniaxial tests were conducted on the other materials to obtain data which could be used to predict the biaxial strain performance of these materials at the various strength levels. Each material was heat treated to two different strength levels that were lower than those used in Phase I and II.

In Phase IV 1:1 and 2:1 biaxial tests were conducted on one of the test materials to determine weld joint efficiency under biaxial loading conditions. In addition, welded uniaxial specimens fabricated from the other materials were tested to obtain data for predicting weld joint efficiency of these materials under biaxial loading conditions.

Cylindrical pressure vessels were tested in Phase V in order to establish a correlation between the strain and fracture behavior of the pressure vessels and the biaxial test specimens.

Notch toughness tests were conducted in Phase VI in order to obtain a correlation between these tests and the biaxial specimen tests.

SECTION 3

TEST MATERIALS

3.1 General

A summary of the materials which were evaluated under biaxial and uniaxial loading is shown below:

2014-T6 (QQ-A-255) Aluminum Alloy
B-120VCA (RS-120B) Titanium Alloy
5CrMoV (Potomac A) Vacuum Melted Tool Steel
D6A-C Air Melted Steel Alloy
Airsteel X-200

All material was received in the form of 0.125 inch nominal thickness sheet from which the test specimens were machined. All sheets of a given alloy were taken from the same mill heat. A complete chemistry analysis of each material is shown in Table 1. The mill processing history and fabrication history for each lot of material is summarized below.

3.2 Mill Processing History and Fabrication History

1. 2014-T6 Aluminum Alloy

Mill Process History - The 0.125 x 48 x 144 inch sheets were produced from 12 x 49 inch DC ingots as follows:

a. Ingot homogenized, scalped and cladded with 6053 alloy to produce a clad thickness of 2.5 percent per side nominal.

b. Ingot hot rolled to gauge, cut into sheets and solution heat treated in accordance with amendment 3 of MIL-H-6088B as follows:

Heat treated at 925° - 945° F for 40-50 minutes; quenched.

c. Heat treated sheet flattened through a two - high rolling mill, stretcher leveled to the necessary flatness requirements and then artificially aged in accordance with amendment 3 of MIL-H-6088B as follows:

Aged at 340° to 360° F for 7 1/2 to 8 1/2 hours.

Fabrication Process History - Clad material was purchased since the bare material could be obtained only by ordering a complete mill run. The cladding was removed from the test section in the biaxial specimens as a normal procedure when the depressions were machined. For the required uniaxial tensile specimens, the cladding was removed by mechanical means prior to testing.

The 2014-T6 specimens were machined from the sheet in the T6 condition according to the method described in Section 4.

2. B-120VCA Titanium Alloy

Mill Process History - The 0.125 x 36 inch wide titanium sheet was produced in the following manner:

a. 3/4 x 27 1/2 inch x various lengths slabs rolled to 3/8 x 39 x 34 inch plate at 1500° F.

b. Sheet rolled to final thickness at 1425° - 1450° F.

c. Final anneal at 1450° F.

Fabrication Process History - The B-120VCA titanium specimens were contoured while the material was in the annealed condition according to the method described in Section 4 and then aged as required. The depressions were machined into the biaxial specimens after aging.

3. 5CrMoV Tool Steel

Mill Process History - The 0.125 x 36 inch wide steel sheet was produced in the following manner:

a. 20 inch diameter ingot obtained by vacuum melting

b. 3 1/2 x 39 inch slab cut from ingot

c. Slab unidirectional rolled to sheet size

d. Continuous annealed at 1425° F

Fabrication Process History - The 5CrMoV specimens were machined while the material was in the annealed condition according to the method described in Section 4 and then heat treated as required.

4. D6A-C Air Melted Steel

Mill Process History - The 0.125 x 36 inch wide steel sheet was produced in the following manner:

a. 19 inch square slabs cut from 26 inch diameter ingot

b. 19 inch square rolled to 4" x 20" x RL slab and in turn re-rolled to 0.970" x 20" x RL sheet bar.

c. Sheet bar rolled to final thickness

d. Final anneal was box anneal cycle at 1350° - 1400° F held long enough for complete spheroidization in protective atmosphere followed by very slow cool to 800° F, then air cooled.

Fabrication Process History - The D6A-C steel specimens were machined while the material was in the annealed condition according to the method described in Section 4 and then heat treated as required.

5. Airsteel X-200

Mill Process History - The 0.125 x 36 inch wide steel sheet was produced in the following manner:

a. Electric furnace steel melted

b. Rolled to slab

c. Rolled to breakdown gauge

d. Hot rolled to finish size of 0.125 inches

e. Pickled

f. Spheroidize annealed at 1330° to 1380° F for 40 hours

g. Temper rolled

h. Unger leveled to flatten

i. Sheared to size

Fabrication Process History - The X-200 steel specimens were machined while the material was in the annealed condition according to the method described in Section 4 and then heat treated as required.

3.3 Decarburization Check

The results of a metallurgical examination to determine the decarburization which was present on each surface of the as-received steels are summarized below:

Material	Partial Decarburization	Total Decarburization
5CrMoV	0.003 inches	none
D6A-C	none	none
X-200	0.004 inches	0.001 inches

TABLE 1 - CHEMISTRY ANALYSIS OF TEST MATERIALS

MATERIAL	SUPPLIER	HEAT NO.	CHEMISTRY ANALYSIS								
2014-T6	Kaiser Aluminum	170351	Si 0.50-1.20	Fe 1.00	Cu 3.90-5.00	Mn 0.40-1.20	Cr 0.10	Zn 0.25	Mg 0.20-0.80	Ti 0.15	Al Balance
B-120VCA	Republic Steel	3930046	C 0.035	Cr 10.65	V 13.00	Al 3.40	N 0.008	H 0.009	Ti Balance		
5CrMoV	Allegheny Ludlum	W-23448	C 0.43	Mn 0.37	P 0.001	S 0.003	Si 0.89	Cr 4.84	Ni ----	Mo 1.29	V 0.54	Fe Balance
D6A-C	Allegheny Ludlum	30959	0.487	0.78	0.007	0.006	0.25	1.01	0.53	1.05	0.06	Balance
X-200	U.S. Steel	X39101	0.43	0.87	0.010	0.008	1.59	2.15	----	0.58	0.07	Balance

SECTION 4

TEST SPECIMENS

4.1 Unwelded Biaxial Specimens

The biaxial specimens for conducting the 1:1 and 2:1 tensile stress ratio tests were machined to the configuration shown in Figure 1. All specimens except 2014-T6 and B-120VCA were fabricated from annealed material. The 2014-T6 specimens were fabricated from as-received T-6 material. The B-120VCA specimens were contoured and drilled from annealed material and then aged as required. The depressions were machined into these specimens after aging. After heat treating, all specimens were carefully inspected for tool marks and scratches. These deficiencies were removed by polishing and all corners were given a final breaking if necessary. Initial tests on the 5CrMoV steel showed that notch sensitive materials must be flawless to avoid premature failure outside of the test section.

The specimen configuration shown in Figure 1 evolved from an experimental study to determine the most satisfactory configuration for 1:1 and 2:1 biaxial loading. The configuration was considered to be satisfactory if the fracture always initiated in or very near the area where a known 2:1 or 1:1 stress ratio existed. A summary of the various configurations which were evaluated under 1:1 loading is shown by Figure 2. The specimen shown in Figure 1 was the only shape which was studied under 2:1 loading. Photo stress was used extensively in working out the configuration shown in Figure 1. The specimens shown in Figure 2 were not successful either because the fracture initiated outside of the test area or because the fracture did not consistently initiate in the test area upon repeated tests. The tests showed that configurations B_3 and C were the most satisfactory of the group shown in Figure 2.

4.2 Unwelded Uniaxial Tensile Specimens

The standard sheet tensile specimens that were used to obtain full range stress-strain curves had a 1/2 inch width by 2 1/2 inch long test section. The specimen surfaces were left in the as-received condition except for the X-200 and 2014-T6 materials. Approximately 0.002 inches were ground from each surface of the X-200 specimens to remove the totally decarburized material. The cladding on the test section of the 2014-T6 specimens was removed by sanding.

4.3 Welded Biaxial and Uniaxial Specimens

Welded biaxial specimens were fabricated from the 5CrMoV tool steel sheet material. Plates measuring 10 x 10 x 0.125 inches were welded together to form 20 x 20 inch blanks from which the biaxial specimens were fabricated. The 2:1 and 1:1 specimens were fabricated in accordance with Figure 1. The locations of the welds in the biaxial specimens are shown in Figure 3. The machine fusion welds were made in two passes by the inert-gas-shielded-tungsten-arc method. After the first pass, the plates were immediately turned over to make the second pass. Approximately 95 percent penetration was made in each pass without use of filler wire. Protective inert gas was utilized to prevent underbead oxidation during welding. The joint was preheated to between 600° and 800° F, and was not allowed to cool below 600° F during the welding cycle or prior to stress relieving. The blanks were stress relieved at 1200° F for one hour, then air cooled to room

temperature. After the welds were inspected by the magnaglow and X-ray processes, the welded blanks were annealed, then straightened as required and again stress relieved. Annealing was accomplished by holding the blanks at 1625° F for one hour in argon, then cooling the blanks in the furnace to 800° F at a rate of 50° F per hour. From 800° F the blanks were air cooled to room temperature.

Welded uniaxial tensile specimens were fabricated from the 5CrMoV, 2014-T6, X-200 and B-120VCA sheet materials. The welded specimens, which were identical in size to the unwelded specimens, were fabricated so that the weld was normal to the direction of loading. The processes which were used to weld the blanks for fabricating the specimens are summarized as follows:

MATERIAL	WELD METHOD	PREHEAT	FILLER WIRE	NO. PASSES	STRESS RELIEF
2014-T6	Inert-gas-shielded-w-arc	None	None	2	None
5CrMoV	Same as Biaxial Specimens				
B-120VCA	Inert-gas-shielded-w-arc	None	B-120VCA	3	None
X-200	Inert-gas-shielded-w-arc	None	None	2	1200°F one hour

4.4 Poisson's Ratio Specimens

The specimens for determining the elastic and plastic values of Poisson's ratio were identical to the uniaxial specimens except for the test section size. The Poisson's ratio specimens had a 3/4 inch wide by 2.0 inch long test section.

4.5 Pressure Vessels

Pressure vessels for burst testing were fabricated from the 5CrMoV vacuum melted tool steel by the hydrospin process. A description of the vessels is shown in Figures 4 and 5. The vessels were fabricated by circumferentially welding together two identical vessel halves. The following summarizes the specifications which were followed in fabricating the vessels:

Preformed Blanks - Blanks for hydrospinning the vessel halves were formed into cups from 0.125 inch sheet material by the hydroform process.

Hydrospinning - Two hydrospin passes were made to reduce the wall to the required 0.040 inch thickness. After hydrospinning, the vessel halves were trimmed and stress relieved by heating to 1200° F for one hour then air cooling to room temperature.

Corrosion Prevention - A rust inhibiting oil was used throughout the manufacture of the vessels. The oil was maintained on the parts at all times except when welding, stress relieving, annealing and heat treating.

Circumferential Joint - The maximum gap between the mating halves at the circumferential joint was no greater than 0.010 inches before the halves were welded together. The joint was the square butt type.

Circumferential Weld Joint - Before welding, the inside and outside of the vessel halves were cleaned by a suitable process. The circumferential weld was made by machine fusion welding by the inert-gas-shielded-tungsten-arc method. Complete penetration was accomplished in one pass without use of filler wire. Protective inert gas was utilized to prevent underbead oxidation during welding. The joint was preheated to between 600° and 800° F, and was not allowed to cool below 600° F during the welding cycle or prior to stress relieving. The welds were of such quality that post weld grinding was not necessary. Top bead build-up did not exceed 0.020 inches. Weld drop-through did not exceed 0.020 inches. The radial misalignment of the cylinders at the weld joint did not exceed 0.006 inches. After welding and before cooling to below 600° F, the vessels were stress relieved at 1200° F for one hour, then air cooled to room temperature.

Weld Inspection - The welded joint was inspected by the magnaglow and X-ray processes.

Annealing - After welding, the vessels were annealed at 1625° F for one hour in argon then cooled in the furnace to 800° F at a rate of 50° F per hour. From 800° F the vessels were air cooled to room temperature.

Heat Treating - The inside and outside of the vessels were cleaned by a suitable process before heat treating. The heat treat schedule is shown in Table 2. All vessels were internally purged with helium for 5 minutes at a rate of 50 CFH immediately prior to charging into the furnace.

4.6 Notch Toughness Specimens

The configuration of the notch toughness specimens is shown in Figure 6. The specimen configuration is in accordance with the specifications given in reference 4. The specimens were fatigue cracked before heat treating.

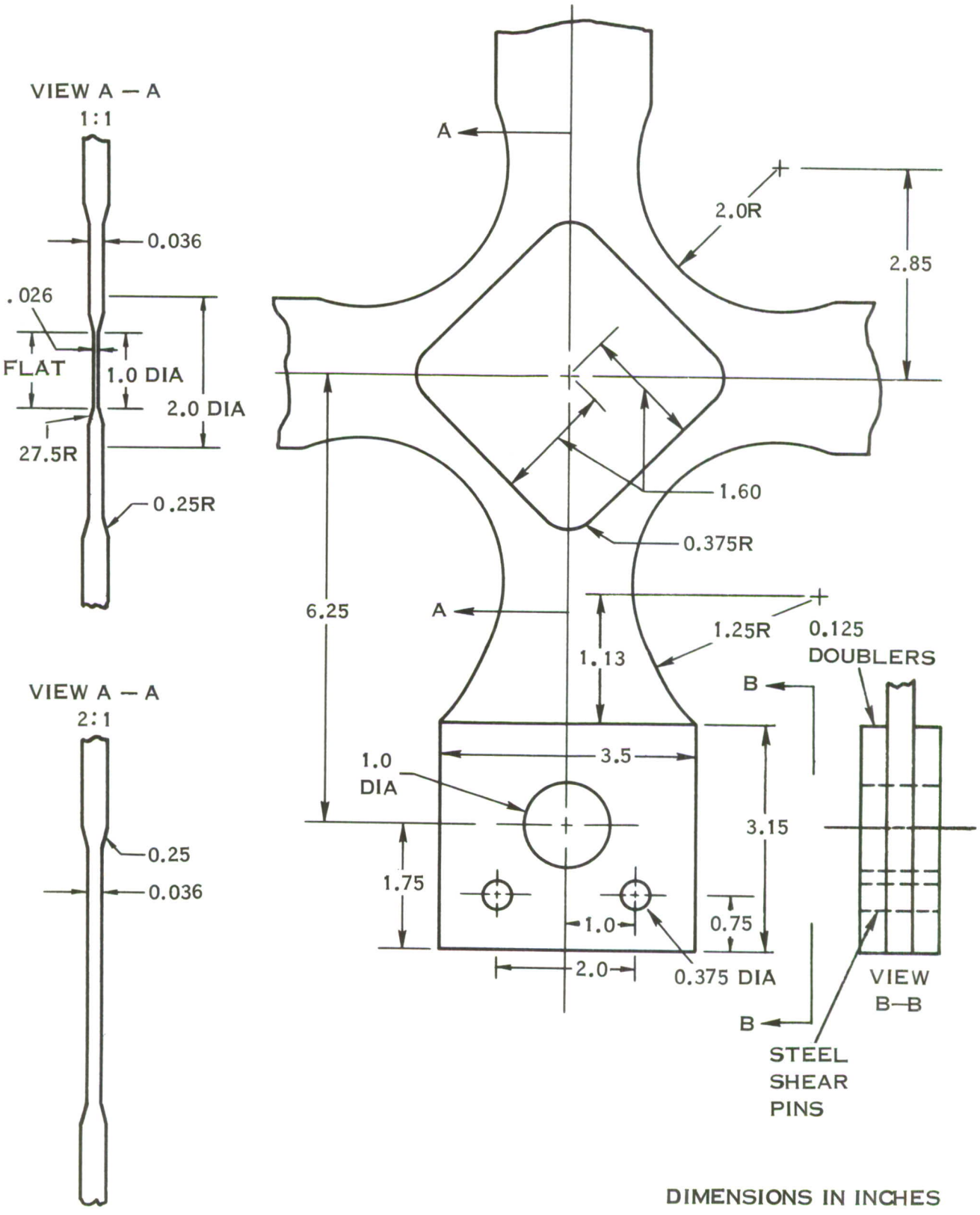

FIGURE 1 – BIAXIAL SPECIMEN CONFIGURATION FOR 2:1 AND 1:1 LOADING

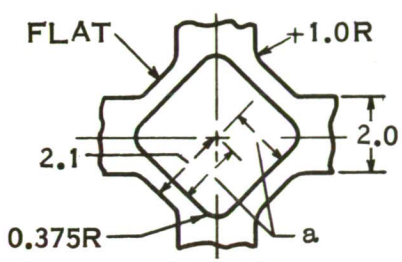

DIAMOND DEPRESSION TYPE A

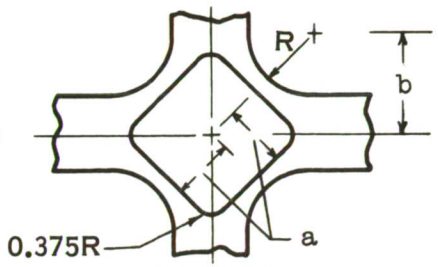

DIAMOND DEPRESSION TYPE B

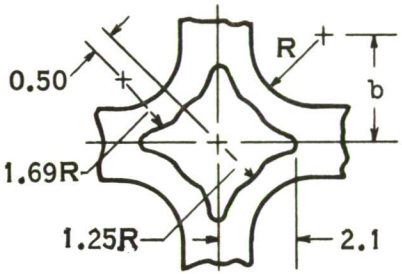

STAR DEPRESSION TYPE C

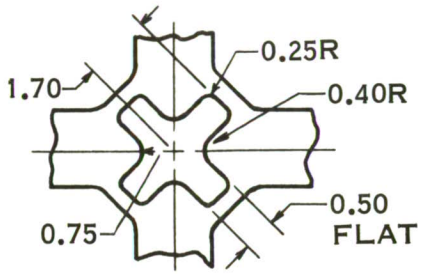

CLOVER LEAF DEPRESSION TYPE D

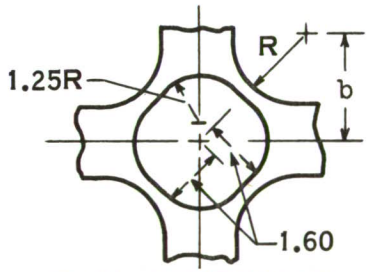

OVAL DEPRESSION TYPE E

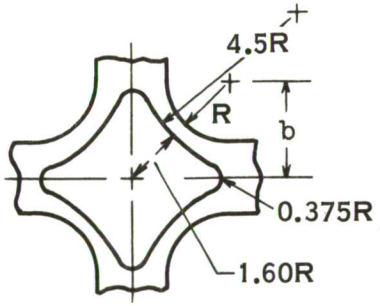

MODIFIED DIAMOND DEPRESSION TYPE F

TYPE DEPRESSION	SHOWN AS TYPE	a IN.	b IN.	R IN.	DEPRESSION THICKNESS IN.
DIAMOND	A	1.60	—	1.00	0.040
DIAMOND	B_1	1.60	2.5	1.50	0.040
DIAMOND	B_2	1.60	2.65	1.75	0.040
DIAMOND	B_3	1.60	2.85	2.00	0.040
DIAMOND	B_4	1.25	1.36	1.50	0.040
DIAMOND	B_5	1.60	2.85	2.00	0.036
DIAMOND	B_6	1.45	2.85	2.00	0.036
DIAMOND	B_7	1.75	2.85	2.00	0.036
STAR	C	—	1.36	1.50	0.036
CLOVER LEAF	D	—	—	—	0.036
OVAL	E	—	2.85	2.00	0.036
MODIFIED DIAMOND	F	—	2.85	2.00	0.036

NOTES:

1. IN ALL CASES THE THICKNESSES WERE CONSTANT OVER THE ENTIRE DEPRESSION
2. LOADING GRIP GEOMETRY ON ALL SPECIMENS WAS THE SAME AS SHOWN BY FIGURE 1

FIGURE 2 SUMMARY OF SPECIMENS TESTED IN THE DEVELOPMENT OF THE CONFIGURATION SHOWN IN FIGURE 1

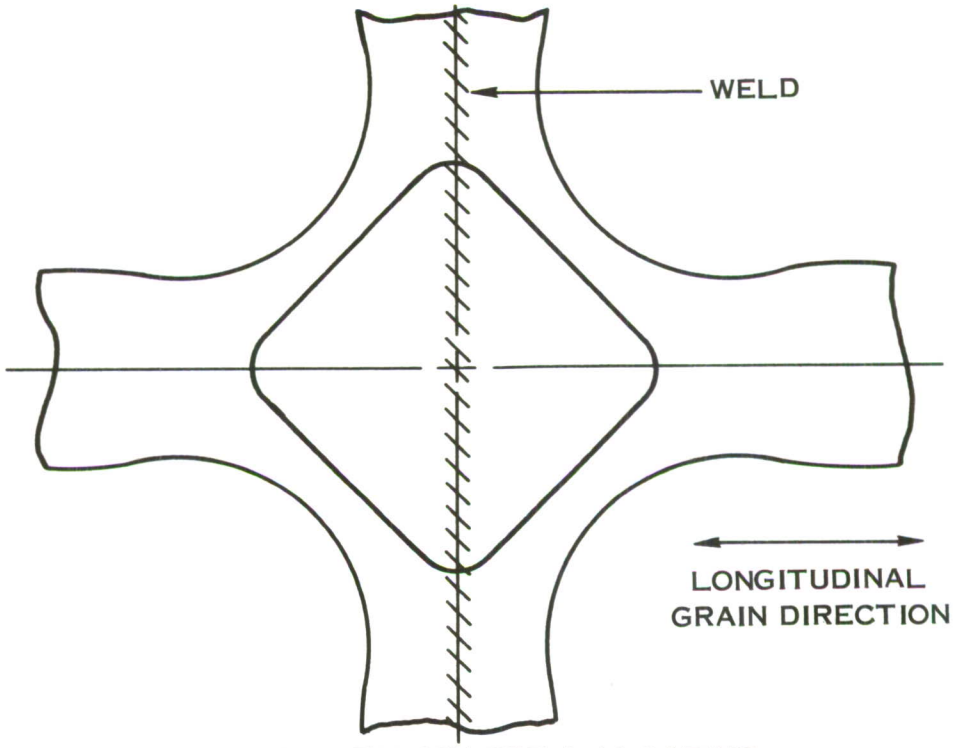

WELDED SPECIMEN FOR 1:1 LOADING

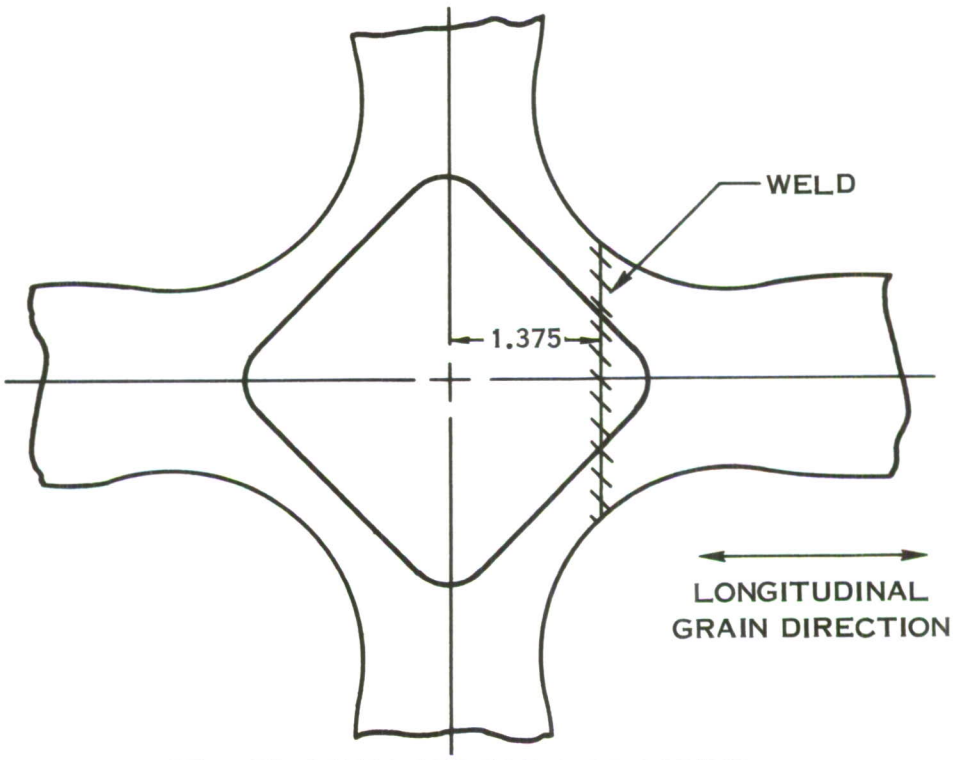

WELDED SPECIMEN FOR 2:1 LOADING

FIGURE 3 — WELD LOCATION FOR 1:1 AND 2:1 LOADING CONDITIONS

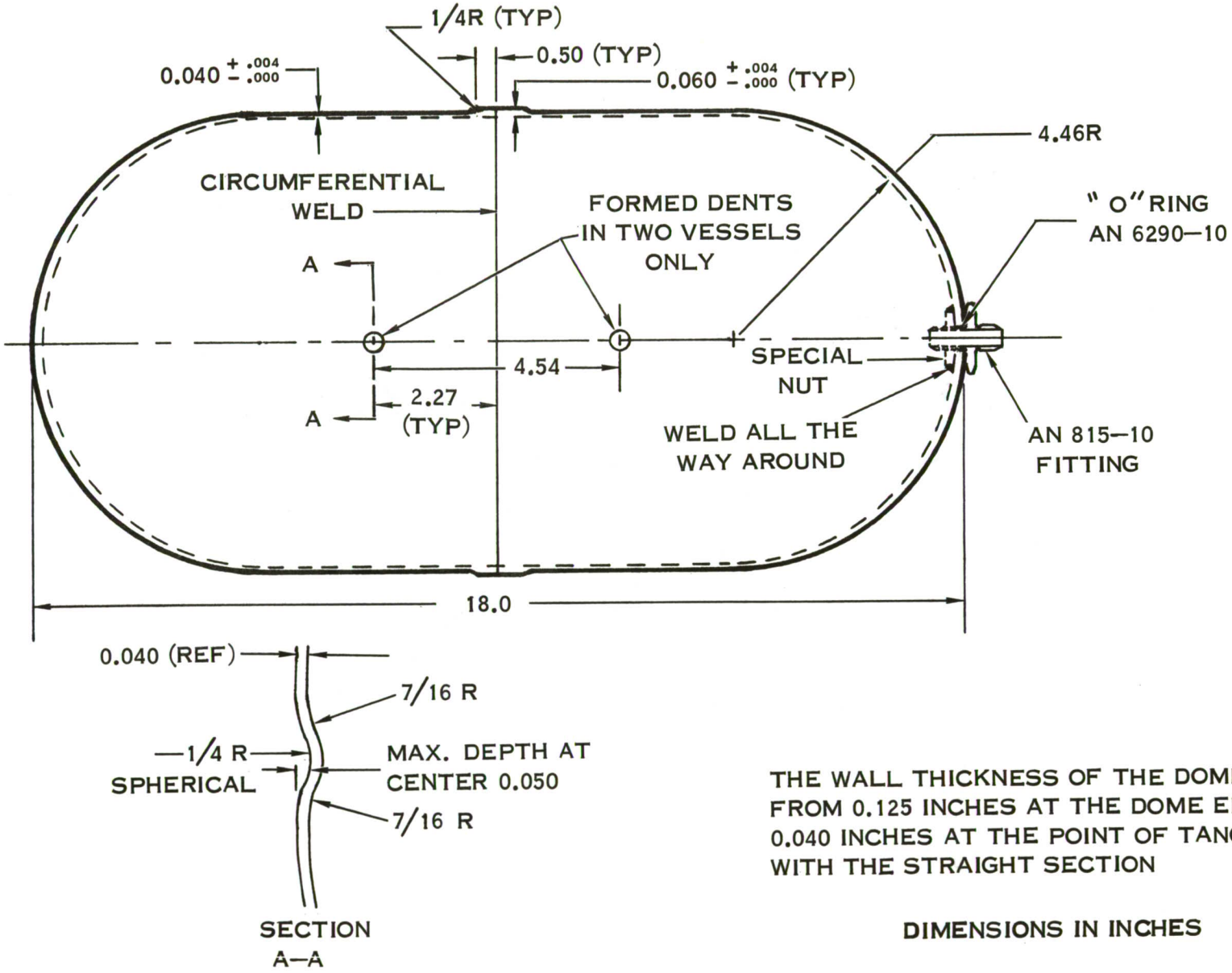

FIGURE 4 — PRESSURE VESSEL CONFIGURATION

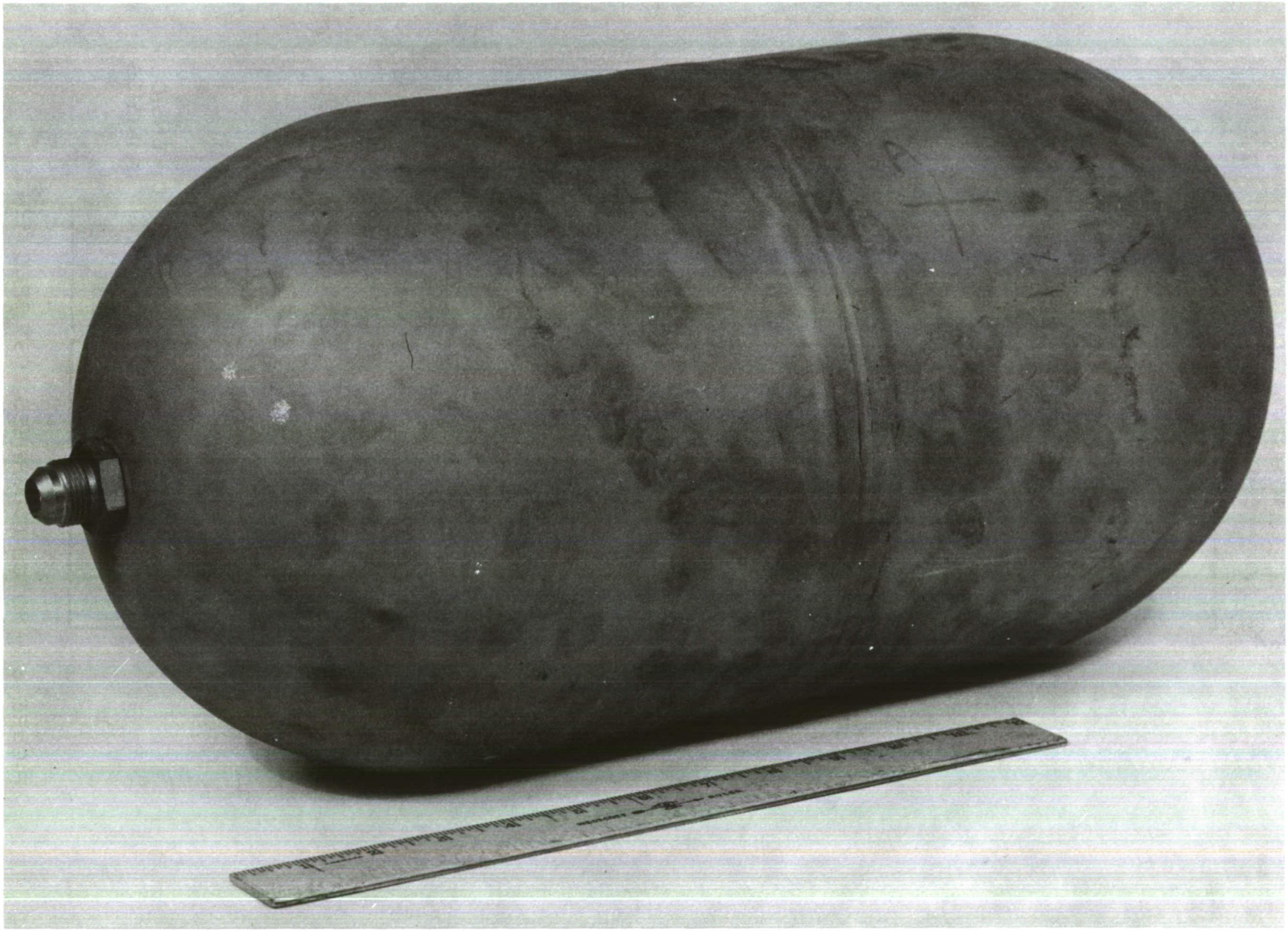

FIGURE 5 — 5CrMoV PRESSURE VESSEL FABRICATED BY HYDRO SPIN PROCESS.

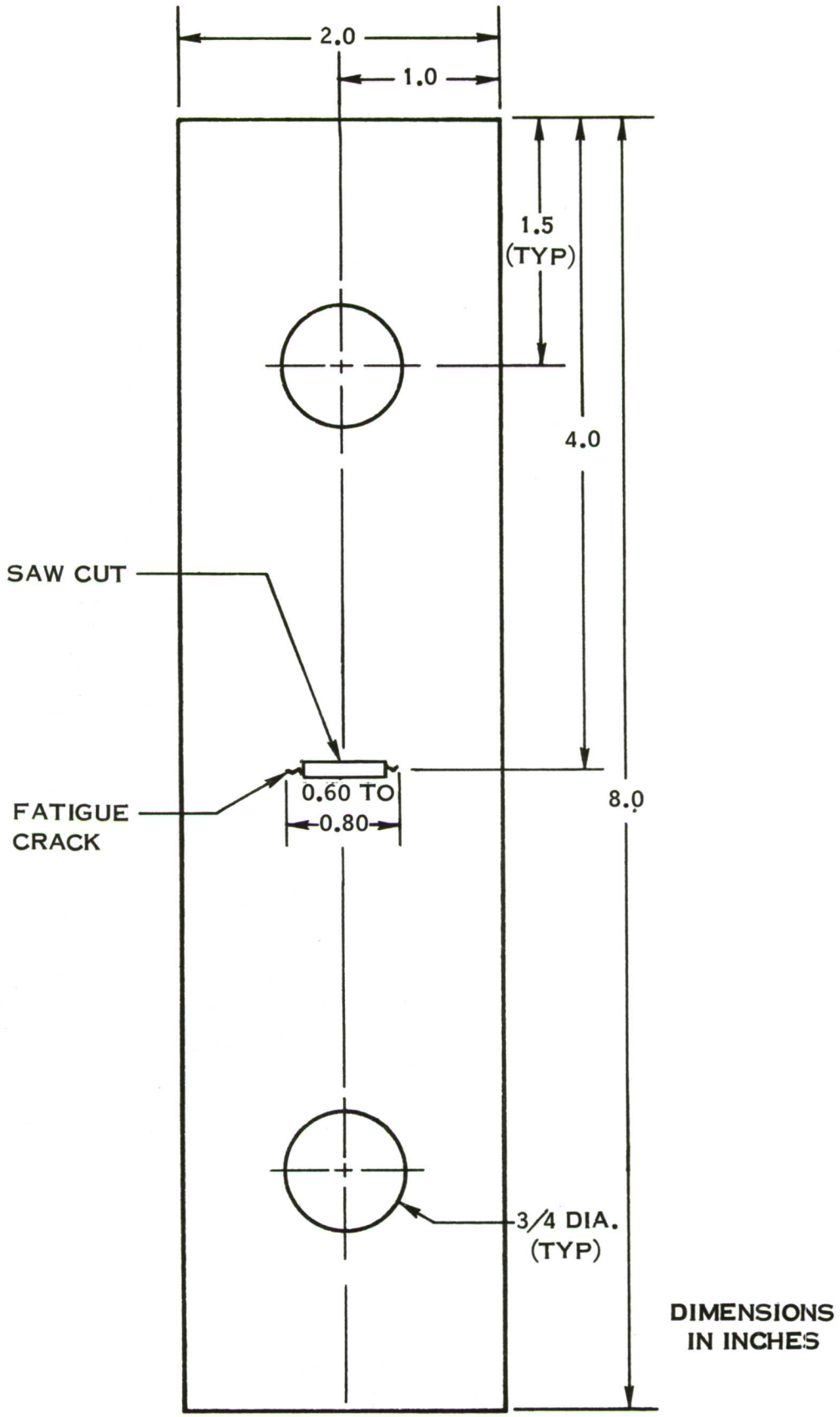

FIGURE 6 — NOTCH TOUGHNESS TEST SPECIMEN

SECTION 5

HEAT TREATING

The heat treatment that was given to each of the materials is shown in Table 2. In all instances the uniaxial and Poisson's ratio specimens were heat treated along with the biaxial specimens. The procedures that were used in heat treating the steels and the titanium alloy are outlined below.

B-120VCA Titanium Alloy

Special hold-down fixtures were utilized during heat treating to prevent warpage in the biaxial specimen. A description of the fixtures is shown by Figure 7. No special precautions were required to prevent bulging in the test section since the depressions were machined after aging. The fixtures were clamped to the biaxial specimens throughout the 60 hour age at 900° F and the "flash anneal" treatment at 1050° F for 30 minutes.

5CrMoV Steel

The hold-down fixtures shown in Figure 7 were used to heat treat the 5CrMoV biaxial specimens. However, since the depressions were machined into these specimens before heat treating, a metal pad was inserted in the depressions to prevent bulging. As a special precaution, NO-CARB was painted on the surface of the biaxial, uniaxial and Poisson's ratio specimens. After the austenitizing treatment at 1850° F the specimens were cleaned and recoated with NO-CARB. The hold-down fixtures were clamped to the biaxial specimens throughout the entire heating and cooling cycles.

D6A-C Steel

The D6A-C biaxial specimens were coated with NO-CARB and clamped in the hold-down fixtures shown by Figure 7 for the normalizing treatment. Again, the metal pads were inserted in the depressions to prevent bulging. After cooling to room temperature in argon, the biaxial, uniaxial and Poisson's ratio specimens were cleaned and recoated with NO-CARB. Since the D6A-C material requires a fast cooling rate from the 1550° F austenitizing temperature, there was not sufficient time to remove the biaxial specimens from the hold-down fixtures. Therefore, 1/2 inch thick metal spacers were inserted between the specimens and the fixtures at the clamping bolts and the center of the metal pads in order that the specimens could air cool in the fixtures. The metal pads prevented the depression from bulging due to the differential cooling rate between the thin test section and the thicker portion of the specimen. After austenitizing, the specimens were cleaned, recoated with NO-CARB and tempered. The biaxial specimens were tempered in the hold-down fixtures.

X-200 Steel

The procedures for heat treating the X-200 specimens were similar to those for the 5CrMoV specimens. However, since this material requires a higher cooling rate from the austenitizing temperature, the biaxial specimens were removed from the hold-down fixtures immediately after removing from the furnace. The specimen temperature was approximately 1400° F when the fixtures were unbolted from the specimens.

TABLE 2 - HEAT TREAT PROCESS

Material	Process	Strength Level	Phase
5CrMoV	Preheat at 1550°F; austenitize at 1850°F for 1/2 hour in argon; cool in air; double temper for 2 hours at 1000°F	High	I, II, IV, V
X-200	Austenitize at 1750°F for 1/2 hours in argon; cool in air; temper for one hour at 600°F	High	I, II, IV
D6A-C	Normalize at 1650°F for one hour in argon; cool to below 150°F in argon; harden at 1550°F for one hour in argon; cool in air; double temper for 2 hours at 600°F	High	I
B-120VCA	Age solution treated material at 900°F for 60 hours followed by 30 minutes at 1050°F	High	I, II, IV
2014-T6	As received T6 condition	High	I, II
5CrMoV	Preheat at 1550°F; austenitize at 1850°F for 1/2 hour in argon; cool in air; double temper for 2 hours at 1050°F	Medium	III
X-200	Austenitize at 1750°F for 1/2 hour in argon; cool in air; temper for one hour at 800°F	Medium	III
B-120VCA	Age solution treated material at 900°F for 60 hours followed by 20 minutes at 1100°F	Medium	III
5CrMoV	Preheat at 1550°F; austenitize at 1850°F for 1/2 hour in argon; cool in air; double temper for 2 hours at 1100°F	Low	III, V
X-200	Austenitize at 1750°F for 1/2 hour in argon; cool in air; temper for one hour at 1000°F	Low	III
B-120VCA	As received solution treated condition	Low	III

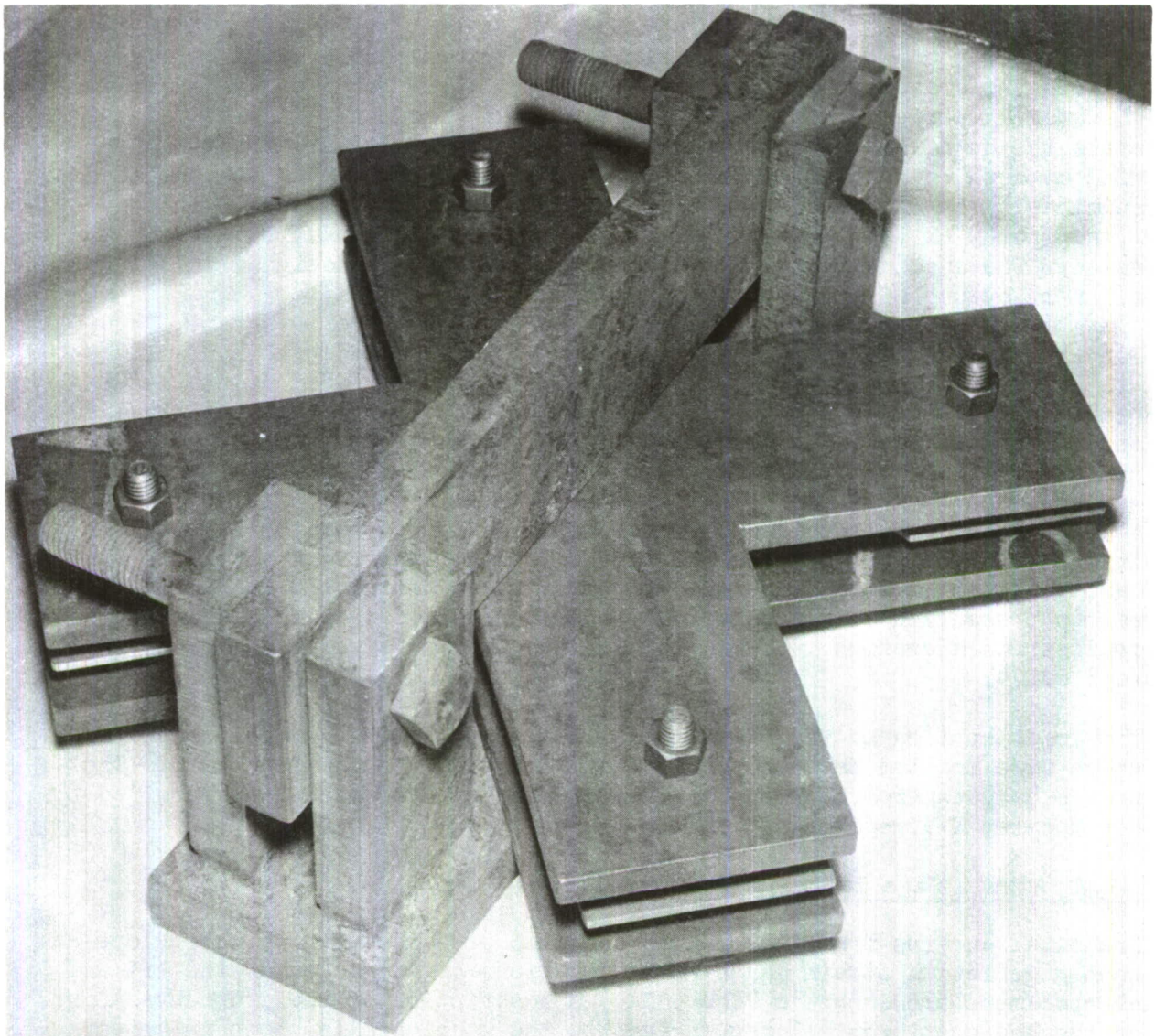

THE WEDGE WHICH IS DRIVEN BETWEEN THE CROSS SHAPED HOLD–DOWN PLATES AND THE RECTANGULAR FIXTURE IS NOT SHOWN. THIS WEDGE WAS USED TO PROVIDE ADDITIONAL CLAMPING AT THE CENTER OF THE SPECIMEN.

FIGURE 7 HOLD–DOWN FIXTURE FOR HEAT TREATING BIAXIAL SPECIMENS.

SECTION 6

TEST SET-UP AND PROCEDURE

6.1 Biaxial Tests

6.1.1 Loading System

The 120,000 pound capacity biaxial loading system consisted of two independent, self-aligning jigs assembled so that synchronized axial loads could be applied to the two mutually perpendicular legs of the biaxial specimen. Figures 8 and 9 illustrate the details of the loading jigs. The vertical jig was rigidly supported at both ends by universal joints. The horizontal jig was designed to be free floating by use of counterweights and low friction pulleys. In this manner, any nonaxial loading that might result from specimen strain was eliminated. The loading system for the horizontal jig was designed to be self-aligning by use of spherical bearings.

For 1:1 loading, the two loading jacks were pressurized with hydraulic fluid supplied by a Marginator Company, Model D, Hydraulic Load Maintainer which was powered by a 3,000 psi hydraulic pump. The load maintainer provided a constant-load-ratio-output to the two hydraulic jacks throughout the entire loading range during the 1:1 tests.

A servo valve was installed in the loading system to monitor the load in the minimum principal stress direction during the 2:1 tests. A schematic of the loading system is shown in Figure 10. For these tests, the load maintainer was used to pressurize only the jack for applying the load in the maximum principal stress direction. The function of the servo valve is described in paragraph 6.1.4.

The loads applied to the biaxial specimen were measured by calibrated load bars which were located between the loading jacks and the test specimen. The strain gage outputs from both the horizontal and vertical load bars were fed to separate Moseley X-Y recorders.

6.1.2 Strain Gage Instrumentation

Principal strains from the biaxial specimen were measured by use of one-half inch gage length strain gages. The locations of the gages on the 1:1 and 2:1 biaxial specimens are shown in Figure 11. A description of the procedures for bonding the low cost, nominal range gages to the specimens is shown in Appendix A. Outputs from the strain gages were recorded on one axis of the X-Y plotters to obtain continuous plots of load versus strain. Under 1:1 loading, two load-strain plots were recorded, one in the longitudinal grain direction and one in the transverse grain direction. Under 2:1 loading, failure could occur in either leg since the specimens were symmetrical. For this reason, gages for measuring the maximum principal strain were placed at both locations. However, strain in the minimum principal stress direction was measured at only one of the points. This was done primarily to reduce the amount of instrumentation required since the failure location could usually be forecasted by comparing the cross-sectional areas at the two critical locations. It was found that failure occurred in the leg which had the smallest cross-sectional area about 90 percent of the time. Thus, under

2:1 loading three load-strain plots were recorded during each test, two in the maximum principal stress direction and one in the minimum principal stress direction.

6.1.3 Failure Wire Instrumentation

The region of the origin of fracture in the biaxial specimen was determined by bonding to the specimen two loops of three mil enamel coated wires which were connected to a semi-conductor device. A description of this device, which has a response time of 10^{-9} seconds, is presented in Appendix B. The wires were bonded to the specimens with a mixture consisting of 50 percent of Type S and 50 percent of Type M Tatnall photoelastic cement by weight. A summary of the results from tests made to evaluate the best type of adhesive for bonding failure wires is presented in Appendix C. The two loops of failure wires were connected to the semi-conductor device so that a small light was turned on if the wire nearest the area of 1:1 or 2:1 stress broke first. Two loops of wires did not pinpoint the origin of fracture, but this scheme did identify the area in which the fracture initiated. With this information the exact origin of fracture could usually be detected by means of low power magnification. The failure wires are shown in Figure 13.

Attempts to determine the sequence of failure of the failure wires by use of E-Put meters were not very successful. The time interval recorded by the E-Put meters between the failure of the two wires was very small for the majority of the tests. This interval was sufficiently small that the probable error in the instrumentation was almost the same as the recorded interval. For this reason, the E-Put meters were discarded. The semi-conductor device is highly reliable and simple to operate. The E-Put meters used had a response time of 10^{-6} seconds.

6.1.4 Function of Servo Valve During 2:1 Stress Ratio Tests

The servo valve monitored the jack load in the minimum principal stress direction so that a state of 2:1 stress was maintained at the same location in the biaxial specimen throughout the entire loading range up to failure. The following discussion summarizes the procedures which were followed in conducting the 2:1 tests.

Under 2:1 biaxial tensile loading, no plastic flow occurs in the minimum principal stress direction if Poisson's ratio is 0.50 in the plastic range. In fact the stress-strain curve in the minimum principal stress direction appears as a straight line up to failure. The shape of the stress-strain curve in the maximum principal stress direction is not unlike the shape of the uniaxial stress-strain curve; i.e., the curve appears as a straight line up to the proportional limit and then curves as the material flows plastically. The principal plastic strains may be expressed in terms of the principal stresses for 2:1 loading as follows:

$$\epsilon_1 = \frac{\sigma_1}{E_s}\left(1 - \frac{\mu_p}{2}\right) = 0.75\,\frac{\sigma_1}{E_s} \qquad (1)$$

$$\epsilon_2 = \frac{\sigma_2}{E_s}\left(0.50 - \mu_p\right) = 0 \qquad (2)$$

as long as the plastic value of Poisson's ratio μ_p is 0.50. As shown in Table 9 μ_p is very close to 0.50 for all materials in this program. The elastic portion

of the principal stress-strain curves that are obtained under 2:1 loading can be expressed as follows:

$$e_1 = \frac{\sigma_1}{E_1}\left(1 - \frac{\mu_{E_1}}{2}\right) \tag{3}$$

$$e_2 = \frac{\sigma_1}{E_2}\left(0.50 - \mu_{E_2}\right) \tag{4}$$

At all times during loading in the elastic range the ratio of the principal strains under 2:1 loading remains constant. The constant is obtained from equations (3) and (4) and may be expressed as follows:

$$\frac{e_1}{e_2} = \frac{E_2}{E_1}\left(\frac{1 - \mu_{E_1}/2}{0.50 - \mu_{E_2}}\right) \tag{5}$$

A 2:1 stress state was maintained in the critical area of the biaxial specimen up to failure by maintaining the straight line stress-strain relationship expressed by equation (4).

In order to obtain a 2:1 stress ratio in the critical location, the jack loads were adjusted until the strain ratio in equation (5) was obtained. The loads were always sufficiently low so that no plastic flow occurred in the test area. The load-strain curves in both the maximum and minimum principal stress directions were always a straight line as long as the test section remained elastic. Once the strain ratio in equation (5) was obtained, the slope of the straight line load-strain curve in the minimum principal stress direction could be calculated. The servo valve was adjusted until this slope was obtained. This slope was maintained up to failure by the servo valve continually monitoring the jack load in the minimum principal stress direction. The load-strain curves recorded from the maximum principal stress direction were similar in shape to a stress-strain curve.

6.2 Uniaxial Tests

The uniaxial tensile specimens and the Poisson's ratio specimens were tested in either a 120,000 pound Baldwin, a 50,000 pound FGT Baldwin or a 160,000 pound FS-160 Reihle test machine. The specimens were tested at a strain rate of 0.005 inches/inch/minute in the elastic range and the total elapsed time during each uniaxial test was three to six minutes.

The uniaxial specimens were instrumented with the one-half inch strain gages described in Appendix A to obtain stress-strain curves. During the initial uniaxial tests, full range load-strain curves were recorded by use of the strain gages. If the gage malfunctioned before the test was completed, the specimen was unloaded, reinstrumented and then loaded to failure. All specimens were refrigerated between loadings to prevent possible occurrence of strain aging. These tests showed that the gages operated satisfactorily up to and beyond the point of maximum load in all cases. For this reason, the remaining specimens were not reinstrumented if the gage malfunctioned before failure occurred. The strain at failure was measured by use of one-half inch gage marks. In most instances the failure strain values as obtained from the strain gages and the gage marks agreed reasonably well.

The Poisson's ratio specimens were instrumented with one-half inch gage length strain gages to obtain elastic Poisson's ratio values. Plots of load versus strain in the loading direction and strain normal to the loading direction were recorded simultaneously by use of two SR-4 drum recorders. Plastic Poisson's ratio values were obtained by determining the width and thickness strains from the unstrained and strained specimen dimensions and the strain in loading direction by use of one-half inch gage length strain gages. The specimens were first strained up to or near maximum load and then were unloaded to measure the permanent set in the width and thickness directions.

6.3 Pressure Vessel Tests

The pressure vessels were instrumented with the one-half inch gage length strain gages described in Appendix A. The gages were placed on the cylindrical portion of the vessels in the areas where the wall thickness was a minimum. Two gages were bonded at each location in order to record the minimum and maximum principal strains. In addition, two HE-121 one-eighth inch gage length strain gages were placed in each of the formed dents in the pressure vessels.

The pressure vessels were pressurized with hydraulic oil by use of a 5,000 psi hydraulic pump. Continuous plots of strain from each strain gage versus pressure were recorded up to failure by use of a 24 channel oscillograph.

6.4 Notch Toughness Tests

The notch toughness specimens were tested in a 50,000 pound FGT Baldwin Test Machine at a load rate of approximately 10,000 pounds per minute. Chart recorder ink was used to measure slow crack growth.

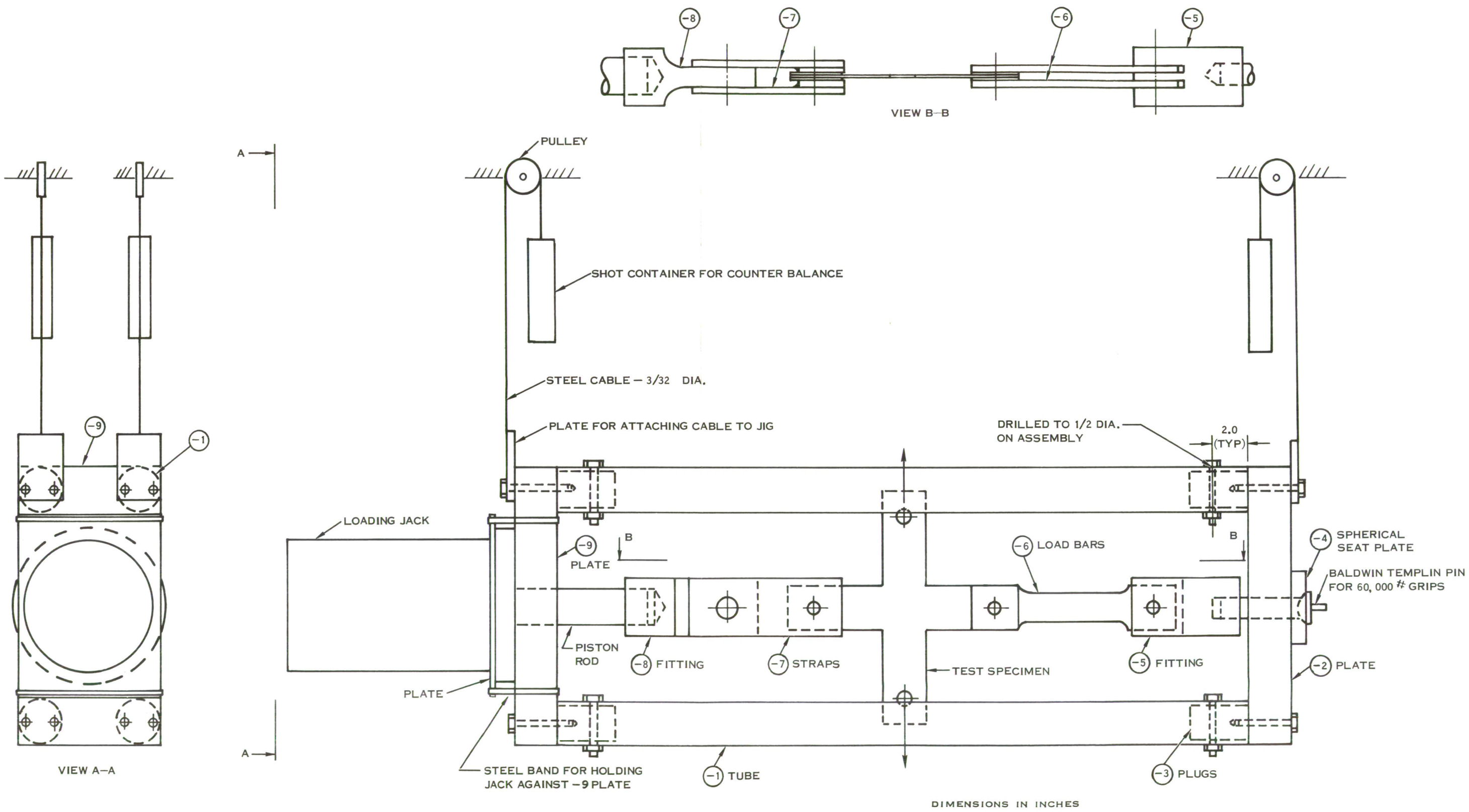

FIGURE 8 HORIZONTAL PORTION OF THE JIG FOR LOADING BIAXIAL SPECIMENS

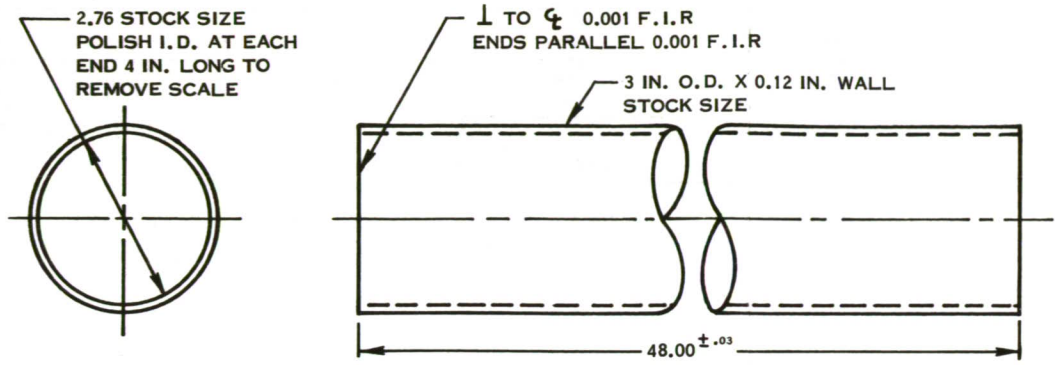

— 1 TUBE
FOUR REQUIRED
4130 — 150 KSI H.T.

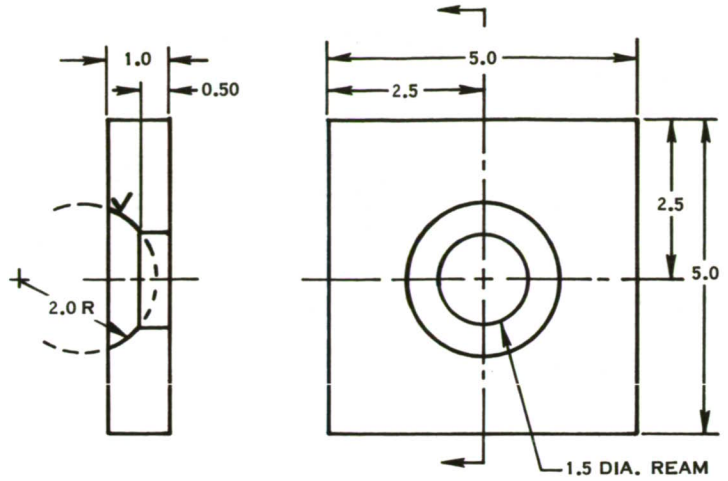

— 4 PLATE
ONE REQUIRED
7075 — T6 ALUM. ALLOY

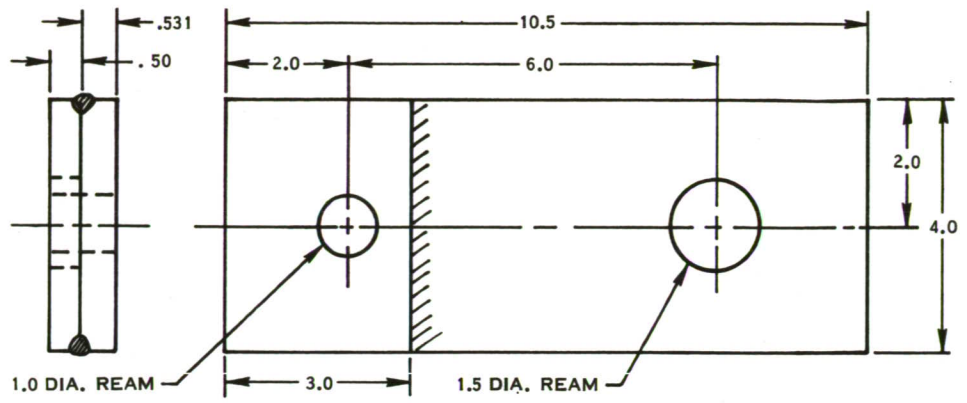

— 7 STRAP
TWO REQ'D — DRILLED & REAMED TOGETHER
4130 — 150 KSI H.T.

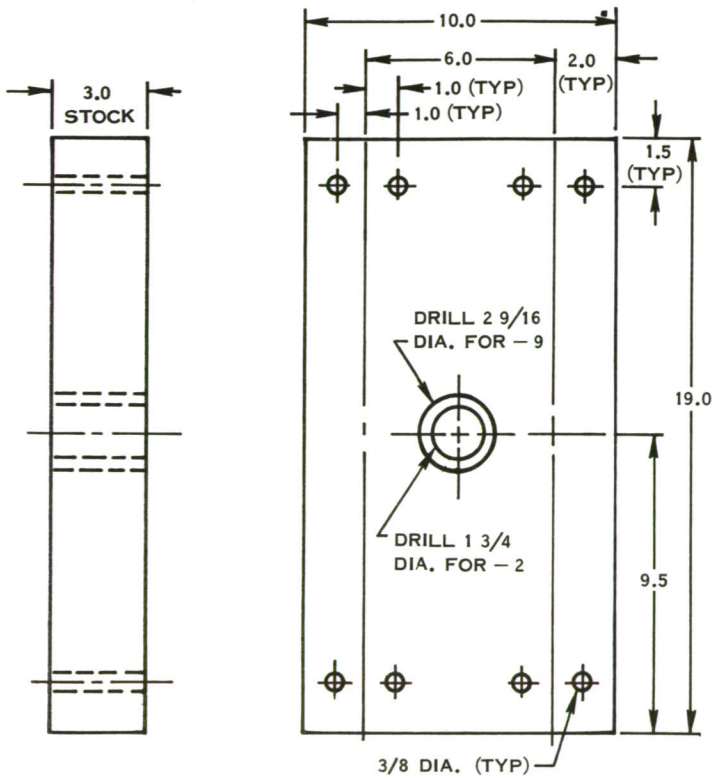

— 2 & — 9 PLATES
ONE OF EACH DASH NO. REQ'D
7075 — T6 ALUM. ALLOY

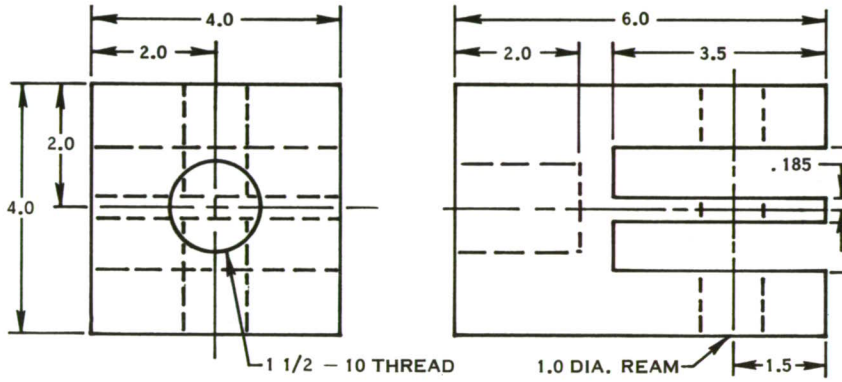

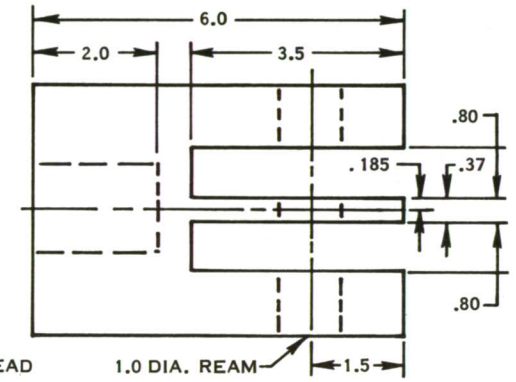

— 5 FITTING
ONE REQUIRED
4340 — 180 KSI H.T.

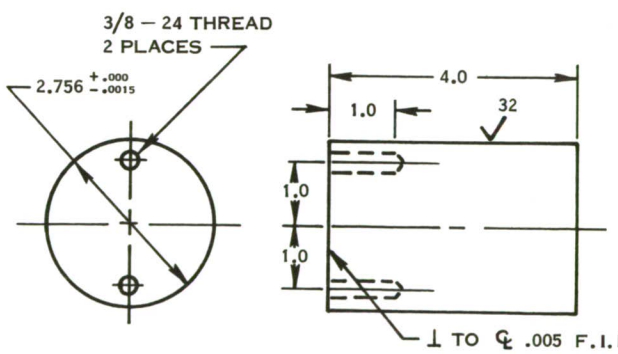

— 3 PLUG
EIGHT REQUIRED
7075 — T6 ALUM. ALLOY

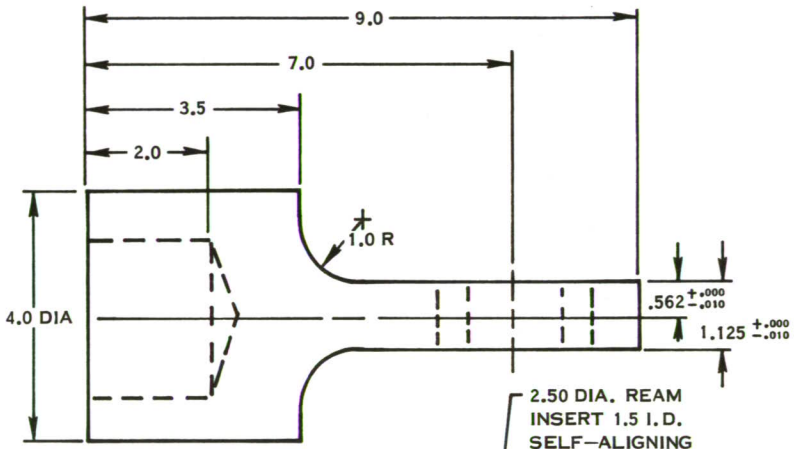

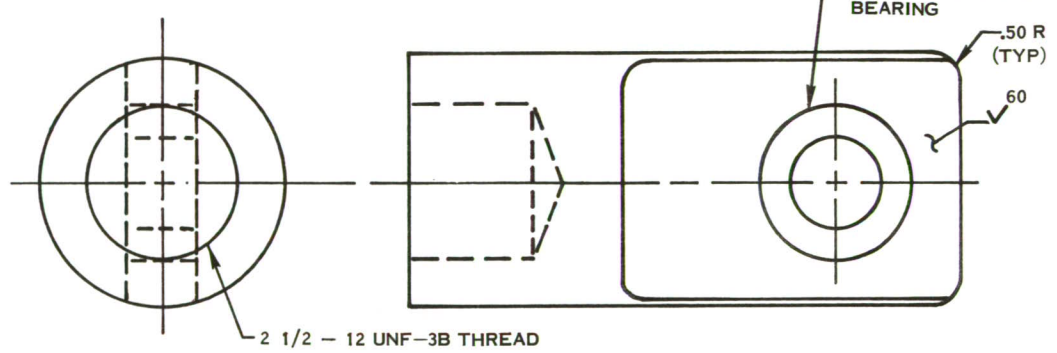

— 8 FITTING
ONE REQUIRED
4340 — 180 KSI H.T.

DIMENSIONS IN INCHES

FIGURE 8 HORIZONTAL PORTION OF THE JIG FOR LOADING BIAXIAL SPECIMENS (CONTINUED)

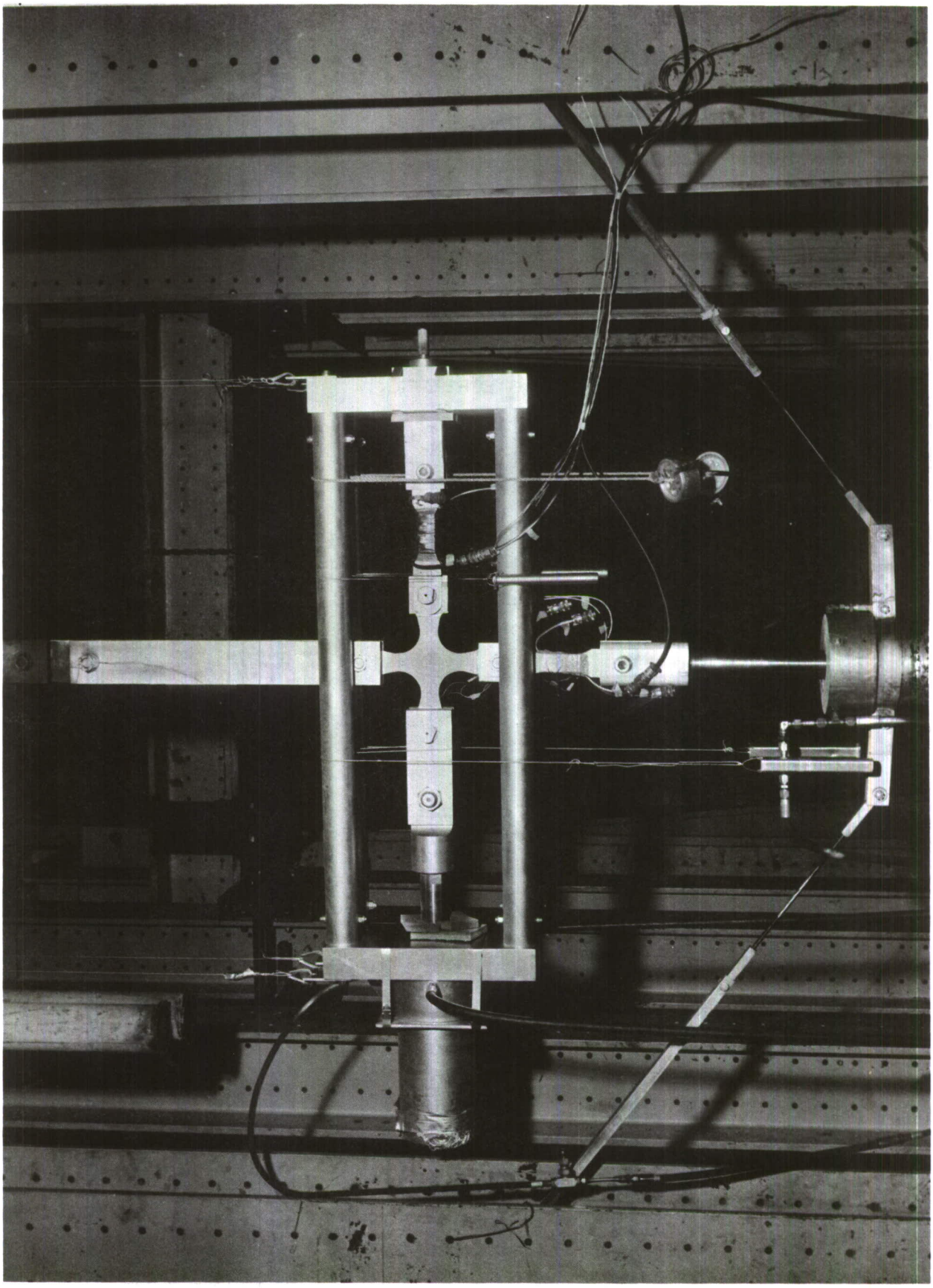

FIGURE 9 — TEST SET-UP FOR LOADING BIAXIAL SPECIMEN.

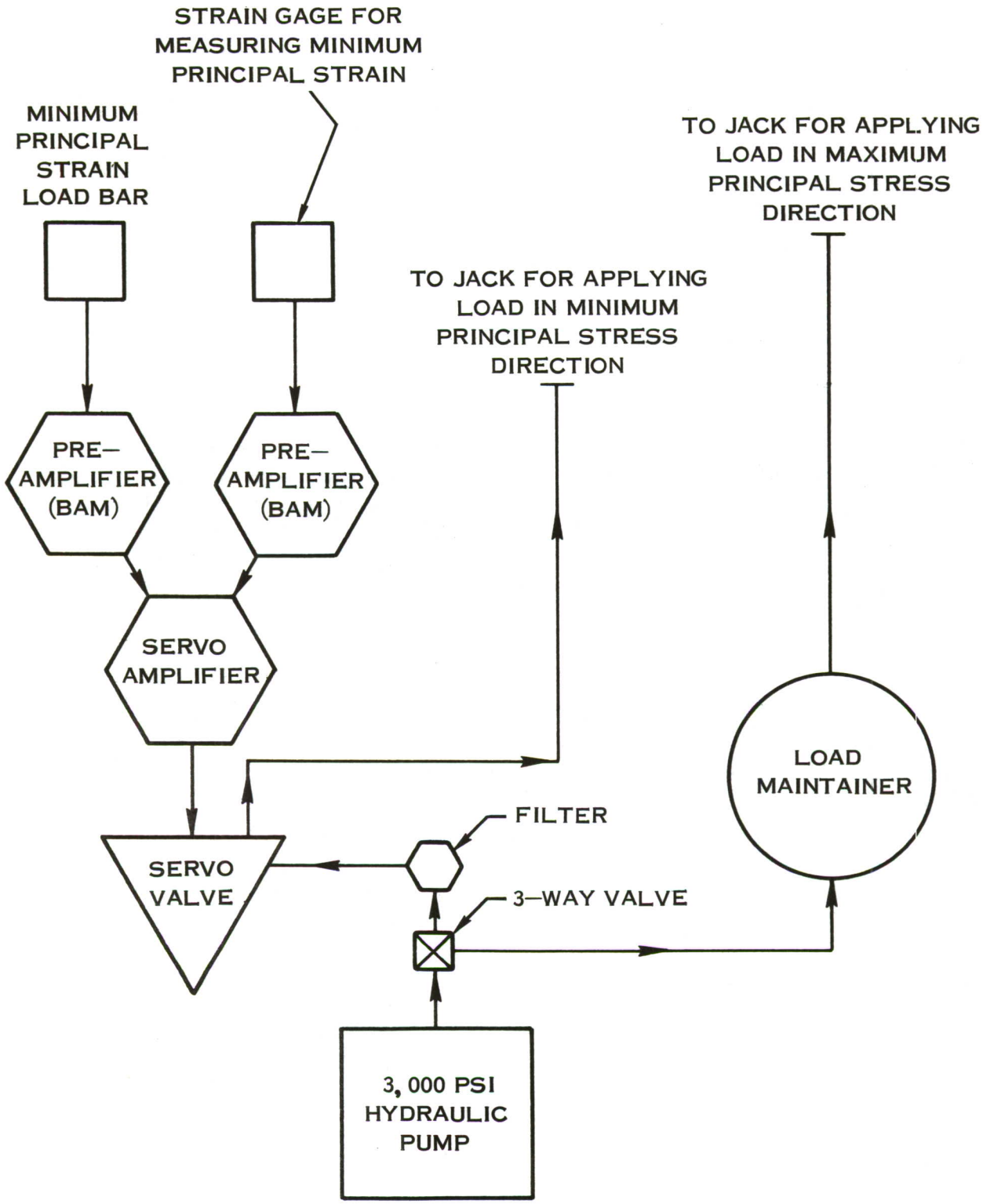

FIGURE 10 SCHEMATIC OF HYDRAULIC INSTALLATION FOR TESTING BIAXIAL SPECIMEN UNDER 2:1 LOADING

NOTES:

1. FAILURE WIRES FOR 1:1 TESTS CENTERED ABOUT 1:1 STRAIN GAGE LOCATION
2. FAILURE WIRES FOR 2:1 TESTS CENTERED ABOUT 2:1 STRAIN GAGE LOCATION
3. LOCATION OF INNER FAILURE WIRES IS SHOWN BELOW BY DASHED CIRCLES
4. REFERENCE FIGURES 13 AND 16

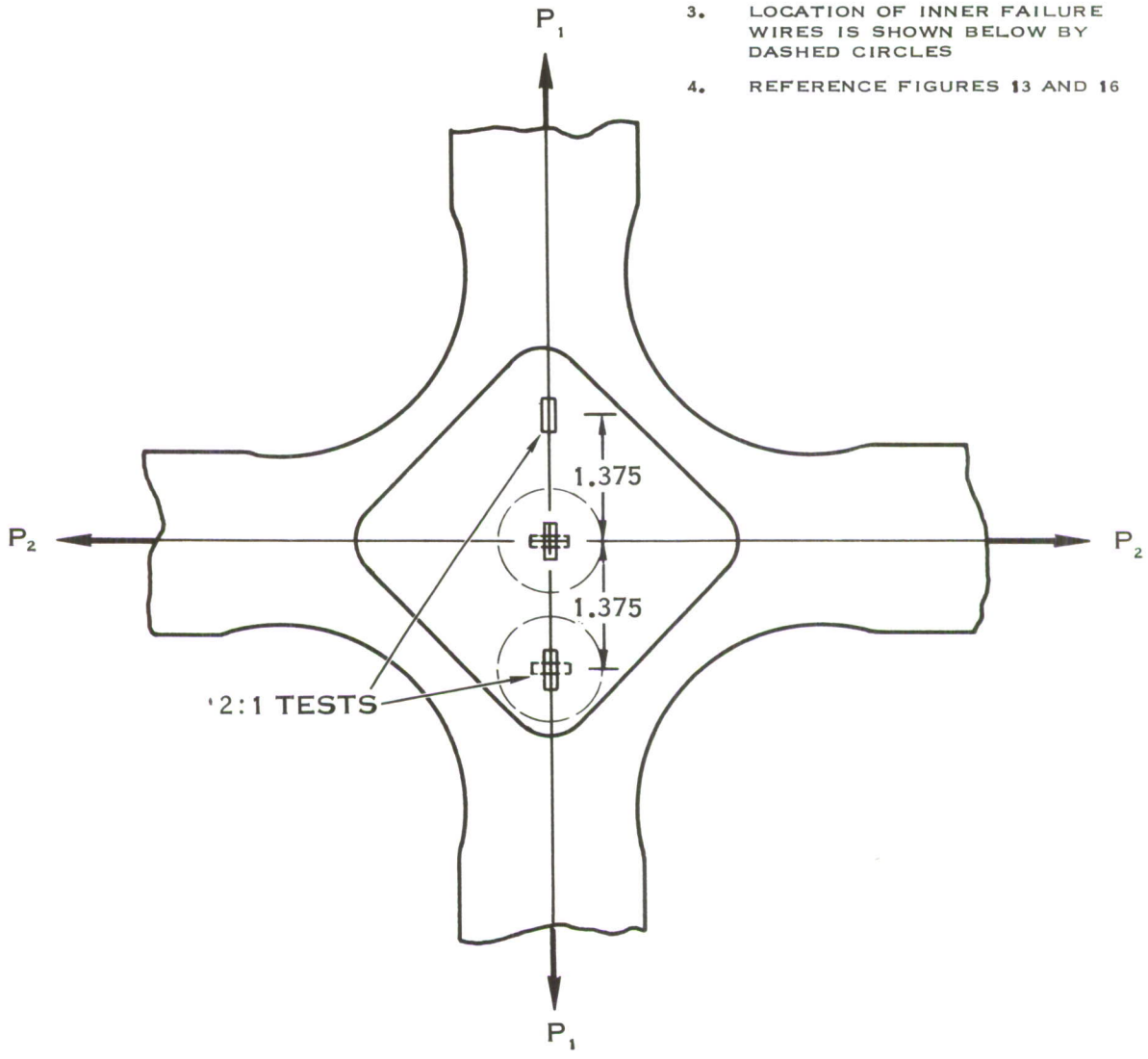

FIGURE 11 STRAIN GAGE LOCATION FOR MEASURING PRINCIPAL STRAINS DURING 2:1 TESTS AND 1:1 TESTS

SECTION 7

SUMMARY OF UNIAXIAL AND POISSON'S RATIO TEST RESULTS

Tables 3 through 8 summarize the uniaxial tensile properties of the test materials. True stress and strain values were obtained from nominal stress and strain values by use of equations shown in Appendix D which are as follows:

$$\sigma = \sigma'(1 + \epsilon') \tag{6}$$

$$\epsilon = \ln(1 + \epsilon') \tag{7}$$

The strain hardening coefficient n was obtained by measuring the geometric slope of the plastic portion of the true stress-strain curve plotted on a log-log scale. The fictitious stress σ_o was calculated from the Ludwik law by using a succession of different points on the plastic portion of the true stress-strain curve and taking an average of the σ_o values thus obtained. The Ludwik law, which is described in Appendix D, can be expressed as follows:

$$\sigma_o = \frac{\sigma}{\epsilon^n} \tag{8}$$

The nominal and true uniaxial stress-strain curves obtained from the test materials are shown in Appendix E. The nominal stress-strain curves were converted to true stress-strain curves by use of equations (6) and (7).

One specimen from each material was loaded in the longitudinal grain direction and one specimen from each material was loaded in the transverse grain direction to determine elastic and plastic Poisson's ratio values. A summary of the values obtained is shown in Table 9. The elastic Poisson's ratio values were calculated from the ratio of normal to axial strain gage readings. Plastic Poisson's ratio values were calculated from the following relation:

$$\mu_p = \frac{1}{2}\left(\frac{\epsilon'_{pw}}{\epsilon'_{pa}} + \frac{\epsilon'_{pt}}{\epsilon'_{pa}}\right) \tag{9}$$

where ϵ'_{pw}, ϵ'_{pt} and ϵ'_{pa} are the nominal plastic strains in the width, thickness and loading directions, respectively.

TABLE 3 - UNIAXIAL TENSILE PROPERTIES OF MATERIALS TESTED IN PHASE I

MATERIAL(1)	SPEC. NO.	GRAIN	σ'_u ksi	σ_u ksi	σ_y ksi	E 10^6 psi	ϵ'_u %	ϵ_u %	$\epsilon'_{MAX.}$ 1/2" GAGE %	n	σ_o ksi
2014-T6	L1	Long.	72.2	77.9	66.3	10.0	7.2	6.95	11.8	0.091	98.75
	L2	Long.	71.1	78.1	65.2	10.0	9.2	8.8	15.3	0.084	94.85
	T3	Tran.	70.8	76.4	63.6	9.5	7.2	6.95	10.4	0.081	93.75
	T4	Tran.	72.1	78.6	63.9	9.7	8.2	7.9	12.4	0.088	97.50
B-120 VCA	L1	Long.	184.0	197.0	168.0	16.9	7.8	7.46	7.8	0.09	253.0
	L2	Long.	183.0	194.0	168.0	16.5	6.4	6.18	6.4	0.09	253.0
	T1	Tran.	188.0	199.0	177.0	17.9	5.9	5.70	5.9	0.06	239.0
	T2	Tran.	188.0	202.0	178.0	17.2	7.8	7.51	7.8	0.06	239.0
5CrMoV	L1	Long.	275.0	305.0	252.5	28.2	8.1	10.6	11.4	0.082	367.5
	L2	Long.	275.0	309.0	252.5	29.5	8.1	14.9	16.3	0.082	367.5
	T1	Tran.	286.0	305.0	235.0	30.8	5.6	6.6	9.1	0.092	398.0
	T2(2)	Tran.	---	---	234.5	30.9	---	----	----	----	----
D6A-C	L1(2)	Long.	---	---	---	30.3	---	----	----	----	----
	L2	Long.	274.0	286.0	250.0	30.9	3.2	3.5	4.45	0.084	377.7
	T1	Tran.	272.0	283.0	247.0	30.0	3.2	3.6	5.02	0.084	377.7
	T2(2)	Tran.	---	---	228.0	30.2	---	----	----	----	----
X-200	L1	Long.	284.0	302.0	256.5	30.1	4.20	5.60	6.8	0.11	424.0
	L2	Long.	280.0	296.5	247.0	29.0	4.70	6.35	8.0	0.109	414.0
	T1(2)	Tran.	---	---	261.0	30.3	---	----	----	----	----
	T2(2)	Tran.	---	---	257.5	30.4	---	----	----	----	----

(1) All material heat treated to "high" strength level shown by Table 2. All specimens heat treated along with biaxial specimens shown in Table 10.
(2) Failed outside of middle third of test section.

TABLE 4 - UNIAXIAL TENSILE PROPERTIES OF MATERIALS TESTED IN PHASE II

MATERIAL(1)	SPEC NO.	GRAIN	σ'_u ksi	σ_u ksi	σ_y ksi	E 10^6 psi	ϵ'_u %	ϵ_u %	$\epsilon'_{max.}$ 1/2" GAGE %	n	σ_o ksi
2014-T6	L1	Long.	72.2	77.9	66.3	10.0	7.2	6.95	11.8	0.091	98.75
	L2	Long.	71.1	78.1	65.2	10.0	9.2	8.80	15.3	0.084	94.85
	T3	Tran.	70.8	76.4	63.6	9.5	7.2	6.95	10.4	0.081	93.75
	T4	Tran.	72.1	78.6	63.9	9.7	8.2	7.90	12.4	0.088	97.50
B-120 VCA	TL1	Long.	188.0	200.0	171.0	16.3	6.20	5.98	6.2	0.085	256.0
	TL2(2)	Long.	186.0	195.0	168.0	17.9	4.90	4.80	4.9	0.085	256.0
	TT1	Tran.	197.0	208.0	188.0	17.3	5.76	5.60	14.0	0.025	223.5
	TT2	Tran.	195.0	207.0	178.0	17.0	5.50	5.36	5.5	0.049	225.6
5CrMoV	HL4	Long.	266.0	277.0	230.0	31.9	4.00	3.92	9.2	0.071	342.0
	HL5	Long.	268.0	277.0	236.0	31.9	3.40	3.31	3.4	0.065	343.0
	HL12	Long.	295,0	308.0	270.0	28.7	4.40	4.31	22.0	0.060	364.5
	HL13	Long.	273.0	285.0	225.0	30.0	4.24	4.15	23.7	0.060	340.8
	HT4	Tran.	276.0	283.0	220.0	32.0	2.60	2.53	2.6	0.040	326.0
	HT5	Tran.	272.0	280.0	204.0	32.0	2.76	2.72	3.5	0.061	343.2
	HT14	Tran.	275.0	285.0	212.0	30.9	3.52	3.46	19.7	0.068	345.5
	HT15	Tran.	272.0	283.0	198.0	29.1	4.00	3.92	21.8	0.068	345.5
X-200	XL16	Long.	292.0	302.0	240.0	29.6	3.20	3.15	8.8	0.102	424.2
	XL18(2)	Long.	292.0	303.0	240.0	29.6	3.36	3.31	7.8	0.102	424.2
	XT22	Tran.	296.0	306.0	241.0	30.0	3.20	3.15	8.0	0.131	472.4
	XT23	Tran.	296.0	305.0	241.0	29.8	3.04	2.99	7.8	0.131	472.4

(1) All material heat treated to "high" strength level shown in Table 2. All specimens heat treated along with biaxial specimens shown in Table 13.

(2) Failed outside middle third of test section.

TABLE 5 - UNIAXIAL TENSILE PROPERTIES OF MATERIALS TESTED IN PHASE III

MATERIAL	SPEC. (2) NO.	GRAIN	σ_{u}' ksi	σ_{u} ksi	σ_{y} ksi	E 10^6 psi	ϵ_{u}' %	ϵ_{u} %	$\epsilon'_{MAX.}$ 1/2" GAGE	n	σ_{o} ksi
B-120 VCA	TL2(1) (M)	Long.	175.0	185.0	160.0	16.6	5.30	5.29	5.3	0.081	233.0
	TL6(1) (M)	Long.	176.0	185.0	162.0	16.4	4.90	4.80	4.9	0.081	233.0
	TT3(1) (M)	Tran.	182.0	195.0	172.0	16.8	7.20	6.92	7.7	0.065	231.3
	TT4(1) (M)	Tran.	182.0	194.0	168.4	17.3	6.96	6.74	9.9	0.065	231.3
	TL1 (L)	Long.	128.0	135.0	133.0	16.7	5.28	5.15	22.0	0.043	156.0
	TL5 (L)	Long.	133.0	140.0	136.0	15.1	5.20	5.06	20.4	0.060	168.0
	TT7(1) (L)	Tran.	135.5	139.0	133.5	16.3	2.40	2.37	8.1	0.049	161.0
	TT8(1) (L)	Tran.	134.5	138.0	132.0	16.2	2.40	2.37	8.6	0.046	158.0
5CrMoV(3)	HL1 (M)	Long.	254.0	264.0	212.0	31.6	3.76	3.69	23.4	0.069	326.1
	HL2 (M)	Long.	258.0	272.5	217.0	32.3	5.50	5.36	23.5	0.069	331.6
	HT3 (M)	Tran.	260.0	270.6	233.0	31.5	4.16	4.07	23.3	0.069	336.0
	HT4 (M)	Tran.	258.0	266.5	220.0	31.4	3.20	3.15	23.5	0.043	306.0
	HL1 (L)	Long.	216.0	228.0	184.0	32.1	5.76	5.61	27.4	0.029	247.0
	HL4 (L)	Long.	220.0	232.0	184.0	32.5	5.50	5.36	25.4	0.088	301.0
	HT2 (L)	Tran.	218.0	229.6	179.5	32.0	5.28	5.15	27.4	0.053	265.0
	HT3 (L)	Tran.	215.0	226.0	179.5	29.7	5.12	5.00	27.5	0.053	262.5
X-200	XL8 (M)	Long.	259.0	276.5	218.0	31.2	6.80	6.58	8.4	0.080	341.0
	XL17 (M)	Long.	258.0	274.5	218.0	29.8	6.40	6.20	7.8	0.080	341.0
	XT21 (M)	Tran.	260.0	276.0	204.0	30.1	6.30	6.11	7.9	0.088	355.0
	XT24 (M)	Tran.	258.0	273.5	204.0	30.4	6.00	5.84	8.9	0.074	334.0
	XL14(1) (L)	Long.	239.0	251.0	190.0	31.8	4.80	4.69	5.7	0.053	291.0
	XL15 (L)	Long.	237.0	247.0	196.0	31.4	4.12	4.04	5.8	0.052	287.0
	XT5 (L)	Tran.	240.0	253.5	196.0	31.6	5.36	5.22	11.2	0.066	302.3
	XT20 (L)	Tran.	237.0	248.5	188.5	30.4	4.80	4.69	9.4	0.066	302.3

(1) Failed outside middle.
(2) (M) indicates "medium" strength level, (L) indicates "low" stength level as shown in Table 2.
(3) 5CrMoV specimens heat treated along with biaxial specimens shown in Table 11.

TABLE 6 - UNIAXIAL TENSILE PROPERTIES OF MATERIALS TESTED IN PHASE IV-WELDED SPECIMENS

MATERIAL (1)	SPEC. NO.	GRAIN	σ'_u ksi	σ_u ksi	σ_y ksi	E 10^6 ksi	ϵ'_u %	ϵ_u %	$\epsilon'_{MAX.}$ 1/2" GAGE	n	σ_o ksi
2014-T6	AWL-1	Long.	46.0	48.0	32.0	9.9	4.4	4.3	4.4	0.24	98.7
	AWL-2	Long.	46.5	51.5	31.5	12.0	7.6	7.1	7.6	0.22	88.6
	AWT-1	Tran.	42.0	43.0	24.5	11.2	2.5	2.4	2.5	0.24	90.0
	AWT-2	Tran.	44.3	45.5	27.0	12.0	3.0	2.8	3.0	0.21	105.0
B-120VCA	TWL-1	Long.	160.4	172.0	145.0	16.0	5.5	5.2	5.5	0.052	198.7
	TWL-2	Long.	159.0	171.0	142.0	15.0	8.6	8.1	8.6	0.052	192.8
	TWT-1	Tran.	170.0	180.0	153.0	16.2	5.1	4.7	5.1	0.059	212.0
	TWT-2	Tran.	162.0	172.0	149.0	16.0	5.4	5.3	5.4	0.052	199.0
5CrMoV(2)	HWL-1	Long.	279.0	294.0	220.0	31.6	4.8	4.7	8.2	0.063	352.0
	HWL-2	Long.	278.0	291.0	202.0	30.4	4.2	4.1	8.2	0.070	356.0
	HWL-3	Long.	280.0	297.0	230.0	29.9	5.5	5.3	8.1	0.062	338.0
	HWL-4	Long.	268.0	283.0	216.0	30.7	4.8	4.7	8.2	0.063	352.5
X-200	XWL-1	Long.	275.0	288.5	246.0	30.0	4.2	4.1	8.2	0.044	329.0
	XWL-2	Long.	278.0	285.0	260.0	31.0	1.8	1.8	4.3	0.040	329.0
	XWT-1	Tran.	277.0	287.0	244.0	31.0	2.8	2.8	2.8	0.070	366.0
	XWT-2	Tran.	275.0	290.0	240.0	30.0	4.8	4.7	5.8	0.048	331.5

(1) All material except 2014-T6 heat treated to "high" strength level shown in Table 2. 2014-T6 specimens tested in as-welded condition.

(2) 5CrMoV specimens heat treated along with biaxial specimens shown in Tables 12 and 15.

TABLE 7 - UNIAXIAL TENSILE PROPERTIES OF 5CrMoV MATERIAL TESTED IN PHASE V

MATERIAL	SPEC. (2) NO.	GRAIN	σ'_u ksi	σ_u ksi	σ_y ksi	E 10^6 psi	ϵ'_u %	ϵ_u %	$\epsilon'_{MAX.}$ 1/2" GAGE	n	σ_o ksi
5CrMoV	HHL-1 (H)	Long.	280.0	296.0	222.0	29.2	4.5	4.40	7.9	0.049	337.2
	HHL-2 (H)	Long.	277.0	293.0	222.0	29.5	4.6	4.50	8.0	0.049	335.0
	HHT-1(1)(H)	Tran.	- - -	- - -	221.0	31.1	- - -	- - -	- - -	- - -	- - -
	HHT-2 (H)	Tran.	274.0	290.0	221.0	29.2	4.6	4.50	8.3	0.052	335.0
	HLL-1 (L)	Long.	239.0	260.0	200.0	29.8	7.4	7.13	8.2	0.073	310.7
	HLL-2 (L)	Long.	228.0	244.0	194.0	31.0	6.3	6.11	8.0	0.063	289.0
	HLT-1(1)(L)	Tran.	230.0	242.2	198.0	31.8	4.5	4.40	- - -	0.058	288.0
	HLT-2 (L)	Tran.	222.0	237.0	185.0	31.0	6.1	5.93	8.5	0.056	278.0

(1) Failed outside of middle third of test section.
(2) (H) indicates "high" strength level, (L) indicates "low" strength level as shown in Table 2. Specimens heat treated along with cylindrical pressure vessels.

TABLE 8 - UNIAXIAL TENSILE PROPERTIES OF MATERIALS TESTED IN PHASE VI

MATERIAL	SPEC. (1) No.	GRAIN	σ_u' ksi	σ_y ksi	ϵ' max. 1/2" GAGE %
2014-T6	T3 (H)	Tran.	70.8	63.6	10.4
	T4 (H)	Tran.	72.1	63.9	12.4
B-120VCA	TT-1 (H)	Tran.	178.0	168.0	6.0
	TT-2 (H)	Tran.	189.0	178.0	12.0
5CrMoV	HL-4 (H)	Long.	290.0	241.0	16.0
	HL-5 (H)	Long.	288.0	239.0	22.0
	HT-4 (H)	Tran.	285.0	234.0	14.0
	HT-5 (H)	Tran.	288.0	236.0	7.3
	HL-4 (M)	Long.	265.0	222.0	7.5
	HL-5 (M)	Long.	268.0	225.0	16.0
	HL-1 (L)	Long.	251.0	212.0	22.0
	HT-1 (L)	Tran.	251.0	208.0	20.0
	HT-2 (L)	Tran.	254.0	211.0	22.0
D6A-C	D-4 (H)	Long.	274.0	250.0	8.0
	D-2 (H)	Tran.	279.0	253.0	6.0
	D-3 (H)	Tran.	279.0	253.0	8.0
X-200	X-11 (H)	Long.	289.0	237.0	16.0
	X-13 (H)	Long.	298.0	245.0	14.0

(1) (H) indicates "high" strength level, (M) indicates "medium" strengt level, (L) indicates "low" strength level as shown in Table 2. Specime heat treated along with notch toughness specimens.

TABLE 9 - ELASTIC AND PLASTIC POISSON'S RATIO VALUES

MATERIAL	GRAIN DIRECTION	μ_E	μ_P
2014-T6	Long. Tran.	0.33 0.27	0.48 0.52
B-120VCA	Long. Tran.	0.28 0.34	0.53 0.47
5CrMoV	Long. Tran.	0.26 0.30	0.52 0.50
D6A-C	Long. Tran.	0.27 0.29	0.52 0.51
X-200	Long. Tran.	0.27 0.27	0.47 0.48

SECTION 8

SUMMARY OF 1:1 BIAXIAL TEST RESULTS

8.1 General

Tests under 1:1 biaxial tension stress ratio loading were conducted in Phase I on all five of the test materials and in Phases III and IV on the 5CrMoV tool steel. The objectives of the tests in Phase I were to (1) develop a suitable specimen configuration for determining allowable biaxial strain under 1:1 loading and (2) generate biaxial stress-strain data under 1:1 loading from several high strength materials. All uniaxial and biaxial specimens in Phase I were heat treated to the "high" strength level as shown by Table 2.

The purpose of the tests in Phase III was to demonstrate the effect of strength level on allowable biaxial strain. Pressure vessel tests (Ref. 1, 2, and 3) have shown that unpredictable behavior is often encountered when the material is processed to achieve a very high strength level. Brittle fractures are often experienced in some of these materials even though they exhibit appreciable uniaxial elongation. It is probable that most ultra-high-strength materials would perform satisfactorily in pressurized components if there were no structural discontinuities that produce stress concentrations. However, most practical structures contain stress concentrations which require some plastic flow in order that high nominal stress levels can be obtained. From tests, such as those reported in references 1, 2 and 3, it appears that a threshold may exist for some materials above which the behavior under biaxial loading is inferior. The establishment of such a threshold should be of great value in selecting and processing materials for pressurized component applications.

Half of the Phase III 5CrMoV biaxial and uniaxial specimens were heat treated to a "medium" strength and half were heat treated to a "low" strength level as shown by Table 2. In addition to the 5CrMoV biaxial and uniaxial tests, uniaxial tests were conducted in Phase III on specimens fabricated from the B-120VCA titanium and X-200 steel materials. Half of the specimens from each material were heat treated to a "medium" strength level and half were heat treated to a "low" strength level as shown by Table 2. These tests were conducted to obtain data which could be used to predict the strain performance of these materials under biaxial loading. A discussion of these results is presented in Section 13.

The purpose of the biaxial tests in Phase IV was to determine weld joint efficiency based on stress and strain under biaxial tensile loading. Experience in rocket motor case testing indicates that welded joints are frequently a contributing factor when premature failure occurs. Welding may produce mismatch of joining parts, peaking at the seam, residual stresses, warping and internal stress raisers caused by weld voids. These types of imperfections can usually be minimized to a great extent by use of rigid manufacturing procedures. However, one factor which cannot be completely overcome in high strength materials is the lack of homogeneity between the weld metal and the parent material. This lack of homogeneity usually results in a difference in strength and ductility between the weld metal and the parent material. The establishment of weld joint efficiency of high strength materials under biaxial loading should be of great value in the design of pressurized components.

Half of the 5CrMoV welded biaxial specimens were tested under 1:1 stress ratio conditions and half were tested under 2:1 stress ratio conditions. All specimens were heat treated to the "high" strength level shown by Table 2. The results from the 2:1 tests are presented in Section 9. In addition to the 5CrMoV welded biaxial and uniaxial specimens, welded uniaxial specimens fabricated from the 2014-T6, B-120VCA and X-200 materials were tested in Phase IV. These tests were conducted to obtain data which could be used to predict the weld joint efficienty of these materials under biaxial loading. A discussion of these results is presented in Section 14.

The semiconductor-failure-wire instrumentation described in Section 7 was utilized as an aid in locating the failure origin. The test was considered to be completely successful only if the failure initiated in or very near the center of the machined depression where a known 1:1 stress ratio existed. The data is not reported in instances when the fracture did not originate in the area of 1:1 stress.

8.2 Test Results From Unwelded Material

The 1:1 biaxial stress-strain curves which were obtained from the test materials are shown in Appendix G. The method which was used to convert load-strain curves to stress-strain curves is presented in Appendix F. At least five specimens from each material were tested, although the origin of fracture in three of the B-120VCA specimens and one of the D6A-C specimens was not in the area of 1:1 stress. No explanation could be found for the erratic behavior of the B-120VCA material. Metallurgical studies did not indicate any apparent metallurgical deficiency nor any evidence of a heat treat error. As shown in Table 3 the ductility obtained from the uniaxial tests was adequate for the strength level of the material. It is possible that the high strength level B-120VCA titanium alloy represents the threshold of poor reliability of the biaxial specimen.

A summary of the principal stresses and principal plastic strains obtained at failure from the test materials is shown by Tables 10 and 11. The fact that higher stresses and/or strains were not always obtained in the same grain direction can be attributed to normal raw data scatter, slight inaccuracies in loading and absence of grain directionality effects. A discussion of the test results shown in Tables 10 and 11 follows:

1. The 2014-T6 aluminum alloy showed little effects of grain directionality in either the failure stresses or strains.

2. The B-120VCA titanium alloy exhibited significant grain directionality under 1:1 loading. The strains measured in the transverse grain direction were only about one half of the strains measured in the longitudinal grain direction. This type of behavior was not observed in the B-120VCA uniaxial tests.

3. The strains recorded in the transverse grain direction of the 5CrMoV steel alloy were on an average about two-thirds of the longitudinal strain values. However, this material showed little effects of grain directionality in the failure stresses. The biaxial strains obtained from the "medium" and "low" strength 5CrMoV specimens were approximately the same, although these values were lower than the values recorded from the "high" strength specimens.

4. In all instances the D6A-C steel alloy displayed slightly higher stresses and lower strains in the transverse grain direction.

5. The strains recorded in the transverse grain direction of the X-200 steel alloy were considerably lower than the longitudinal strain values. In addition, considerable scatter in both the stresses and strains at failure was obtained. Metallurgical studies on this material showed evidence of banding, which is a chemical segregation of the material that results in a non-homogenous structure.

8.3 Test Results From Welded Material

The 1:1 biaxial stress-strain curves which were obtained from the 5CrMoV welded material are shown in Appendix G. The method which was used to convert load-strain curves to stress-strain curves is presented in Appendix F.

A summary of the principal stresses and principal plastic strains obtained at failure from the 5CrMoV welded material is shown by Table 12. The fact that higher failure stress values were obtained from the welded specimens was apparently due to an inadvertently slight difference in the process used to heat treat the unwelded and welded biaxial specimens. This situation makes it difficult to compare the failure strain values obtained from the welded and unwelded material. However, the strain values obtained from the welded specimens were only about 20 per cent less than the values obtained from the unwelded material.

Not unlike the 5CrMoV unwelded material, the strains recorded from the 5CrMoV welded material in the transverse grain direction were about two-thirds of the longitudinal strain values obtained under 1:1 loading. The welded material showed little effects of grain directionality in the biaxial failure stresses.

8.4 Discussion of Types of Fractures Obtained Under 1:1 Loading

Often times engineers associate explosive type failures with materials having low ductility and failures having one fracture path with materials having high ductility. In addition, explosive type failures are often associated with pressurized components. However, the biaxial tests in this program have demonstrated that this kind of reasoning is not necessarily true.

The 2014-T6, X-200, D6A-C and "medium" and "low" strength 5CrMoV 1:1 biaxial specimens fractured into two pieces; i.e., there was only one fracture path in each specimen. Figure 12 illustrates the type of fracture which was obtained in these specimens. However, the fracture behavior of the "high" strength 5CrMoV welded and unwelded specimens and the B-120VCA specimens was vastly different. In all instances the 5CrMoV specimens shattered into several pieces at failure, although the biaxial strains at failure from the unwelded material were relatively high in comparison with the strain values obtained from the same strength level X-200 and D6A-C specimens. Figure 13 illustrates the explosive type of failures obtained from the "high" strength 5CrMoV unwelded specimens. The rings in the depression are the failure wires. Figure 14 illustrates the type of failures obtained from the 5CrMoV welded biaxial specimens. The degree of shattering was significantly greater in the welded specimens. This was probably a result of the difference in the strength level of the unwelded and welded specimens since the existence of the weld joint did not appear to

appreciably alter the allowable biaxial strain. As discussed previously, the higher strength values obtained from the welded specimens were apparently due to an inadvertently slight difference in the process used to heat treat the unwelded and welded biaxial specimens.

As shown by Figure 15, the B-120VCA 1:1 biaxial specimens shattered, but not as severely as the 5CrMoV steel specimens. The biaxial strain values recorded from the B-120VCA specimens were only one-half to two-thirds of the 5CrMoV strain values obtained from the unwelded specimens.

TABLE 10 - PRINCIPAL STRESSES AND PRINCIPAL PLASTIC STRAINS OBTAINED UNDER 1:1 LOADING AT FAILURE-PHASE I

MATERIAL(1)	SPEC NO.	LONGITUDINAL GRAIN σ_R' ~ ksi	LONGITUDINAL GRAIN ϵ_1' ~ %	TRANSVERSE GRAIN σ_R' ~ ksi	TRANSVERSE GRAIN ϵ_1' ~ %
2014-T6	6	67.0	3.05	68.5	2.22
	14	62.0	1.92	61.0	2.14
	15	66.0	3.89	63.0	3.07
	20	60.0	---	60.0	2.50
	21	66.0	2.27	69.0	2.78
	22	63.0	3.23	66.0	5.58
	23	66.0	4.83	67.5	---
	24	61.0	2.08	66.0	4.10
	AVG. =	64.0	3.04	65.0	3.20
B-120VCA	4T	188.0	1.90	188.0	0.91
	5T	173.0	2.40	179.0	1.29
	AVG. =	180.5	2.15	183.5	1.10
5CrMoV	2H	238.0	---	235.0	2.04
	3H	272.0	2.36	266.0	1.97
	4H	264.0	3.22	250.0	2.05
	5H	264.0	4.15	246.0	2.88
	6H	246.0	2.74	262.0	2.13
	AVG. =	256.8	3.12	251.8	2.21
D6A-C	2D	236.0	0.80	245.0	0.59
	3D	244.0	1.72	254.0	1.30
	4D	266.0	0.89	266.0	0.60
	5D	252.0	0.72	258.0	0.71
	AVG. =	249.5	1.03	255.7	0.80
X-200	1X	272.0	1.36	256.0	0.90
	2X	215.0	2.97	225.0	---
	3X	230.0	3.18	219.0	2.13
	4X	242.0	1.52	232.0	1.00
	5X	244.0	2.70	250.0	1.65
	AVG. =	240.6	2.34	236.4	1.42

(1) All specimens heat treated to "high" strength level shown in Table 2.

TABLE 11 - PRINCIPAL STRESSES AND PRINCIPAL PLASTIC STRAINS OBTAINED UNDER 1:1 LOADING AT FAILURE-PHASE III

MATERIAL	SPEC. NO. (1)	LONGITUDINAL GRAIN $\sigma_R' \sim$ ksi	LONGITUDINAL GRAIN $\epsilon_1' \sim$ %	TRANSVERSE GRAIN $\sigma_R' \sim$ ksi	TRANSVERSE GRAIN $\epsilon_1' \sim$ %
5CrMoV	13H (M)	223.0	3.00	238.0	1.85
	14H (M)	244.0	2.60	250.0	1.45
	15H (M)	236.0	2.28	236.0	1.65
	Avg. =	234.3	2.63	241.3	1.65
	16H (L)	216.0	2.45	218.0	1.70
	17H (L)	216.0	2.55	216.0	2.30
	18H (L)	212.0	3.20	212.0	1.95
	Avg. =	214.5	2.73	215.3	1.99

(1) - (M) indicates "medium" strength level, (L) indicates "low" strength level as shown in Table 2.

TABLE 12 - PRINCIPAL STRESSES AND PRINCIPAL PLASTIC STRAINS OBTAINED UNDER 1:1 LOADING AT FAILURE FROM 5CrMoV WELDED SPECIMENS-PHASE IV

MATERIAL	SPEC. NO. (1)	LONGITUDINAL GRAIN $\sigma_R' \sim$ ksi	LONGITUDINAL GRAIN $\epsilon_1' \sim$ %	TRANSVERSE GRAIN $\sigma_R' \sim$ ksi	TRANSVERSE GRAIN $\epsilon_1' \sim$ %
5CrMoV Welded	19H	306.0	1.70	308.0	1.42
	20H	310.0	4.10	304.0	2.52
	21H	322.0	2.04	302.0	1.19
	Avg. =	312.7	2.61	304.7	1.71

(1) All specimens heat treated to "high" strength level as shown in Table 2.

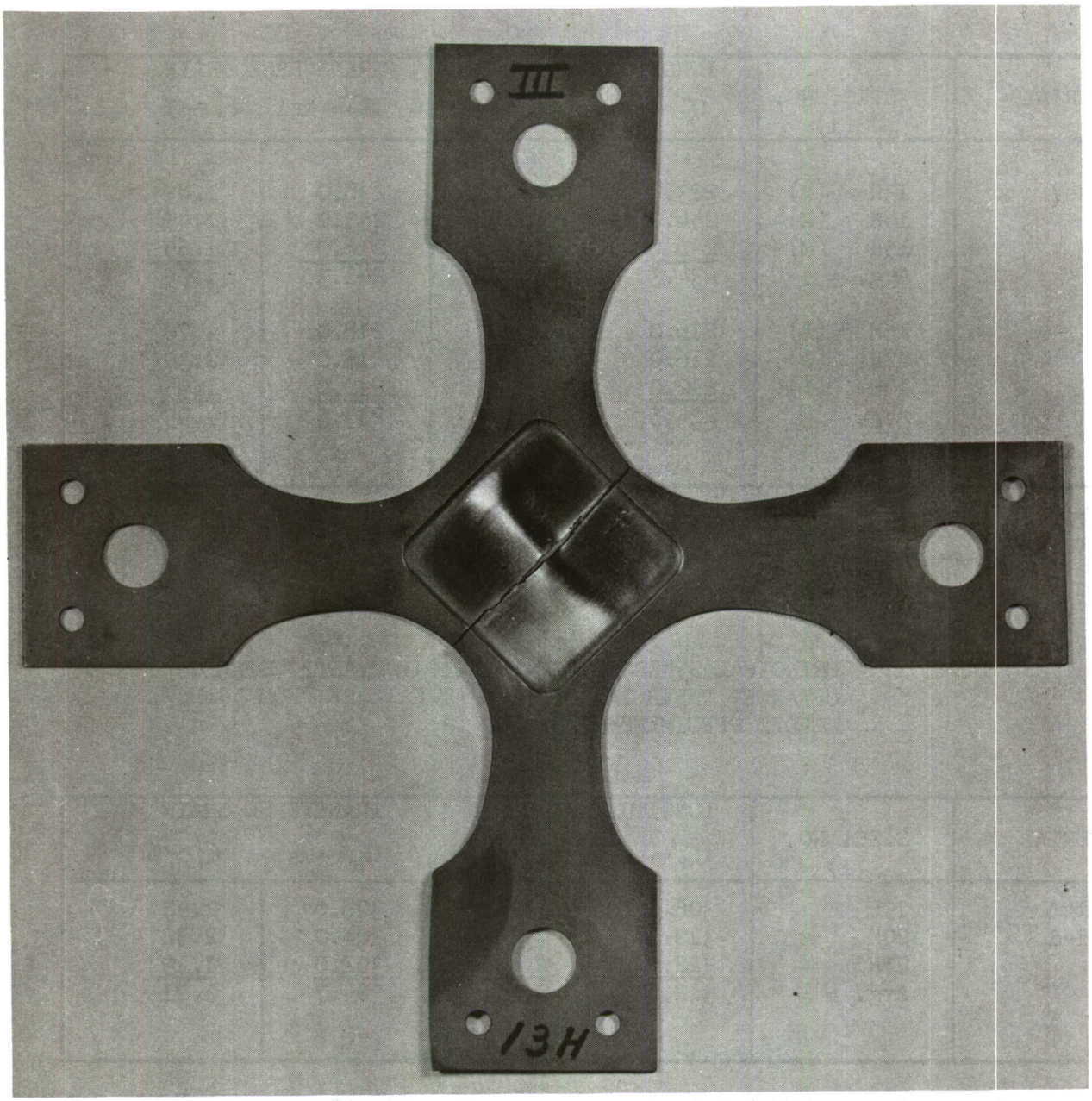

THIS TYPE OF FRACTURE IS REPRESENTATIVE OF THE FRACTURES OBTAINED IN THE 2014 – T6, X–200, D6A–C, AND "LOW" AND "MEDIUM" STRENGTH 5CrMoV 1:1 BIAXIAL SPECIMENS.

FIGURE 12 – FRACTURE PATTERN IN 5CrMoV STEEL BIAXIAL SPECIMEN NO. 13H 1:1 STRESS RATIO – "MEDIUM" STRENGTH – PHASE III

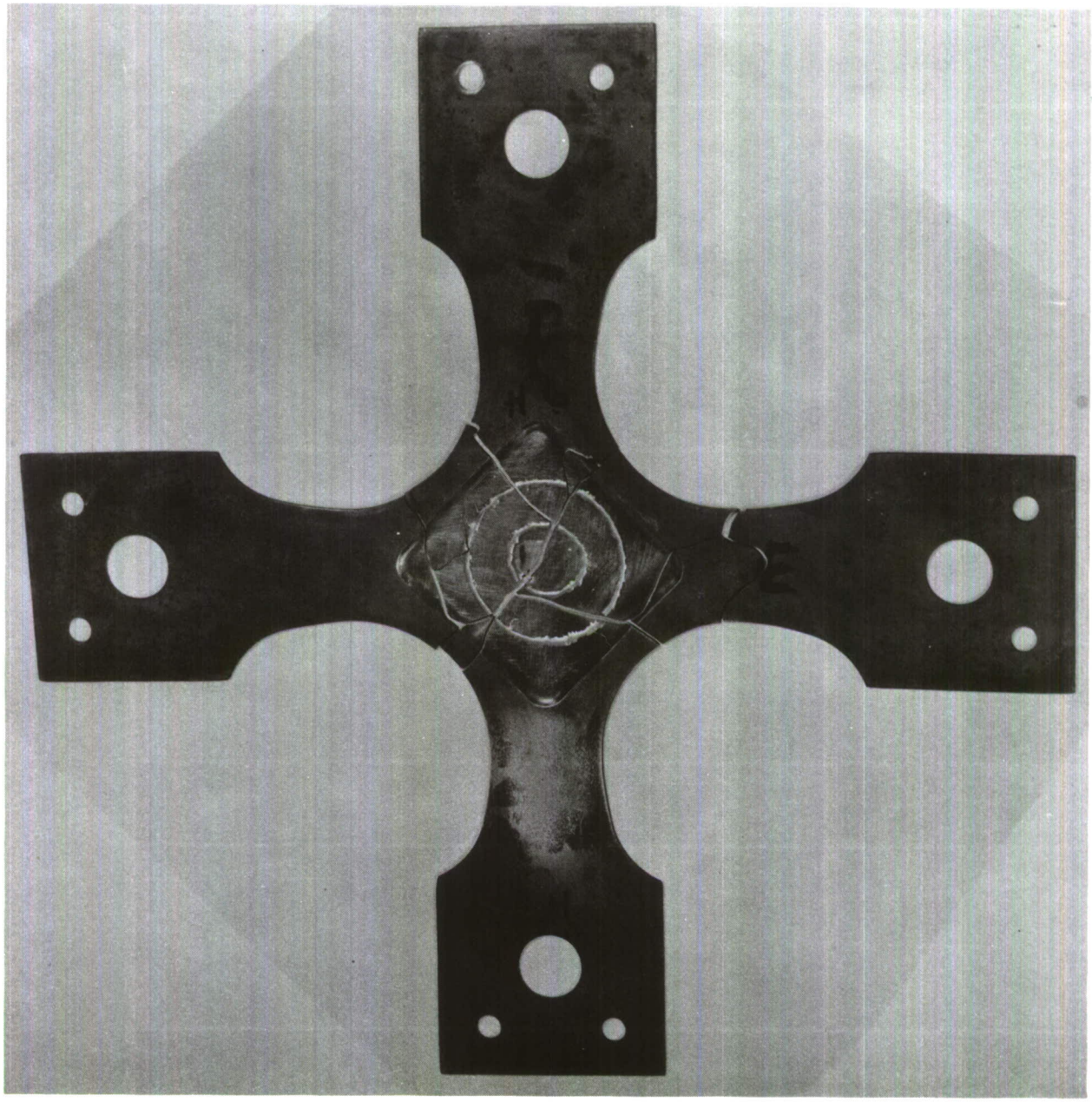

FIGURE 13 — FRACTURE PATTERN IN 5CrMoV STEEL BIAXIAL SPECIMEN NO. 4H 1:1 STRESS RATIO — "HIGH" STRENGTH — PHASE I

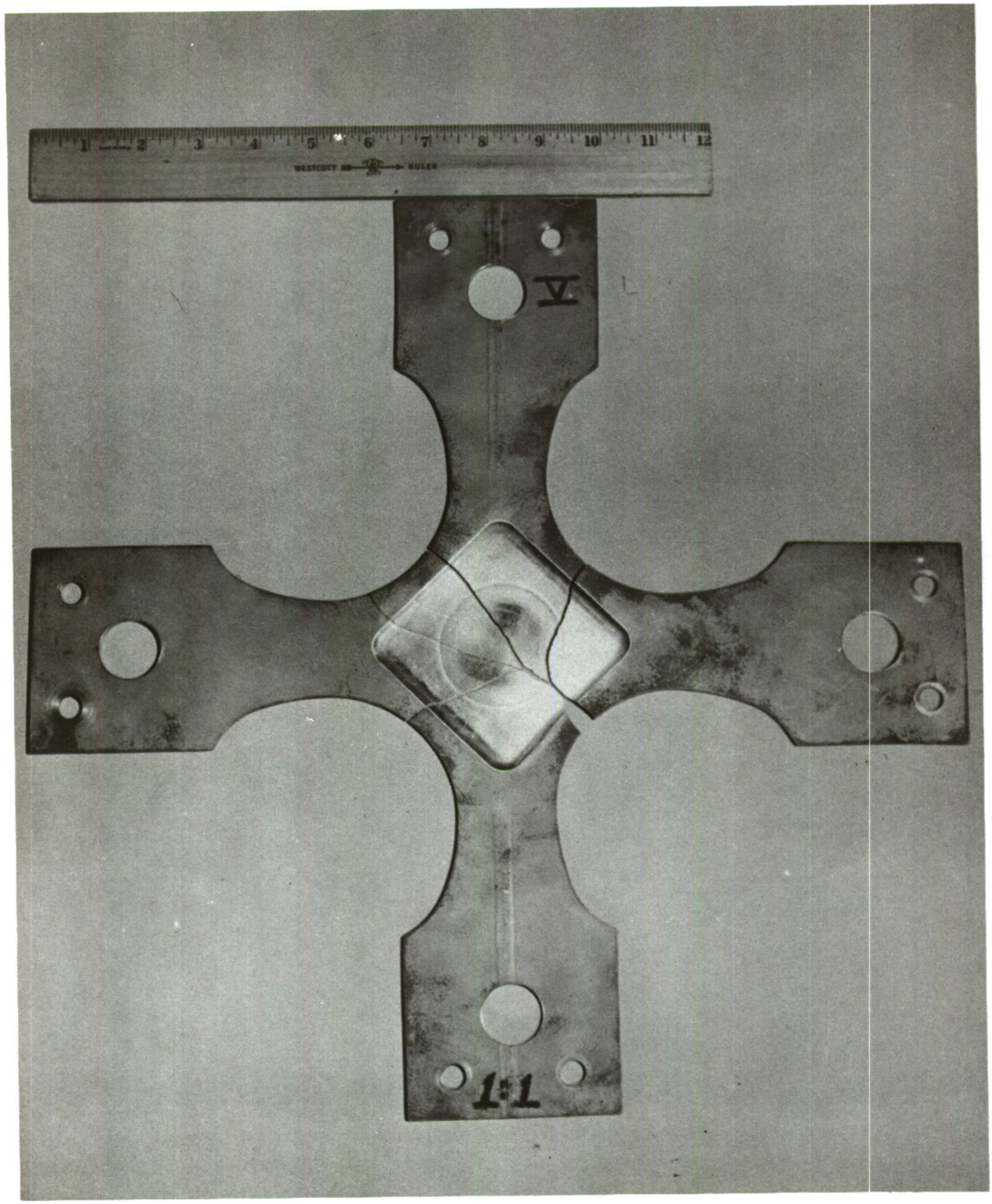

FIGURE 14 — FRACTURE PATTERN IN 5CrMoV STEEL WELDED BIAXIAL SPECIMEN NO. 19H 1:1 STRESS RATIO — "HIGH" STRENGTH — PHASE IV.

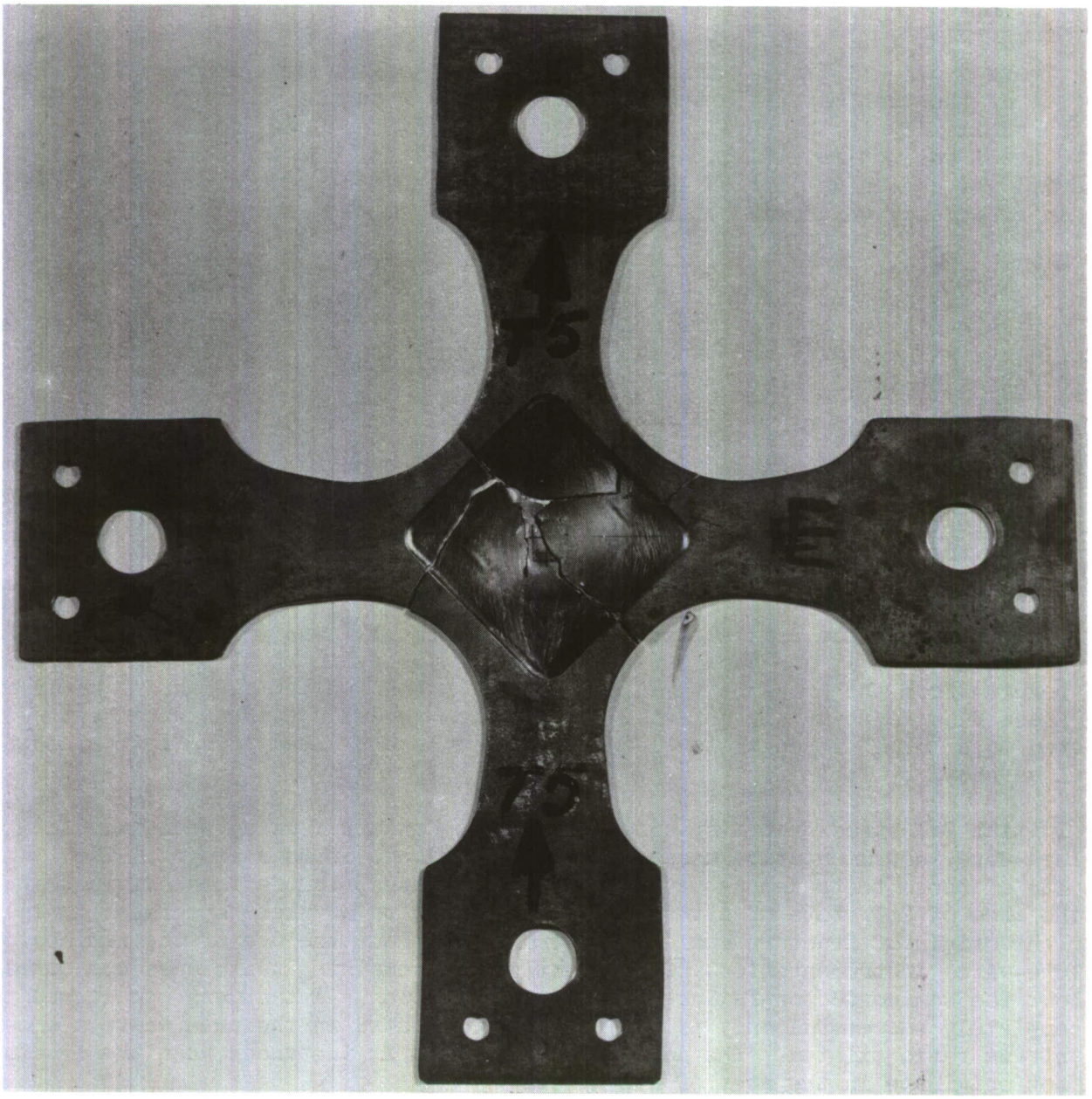

FIGURE 15 — FRACTURE PATTERN IN B—120VCA TITANIUM BIAXIAL SPECIMEN NO. 5T 1:1 STRESS RATIO — "HIGH" STRENGTH — PHASE I.

SECTION 9

SUMMARY OF 2:1 BIAXIAL TEST RESULTS

9.1 General

Tests under 2:1 biaxial tension stress ratio loading were conducted in Phase II on four of the test materials and in Phases IV and V on the 5CrMoV tool steel. Due to the similarity in the physical characteristics of the D6A-C and X-200 steel, the D6A-C steel was not investigated beyond the Phase I 1:1 biaxial tests. The X-200 material was chosen in lieu of the D6A-C material because of the superior biaxial strain efficiency which was obtained in the 1:1 tests.

The objectives of the tests in Phase II were to (1) develop a suitable specimen configuration for determining allowable strain under 2:1 loading and (2) generate biaxial stress-strain data under 2:1 loading from several high strength materials. All uniaxial and biaxial specimens in Phase II were heat treated to "high" strength level shown by Table 2.

The purpose of the biaxial tests in Phase IV was to determine weld joint efficiency based on stress and strain under biaxial tensile loading. Half of the 5CrMoV welded biaxial specimens were tested under 1:1 stress ratio conditions and half were tested under 2:1 stress ratio conditions. All specimens were heat treated to the "high" strength level shown by Table 2. The results from the 1:1 tests are presented in Section 8.

The purpose of the biaxial specimen tests in Phase V was to obtain 2:1 biaxial stress-strain data at the same strength level as the cylindrical pressure vessels. The results from the pressure vessels tests are presented in Section 10. Half of the Phase V 5CrMoV biaxial, uniaxial and pressure vessel specimens were heat treated to a "high" strength level and half were heat treated to a "low" strength level as shown by Table 2.

Initial 2:1 stress ratio specimen tests were conducted using semiconductor-failure-wire instrumentation as described in Section 6 of this report. The results of these tests demonstrated that, in all cases, the failure originated in the area of 2:1 state of stress. Visual inspection of these specimens indicated that the origin of fracture could be determined without the use of the semiconductor-failure-wire instrumentation. Consequently, the remaining tests were conducted without the semiconductor-failure-wire instrumentation. A test was considered to be completely successful only if the failure originated in the area where a known 2:1 stress ratio existed. The data is not reported in instances when the fracture did not originate in the area of 2:1 stress.

9.2 Test Results From Unwelded Material

The 2:1 biaxial stress-strain curves which were obtained from the test materials are shown in Appendix G. The method which was used to convert load-strain curves to stress-strain curves is presented in Appendix F. The test data from one of the Phase II 5CrMoV "high" strength specimens and two of the Phase V 5CrMoV "low" strength specimens are not reported since the fractures originated outside of the area of 2:1 stress. During the tests of these specimens the jack load in the minimum principal stress direction at failure exceeded the jack load

in the maximum principal stress direction. This caused the fracture to initiate in the leg of the specimen which was in the minimum principal stress direction. The jack load in the minimum principal stress direction was controlled by the servo valve system, which maintained a state of 2:1 stress in the test area up to failure.

A summary of the principal stresses and principal plastic strains obtained at failure from the test materials is shown in Tables 13 and 14. These tables show the methods used to locate the area of failure initiation. A discussion of the test results shown in Tables 13 and 14 follows:

1. There was little scatter in the failure stresses from the 2014-T6 aluminum alloy. Since the failure stresses obtained in the longitudinal and transverse grain directions were approximately the same, this material did not exhibit any effects of grain directionality on failure stresses. However, the failure strains recorded from the specimens tested with the high stress in the transverse grain direction were significantly less than the strains recorded from the longitudinal specimens. This behavior was not obtained from the 1:1 biaxial tests on the 2014-T6 aluminum alloy.

2. The failure stresses obtained from the longitudinal and transverse B-120VCA titanium alloy specimens were approximately equal, although the strains obtained from the transverse specimens were significantly lower than the values recorded from the longitudinal specimens. Similar behavior was obtained from the B-120VCA specimens that were tested under 1:1 biaxial loading.

3. The failure stresses and strains from the 5CrMoV biaxial specimens that were tested with the maximum stress in the longitudinal grain direction were somewhat higher than the values from the specimens that were tested with the maximum stress in the transverse grain direction. The 5CrMoV 1:1 biaxial test results showed similar behavior. The effects of grain directionality on the 5CrMoV failure strains were more pronounced under 2:1 loading than under 1:1 loading. This was true of all of the test materials except the X-200 steel alloy.

4. The failure stresses from the X-200 biaxial specimens that were tested with the maximum stress in the longitudinal grain direction were approximately equal to the values obtained from the transverse specimens. The strains recorded from the transverse specimens were considerably higher on an average than the strains recorded from the longitudinal specimens. Such behavior is, of course, uncommon since this was not evidenced from the 1:1 biaxial or the uniaxial tests. However, the results from the 2:1 tests may be misleading because of the relatively small number of tests conducted. It is possible that the average transverse strain would be less than the average longitudinal strain if a sufficient number of tests were conducted. The scatter in the 2:1 failure stresses was significantly less than the scatter in the 1:1 failure stresses.

9.3 Test Results From Welded Material

The 2:1 biaxial stress-strain curves which were obtained from the 5CrMoV welded material are shown in Appendix G. The method which was used to convert load-strain curves to stress-strain curves is presented in Appendix F. The test data from one of the welded specimens which was tested is not shown since the specimen failed in the loading grips.

A summary of the principal stresses and principal plastic strains obtained from the 5CrMoV welded biaxial specimens is shown by Table 15. This table shows the methods used to locate the area of failure initiation. The strain values obtained from the welded material were considerably less than the values obtained from the unwelded material.

9.4 Discussion of Types of Fractures Obtained Under 2:1 Loading

The types of fractures obtained from the materials tested under 2:1 and 1:1 biaxial stress ratio loading were similar; i.e., the B-120VCA and the "high" strength 5CrMoV specimens shattered and the 2014-T6 and X-200 specimens did not. Figure 16 illustrates the type of fracture which was obtained from the 2014-T6, X-200 and low strength 5CrMoV specimens. The fracture initiated in the leg of the specimen which is at the bottom of the picture. The maximum principal stress direction was normal to this fracture. The fracture running vertically in the picture occurred last. This fracture occurred because the jack load in the minimum principal stress direction was always only a few percent less than the jack load in the maximum principal stress direction at failure. The vertical fracture initiated just after the primary fracture propagated out of the area of 2:1 stress.

Figure 17 illustrates the shattering type of failures obtained from the high strength 5CrMoV unwelded specimens. The fracture initiated in the leg of the specimen which is at the bottom of the picture. As shown by Figure 18, the B-120VCA 2:1 biaxial specimens shattered, but not as severely as the 5CrMoV steel specimens. Figure 19 illustrates the type of fracture obtained from the "high" strength 5CrMoV welded biaxial specimens.

Studies of the fracture origins under low power magnification did not indicate any apparent difference in the appearance of the 2:1 and 1:1 specimens. In most instances many shear lips were formed in and near the origin of fracture in both the 2:1 and 1:1 specimens.

TABLE 13 - PRINCIPAL STRESSES AND PRINCIPAL PLASTIC STRAINS OBTAINED UNDER 2:1 LOADING AT FAILURE-PHASE II

MATERIAL (1)	SPEC. NO.	LONG. GRAIN σ_R' ~ ksi	LONG. GRAIN ϵ_1' ~ %	TRAN. GRAIN σ_R' ~ ksi	TRAN. GRAIN ϵ_1' ~ %	FAILURE WIRES ON SPECIMEN (2)
2014-T6	25	75.7	3.85	----	----	YES
	26	----	----	81.0	1.85	YES
	27	77.5	4.75	----	----	YES
	28	81.0	4.30	----	----	YES
	29	----	----	80.0	1.02	YES
	30	----	----	80.0	2.80	YES
	Avg. =	78.1	4.30	80.3	1.89	
B-120 VCA	6T	-----	----	238.0	0.68	NO
	7T	-----	----	213.0	0.90	NO
	8T	-----	----	208.0	0.70	NO
	9T	239.0	2.25	-----	----	NO
	10T	226.0	2.30	-----	----	NO
	11T	220.0	2.35	-----	----	YES
	Avg. =	228.3	2.30	219.6	0.76	
5CrMoV	8H	-----	----	318.0	1.95	NO
	9H	-----	----	304.0	3.10	NO
	10H	-----	----	284.0	3.25	NO
	11H	347.0	4.65	-----	----	YES
	12H	309.0	5.60	-----	----	YES
	Avg. =	328.0	5.12	302.0	2.77	
X-200	6X	348.0	1.30	-----	----	NO
	7X	327.0	1.53	-----	----	NO
	9X	330.0	1.80	-----	----	NO
	10X	-----	----	340.0	3.40	NO
	11X	-----	----	340.0	1.00	NO
	Avg. =	335.0	1.54	340.0	2.20	

(1) All specimens heat treated to "high" strength level shown in Table 2.

(2) All specimens, including those instrumented with failure wires, received a thorough visual examination of the fracture surface in order to determine that the fracture originated within the critical area.

TABLE 14 - PRINCIPAL STRESSES AND PRINCIPAL PLASTIC STRAINS OBTAINED UNDER 2:1 LOADING AT FAILURE-PHASE V

MATERIAL (1)	SPEC. NO. (1)	LONGITUDINAL GRAIN σ_R' ~ ksi	ϵ_1' ~ %	FAILURE WIRES ON SPECIMEN (2)
5CrMoV	24H (H)	379.0	2.13	NO
	25H (H)	357.0	2.54	NO
	26H (H)	357.0	3.30	NO
	Avg. =	364.3	2.66	
	27H (L)	287.0	4.32	NO
	30H (L)	252.0	2.80	NO
	Avg. =	269.5	3.56	

(1) (H) indicates "high" strength level, (L) indicates "low" strength level as shown in Table 2.

(2) All specimens, including those instrumented with failure wires, received a thorough visual examination of the fracture surface in order to determine that the fracture originated within the critical area.

TABLE 15 - PRINCIPAL STRESSES AND PRINCIPAL PLASTIC STRAINS OBTAINED UNDER 2:1 LOADING AT FAILURE-PHASE IV

MATERIAL (1)	SPEC. NO.	LONGITUDINAL GRAIN σ_R' ~ ksi	ϵ_1' ~ %	FAILURE WIRES ON SPECIMEN (2)
5CrMoV Welded	22H	318.0	1.25	NO
	23H	312.0	1.95	NO
	Avg. =	315.0	1.60	

(1) All specimes heat treated to "high" strength level shown in Table 2.

(2) All specimens, including those instrumented with failure wires, received a thorough visual examination of the fracture surface in order to determine that the fracture originated within the critical area.

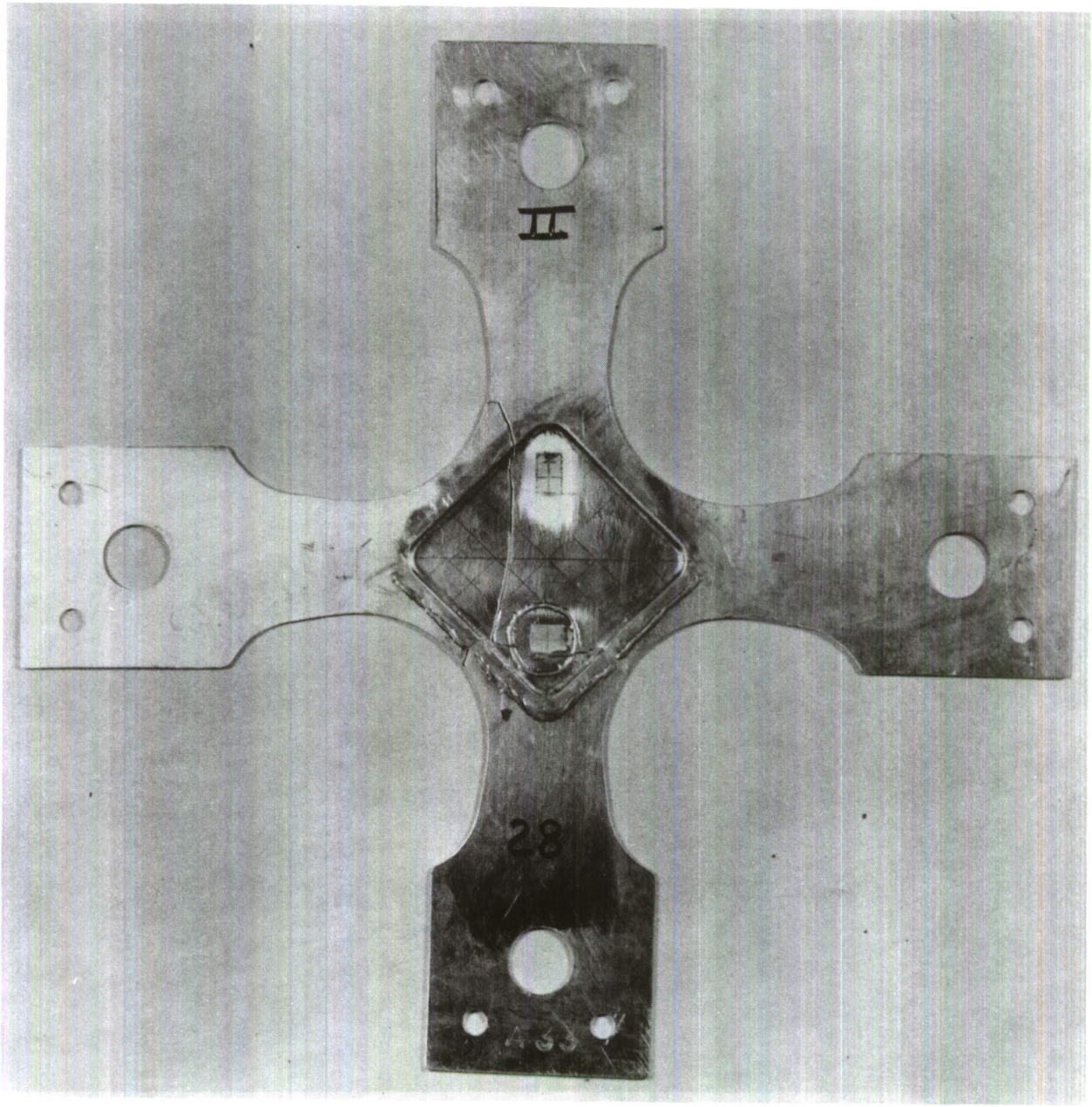

THIS TYPE OF FRACTURE IS REPRESENTATIVE OF THE FRACTURES OBTAINED IN THE 2014—T6 ALUMINUM, X—200 AND "LOW" STRENGTH 5CrMoV STEEL 2:1 BIAXIAL SPECIMENS.

FIGURE 16 — FRACTURE PATTERN IN 2014 — T6 ALUMINUM BIAXIAL SPECIMEN NO. 28 2:1 STRESS RATIO —"HIGH" STRENGTH — PHASE II.

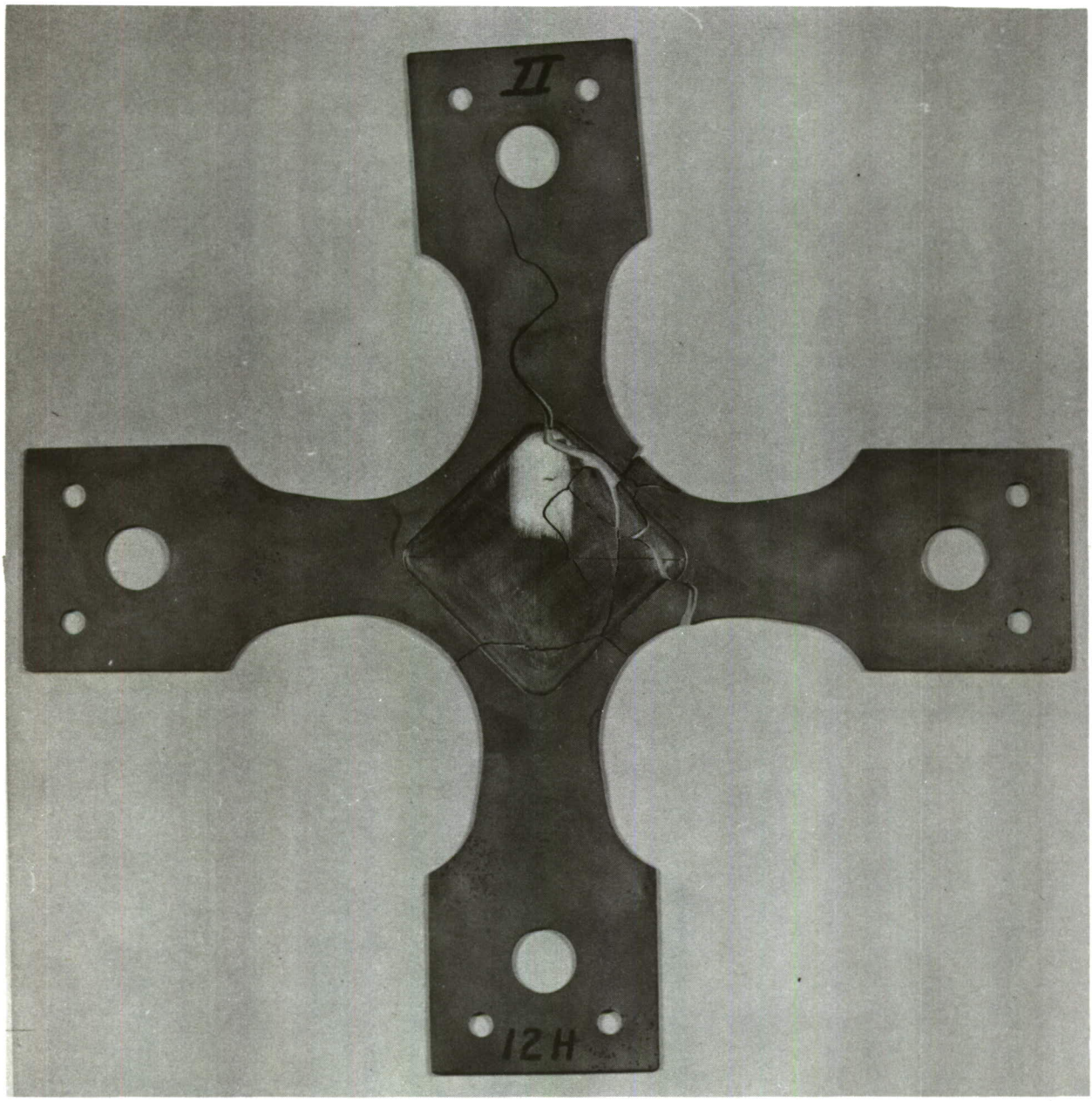

FIGURE 17 — FRACTURE PATTERN IN 5CrMoV BIAXIAL SPECIMEN NO. 12H
2:1 STRESS RATIO — "HIGH" STRENGTH — PHASE II.

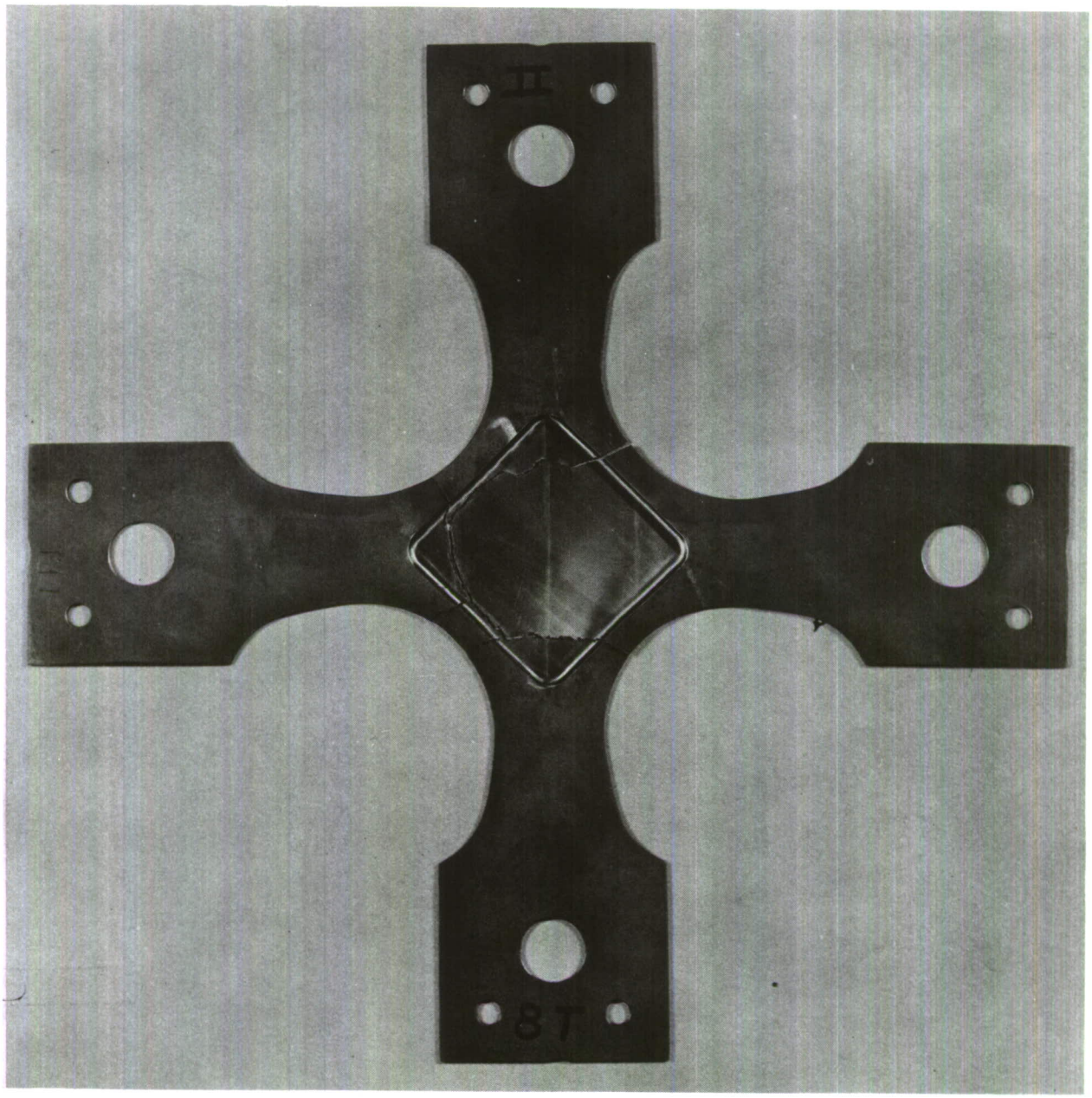

FIGURE 18 — FRACTURE PATTERN IN B—120VCA TITANIUM BIAXIAL SPECIMEN NO. 8T 2:1 STRESS RATIO —"HIGH" STRENGTH — PHASE II.

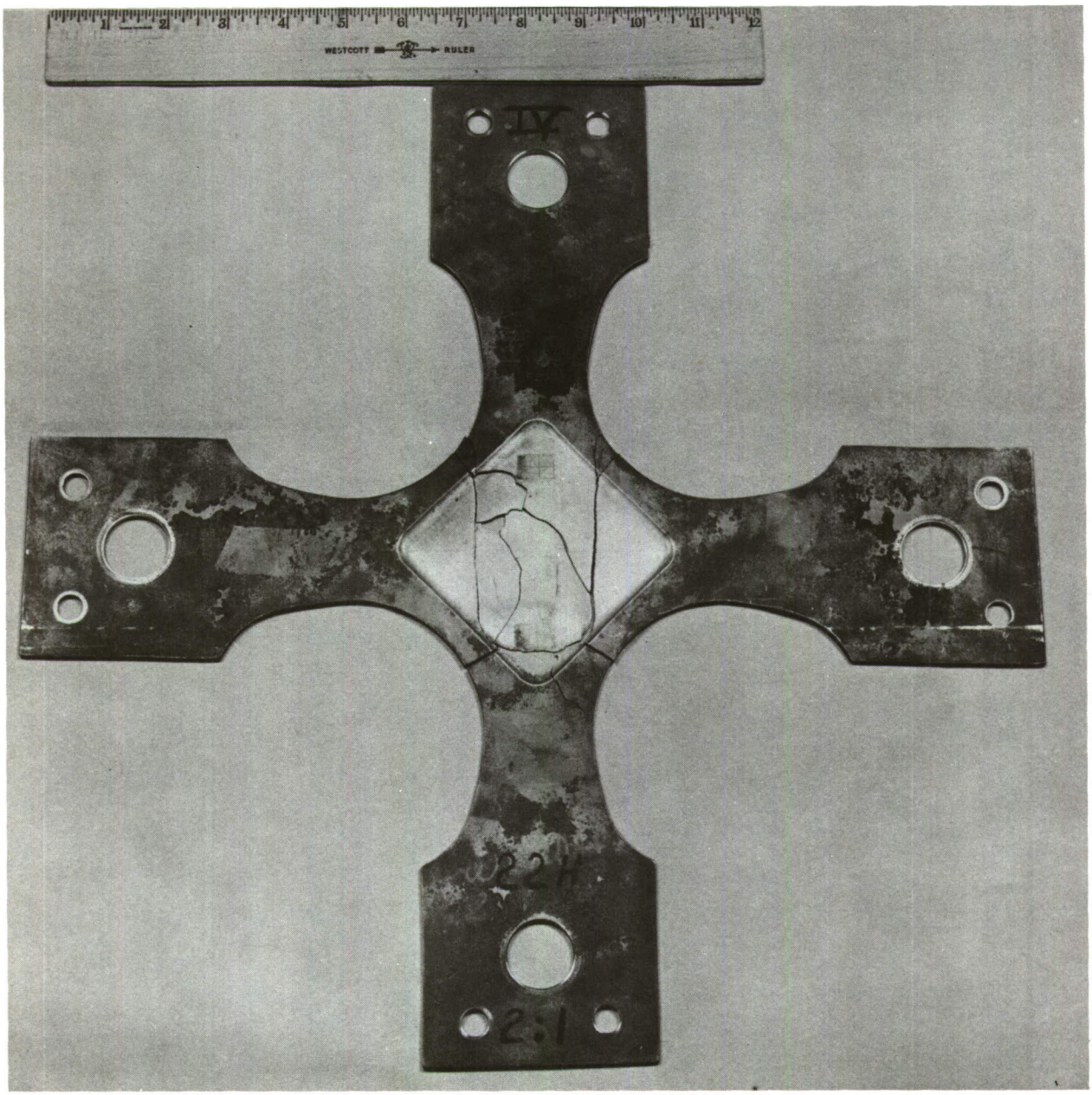

FIGURE 19 — FRACTURE PATTERN IN 5CrMoV STEEL WELDED BIAXIAL SPECIMEN NO. 22H 2:1 STRESS RATIO — "HIGH" STRENGTH — PHASE IV.

SECTION 10

SUMMARY OF CYLINDRICAL PRESSURE VESSEL TESTS AND CORRELATION OF RESULTS WITH RESULTS FROM BIAXIAL SPECIMEN TESTS

10.1 General

Seven cylindrical pressure vessels were fabricated from the 5CrMoV material by the hydrospin process. The configuration of the vessels is shown in Figure 4. Three vessels were heat treated to the "high" strength level and four were heat treated to the "low" strength level shown in Table 2.

One of the "high" strength and one of the "low" strength vessels was dented according to Figure 4 in order to determine the effect of a high strain concentration on failure behavior.

10.2 Pressure Vessel Test Results

A summary of the failure stresses obtained from the pressure vessels is shown in Table 16. The failure in the vessels that were dented, PVL-2 and PVH-2, initiated in an area away from the dents. In both instances the wall thickness at the failure origin was slightly less than in the area of the dents. The failure in vessels PVL-4 and PVH-3 occurred in weld voids. The void in the "high" strength vessel was considerably smaller than the void in the "low" strength vessel. As a result of the weld void, the "high" strength vessel failed prematurely at a stress level of about 70 percent of the values that were obtained from the other "high" strength vessels. However, the weld void did not affect the load carrying capability of the "low" strength vessel.

As illustrated by Figures 20 and 21, only one fracture path occurred in the "low" strength vessels, although the "high" strength vessels shattered at failure. The "high" and "low" strength biaxial specimens displayed the same type of behavior.

The 2:1 biaxial stress-strain curves that were obtained from the vessels are presented in Appendix G. None of the failures in the vessels initiated in areas where strain gages were located. For this reason, the strain values shown by the curves in Appendix G at failure may be considerably less than the values that might have been recorded at the failure origin. The bulges which occurred at the point of failure initiation give support to this conclusion. The stress-strain curves in Appendix G were calculated from the gages which showed the greatest amount of strain.

10.3 Correlation of Results Obtained From Pressure Vessel Tests and Biaxial Specimen Tests

The failure stress values obtained from the pressure vessels and the biaxial specimens show close agreement, although the strain values recorded from the vessels are considerably less than those recorded from the biaxial specimens. This can be attributed to the fact that the strain gages were not located at the failure origins in the pressure vessels. A comparison of the average failure stress

and strain values from the pressure vessels and the biaxial specimens is shown in the following table.

STRENGTH LEVEL	BIAXIAL SPECIMEN (1)				PRESSURE VESSEL	
	LONG. GRAIN		TRAN. GRAIN			
	σ_R'~Ksi	ϵ_i'~%	σ_R'~Ksi	ϵ_i'~%	σ_R'~Ksi	ϵ_i'~%
"Low"	269.5	3.56	----	----	257.0	1.81
"High"	328.0	5.12	302.0	2.77	315.5	1.47

(1) "Low" strength values obtained from Table 14 and "high" strength values obtained from Table 13.

As discussed previously, the fracture behavior of the pressure vessels and the biaxial specimens was identical. The significance of the shattering type fracture versus the ductile appearing fracture in the vessels and biaxial specimens is discussed in Section 15.

The types of grain structure in the 5CrMoV tool steel at various stages are shown in Figure 22. The hydrospin process used to fabricate the pressure vessels resulted in highly elongated grains. However, the annealing treatment that was given to the as-spun vessels restored the grains to the original size.

TABLE 16 - SUMMARY OF TEST RESULTS FROM 5CrMoV CYLINDRICAL PRESSURE VESSELS

SPEC. NO. (1)	FAILURE STRESS (2) σ_R' ~ Ksi	ORIGIN OF FAILURE	TYPE FRACTURE
PVL-1 (L)	250.0	Parent Metal	One Path
PVL-2 (L)	253.0	Parent Metal	One Path
PVL-3 (L)	275.0	Parent Metal	One Path
PVL-4 (L)	250.0	Weld Void	One Path
PVH-1 (H)	320.0	Parent Metal	Shatter
PVH-2 (H)	311.0	Parent Metal	Shatter
PVH-3 (H)	227.0	Weld Void	Shatter

(1) (H) indicates "high" strength, (L) indicates "low" strength as shown in Table 2. Results from uniaxial specimens that were heat treated with vessels are shown in Table 7.

(2) calculated by $\sigma_R' = \frac{\bar{p}R_i}{t_i}$

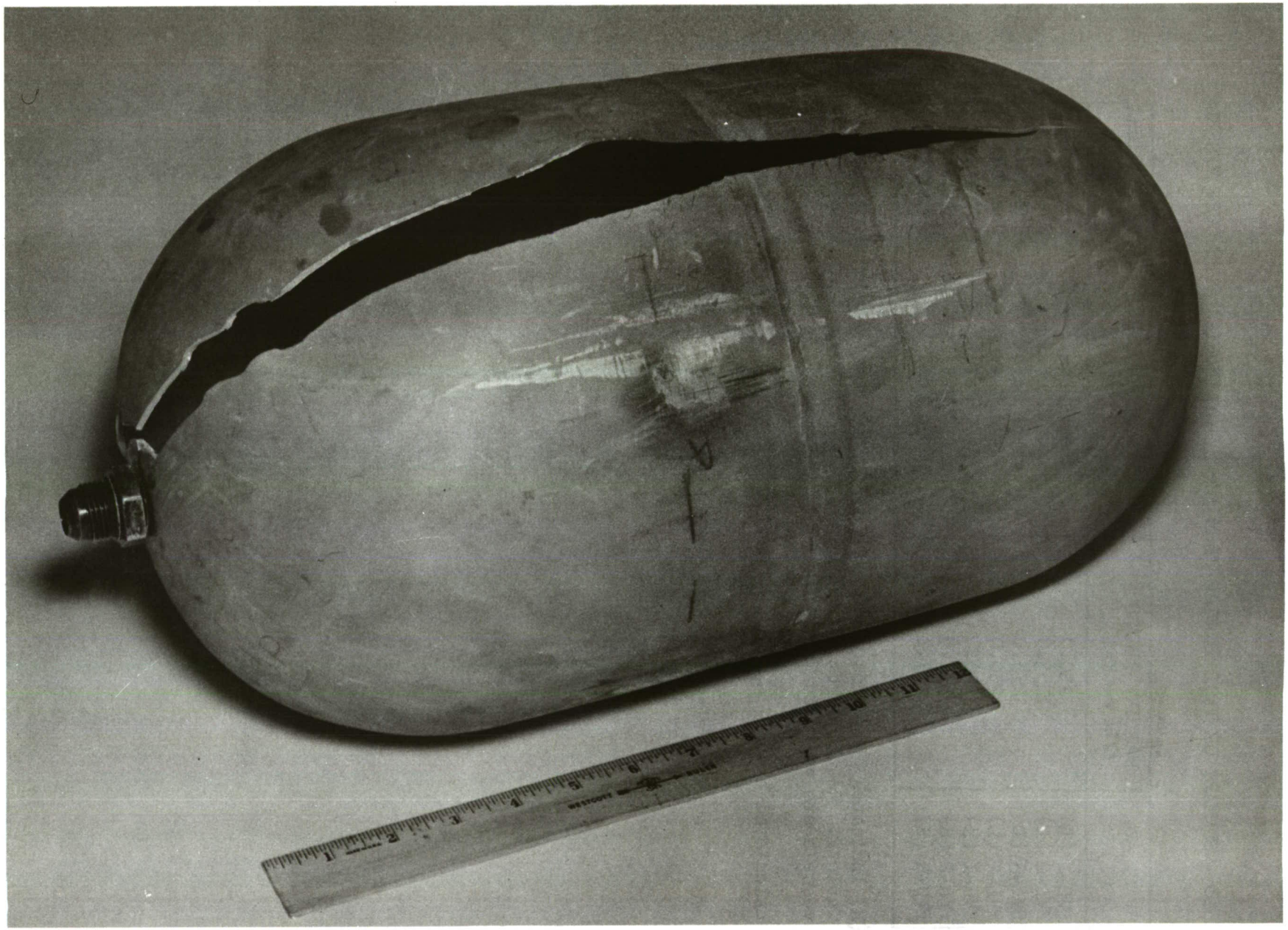

FIGURE 20 — FRACTURE PATTERN IN "LOW" STRENGTH 5CrMoV PRESSURE VESSEL — NO. PVL-1.

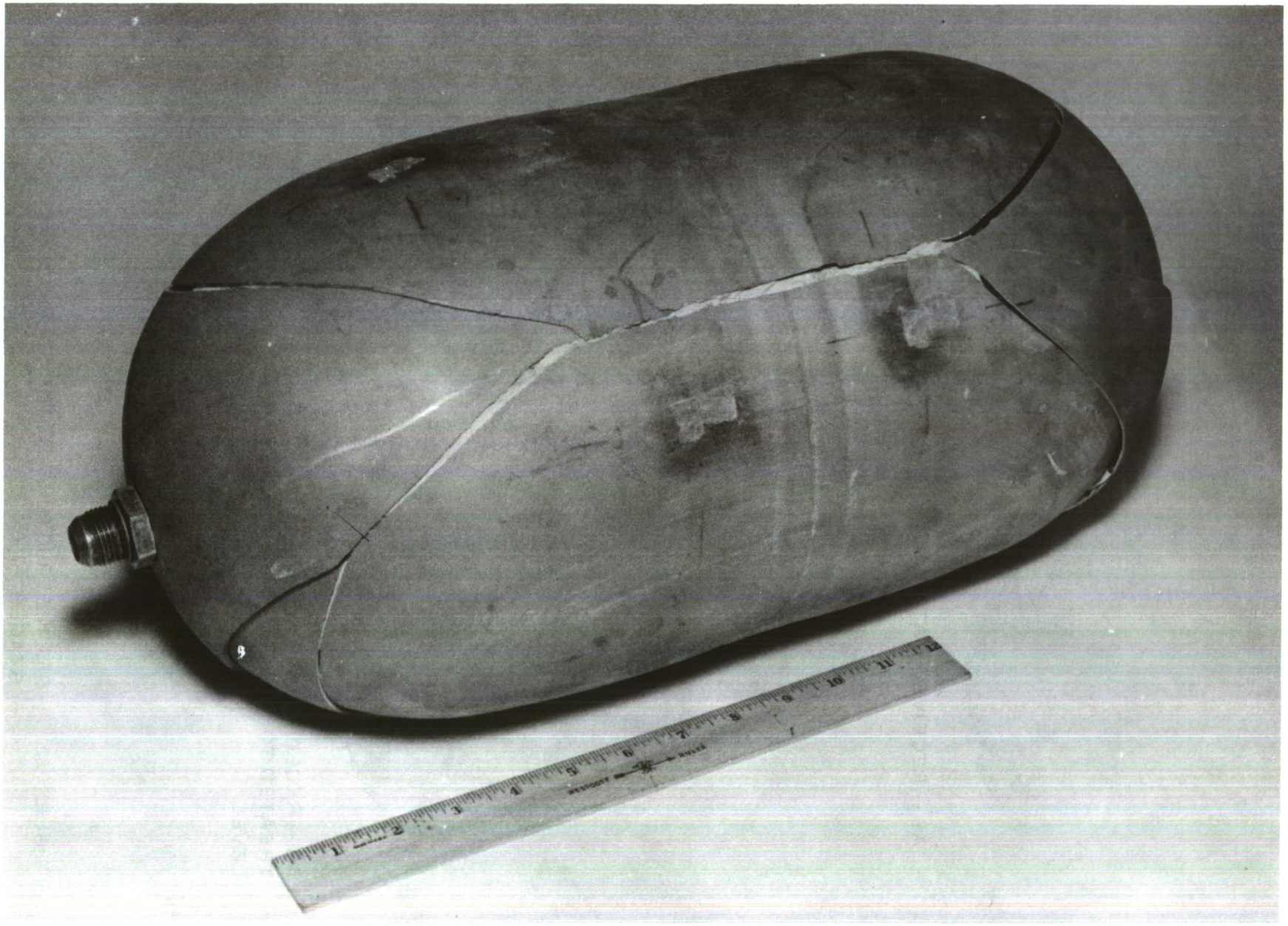

FIGURE 21 — FRACTURE PATTERN IN "HIGH" STRENGTH 5CrMoV PRESSURE VESSEL — NO. PVH-1

AS – RECEIVED MATERIAL

AS – SPUN MATERIAL

AS – RECEIVED MATERIAL HEAT TREATED TO "HIGH" STRENGTH LEVEL

AS – SPUN MATERIAL ANNEALED AND THEN HEAT TREATED TO "HIGH" STRENGTH LEVEL

FIGURE 22 – GRAIN STRUCTURE OF THE 5CrMoV STEEL AT VARIOUS STAGES –750X

SECTION 11

SUMMARY OF NOTCH TOUGHNESS TESTS AND CORRELATION OF RESULTS WITH RESULTS FROM BIAXIAL TESTS

11.1 General

Notch toughness tests were conducted on the five test materials to obtain a correlation between these tests and the biaxial specimen tests. The configuration of the notch toughness specimen is shown in Figure 6. Data was obtained from the 5CrMoV steel at the "high," "medium" and "low" strength levels and the other four test materials at the "high" strength level shown in Table 2.

11.2 Test Results

Table 17 summarizes the results from the notch toughness tests. The data is shown in the form of fracture toughness values, Kc_1, which were calculated according to the procedures outlined in reference 4.

As shown in Figure 23 the fracture toughness values obtained from the 5CrMoV steel increase as the strength level of the material decreases. This situation indicates that for a given crack length the "low" strength material can sustain higher stresses than either the "medium" or "high" strength material before the onset of rapid crack growth. Likewise, the "medium" strength material can sustain a higher stress level than the "high" strength material for a given crack length.

A comparison of the fracture toughness values obtained from the 5CrMoV, D6A-C and X-200 steel alloys heat treated to the "high" strength level is shown in Figure 24. This figure shows that the X-200 material has better resistance to crack-like flaws than either of the other two materials, and the D6A-C material is somewhat better than the 5CrMoV material.

The fracture toughness values obtained from the 2014-T6 aluminum alloy indicate that this material has high resistance to crack-like flaws. The results obtained from the B-120VCA titanium alloy are not conclusive because of the extreme scatter obtained. Additional B-120VCA specimens which were tested fractured through the loading holes. This same type of erratic behavior was obtained during the uniaxial and biaxial tests of this material.

11.3 Correlation of Results Obtained from Notch Toughness Tests and Biaxial Tests

The notch toughness tests on the 5CrMoV material showed that the shattering behavior of this material under biaxial loading is indicative of poor resistance to crack-like flaws. In addition the notch toughness tests verified the conclusion that poor resistance to crack-like flaws caused the premature failure in the "high" strength pressure vessel that contained a weld void.

No correlation can be shown between the notch toughness values and biaxial failure strains. For example, significantly higher notch toughness values were obtained from the X-200 material than the 5CrMoV material, although the X-200 biaxial strain values were considerably lower than the values obtained from the 5CrMoV material.

TABLE 17 - FRACTURE TOUGHNESS VALUES

MATERIAL	SPEC. NO. (1)	GRAIN	FRACTURE TOUGHNESS Kc_1 - Ksi$\sqrt{in.}$
2014-T6	A-2 (H)	Tran.	69.0
	A-3 (H)	Tran.	65.5
B-120VCA	TT-1 (H)	Tran.	121.0
	TT-2 (H)	Tran.	57.5
5CrMoV	HL-1 (H)	Long.	60.1
	HL-2 (H)	Long.	60.0
	HL-3 (H)	Long.	57.0
	HT-1 (H)	Tran.	52.4
	HT-2 (H)	Tran.	51.0
	HT-3 (H)	Tran.	55.8
	HL-2 (M)	Long.	60.0
	HL-3 (M)	Long.	70.0
	HL-1 (L)	Long.	71.8
	HL-2 (L)	Long.	77.1
	HL-3 (L)	Long.	77.0
D6A-C	D-1 (H)	Long.	64.5
	D-2 (H)	Long.	69.0
	D-3 (H)	Long.	68.7
X-200	X-1 (H)	Long.	152.0
	X-2 (H)	Long.	169.0
	X-3 (H)	Long.	167.0

(1) (H) indicates "high" strength, (M) indicates "medium" strength, (L) indicates "low" strength as shown in Table 2

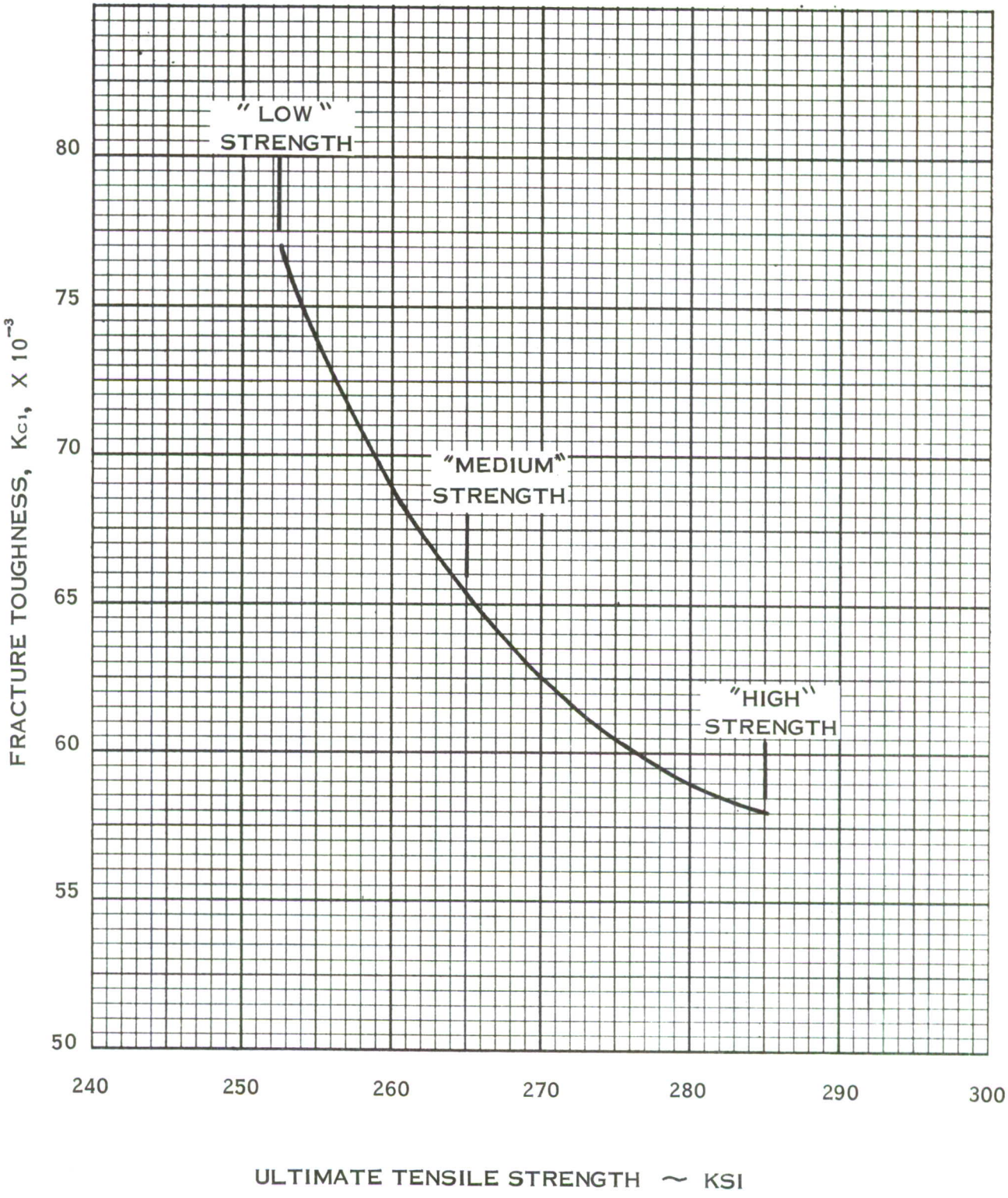

FIGURE 23 — INFLUENCE OF STRENGTH LEVEL ON FRACTURE TOUGHNESS OF 5CrMoV STEEL ALLOY

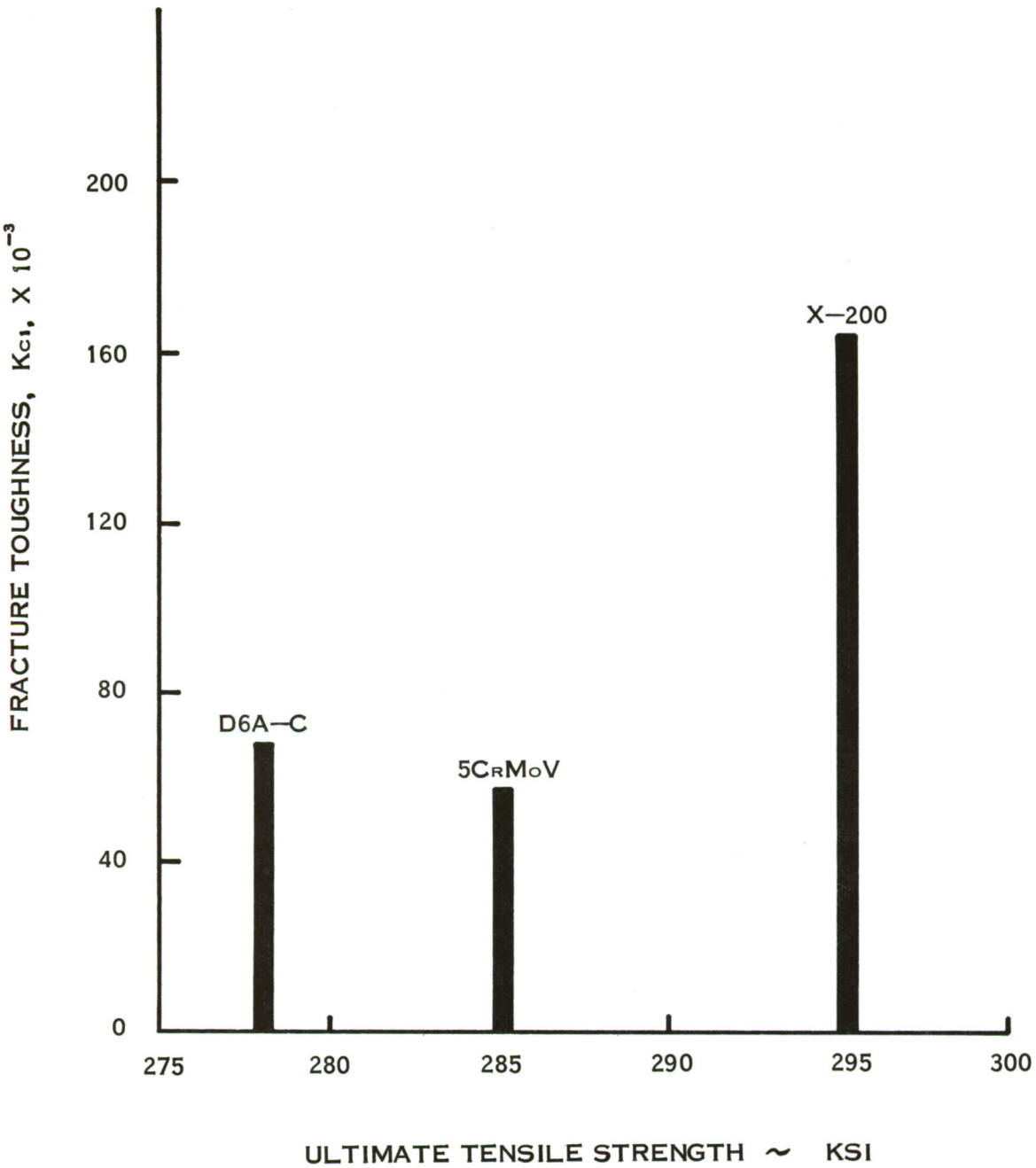

FIGURE 24 — COMPARISON OF FRACTURE TOUGHNESS VALUES OBTAINED FROM THE STEEL ALLOYS HEAT TREATED TO HIGH STRENGTH LEVEL

SECTION 12

COMPARISON OF BIAXIAL TEST RESULTS WITH THE DEFORMATION ENERGY THEORY OF FAILURE

12.1 General

The deformation energy theory of flow and fracture is discussed and pertinent relationships are derived in Appendix D. This particular theory was chosen for comparison with the test data because of its applicability to practical problems and its correlation with the test data. A brief summary of other theories of failure is presented in Appendix D. The comparison of the test data with the deformation energy theory is made not only to determine the validity of the theory but also to form a common basis for comparing and ranking the materials.

The analyses presented in Appendix D consider only axial loading, or in the case of pressure vessels pure membrane loading. For many practical applications, consideration of pure axial loading is not adequate. For example, local strain concentrations due to out-of-roundness, dents, mismatch, discontinuity loads, etc. will probably exist to some degree on any structural member. These concentrations may cause a substantial loss in the strength of the part. Whenever these conditions exist, appropriate equations that consider axial loading combined with bending or some other type of loading would have to be used in conjunction with allowable biaxial strain data to predict the performance of the part.

12.2 Stress and Strain Relations for Combined Tension-Tension Loading Based Upon the Deformation Theory

The pertinent relationships for stress and strain at maximum load for 1:1 and 2:1 loading are derived in Appendix D. These relations are based on the assumption that there is an effective stress, σ_e , and an effective strain, ϵ_e , that coincide with the true stress and true strain obtained from a uniaxial tension test. These relations are combined with the expressions for burst pressure and principal stresses and strains for a sphere, 1:1 loading, and a cylinder, 2:1 loading, to obtain expressions that can be compared with experimental data. It is further assumed in these derivations that the Ludwik law can be used to define the shape of the uniaxial true stress-strain curve and that the equation for constancy of volume is applicable.

Based on the above and the derivations in Appendix D the significant relationships that are required to compare theory with the 1:1 biaxial test data may be summarized as follows:

Ratio of Nominal Principal Strains at Maximum Pressure to Uniaxial Nominal Strain at Maximum Load,

$$\frac{\epsilon_1'}{\epsilon_u'} = \frac{\epsilon_2'}{\epsilon_u'} = \frac{e^{n/3} - 1}{e^n - 1} \qquad (10)$$

Ratio of Nominal Principal Stress at Maximum Pressure to σ_o ,

$$\frac{\sigma_R'}{\sigma_o} = \left(\frac{2n}{3e}\right)^n \tag{11}$$

The above equation is considered to be theoretically exact if the value of σ_o used causes the Ludwik law to exactly fit the uniaxial true stress-strain curve.

Ratio of Nominal Principal Stress at Maximum Pressure to Nominal Uniaxial Ultimate Tensile Stress,

$$\frac{\sigma_R'}{\sigma_u'} = \left(\frac{2}{3}\right)^n \tag{12}$$

The above equation is not considered to be theoretically exact since the approximate value for σ_o at maximum pressure is used.

Similar expressions for 2:1 biaxial stress ratio loading may be summarized as follows:

Ratio of Nominal Principal Strain at Maximum Pressure to Uniaxial Nominal Strain at Maximum Load,

$$\frac{\epsilon_1'}{\epsilon_u'} = \frac{e^{n/2} - 1}{e^n - 1} \tag{13}$$

Ratio of Nominal Principal Stress at Maximum Pressure to σ_o ,

$$\frac{\sigma_R'}{\sigma_o} = \frac{2}{(\sqrt{3})^{n+1}} \left(\frac{n}{e}\right)^n \tag{14}$$

The above equation is considered to be theoretically exact if the value of σ_o used causes the Ludwik law to exactly fit the uniaxial true stress-strain curve.

Ratio of Nominal Principal Stress at Maximum Pressure to Nominal Uniaxial Ultimate Tensile Stress,

$$\frac{\sigma_R'}{\sigma_u'} = \frac{2}{(\sqrt{3})^{n+1}} \tag{15}$$

The above equation is not considered to be theoretically exact since the approximate value for σ_o at maximum pressure is used.

The stress and strain relationships at maximum load for 1:1 and 2:1 tension-tension loading can be plotted to show the significance of the strain hardening coefficient. The ratios of nominal principal strain at maximum load under 1:1 and 2:1 loading to the nominal uniaxial strain at maximum load, equations (10)

and (13), are shown by Figure 25 for strain hardening values up to 0.32. These plots show that the ratios remain about the same over the strain hardening range considered.

The influence of strain hardening on the ratio of σ_R'/σ_o for 1:1 and 2:1 loading, equations (11) and (14), is shown by Figure 26. These equations are considered to be theoretically exact if the value of σ_o used causes the Ludwik law to exactly fit the uniaxial true stress-strain curve.

Figure 25 also shows a plot of equations (12) and (15). These equations express the relationship between nominal principal stress at maximum load to nominal uniaxial ultimate for 1:1 and 2:1 loading. The ratios shown by Figure 25 may be plotted to form several loci of failure points as shown by Figure 27. The locus of failure points is an ellipse only when the strain hardening coefficient is zero.

12.3 Comparison of 1:1 Biaxial Test Results With Deformation Energy Theory of Failure

A comparison of the failure stresses and strains that were obtained under 1:1 loading from the test materials is shown by Figures 28 through 35. The σ_R'/σ_u' curves shown by Figures 28 through 32 are expressed by equations (12) and the σ_R'/σ_o curves are expressed by equation (11). The conclusions from the comparison study follows:

1. Both the approximate and theoretically exact relationships predict failure stresses which are on an average about seven percent higher than the experimental values from the 2014-T6 aluminum alloy. The 2014-T6 biaxial failure strains recorded at maximum load are considerably higher on an average than the values predicted by the deformation energy theory.

2. The principal stress values from the B-120VCA titanium alloy in both grain directions and the principal strains in the longitudinal grain direction agree well with the theory. However, the principal strains measured in the transverse grain direction are considerably less than the theoretical value.

3. The failure stress values obtained from the 5CrMoV welded and unwelded specimens are in fair agreement with the theory. The stresses measured in the transverse grain direction are, in most instances, somewhat lower than the values predicted by theory. The experimental strain values recorded from this material are on an average higher than the theory.

4. The experimental stresses obtained from the D6A-C steel alloy and the deformation energy are in fair agreement, although the experimental strain values fall well above and below the theory.

5. The experimental stresses obtained from the X-200 steel material are lower than the values predicted by the theory. The strain values measured in the longitudinal grain direction are on an average considerably higher than the theory, although the transverse strain values fall well above and below the theory.

12.4 Comparison of 2:1 Biaxial Test Results With Deformation Energy Theory of Failure

A comparison of the failure stresses and strains that were obtained under 2:1 loading from the test materials is shown by Figures 36 through 40. The σ_R'/σ_u' curves shown by Figures 36 through 38 are expressed by equation (15) and the σ_R'/σ_o curves are expressed by equation (14). The conclusion from the comparison study follows:

1. Both the approximate and theoretically exact relationships predict failure stresses which are exceptionally close to the 2014-T6 experimental values. The biaxial strains recorded at maximum load from the specimens tested with the maximum principal stress in the longitudinal grain direction and the theory are in close agreement. However, the biaxial strains recorded from the transverse specimens are considerably less than the value predicted by theory. This behavior is unusual since both the longitudinal and transverse strains that were obtained under 1:1 loading were somewhat higher than the theory.

2. The experimental stress values obtained from the B-120VCA titanium alloy and the theory are in fair agreement. The experimental strain values, however, are considerably less than the values predicted by theory. The strains recorded from the specimens tested with the maximum load in the transverse grain direction are only about 25 percent of the theoretical value.

3. Both the approximate and theoretically exact relationships predict failure stresses which are close to the values obtained from the 5CrMoV steel alloy. The strain values obtained from the unwelded specimens are considerably higher than the theory. However, the strains recorded from the welded specimens are only about 70 percent of the theoretical value.

4. The theory and the experimental stress values obtained from the X-200 steel alloy are in good agreement, although the theory is not as successful in predicting the strain values. The strains measured from the specimens tested with the maximum principal stress in the transverse grain direction are on an average conserably higher than the theory.

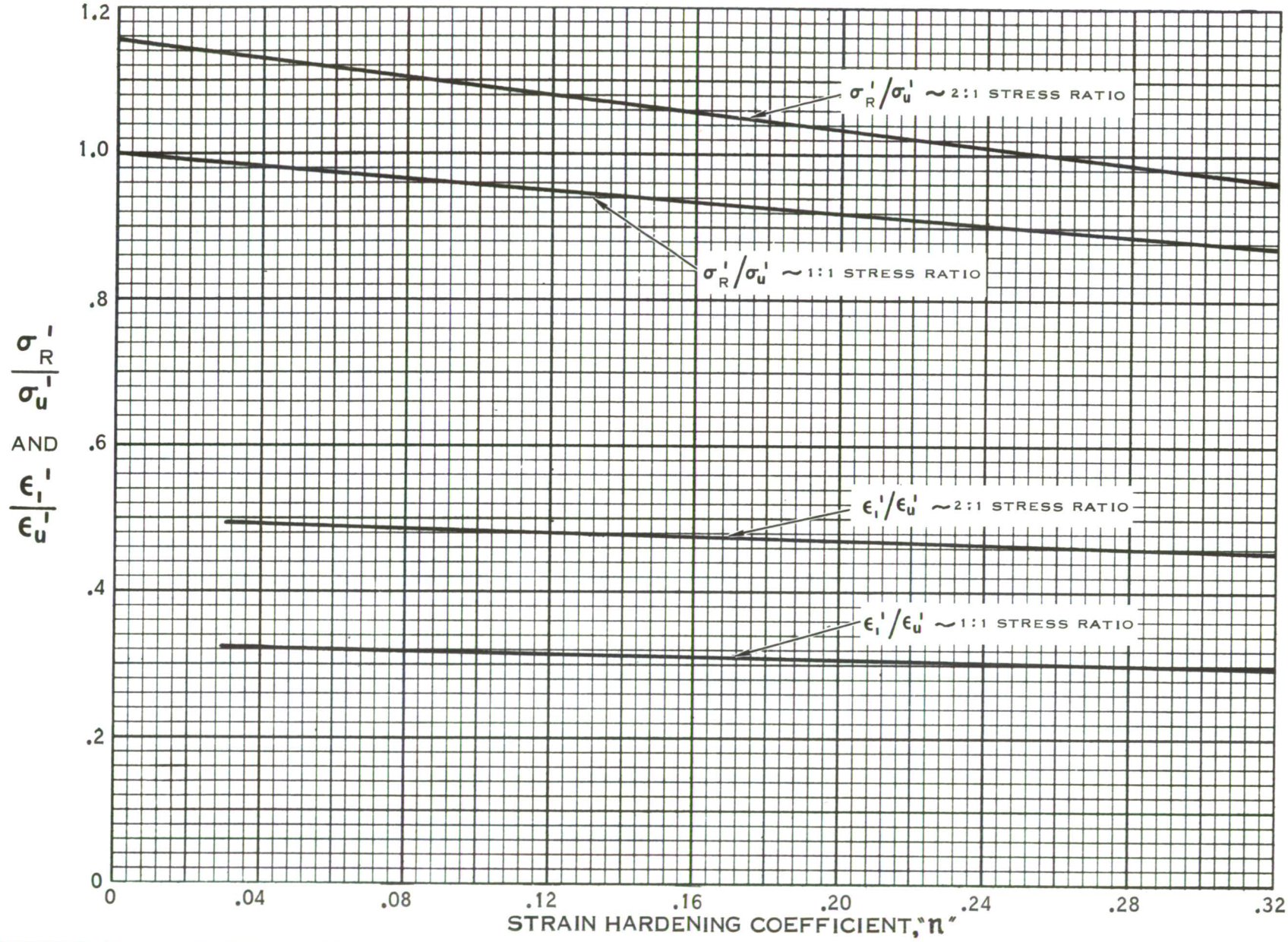

FIGURE 25 — RATIO OF PRINCIPAL STRESS AND STRAIN AT MAXIMUM LOAD TO UNIAXIAL TENSILE STRESS AND STRAIN AT MAXIMUM LOAD FOR 2:1 AND 1:1 TENSION LOADING

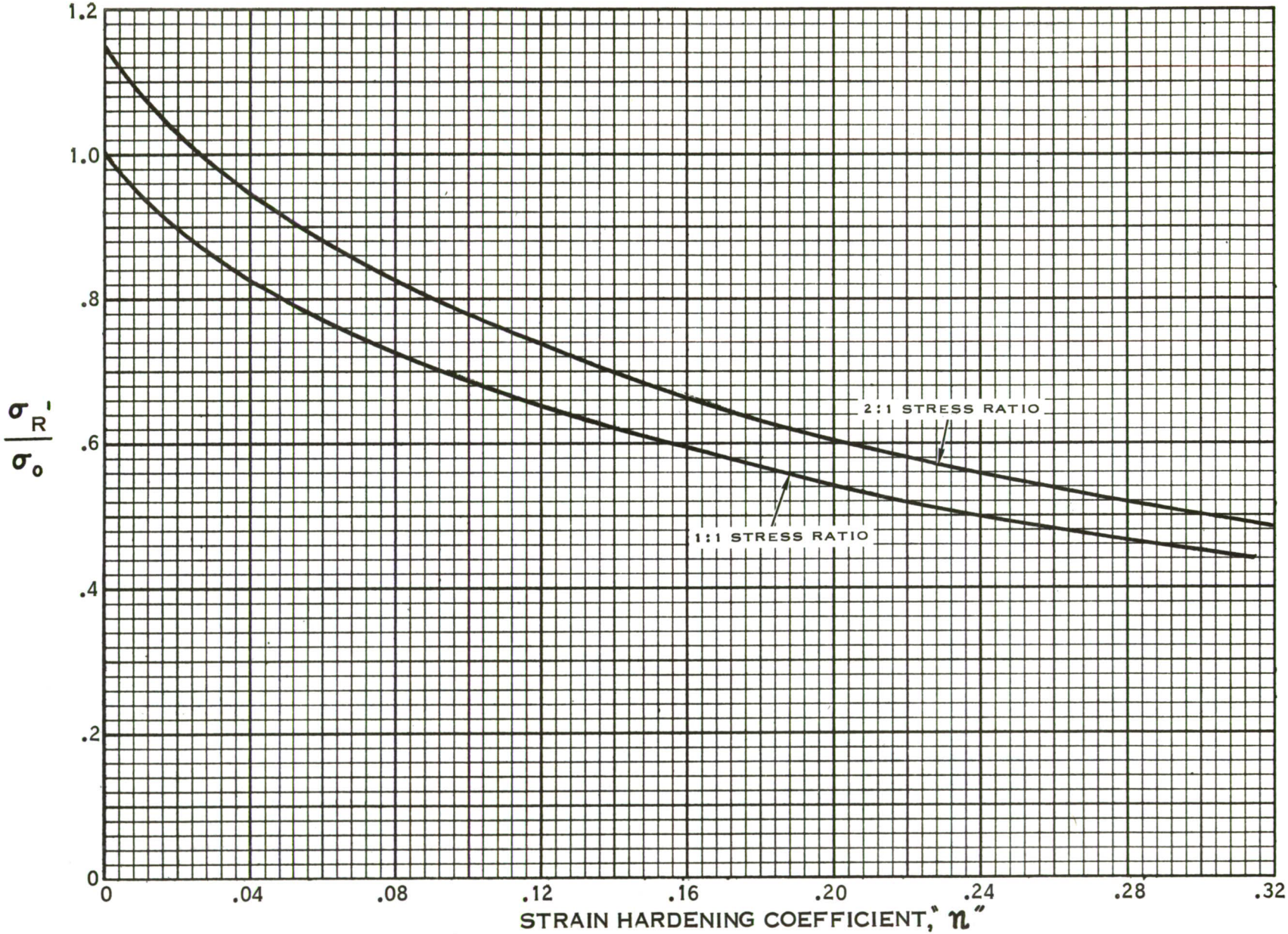

FIGURE 26 — RATIO OF PRINCIPAL STRESS AT MAXIMUM LOAD TO σ_0 FOR 2:1 AND 1:1 TENSION LOADING

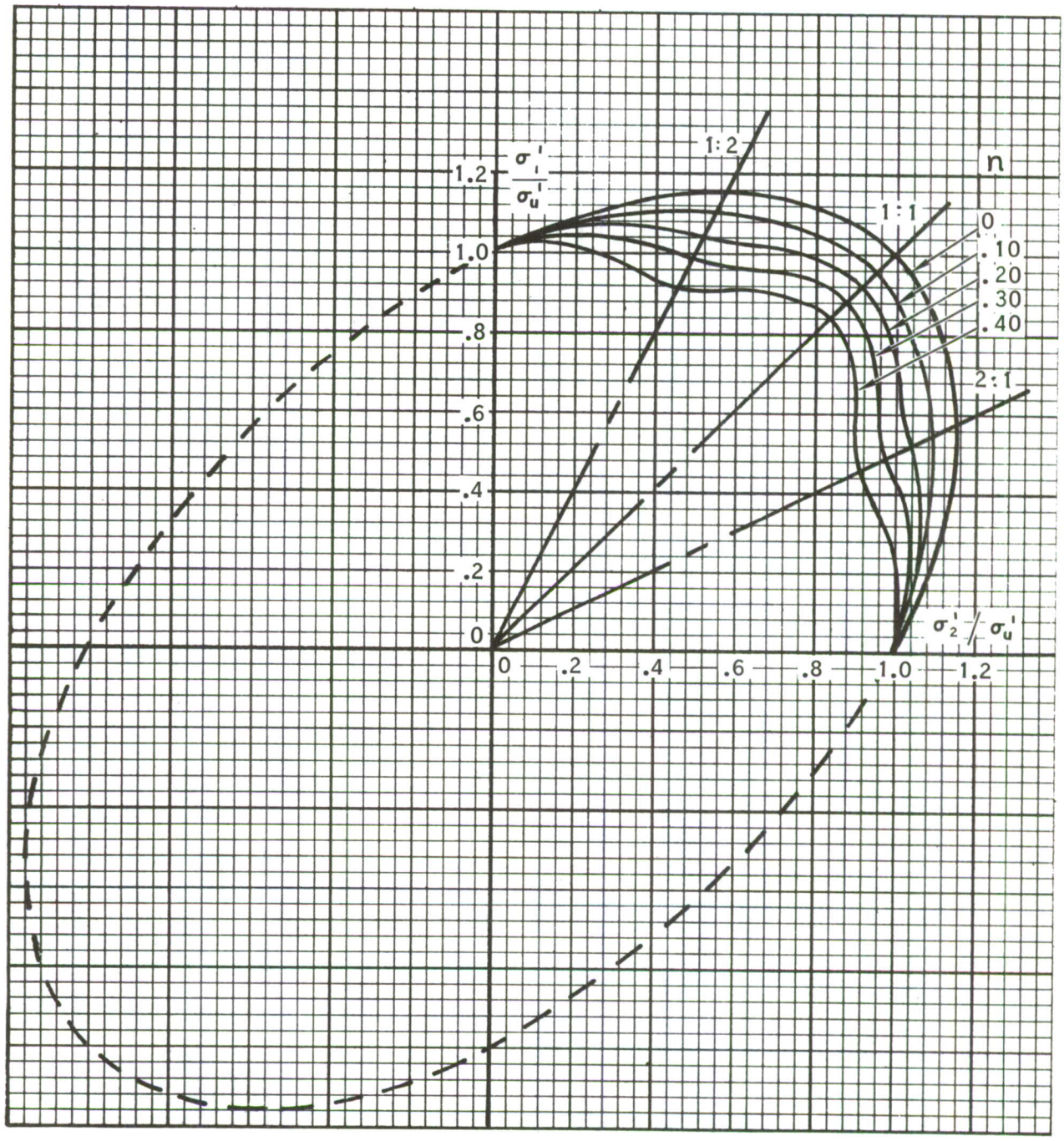

FIGURE 27 — RELATIONSHIP BETWEEN NOMINAL PRINCIPAL STRESS AT MAXIMUM LOAD TO NOMINAL UNIAXIAL ULTIMATE FOR TENSION — TENSION LOADING

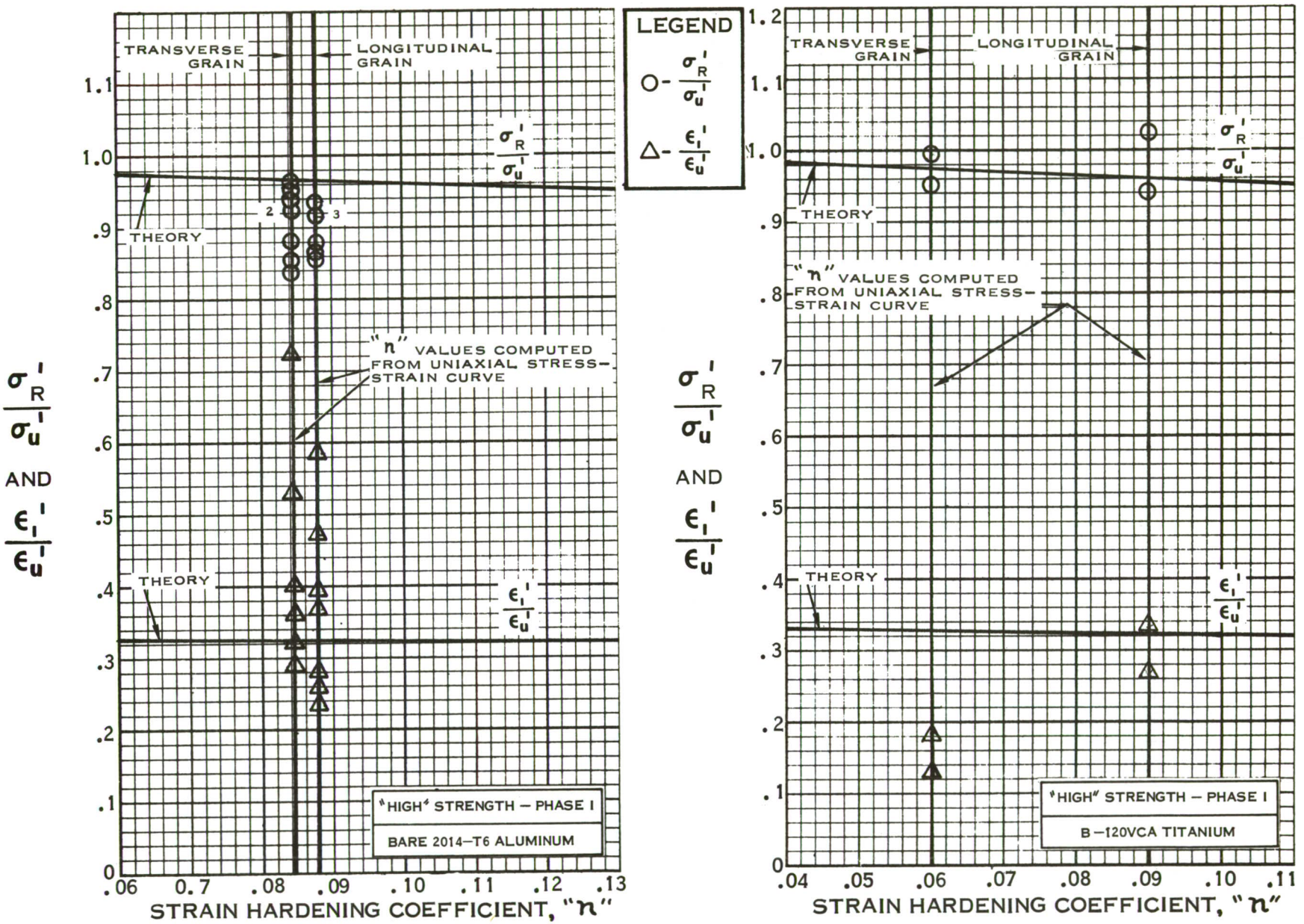

FIGURE 28 – COMPARISON OF STRESSES AND STRAINS AT MAXIMUM LOAD UNDER 1:1 LOADING WITH THE DEFORMATION ENERGY THEORY

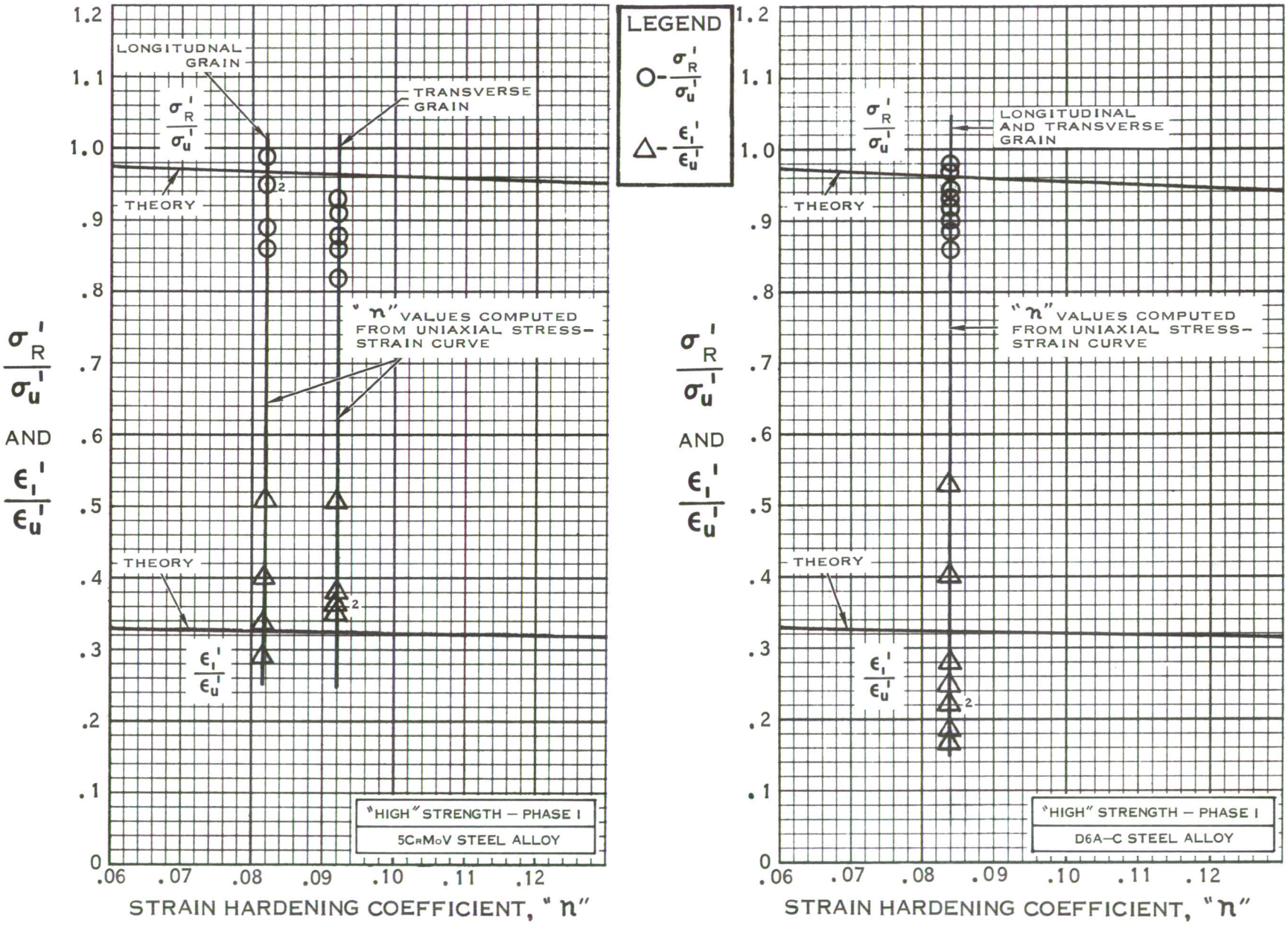

FIGURE 29 – COMPARISON OF STRESSES AND STRAINS AT MAXIMUM LOAD UNDER 1:1 LOADING WITH THE DEFORMATION ENERGY THEORY

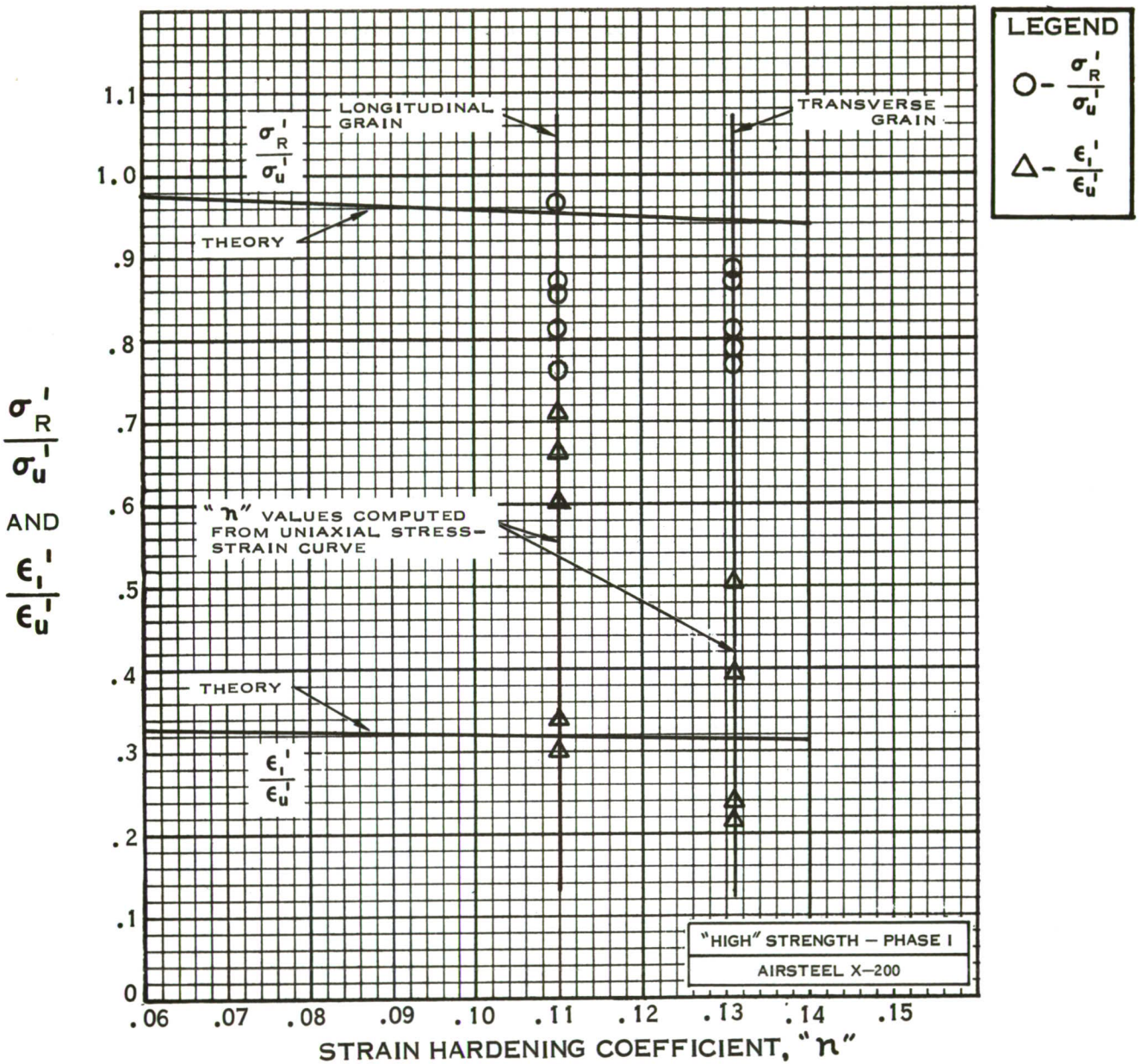

FIGURE 30 – COMPARISON OF STRESSES AND STRAINS AT MAXIMUM LOAD UNDER 1:1 LOADING WITH THE DEFORMATION ENERGY THEORY

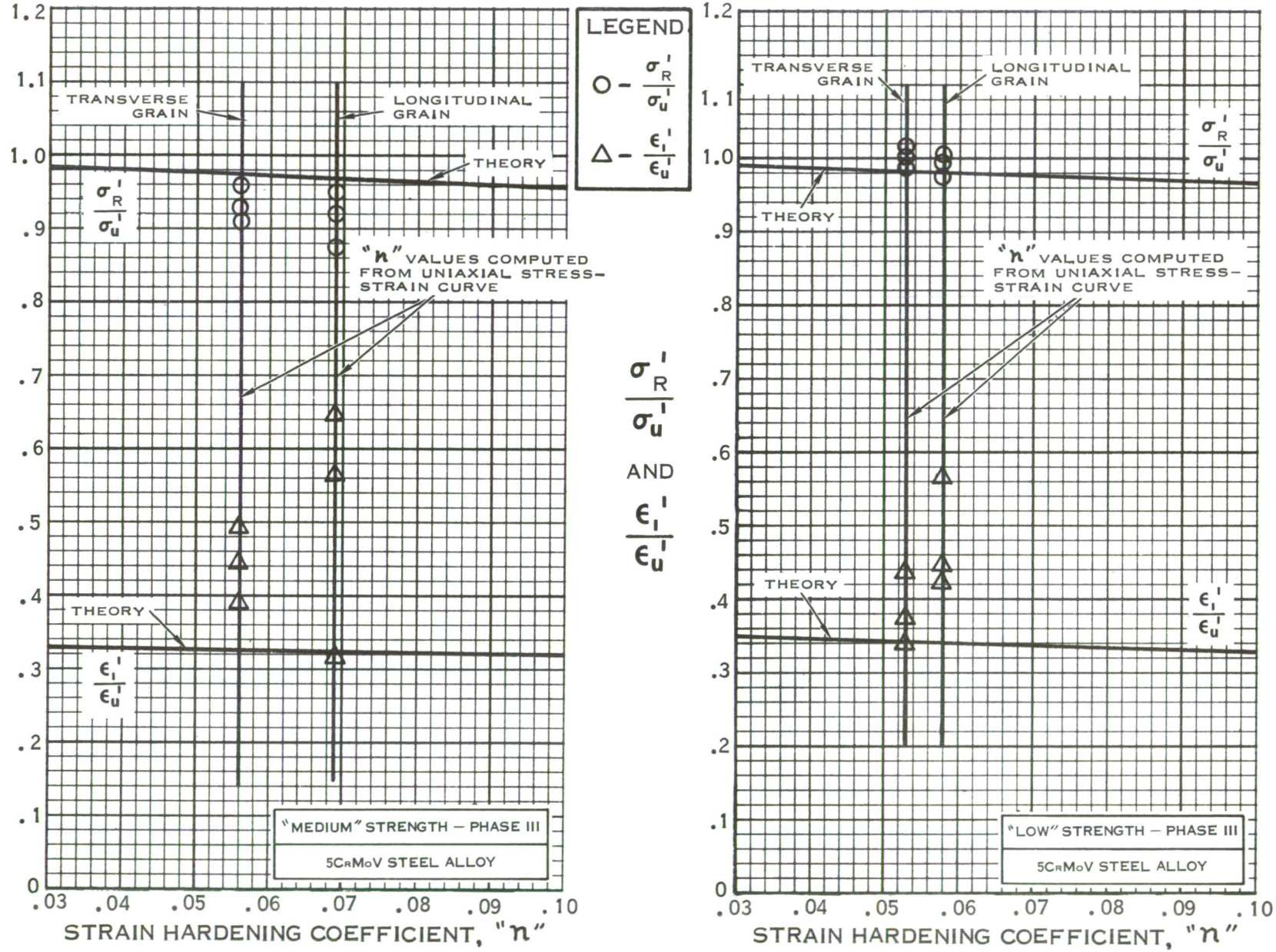

FIGURE 31 — COMPARISON OF STRESSES AND STRAINS AT MAXIMUM LOAD UNDER 1:1 LOADING WITH THE DEFORMATION ENERGY THEORY

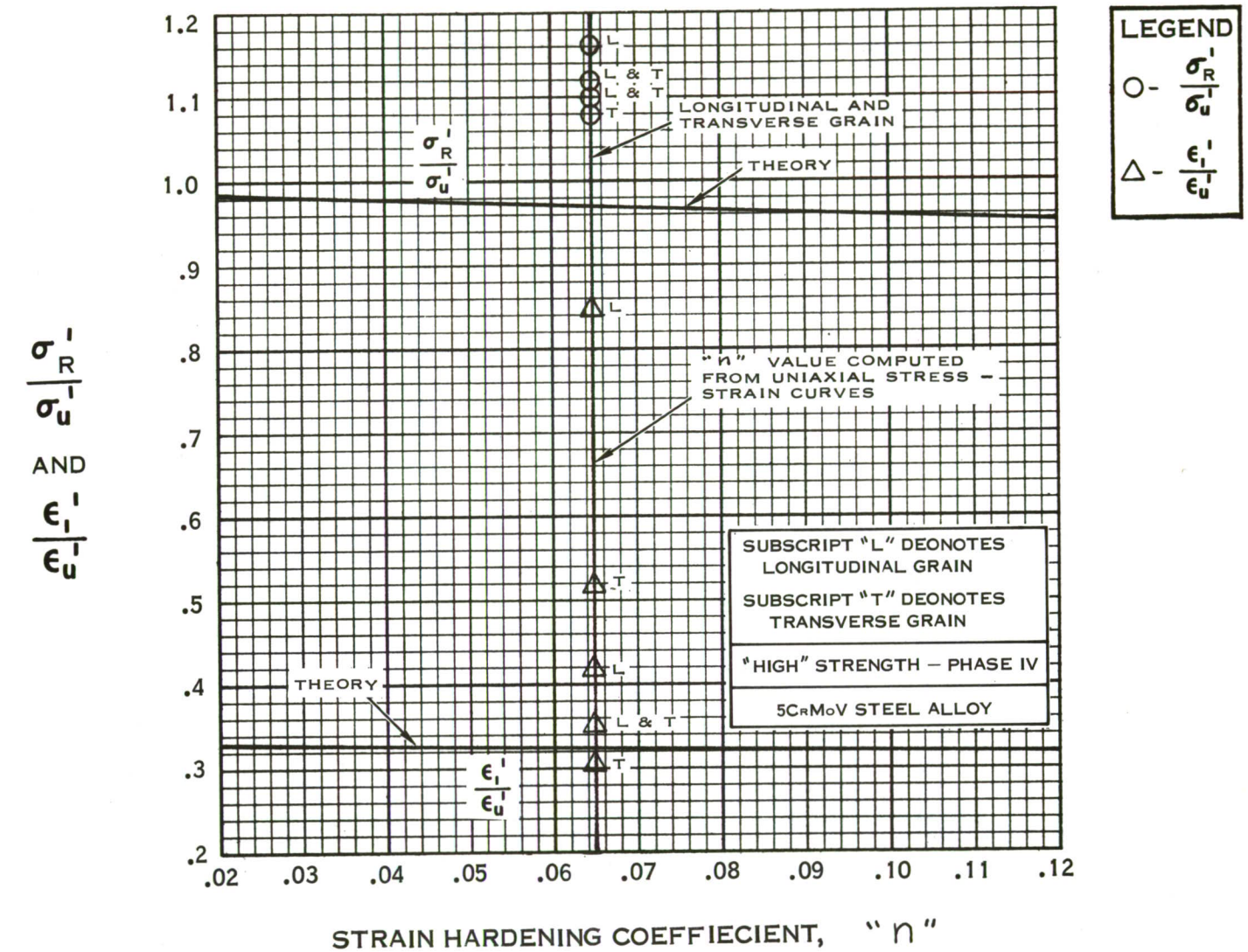

FIGURE 32 — COMPARISON OF STRESSES AND STRAINS AT MAXIMUM LOAD UNDER 1:1 LOADING WITH THE DEFORMATION ENERGY THEORY — WELDED SPECIMENS

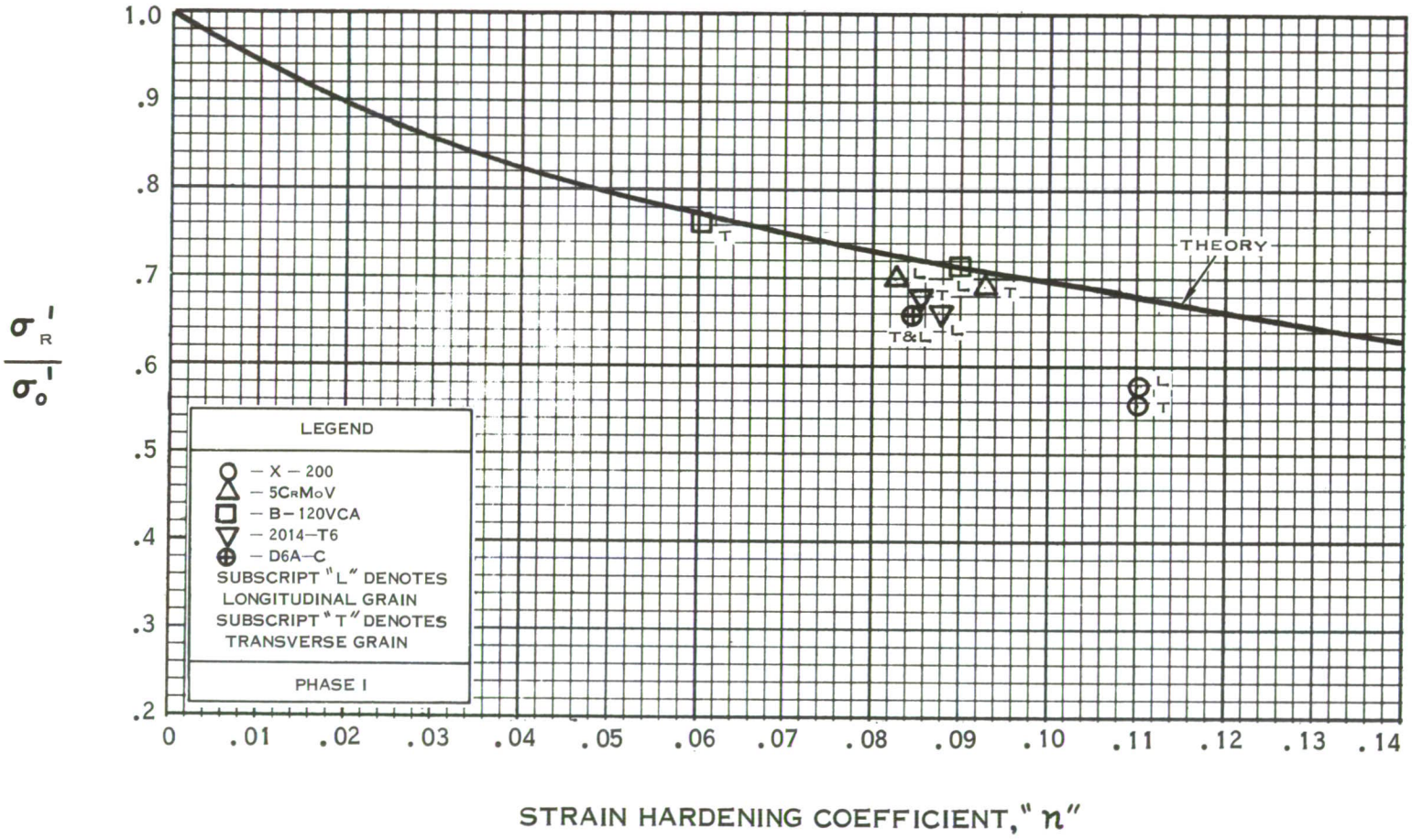

FIGURE 33 — COMPARISON OF STRESSES AT MAXIMUM LOAD UNDER 1:1 LOADING WITH THE DEFORMATION ENERGY THEORY

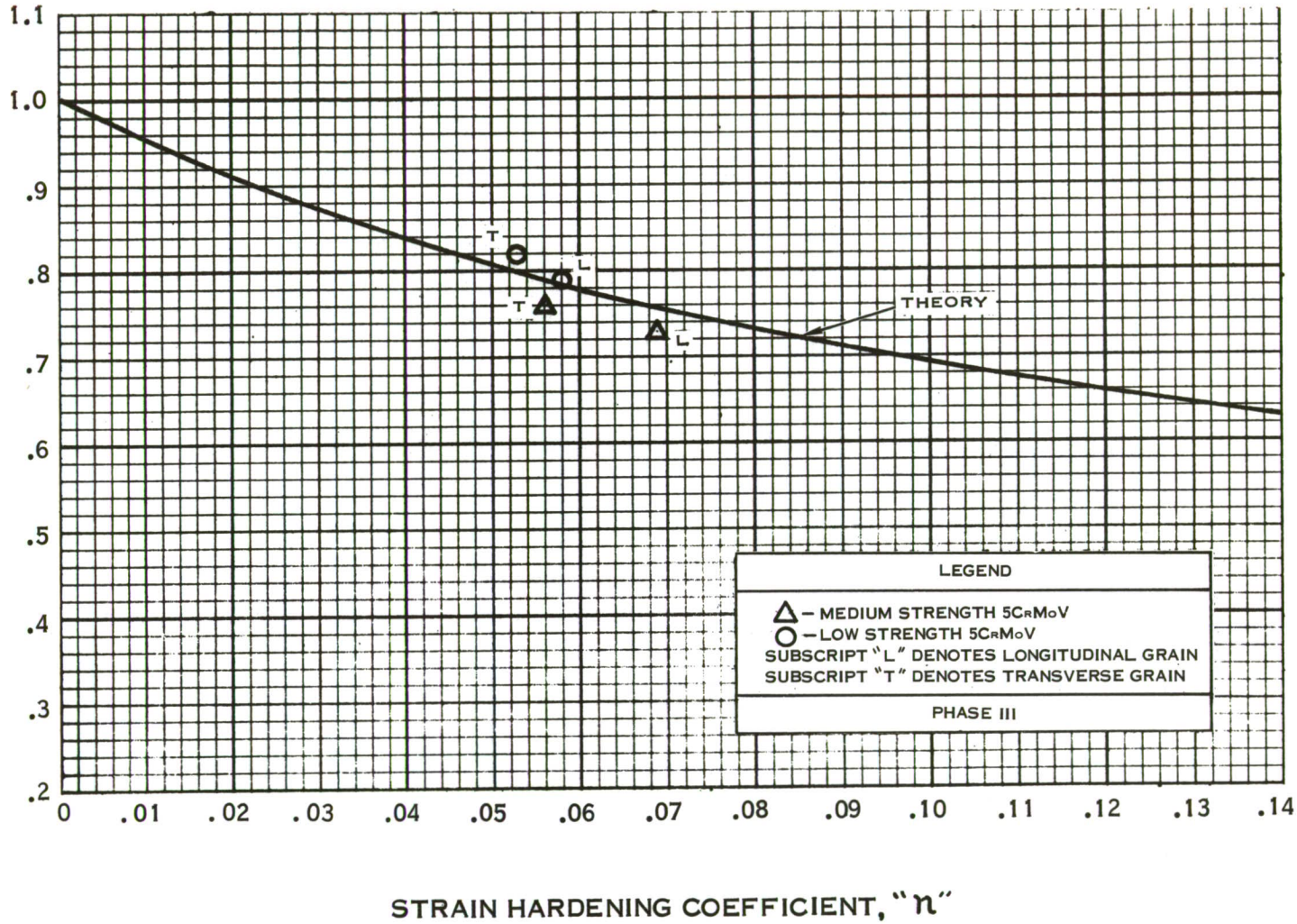

FIGURE 34 COMPARISON OF STRESSES AT MAXIMUM LOAD UNDER 1:1 LOADING WITH THE DEFORMATION ENERGY THEORY

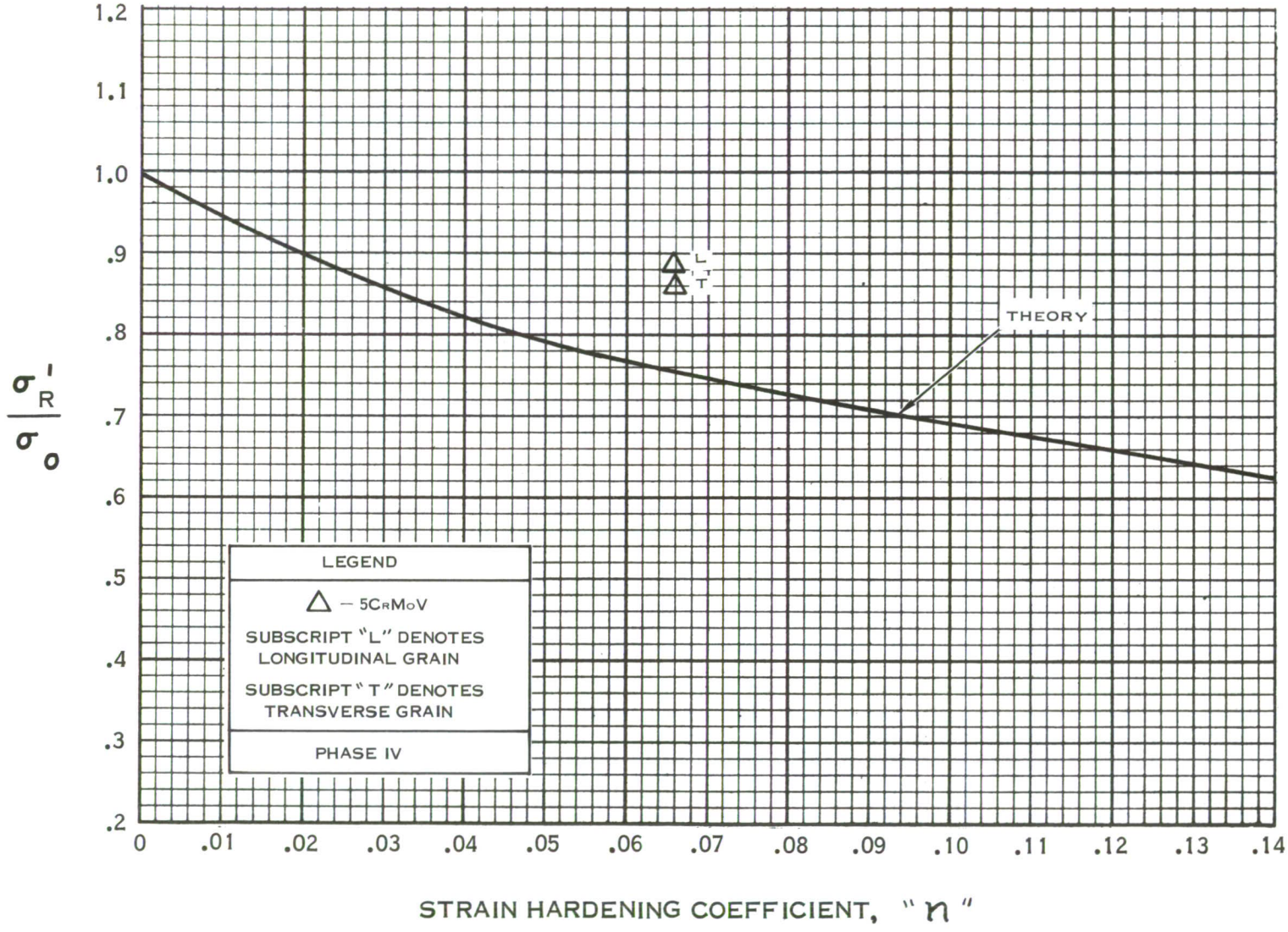

FIGURE 35 — COMPARISON OF STRESSES AT MAXIMUM LOAD UNDER 1:1 LOADING WITH THE DEFORMATION ENERGY THEORY — WELDED SPECIMENS

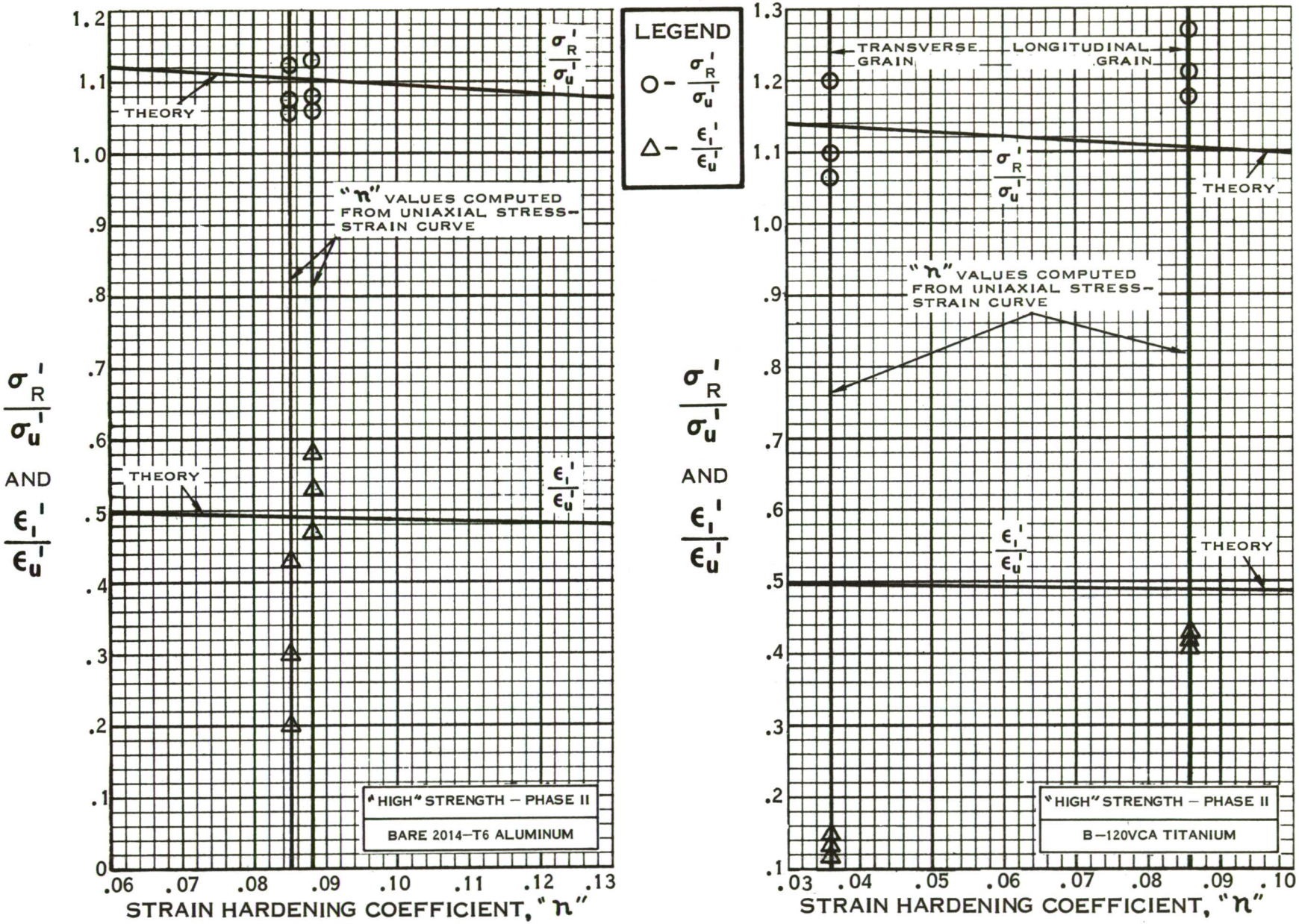

FIGURE 36 – COMPARISON OF STRESSES AT MAXIMUM LOAD UNDER 2:1 LOADING WITH THE DEFORMATION ENERGY THEORY

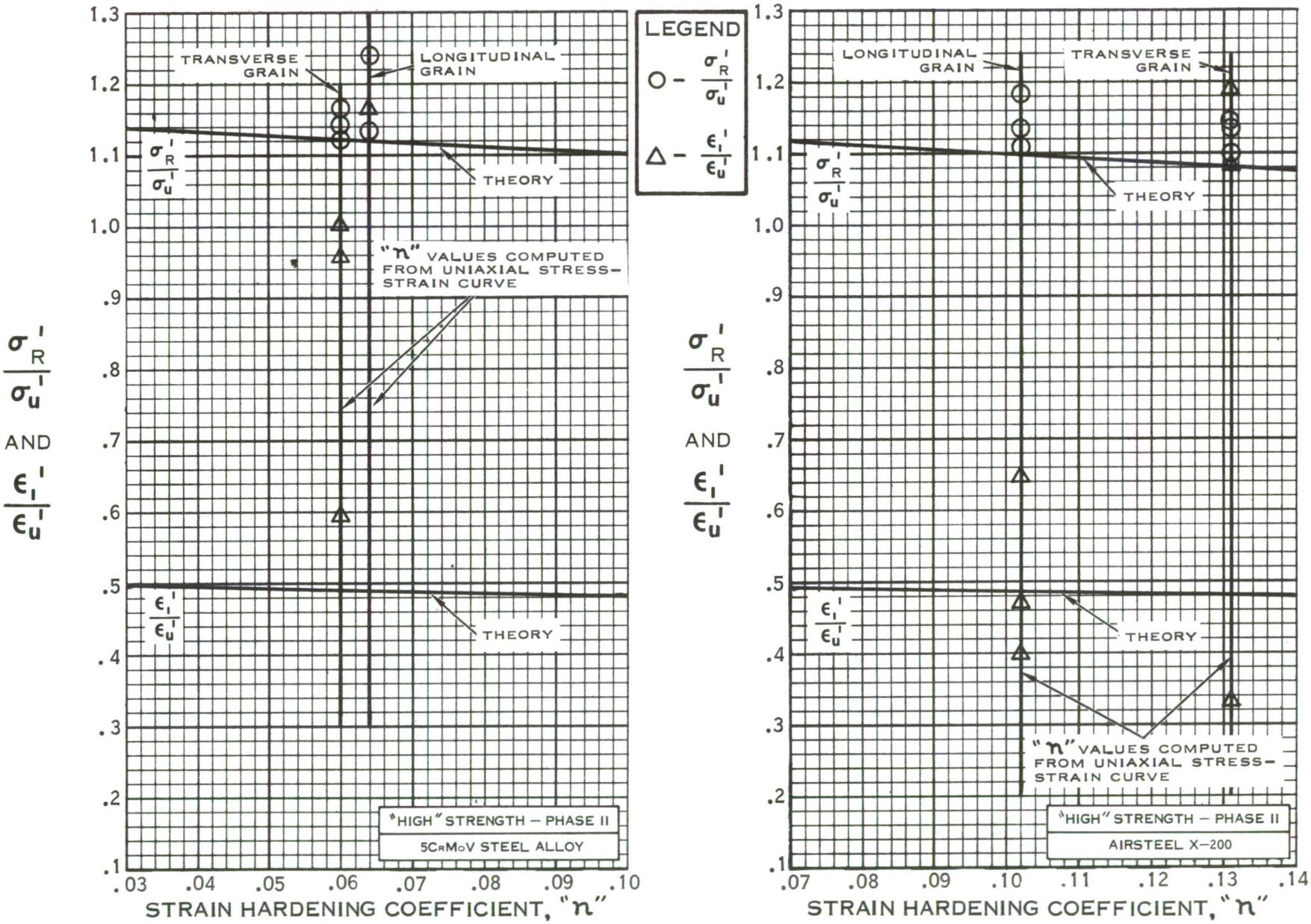

FIGURE 37 – COMPARISON OF STRESSES AND STRAINS AT MAXIMUM LOAD UNDER 2:1 LOADING WITH THE DEFORMATION ENERGY THEORY

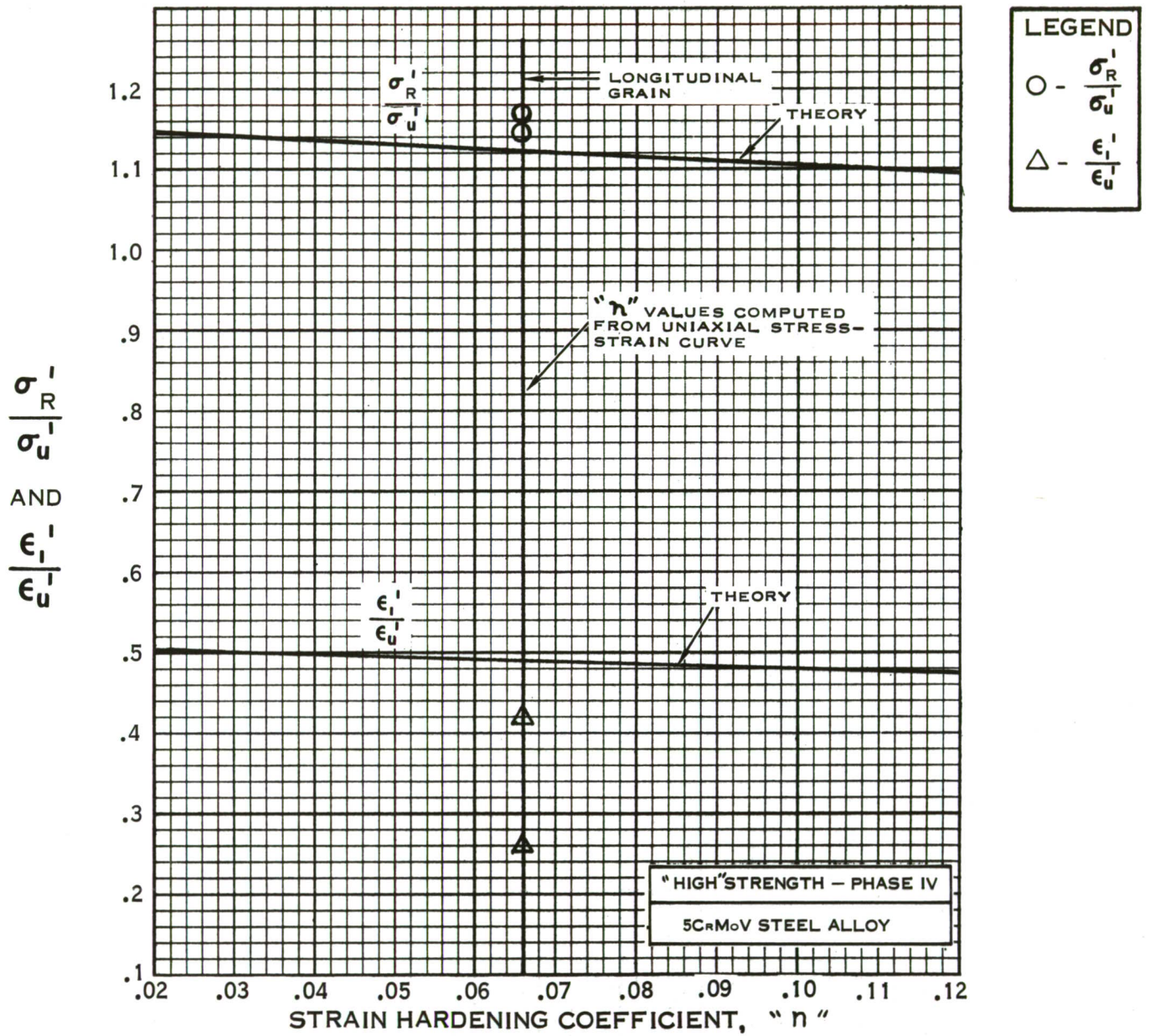

FIGURE 38 – COMPARISON OF STRESSES AND STRAINS AT MAXIMUM LOAD UNDER 2:1 LOADING WITH THE DEFORMATION ENERGY THEORY – WELDED SPECIMENS

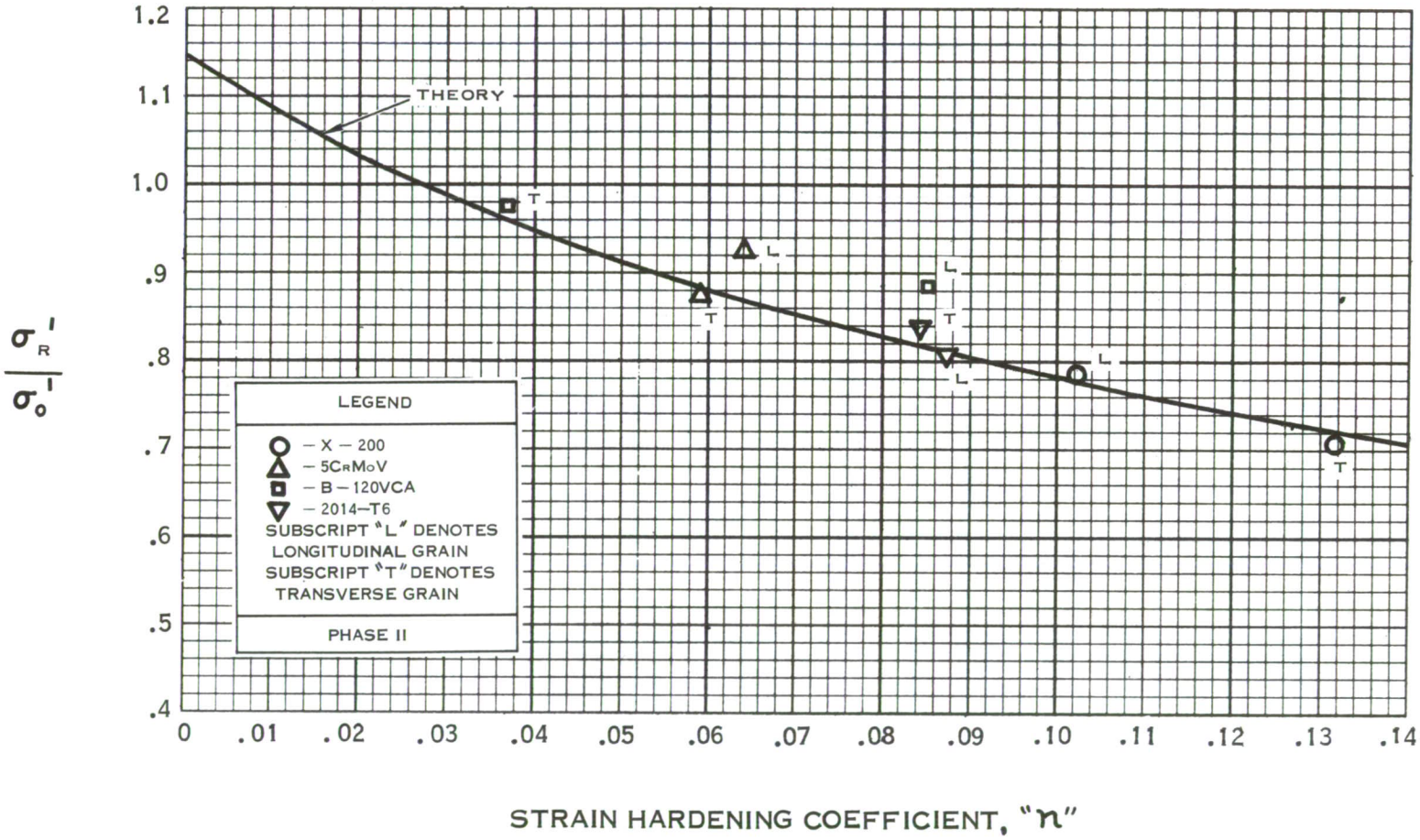

FIGURE 39 COMPARISON OF STRESSES AT MAXIMUM LOAD UNDER 2:1 LOADING WITH THE DEFORMATION ENERGY THEORY

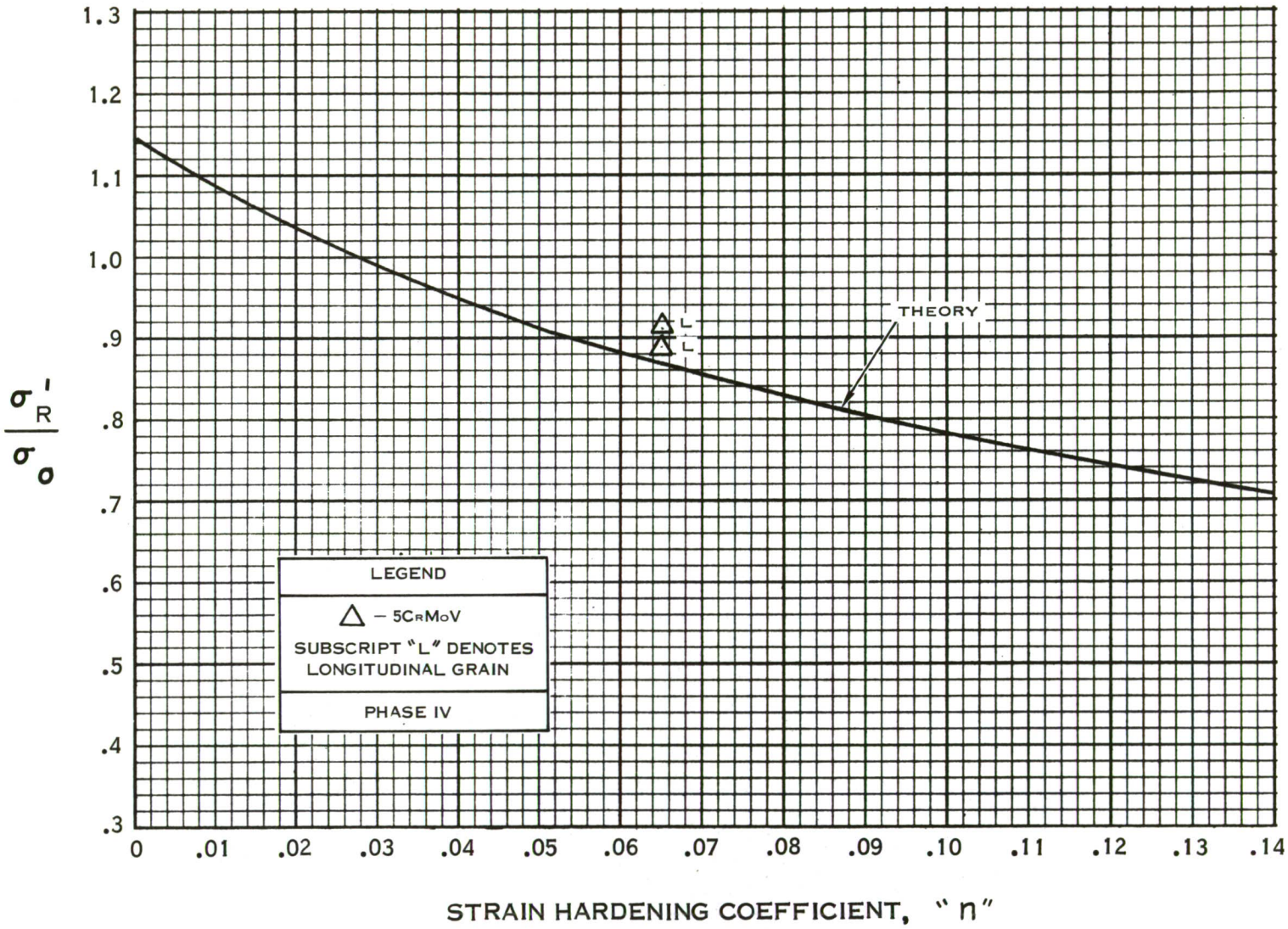

FIGURE 40 —COMPARISON OF STRESSES AT MAXIMUM LOAD UNDER 2:1 LOADING WITH THE DEFORMATION THEORY — WELDED SPECIMENS

SECTION 13

EFFECTS OF STRENGTH LEVEL ON BEHAVIOR OF MATERIALS UNDER BIAXIAL LOADING AS ESTIMATED FROM UNIAXIAL TESTS

13.1 Discussion of Effects of Strength Level on Biaxial Strain Behavior of 5CrMoV Material

The biaxial tests which were conducted on the "high," "medium" and "low" strength 5CrMoV steel showed that decreasing the strength level did not increase the biaxial ductility. For most materials, decreasing the strength level usually results in an increase in uniaxial failure strain. The biaxial failure stresses from the 5CrMoV material decreased at about the same rate as the tensile ultimate strength when the heat treat tempering temperature was increased.

Figures 41 and 42 show a plot of the principal stresses and principal plastic strains versus uniaxial tensile ultimate for the various strength levels of the 5CrMoV material which were investigated. The relationship between the biaxial and uniaxial stresses is about what would be predicted by the deformation energy theory. The deformation energy theory, discussed in Section 12 and Appendix D, shows that failure of the 5CrMoV material under 1:1 and 2:1 loading will occur at stress levels slightly less than uniaxial tensile ultimate and slightly greater than uniaxial tensile ultimate, respectively. The biaxial strain behavior shown by Figures 41 and 42 is remarkable. Higher strain values were recorded from the "high" strength specimens than from either the "medium" or "low" strength specimens. The nominal strains, ϵ_u, recorded at maximum load from the 5CrMoV "high," "medimum" and "low" strength uniaxial specimens follow the same trend. The uniaxial failure strain values, ϵ'_{MAX}, do not show such a behavior. As shown by Tables 3, 4, and 5 the ϵ'_{MAX} values increase as the strength level decreases. This situation indicates that strain at maximum load rather than failure strain in the uniaxial test is a better indicator of strain performance under biaxial loading. The deformation energy theory expresses biaxial strain at maximum load in terms of uniaxial strain at maximum load. However, as shown by the ϵ'_1/ϵ'_u curves in Figures 43 and 44, strain at maximum load serves only as an indicator for the 5CrMoV material since the curves do not follow any particular trend.

As discussed in Section 8 and 9, the 5CrMoV "medium" and "low" strength biaxial specimens did not display the shattering behavior that was obtained during the tests on the "high" strength specimens. The significance of this behavior is discussed in Section 15.

13.2 Effects of Strength Level on Biaxial Strain Behavior of Other Test Materials as Estimated From Uniaxial Tests

In view of the above discussion, it appears that some measure of the biaxial strain performance of the B-120VCA and X-200 materials at the "medium" and "low" strength levels can be estimated from the uniaxial tests. From the curves shown in Section 12, it appears that biaxial stress and strain values as high as those predicted by the deformation energy theory can be expected from the X-200 material at the "medium" and "low" strength levels. By use of the n and ϵ_u values shown in Table 5 and the deformation energy theory, the estimated biaxial failure stresses and strains for the X-200 material are as follows:

Uniaxial Strength ksi	1:1 Loading				2:1 Loading			
	Long. Grain		Tran. Grain		Long. Grain		Tran. Grain	
	σ_R' -ksi	ϵ_i' -%	σ_R' -ksi	ϵ_i' -%	σ_R' -ksi	ϵ_i' -%	σ_R' -ksi	ϵ_i' -%
259.0	250.0	2.13	250.0	1.98	287.5	3.23	287.5	3.07
238.0	232.5	1.50	231.0	1.65	268.0	2.25	266.0	2.49

The "flash anneal" treatment at 1100° F for 20 minutes which was given to the "medium" strength B-120VCA uniaxial specimens resulted in a strength level higher than was desired. In fact the tensile ultimate strength of the Phase III "medium" strength specimens was only five to ten percent lower than the strength of the Phase I and II "high" strength specimens. For this reason, biaxial specimens subjected to the "medium" strength heat treatment would probably display the same poor strain performance that was obtained from the "high" strength 1:1 and 2:1 specimens. However, satisfactory biaxial strain behavior would be expected from the B-120VCA "low" strength material. By use of the n and ϵ_u' values shown in Table 5 and the deformation energy theory, the estimated biaxial failure stresses and strains for the B-120VCA "low" strength material are as follows:

Uniaxial(1) Strength ksi	1:1 Loading				2:1 Loading			
	Long. Grain		Tran. Grain		Long. Grain		Tran. Grain	
	σ_R' -ksi	ϵ_i' -%	σ_R' -ksi	ϵ_i' -%	σ_R' -ksi	ϵ_i' -%	σ_R' -ksi	ϵ_i' -%
132.7	127.7	1.72	132.0	0.79	147.0	2.58	152.6	1.18

(1) Average of longitudinal and transverse values.

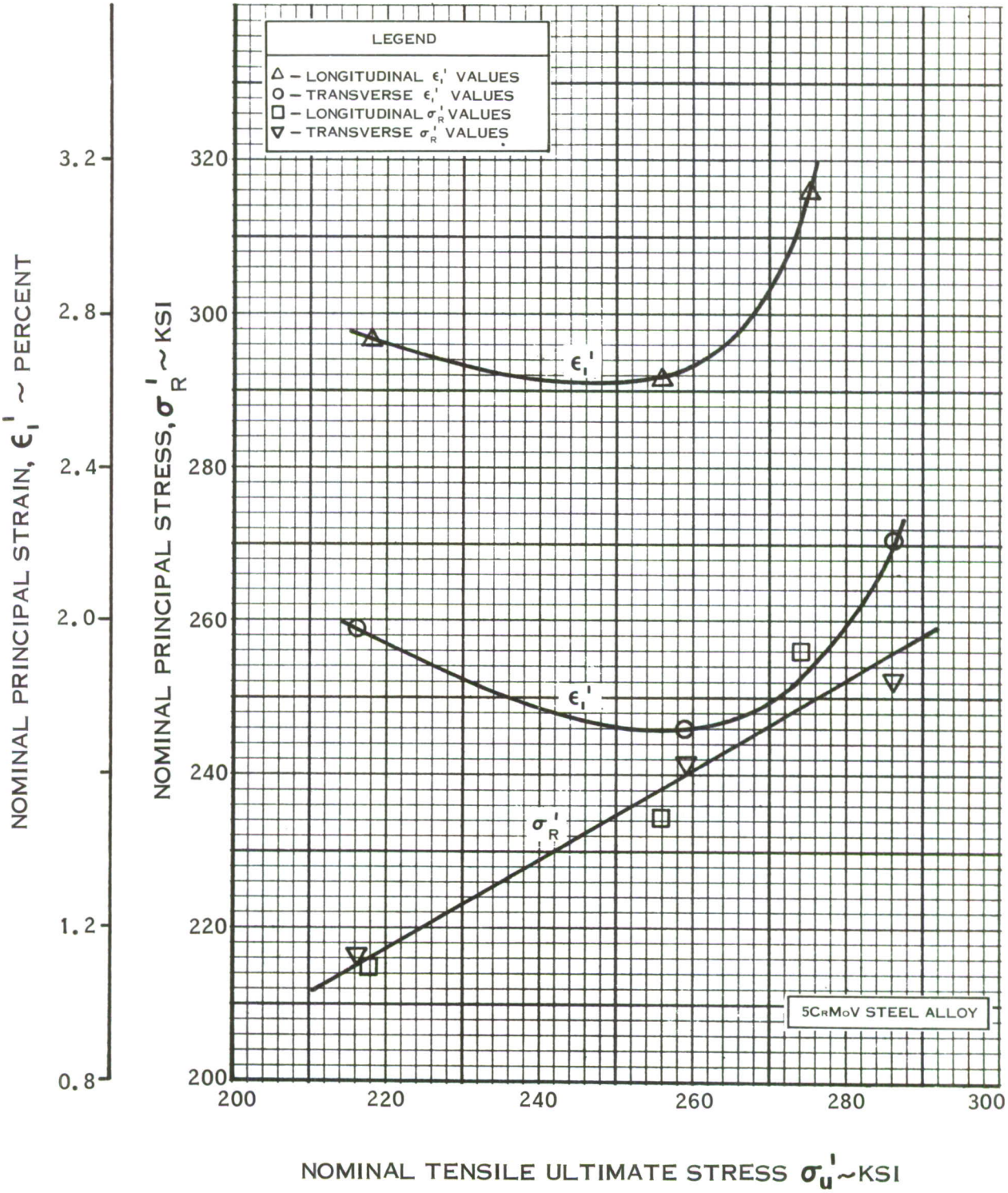

FIGURE 41 – EFFECT OF STRENGTH LEVEL ON FAILURE STRESS AND STRAIN UNDER 1:1 LOADING

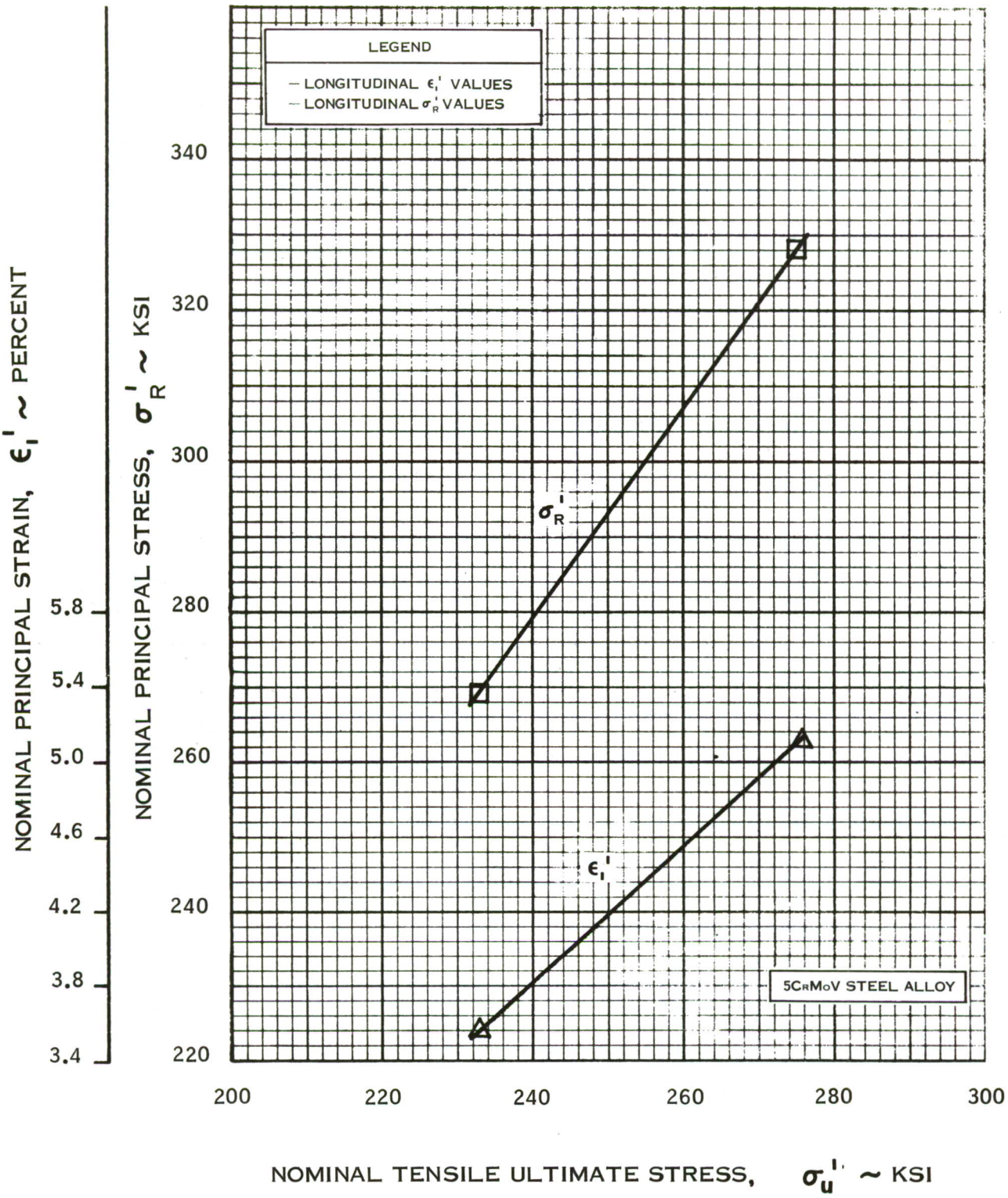

FIGURE 42 — EFFECT OF STRENGTH LEVEL ON FAILURE STRESS AND STRAIN UNDER 2: 1 LOADING

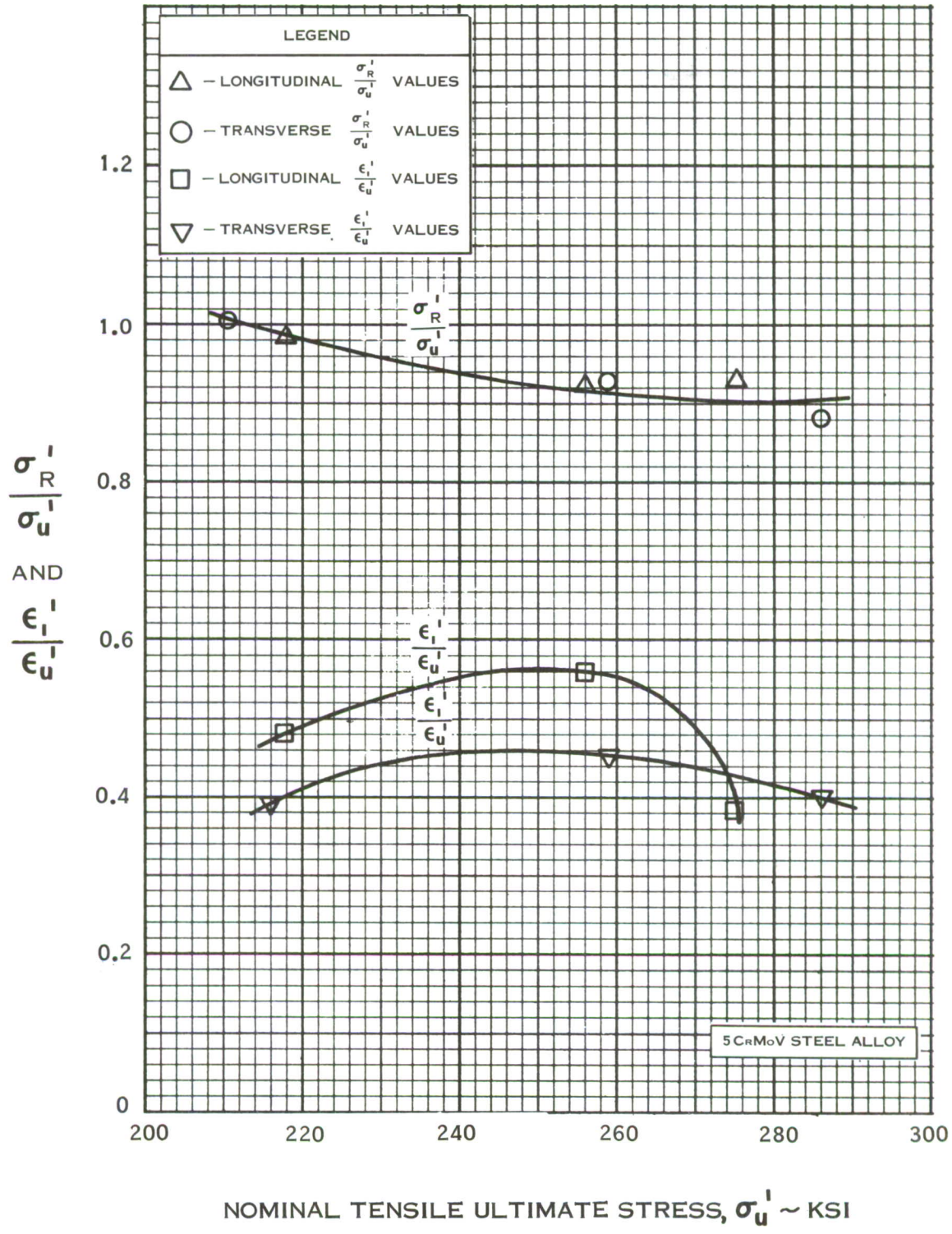

FIGURE 43 – EFFECT OF STRENGTH LEVEL ON RATIO OF $\frac{\epsilon_1'}{\epsilon_u'}$ AND $\frac{\sigma_R'}{\sigma_u'}$
1: 1 LOADING

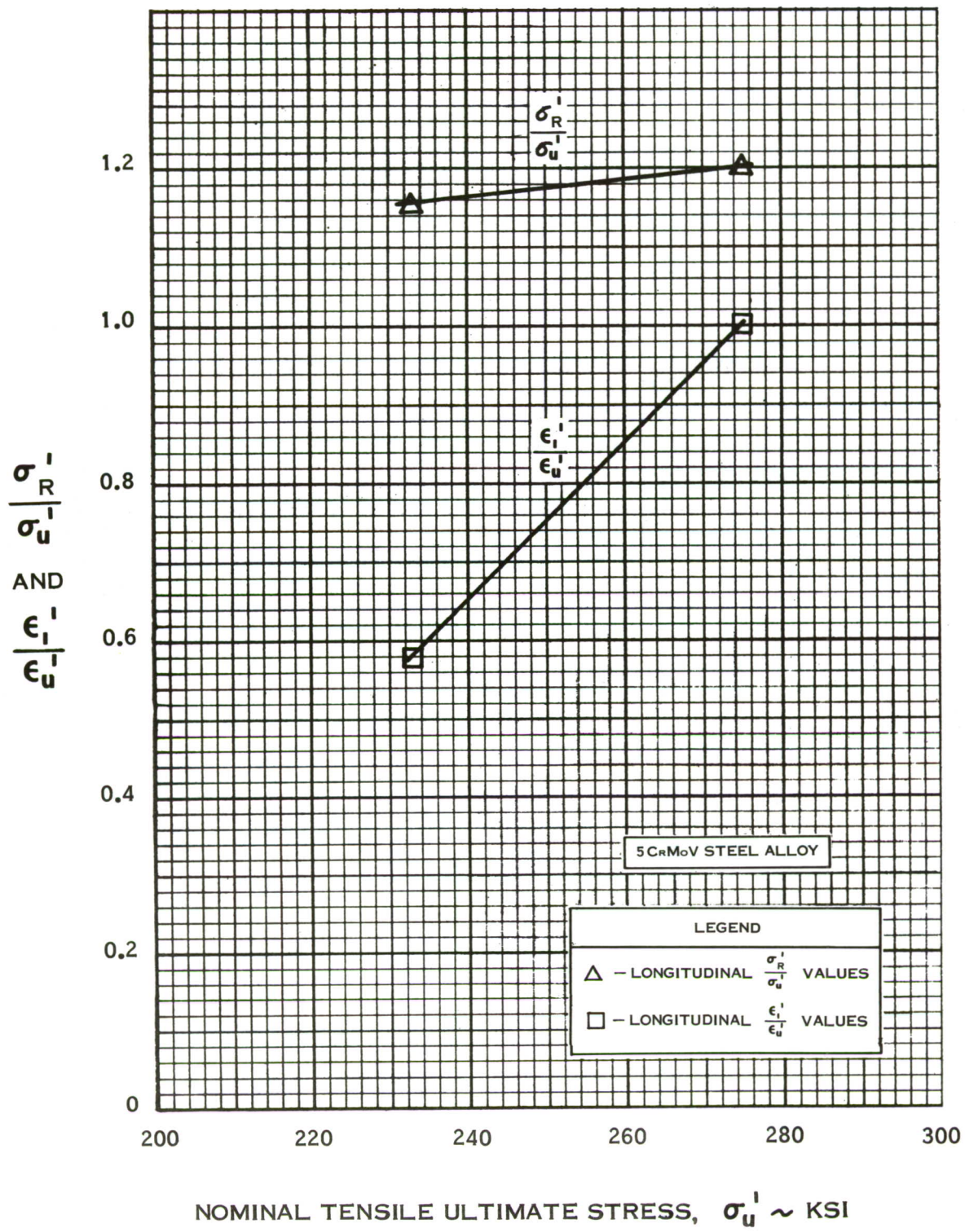

FIGURE 44 – EFFECT OF STRENGTH LEVEL ON RATIO OF $\frac{\epsilon_1'}{\epsilon_u'}$ AND $\frac{\sigma_R'}{\sigma_u'}$ 2:1 LOADING

SECTION 14

WELD JOINT EFFICIENCY UNDER BIAXIAL LOADING AS ESTIMATED FROM UNIAXIAL TESTS OF WELDED SPECIMENS

As shown by Tables 10, 12, 13 and 15, 100 percent joint efficiency based on stress was obtained from the 5CrMoV welded biaxial specimens under both 1:1 and 2:1 loading. The joint efficiency of the specimens tested under 1:1 loading was about 80 percent based on biaxial strain. However, the joint efficiency of the specimens tested under 2:1 loading was only about 30 percent based on biaxial strain. This wide discrepancy makes it difficult to estimate weld joint efficiency of other materials under biaxial loading from uniaxial tests of welded specimens. From the limited tests, it may be assumed that 100 percent biaxial joint efficiency based on stress can be obtained if the joint efficiency as obtained from the uniaxial test is 100 percent.

The uniaxial test results in Table 6 show that the processes used to weld the specimens resulted in highly efficient joints except for the 2014-T6 material. The 2014-T6 specimens were welded in the T6 condition and were not given any heat treatment after welding.

SECTION 15

APPLICATION OF BIAXIAL STRESS-STRAIN DATA TO DESIGN OF BIAXIALLY LOADED COMPONENTS

15.1 General

In this section some of the various applications of the biaxial data are outlined and discussed. The applications which are considered are as follows:

(1) Ranking of test material to determine materials which will show best performance in biaxially loaded components.

(2) Burst pressure analysis of pressure vessels. An example problem is presented to demonstrate the use of the biaxial data.

Statistical parameters are tabulated which will give information for calculating biaxial design allowables for any probability and confidence level.

15.2 Ranking of Test Materials

The ranking of the test materials is shown in Table 18. The following factors were considered in ranking the materials:

(1) Biaxial ductility rating

(2) Resistance to crack-like flaws

(3) Biaxial strength/weight

The biaxial ductility rating is based upon the relative position of the experimental biaxial strain values with the deformation energy theory as shown in Section 12. The ϵ_i/ϵ_u curves shown in Section 12 can be considered the strain required to reach theoretical burst pressure for a perfect cylinder or sphere. The biaxial ductility is rated good if the experimental values are on an average considerably higher than the values predicted by the theory. However, if the strain values are approximately equal to the theory, the rating is termed fair and if the strain values are on an average below the theory the rating is termed poor.

The significance of the biaxial ductility rating can be illustrated by use of the test results from the 5CrMoV pressure vessels which were dented. One "low" strength and one "high" strength vessel was purposely dented to determine the effect of a high strain concentration on failure behavior. The failure did not initiate in the dents in either of the vessels, but in an area where the wall thickness was slightly less than in the area of the dents. The strain values obtained from the "low" and "high" strength 5CrMoV 2:1 biaxial specimens were considerably higher on an average than the minimum required to reach theoretical burst pressure for a perfect cylinder. For this reason, the probability of failure outside of the dented area was just as high as in the dent. However, similar defects in vessels fabricated from materials having a poor biaxial ductility rating, such as the "high" strength D6A-C steel alloy, would probably cause failure at low nominal stress levels.

The pressure vessel tests described in Section 10 showed that the shattering behavior of the "high" strength 5CrMoV biaxial specimens was indicative of poor resistance to crack-like flaws in the material. The fracture in one of the "low" strength 5CrMoV vessels initiated in a weld void after a high nominal stress level had been attained. However, one of the "high" strength 5CrMoV vessels ruptured at a relatively low nominal stress level under similar conditions. In this case the weld void was considerably smaller than the void in the "low" strength vessel. The notch toughness tests described in Section 11 indicated that the 5CrMoV steel in the "high" strength condition has less resistance to the rapid growth of sharp notches than in the "low" strength condition. On the basis of the results from the pressure vessel and notch toughness tests, the resistance of the material to crack-like flaws is termed poor if the biaxial test specimens shattered and good if the biaxial specimens did not shatter.

15.3 Burst Pressure Analysis of Thin-Walled Spheres and Cylinders

Equations are derived in Appendix D which relate the maximum attainable pressure, or burst pressure, of thin-walled spheres and cylinders to vessel geometry and material properties. In these derivations it is assumed that only pure membrane loading exists in the walls of the vessels. As an example, the equations do not account for the effects of stress and strain concentrations due to out-of-roundness, dents, mismatch of mating parts and any discontinuity loads which may exist. Discontinuity loads will always exist at the junction of the end closure and cylindrical portion of pressurized cylinders. However, these loads can be minimized to insignificance by use of end closures approaching the shape of full hemishperes that join the cylindrical portion of the vessel in a tangential manner.

From Appendix D, the significant relationships for a thin-walled sphere, 1:1 loading, and a thin-walled cylinder, 2:1 loading, are summarized as follows:

Theoretical Exact Burst Pressure for Sphere

$$p = \sigma_o \left(\frac{2}{3}^{n+1}\right) \left(\frac{t_i}{R_i}\right)\left(\frac{n}{e}\right)^n \qquad (16)$$

Approximate Burst Pressure for Sphere

$$p = \sigma_u' \left(\frac{2}{3}^{n+1}\right)\left(\frac{t_i}{R_i}\right) \qquad (17)$$

Theoretically Exact Burst Pressure for Cylinder

$$p = \sigma_o \left(\frac{2}{\sqrt{3}}\right)^{n+1}\left(\frac{t_i}{R_i}\right)\left(\frac{n}{e}\right)^n \qquad (18)$$

Approximate Burst Pressure for Cylinder

$$p = \sigma_u' \left(\frac{2}{\sqrt{3}}\right)^{n+1}\left(\frac{t_i}{R_i}\right) \qquad (19)$$

To be consistent with the theory in Appendix D, the strain hardening coefficient n used must be equal to the true strain at maximum load ϵ_u as measured from the uniaxial test.

The above equations do not contain a term for strain since it is assumed in the derivations that the material has adequate biaxial ductility to reach theoretical burst pressure. If the material has a biaxial ductility rating of poor to fair, the burst pressure must be calculated from the general pressure-plastic deformation equations from which equations (16) through (19) were derived. From Appendix D, the general pressure-plastic deformation equations for a thin-walled sphere and a thin-walled cylinder are expressed as follows:

Thin-Walled Sphere

$$\left(\frac{P}{\sigma_0}\right)\left(\frac{R_i}{t_i}\right) = \frac{4\epsilon_1^n}{e^{3\epsilon_1}} \tag{20}$$

Thin-Walled Cylinder

$$\left(\frac{P}{\sigma_0}\right)\left(\frac{R_i}{t_i}\right) = \left(\frac{2}{\sqrt{3}}\right)\frac{\left(\frac{2}{\sqrt{3}}\epsilon_1\right)^n}{e^{2\epsilon_1}} \tag{21}$$

In this case ϵ_1 represents the plastic value of the true principal strain at failure. Plots of equations (20) and (21) are shown in Figures 45 and 46 for various values of strain hardening coefficient n. The ordinates of the cut-off curve are calculated directly from equations (16) and (18) and the abscissas of the cut-off curve are the plastic values of the true principal strain at maximum load or in the case of pressure vessels the strain at maximum attainable pressure. From Appendix D, the true principal strain at maximum pressure for a thin-walled sphere is

$$\epsilon_1 = \frac{\epsilon_u}{3} \tag{22}$$

and for a thin-walled cylinder the true principal strain at maximum pressure is

$$\epsilon_1 = \frac{\epsilon_u}{2} \tag{23}$$

since $\epsilon_u = n$ according to theory.

The curves shown in Figures 45 and 46 must be used to predict burst pressure in cases when the strain values as obtained from the biaxial test are less than the values shown by equations (22) and (23). If the experimental strain values are equal to or greater than those shown by equations (22) and (23), equations (16) through (19) may be used to predict burst pressure.

Failure by actual rupture of the vessel wall is only one of two possible design criteria for a pressure vessel. It may be desired to limit any given

design to the pressure causing a given amount of permanent radial deformation, which corresponds to some amount of permanent hoop strain. In this case the pressure-plastic deformation curves shown in Figures 45 and 46 may be used to establish the design.

To illustrate the use of the burst pressure and pressure-plastic deformation equations the following example problem will be solved.

10 inch radius cylinder

Design pressure = 1,000 psi

Operating pressure = 900 psi

2014-T6 aluminum - longitudinal grain direction

What is required wall thickness t_i to withstand 1,000 psi pressure and what is permanent hoop strain at 900 psi operating pressure?

From Table 4 the material properties required to solve the problem are as follows:

$\sigma'u$ = 71,600 psi
σo = 96,800 psi
ϵu = 7.87%

From equation (23) the true strain at maximum pressure is

$$\epsilon_1 = \frac{7.87}{2} = 3.93\%$$

From Table 13 the average true principal plastic strain obtained from the 2:1 biaxial tests on the 2014-T6 material is

$$\epsilon_1 = \ln (1 + 0.043) = 4.19\%$$

It is evident that this material has sufficient biaxial ductility to reach theoretical burst pressure. From equation (18) the required wall thickness to withstand 1,000 psi pressure is

$$t_i = 0.123 \text{ inches}$$

Use will be made of the curves in Figure 46 to calculate the permanent hoop strain at the 900 psi operating pressure. Entering these curves at an ordinate value of

$$\left(\frac{P}{\sigma_o}\right)\left(\frac{R_i}{t_i}\right) = \frac{900}{96,800} \quad \frac{10}{0.123} = 0.755$$

yields a permanent hoop strain of 0.49%.

15.4 Statistical Analysis of Biaxial Stress and Strain Data

When establishing design allowables the designer is always interested in the reproducibility of test results. In using the biaxial stress and strain data it may be necessary to establish design allowables based on certain probability and confidence levels. Since these levels may vary depending upon the design conditions, the required statistical parameters for calculating design allowables are presented in Table 19. The following equation, together with the statistical parameters in Table 19, will provide the desired tolerence limit:

$$L_{\gamma,\alpha} = \bar{Z} - KS$$

where: $L_{\gamma,\alpha}$ is the tolerance limit for normal distribution, such that the probability is γ that at least a proportion $1-\alpha$ of the distribution is greater than $\bar{Z}$ -KS where:
$\bar{Z}$ is the arithmetic mean of the sample tested.
S is the standard deviation of the sample.
K is the factor which depends on specified values of γ, α, and sample size (N).

The value of $\bar{Z}$ is determined as follows:

$$\bar{Z} = \frac{\sum_{i=1}^{n} Z_i}{N}$$

where N is the number of specimens tested.

The standard deviation of the sample, S, is determined by use of the following relationships:

$$S = \sqrt{\frac{\sum_{i=1}^{n}(Z_i - \bar{Z})^2}{N-1}} \quad \text{or} \quad S = \sqrt{\frac{\sum_{i=1}^{n} Z_i^2 - \left(\sum_{i=1}^{n} Z_i\right)^2/N}{N-1}}$$

When comparing samples whose measurements are small in magnitude with samples whose measurements are large in magnitude, a dimensionless statistic, V, may be calculated ($V = S/\bar{Z}$). This statistic, called the coefficient of variation, is useful for comparing the variations in two samples and, hence, is applicable for comparing the reproducibility of test results of one material with those of another material. The smaller the coefficient of variation, the more reproducible the test results should be in actual practice. Therefore, the different materials and strength levels may be compared directly by this dimensionless coefficient.

As shown in the table of parameters, the values of the coefficient of variation for stresses indicate good reproducibility. However, the "V" values for strain indicate more scatter and hence poorer reproducibility.

In addition to the parameters, $\bar{Z}$, N, S, and V, the minimum and maximum values obtained from each sample are listed in Table 19. These values are designated as $R_{max.}$ and $R_{min.}$

The statistical parameters presented in Table 19 and the equations in this section provide a means of statistically evaluating the data of this program. Design allowables based on specific probability and confidence levels were not calculated since design conditions vary. It should be pointed out that the number of specimens tested was low and therefore, greatly influences any calculated design allowables. However, these statistical parameters do provide a convenient means of comparing reproducibility of data from different materials. This is best illustrated by comparing the coefficients of variation for each material while considering such variables as sample size and scatter ranges.

TABLE 18 - RANKING OF TEST MATERIALS FOR USE IN BIAXIALLY LOADED COMPONENTS

MATERIAL[1]	BIAXIAL DUCTILITY RATING		RESISTANCE TO CRACK-LIKE FLAWS	BIAXIAL STRENGTH/[2] WEIGHT	
	1:1	2:1		1:1	2:1
X-200 (H)	GOOD	FAIR	GOOD	8.43×10^6	11.85×10^6
5CrMoV (M)	GOOD	----	GOOD	8.40	------
5CrMoV (H)	GOOD	GOOD	POOR	8.99	11.12
5CrMoV (L)	GOOD	GOOD	GOOD	7.60	9.52
D6A-C (H)	POOR	----	GOOD	8.93	------
2014-T6 (H)	GOOD	FAIR	GOOD	6.45	7.92
B-120VCA (H)	POOR	POOR	POOR	10.10	14.18

(1) (H) indicates "high" strength, (M) indicates "medium" strength, (L) indicates "low" strength as shown by Table 2

(2) Biaxial strength values are an average of longitudinal and transverse biaxial failure stresses

TABLE 19 - STATISTICAL PARAMETERS OBTAINED FROM BIAXIAL STRESS AND STRAIN DATA

MATERIAL	STRENGTH LEVEL (1)	STRESS RATIO	Longitudinal Grain Direction (2)												Transverse Grain Direction (2)											
			σ_R' (3)						ϵ_i' (4)						σ_R' (3)						ϵ_i' (4)					
			N	Z	S	R_{max}	R_{min}	V	N	Z	S	R_{max}	R_{min}	V	N	Z	S	R_{max}	R_{min}	V	N	Z	S	R_{max}	R_{min}	V
2014-T6	HIGH	1:1	8	64.0	2.7	67.0	60.0	0.042	7	3.04	0.98	4.83	1.92	0.322	8	65.0	3.7	69.0	60.0	0.058	7	3.20	1.15	5.58	2.14	0.348
B-120VCA	HIGH	1:1	2	180.5	11.1	188.0	173.0	0.061	2	2.15	0.34	2.40	1.90	0.136	2	183.5	9.2	188.0	179.0	0.050	2	1.10	0.28	1.29	0.91	0.216
5CrMoV	HIGH	1:1	5	256.8	11.6	272.0	238.0	0.046	4	3.12	0.63	4.15	2.36	0.202	5	251.8	10.5	266.0	235.0	0.042	5	2.21	0.35	2.88	1.97	0.158
	MEDIUM	1:1	3	234.3	10.1	244.0	223.0	0.043	3	2.63	0.35	3.00	2.28	0.133	3	241.3	10.9	250.0	236.0	0.045	3	1.65	0.14	1.85	1.45	0.085
	LOW	1:1	3	214.5	6.4	216.0	212.0	0.030	3	2.73	0.38	3.20	2.45	0.139	3	215.2	7.8	218.0	212.0	0.036	3	1.99	0.32	2.30	1.70	0.161
D6A-C	HIGH	1:1	4	249.5	10.7	266.0	236.0	0.043	4	1.03	0.46	1.72	0.72	0.440	4	255.7	8.7	266.0	245.0	0.034	4	0.80	0.33	1.30	0.59	0.410
X-200	HIGH	1:1	5	240.6	17.4	272.0	215.0	0.072	5	2.34	0.85	3.18	1.36	0.360	5	236.4	13.2	256.0	219.0	0.056	4	1.42	0.57	2.13	0.90	0.400
2014-T6	HIGH	2:1	3	78.1	3.3	81.0	75.7	0.042	3	4.30	0.44	4.75	3.85	0.102	3	80.3	2.0	81.0	80.0	0.025	3	1.89	0.89	2.80	1.02	0.470
B-120VCA	HIGH	2:1	3	228.3	6.9	239.0	220.0	0.032	3	2.30	0.15	2.35	2.25	0.065	3	219.6	11.1	238.0	208.0	0.051	3	0.76	0.12	0.90	0.68	0.158
5CrMoV	HIGH	2:1	5	350.0	14.5	379.0	309.0	0.042	5	3.64	1.45	5.60	2.13	0.398	3	302.0	9.9	318.0	284.0	0.033	3	2.77	0.71	3.25	1.90	0.256
	LOW	2:1	2	269.5	24.5	287.0	252.0	0.091	2	3.56	1.00	4.32	2.80	0.280	-	-	-	-	-	-	-	-	-	-	-	-
X-200	HIGH	2:1	3	335.0	16.7	348.0	327.0	0.050	3	1.54	0.40	1.80	1.30	0.260	3	335.3	7.9	340.0	326.0	0.024	3	2.80	1.58	4.00	1.00	0.560

(1) "High," "medium," and "low" strength level shown in Table 2.

(2) For 2:1 loading, longitudinal and transverse grain direction refers to direction of maximum principal stress.

(3) All units in this section are in ksi, except N and V which are dimensionless.

(4) All units in this section are in percent, except N and V which are dimensionless.

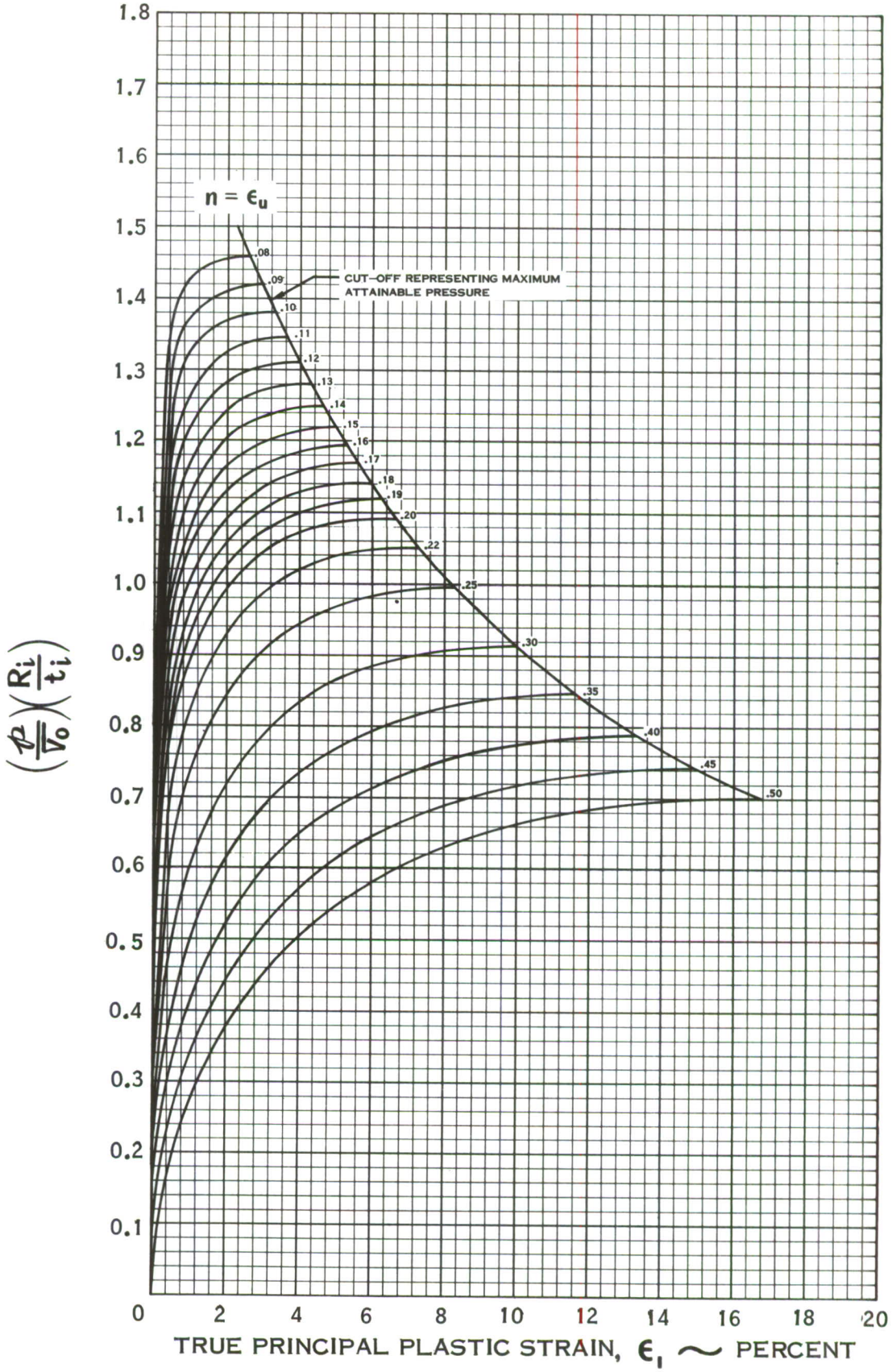

FIGURE 45 PRESSURE – PLASTIC DEFORMATION CURVES FOR INTERNALLY PRESSURIZED THIN–WALLED SPHERES

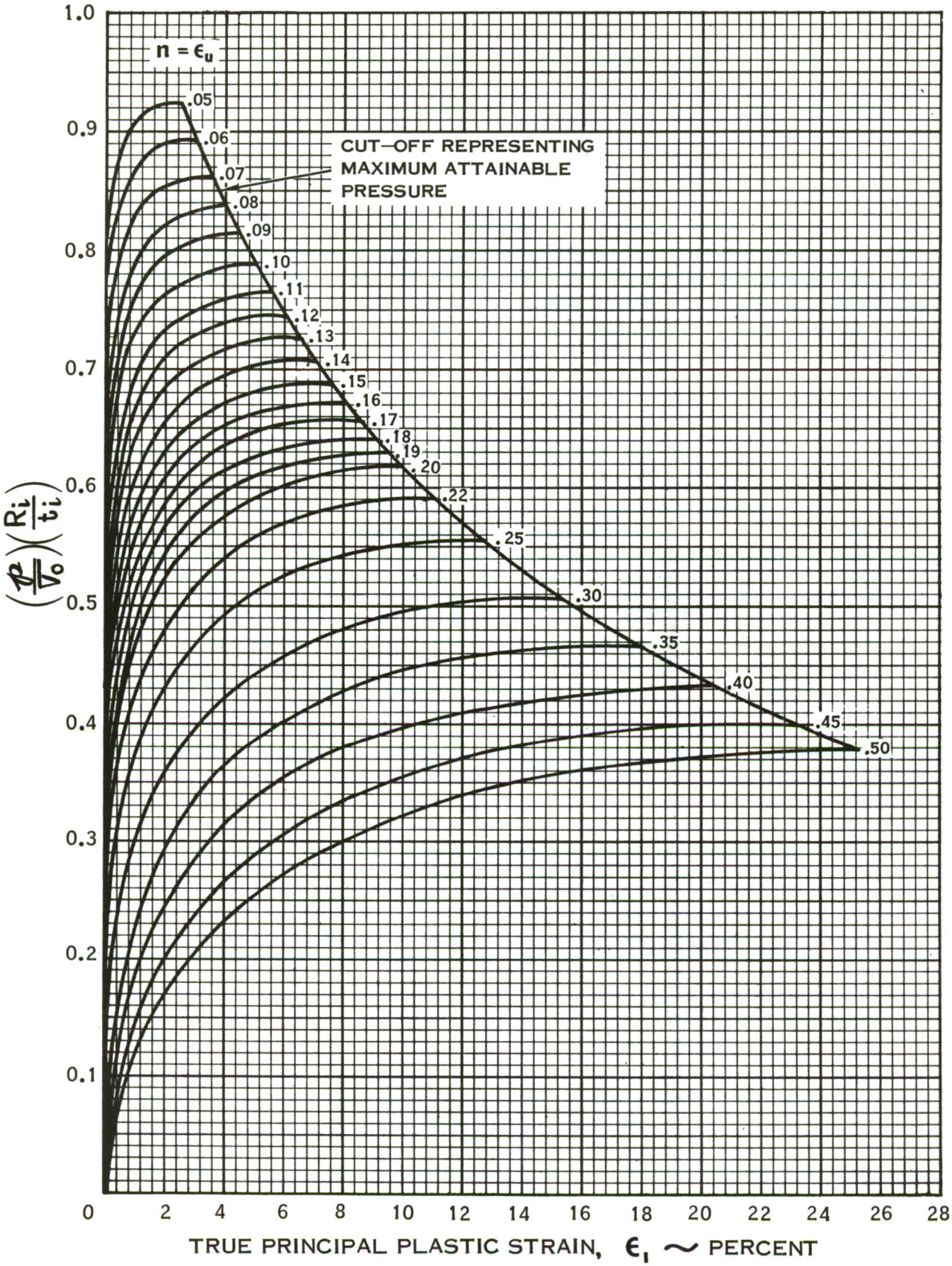

FIGURE 46 — PRESSURE — PLASTIC DEFORMATION CURVES FOR INTERNALLY PRESSURIZED THIN — WALLED CYLINDERS

SECTION 16

CONCLUSIONS AND RECOMMENDATIONS

Conclusions

A. Biaxial Test Specimen

1. For the first time, a biaxial tension specimen has been developed which accurately simulates the state of stress in pressure vessels. In the past it has been necessary to test pressure vessels to generate biaxial stress strain data. The obvious drawbacks of the pressure vessel test are cost and inability to always measure strain at the point of failure. By use of the biaxial cross specimen, it is possible to generate biaxial stress-strain curves up to the instant of failure under both 1:1 and 2:1 loading conditions.

2. Tests of the materials under 1:1 and 2:1 loading have shown that the cross shaped specimen has good reliability.

3. The biaxial test specimen serves to give biaxial stress and strain data and indicates the relative crack resistance of the material.

B. Test Data

1. The pressure vessel tests and the notch toughness tests showed that the shattering behavior of the biaxial specimen is indicative of poor resistance to crack-like flaws in the material.

2. On the basis of this study, it is concluded that the choice of materials for biaxially loaded components should be made by considering allowable biaxial strain as well as fracture toughness. Of the materials investigated in this program, the X-200 steel alloy offers the best advantage of high biaxial strain combined with good fracture toughness.

3. The tests have shown that the possibility of catastrophic failure in biaxially loaded components fabricated from the 5CrMoV tool steel will be alleviated by lowering the strength level from 280,000 psi to 260,000 psi.

4. The principal stresses at maximum load under 1:1 and 2:1 loading agree reasonably well with the deformation energy theory. In general, the stresses obtained under 1:1 loading are slightly lower than the theory. The 2:1 stress values are in better agreement. However, the deformation energy theory is not as successful in predicting the principal strains at maximum load.

5. Decreasing the uniaxial strength level of a material will not necessarily result in an increase in allowable biaxial strain.

6. Uniaxial strain at maximum load serves as a better indicator of strain performance under biaxial loading than uniaxial failure strain.

C. Instrumentation for Biaxial Tests

1. The semiconductor-failure-wire instrumentation provides an economical and accurate means for determining the area of the origin of failure in the biaxial specimen.

2. The A5-1 "folded back" strain gage provides an economical means for measuring strains up to failure from the biaxial specimen.

3. The servo valve system permits an accurate and simple means for maintaining a state of 2:1 stress in the biaxial specimen up to failure.

Recommendations

The following areas should receive consideration for study:

1. Room temperature tests of additional materials.

A data gathering type test program is needed to obtain reliable biaxial design data on all candidate pressure vessel materials. The test results obtained in this investigation have shown that several biaxial tests on each material are required to obtain usable statistical data.

2. Effects of cryogenic temperatures upon performance of materials under biaxial stress conditions.

The biaxial tests conducted in this investigation have shown that some ultra-high strength materials will perform satisfactorily in biaxially loaded components operating at or near room temperature. However, if the operating temperatures are sufficiently below room temperatures, the choice of suitable materials is limited to the face-centered cubic metals such as the austenitic stainless steels and the beryllium-copper alloys. Biaxial tests are needed to determine (1) the most suitable materials for cryogenic applications and (2) data for designing reliable and efficient structures.

3. Effects of biaxial stresses on initiation and growth of stress corrosion cracks.

The biaxial cross specimen is ideally suited for such tests. Biaxial stresses will probably not be any more detrimental than uniaxial stress once the crack has grown through the thickness of the material. However, the initiation of the stress corrosion crack will probably be accelerated under biaxial stress conditions since biaxial stresses usually cause a drastic reduction in failure strain.

REFERENCES

1. Durelli, A. J. and others: An Experimental Study of Large Diameter Thin-Wall Pressure Vessels. Armour Research Foundation.

2. John Hopkins University: Joint-Army-Navy-Air Force Solid Propellant Group Bulletin of the 15th Meeting. June 1959.

3. Kinnaman, E. B. and others: An Approach to the Practical Design of Reliable, Light Weight, High Strength Pressure Vessels. Boeing Airplane Company. June 1959.

4. ASTM Bulletin, Janurary 1960: Fracture Testing of High Strength Sheet Materials: A Report of a Special ASTM Committee.

5. Marin, Joseph, and others: Biaxial Plastic Stress-Strain Relations for 24S-T Aluminum Alloy. NACA TN-1536, May 1948.

6. Nadai, A.: Theory of Flow and Fracture of Solids. Volume 1, Second Edition, McGraw-Hill Book Company, 1950.

7. Svensson, N.L.: The Bursting Pressure of Cylindrical and Spherical Vessels. Journal of Applied Mechanics, Volume 25, Number 1, March 1958, p. 89.

8. Cooper, W. E.: The Significance of the Tensile Test to Pressure Vessel Design. Welding Journal, January 1957, p. 49-s.

9. Griffith, A. A.: The Phenomena of Rupture and Flow in Solids. Physical Trans., Roy. Soc. (London), 1920, p. 163.

10. Orowan, E.: Fundamentals of Brittle Behavior in Metals. (Conf. on Fatigue and Fracture of Metals, held at MIT, June 1950), John Wiley and Sons, N. Y.

11. Irwin, G. R.: Fracture Dynamics, Fracturing of Metals, Am. Soc. Metals, Cleveland, Ohio, 1948.

12. Frocht, M. M.: Photo Elasticity. Volume 1, John Wiley and Sons Inc., 1949.

APPENDIX A

SUMMARY OF RESULTS FROM TESTS CONDUCTED TO DETERMINE SUITABILITY OF LOW COST, NOMINAL RANGE STRAIN GAGES FOR MEASURING LARGE PLASTIC STRAINS

In the initial steel biaxial specimen tests, attempts were made to measure the principal strains by use of SR-4 beams which were mounted between plastic gage blocks bonded to the specimen. The strain beams were severely damaged and even destroyed when the specimen failed. As a result, it became necessary to use strain gages in place of the 1/2 inch gage length strain beams. Plans were made to use 1/4 inch gage length post-yield gages since suitable 1/2 inch gage length gages were not available. However, trial tests on uniaxial specimens showed that these rather expensive gages were not trustworthy beyond five percent strain. For this reason several types of low cost, nominal range gages were evaluated by uniaxial tests. It was found that failure of the A5-1 gage (1/2 inch gage length) always occurred at the weld between the lead wire and the loop. To avoid failure of the welded connection, several gages were folded back between the loop and the welded joint. This prevented straining of the welded joint. As a result, the gages were highly reliable up to four or five percent strain and in several instances the gages would function properly up to eight percent strain.

In addition to the A5-1 gages, the AD-7 and the C6-141 gages were evaluated for measuring large plastic strains. The AD-7 (1/4 inch gage length) folded back gages strained up to three to four percent before failure. The strains obtained from the C6-141 gages (1/4 inch gage length) ranged from zero to five percent. Several types of cement were evaluated. The tests indicated that the PA-3 cement is superior. The following tables summarize the results from the tests:

A5-1 Gage - 1/2 Inch Gage Length

Spec. No.	Material	Folded Back	Cement	Strain Recorded at Failure of Gage %
1	7075-T6	No	PA-3	2.2
2	7075-T6	No	PA-3	2.9
3	7075-T6	No	PA-3	2.1
4	7075-T6	No	PA-3	2.7
5	7075-T6	Yes	PA-3	4.4
6	7075-T6	Yes	PA-3	4.2
7	7075-T6	Yes	PA-3	4.3
8	7075-T6	Yes	PA-3	8.0
9	7075-T6	Yes	PA-3	7.5

AD-7 Gage - 1/4 Inch Gage Length

Spec. No.	Material	Folded Back	Cement	Strain Recorded at Failure of Gage - %
1	7075-T6	No	PA-3	3.60
2	7075-T6	No	PA-3	2.80
3	7075-T6	No	PA-3	4.00
4	7075-T6	No	PA-3	3.20
5	7075-T6	No	DUCO	2.72
6	7075-T6	No	DUCO	3.76
7	7075-T6	Lead Pulled Back	Type M(1)	0.80
8	7075-T6	Yes	Type M(1)	1.60
9	7075-T6	Lead Pulled Back	PA-3	3.20
10	7075-T6	Yes	PA-3	4.24
11	7075-T6	Yes	PA-3	3.42
12	7075-T6	Yes	PA-3	4.08
13	7075-T6	Yes	PA-3	3.90

C6-141 Budd Metalfilm Gages - 1/4 Inch Gage Length

Spec. No.	Material	Folded Back	Cement	Strain Recorded at Failure of Gage - %
1	7075-T6	No	GA5	2.56
2	7075-T6	No	GA5	0
3	7075-T6	No	GA5	5.20
4	7075-T6	No	GA5	3.04
5	7075-T6	No	GA5	0
6	7075-T6	No	GA5	2.96
7	7075-T6	No	GA5	3.52
8	7075-T6	No	GA5	2.24
9	7075-T6	No	70% Type S(1) 30% Type M(1)	1.60
10	7075-T6	No	Type M(1)	0.60
11	7075-T6	Tab Loose	Type M(1)	1.68

(1)Photoelastic cement

APPENDIX B

DESCRIPTION OF SEMI-CONDUCTOR DEVICE

Introduction

In several instances, the time interval recorded between the failure of the two wires used to locate the fracture origin were of the same order of magnitude as the sensitivity of the E-Put meters (10^{-6} seconds). It therefore became necessary to increase the sensitivity of the instrumentation in order to have confidence in the reliability of the results. As a result of a company sponsored R and D program an anti-coincidence detector had been developed which, with design modifications, could be adapted to solve the above sensitivity problem.

Technical Description

The circuit of the device conceived is shown in Figure 47. This circuitry was tested under controlled conditions and proven to function satisfactorily.

A one mil wire was attached to the specimen with one end connected to ground and the other end connected to terminal B. A second one mil wire was attached to the specimen with one end connected to a 28 volt DC source through resistor R1 and the other end connected to terminal B. When the power was applied, the potential at point B was essentially at ground or zero potential except for the small potential due to the resistance in wire CB. This potential was not high enough to trigger the tunnel diode TD1. If the failure in the specimen occurred from left to right wire CB opened first and a voltage was applied at point B sufficient to cause the tunnel diode TD1 to swing to its "on" state. This will bias transistor Q1 "on" and the indicator lamp will light. If the failure occurred from right to left wire AB opened first and the tunnel diode remained in its "off" state, hence, the indicator light remained off. The zener diode RD1 was used to provide a stable voltage to prevent inadvertant firing of the tunnel diode due to line voltage fluctuations. This circuitry has been proven to have a sensitivity of 10^{-9} seconds.

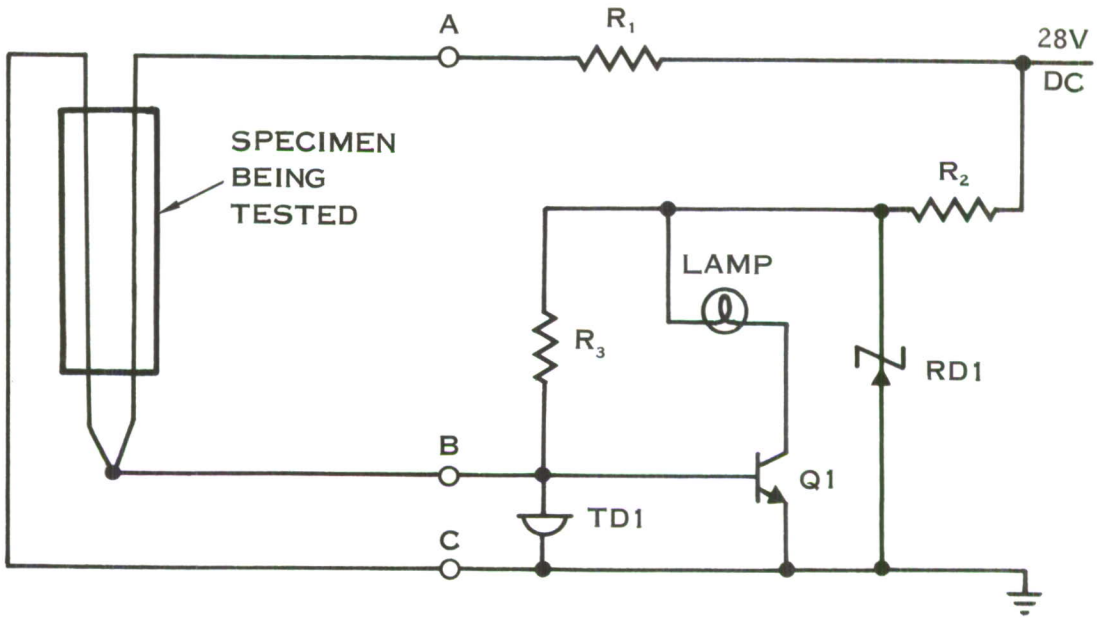

FIGURE 47 SEMI – CONDUCTOR DEVICE

APPENDIX C

SUMMARY OF RESULTS FROM TESTS CONDUCTED TO DETERMINE SUITABLE CEMENT FOR BONDING FAILURE WIRES TO METAL SURFACES

The approximate location of the origin of fracture in the biaxial specimen was determined by bonding to the specimen two loops of three mil enamel coated wires which were connected to a semi-conductor device. The failure wires on the first biaxial specimens were bonded with PA-3 cement. However, this type of cement permitted the failure wires to pull away from the specimens at failure. This caused erratic behavior in the failure wire instrumentation since the wires were not always insulated from the specimen. As a result several types of bonds were evaluated by notched uniaxial tests. One failure wire was bonded to the specimen adjacent to the root of the notch and one wire was bonded to the specimen along the un-notched edge. This permitted a rapid check on the accuracy of the failure wire system since it was known that the failure had to initiate at the root of the notch. The following summarizes the types of cement evaluated:

1. PA-3 cement
2. Type S photoelastic cement
3. Type M photoelastic cement
4. Various mixtures of Type S and Type M cement
5. Flex - T mixed with Type S and Type M cement

These tests revealed that a mixture consisting of 50 percent of Type A and 50 percent of Type M cement by weight gave a highly satisfactory bond. The mixture was evaluated from several tests on 2014-T6 and 7075-T6 aluminum alloy, B-120VCA titanium alloy and 4140 steel alloy.

APPENDIX D

DISCUSSION OF PLASTIC STRESS-STRAIN RELATIONSHIPS AND THEORIES OF FAILURE FOR COMBINED AXIAL LOADING

D.1 General

Many different theories and/or methods have been advanced to account for the plastic behavior of metals under combined loading. Recently the one receiving the most attention has been the deformation energy theory. There are probably two major reasons for the emphasis on this theory. First, its applicability to practical problems exceeds most of the others. Second, in the past few years test data have been obtained from cylinders under combined axial loading which indicate that the deformation energy theory is reasonably valid if the strain hardening characteristics of the material are considered. This theory relates the principal stresses and strains to an "effective" stress and strain. The "effective" stress-strain relationship conincides in theory with the uniaxial stress-strain relationship as obtained from a simple tension test. Strain hardening is introduced by expressing the uniaxial stress-strain curve in the plastic region by the Ludwik exponential law.

In applying the deformation energy theory to practical problems, use is made of the plastic portion of the uniaxial true stress-strain curve. For this reason, the theory of true stresses and true strains from the tensile test will be briefly outlined.

D.2 Uniaxial True Stress-Strain Relationships

In conventional structural analysis, the stresses and strains normally employed are the nominal or engineering stresses and strains, which are the values measured by a conventional test. It can readily be shown that the true tensile stress is related to the nominal tensile stress as follows (Ref. 5):

$$\sigma = \sigma'(1 + \epsilon') \tag{24}$$

Likewise the true strain (sometimes termed natural strain) is related to the nominal tensile strain as follows (Ref. 5):

$$\epsilon = \ln(1 + \epsilon') \tag{25}$$

One of the most common, as well as useful, equations for expressing the true stress-strain curve of a material mathematically is the Ludwik exponential law. This equation can be made to fit the actual shape of the true stress-strain curve for most materials throughout the plastic range, and can be written as follows:

$$\sigma = \sigma_0 \epsilon^n \tag{26}$$

where σ and ϵ represent the true stress and true strain, respectively, σ_o is a constant fictitious value of stress somewhat greater than the tensile ultimate for all materials, and n is a constant which defines the shape of the plastic portion of the true stress-strain curve and is called the strain hardening coefficient. The value of n for most engineering materials ranges from about 0.04 to 0.50. For a perfectly elastic-plastic material n would be equal to zero.

It is evident that if a constant value of n is obtained which will define the shape of the true stress-strain curve in the plastic region, σ_o could be calculated from equation (26) by using a succession of different points on the true stress-strain curve and taking an average of the σ_o values thus obtained. An accurate determination of n can thus be obtained by plotting the true stress-strain curve. This is easily done by calculating true stress-strain values from equations (24) and (25). The plastic portion of the true stress-strain curve can then be plotted on log-log paper, and approximated by a straight line fitted to the points. The geometric slope of this line will then be the value of n. It will be found in some instances that the plastic portion of the true stress-strain curve plotted on log-log paper will not give a straight line beyond the point of maximum load. Since the values beyond the maximum load will not be of primary concern this is not a serious drawback to this method. There is another method by which σ_o and n may be expressed in terms of known values from a nominal stress-strain curve. The drawback to this method is that it produces values of σ_o and n which will cause equation (26), if plotted using these values, to agree at only one point with the experimental true stress-strain curve. The derivation of this second method is presented below.

The true stress in a tension bar is obtained by dividing the axial load, P, by the instantaneous cross-sectional area, A. This stress is shown by the following equation and is the same true stress as shown by equation (24):

$$\sigma = \frac{P}{A} \tag{27}$$

If the volume is assumed to remain constant in the plastic range, then the ratio of original cross-sectional area, A', to instantaneous cross-sectional area, A, may be related to the ratio of instantaneous gage length, L, to original gage length, L', as follows:

$$\frac{A'}{A} = \frac{L}{L'} \tag{28}$$

The nominal strain expressed in terms of the original and instantaneous gage length is,

$$\epsilon' = \frac{\Delta L}{L'} = \frac{L - L'}{L'} = \frac{L}{L'} - 1 \tag{29}$$

By combining equations (25), (28), and (29) the following expression for true strain can be written:

$$\epsilon = \ln \left(\frac{A'}{A}\right) \tag{30}$$

By taking the antilogarithm of both sides of this expression and rearranging, the instantaneous cross-sectional area becomes,

$$A = A' e^{-\epsilon} \tag{31}$$

where e = 2.718. . ., the base of natural logarithms. Inserting this value of A into equation (27) and rearranging, the load P is,

$$P = \sigma e^{-\epsilon} A' \tag{32}$$

This load reaches a maximum and then decreases when the rate of decrease in cross-sectional area is greater than the rate of increase in strain hardening, i.e., when necking commences and a volume change occurs in the material. This maximum load is the highest load which can be sustained by the tensile bar, and is reached at the last instant that the rate of decrease of cross-sectional area still equals the rate of increase in uniform elongation.

By equation (32), P is a function of both ϵ and σ; hence,

$$dP = \frac{\partial P}{\partial \sigma} d\sigma + \frac{\partial P}{\partial \epsilon} d\epsilon \tag{33}$$

and by partial differentiation of equation (32), the following expressions are obtained:

$$\frac{\partial P}{\partial \sigma} = A' e^{-\epsilon} \frac{d\sigma}{d\sigma} = A' e^{-\epsilon} \tag{34}$$

$$\frac{\partial P}{\partial \epsilon} = A' \sigma \frac{d}{d\epsilon}\left(e^{-\epsilon}\right) = -A' \sigma e^{-\epsilon} \tag{35}$$

By placing these values of the derivatives into equation (33), dP becomes,

$$dP = A' e\, d\sigma - A' \sigma e^{-\epsilon} d\epsilon = \left(A' e^{-\epsilon}\right)\left(d\sigma - \sigma\, d\epsilon\right) \tag{36}$$

Since the load P is to be a maximum, it is obvious that

$$dP = (A' e^{-\epsilon})(d\sigma - \sigma d\epsilon) = 0 \tag{37}$$

and since $A' e^{-\epsilon}$ cannot be zero, equation (37) reduces to

$$\frac{d\sigma}{d\epsilon} = \sigma \tag{38}$$

or, at the point of maximum load, the slope of the true stress-strain curve is equal to the value of the true stress. By differentiating equation (26) with respect to ϵ, the following expression is obtained:

$$\frac{d\sigma}{d\epsilon} = \frac{d}{d\epsilon}(\sigma_0 \epsilon^n) = n \sigma_0 \epsilon^{n-1} \tag{39}$$

and by substituting the relationship σ/ϵ^n from equation (26) in the above formula, and equating the result to σ by equation (38), it is found that

$$\frac{d\sigma}{d\epsilon} = n\left(\frac{\sigma}{\epsilon^n}\right)\epsilon^{n-1} = n \sigma \epsilon^{-1} = \frac{n\sigma}{\epsilon} = \sigma \tag{40}$$

Therefore, from the final two terms in the above expression and from equation (25),

$$n = \epsilon_u = \ln(1 + \epsilon'_u) \tag{41}$$

where ϵ_u and ϵ'_u are the true and nominal strains at the point of maximum load. The expression for σ_0 which is compatible with this value of n may be obtained by combining equations (24) and (26). Hence,

$$\sigma_0 = \left(\frac{e^{\epsilon}}{\epsilon^n}\right)\sigma' \tag{42}$$

This equation is true anywhere on the Ludwik curve. The value of σ_0 which will exactly fit test data at the point of maximum load may be obtained by setting $\epsilon = \epsilon_u = n$ and $\sigma' = \sigma'_u$. By making these substitutions in equation (42), becomes,

$$\sigma_0 = \left(\frac{e}{n}\right)^n \sigma'_u \tag{43}$$

D.3 Deformation Energy Theory

The plastic stress-strain relations are determined on the basis of the following postulates:

(1) The directions of the principal strains ϵ_1, ϵ_2, and ϵ_3 coincide with with the directions of the principal stresses σ_1, σ_2, and σ_3.

(2) There is no volume change in the plastic range. With little difficulty it can be shown that for constancy of volume,

$$\epsilon_1 + \epsilon_2 + \epsilon_3 = 0 \tag{44}$$

(3) The ratios of the principal shear strains to the principal shear stresses are equal.

If it is assumed that the principal stress ratios and principal stress directions are constant, the stress-strain relationships may then be expressed as follows (Ref. 5):

$$\left.\begin{aligned} \epsilon_1 &= \left(\frac{\epsilon}{\sigma}\right)\left[\sigma_1 - \tfrac{1}{2}\left(\sigma_2 + \sigma_3\right)\right] \\ \epsilon_2 &= \left(\frac{\epsilon}{\sigma}\right)\left[\sigma_2 - \tfrac{1}{2}\left(\sigma_1 + \sigma_3\right)\right] \\ \epsilon_3 &= \left(\frac{\epsilon}{\sigma}\right)\left[\sigma_3 - \tfrac{1}{2}\left(\sigma_1 + \sigma_2\right)\right] \end{aligned}\right\} \tag{45}$$

where (ϵ/σ) is the reciprocal of the secant modulus of the uniaxial true stress-strain curve. From these equations the principal plastic stresses and strains may be expressed in terms of the true stress and strain in simple tension as follows:

$$\epsilon_e = \frac{\sqrt{2}}{3}\sqrt{\left(\epsilon_1 - \epsilon_2\right)^2 + \left(\epsilon_2 - \epsilon_3\right)^2 + \left(\epsilon_3 - \epsilon_1\right)^2} \tag{46}$$

and

$$\sigma_e = \frac{1}{\sqrt{2}}\sqrt{\left(\sigma_1 - \sigma_2\right)^2 + \left(\sigma_2 - \sigma_3\right)^2 + \left(\sigma_3 - \sigma_1\right)^2} \tag{47}$$

The strain ϵ_e and stress σ_e will be called the effective strain and stress. By this theory the σ_e - ϵ_e relation should coincide with the σ - ϵ relation for simple tension. The effective stress and strain have been shown to be the same as the octahedral shear stress and strain if the above values are multiplied

by a constant (Ref. 6). In particular,

$$\tau_{oct.} = \frac{1}{3}\sqrt{(\sigma_1 - \sigma_2)^2 + (\sigma_2 - \sigma_3)^2 + (\sigma_3 - \sigma_1)^2} \tag{48}$$

and

$$\gamma_{oct.} = \frac{2}{3}\sqrt{(\epsilon_1 - \epsilon_2)^2 + (\epsilon_2 - \epsilon_3)^2 + (\epsilon_3 - \epsilon_1)^2} \tag{49}$$

By combining equations (46), (47), (48), and (49), the relation between the effective stress and strain and octahedral shear stress and shear strain is found to be

$$\tau_{oct.} = \frac{\sqrt{2}}{3}\sigma_e \tag{50}$$

and

$$\gamma_{oct.} = \frac{2}{\sqrt{2}}\epsilon_e \tag{51}$$

Assuming that the effective stress and strain as defined by equations (46) and (47) coincide with the $\sigma - \epsilon$ relations for simple tension, the Ludwik law can be expressed as,

$$\sigma_e = \sigma_o \epsilon_e^n \tag{52}$$

If equations (47) and (52) are combined, the relation between uniaxial true stress and strain and principal stresses becomes

$$\frac{\epsilon_e}{\sigma_e} = \frac{\epsilon}{\sigma} = \frac{1}{\sigma_o^{1/n}}\left[\frac{(\sigma_1 - \sigma_2)^2 + (\sigma_2 - \sigma_3)^2 + (\sigma_3 - \sigma_1)^2}{2}\right]^{\frac{1-n}{2n}} \tag{53}$$

Expressing the principal stress ratios as,

$$\frac{\sigma_2}{\sigma_1} = \alpha$$

$$\frac{\sigma_3}{\sigma_1} = \beta$$

Then, equation (A26) becomes,

$$\frac{\epsilon}{\sigma} = \frac{\sigma_1^{\frac{1-n}{n}}}{\sigma_0^{1/n}}\left(\alpha^2 + \beta^2 - \alpha\beta - \alpha - \beta + 1\right)^{\frac{1-n}{2n}} \qquad (54)$$

If equation (54) is combined with equation (45), the principal strains in terms of the principal stresses may be written as

$$\left.\begin{aligned}
\epsilon_1 &= \left(\frac{\sigma_1}{\sigma_0}\right)^{1/n}\left(\alpha^2 + \beta^2 - \alpha\beta - \alpha - \beta + 1\right)^{\frac{1-n}{2n}}\left(1 - \frac{\alpha}{2} - \frac{\beta}{2}\right) \\
\epsilon_2 &= \left(\frac{\sigma_1}{\sigma_0}\right)^{1/n}\left(\alpha^2 + \beta^2 - \alpha\beta - \alpha - \beta + 1\right)^{\frac{1-n}{2n}}\left(\alpha - \frac{\beta}{2} - \frac{1}{2}\right) \\
\epsilon_3 &= \left(\frac{\sigma_1}{\sigma_0}\right)^{1/n}\left(\alpha^2 + \beta^2 - \alpha\beta - \alpha - \beta + 1\right)^{\frac{1-n}{2n}}\left(\beta - \frac{\alpha}{2} - \frac{1}{2}\right)
\end{aligned}\right] \qquad (55)$$

D.4 Burst Pressure Analysis of Thin-Walled Spheres and Cylinders Based Upon Deformation Energy Theory

Svensson (Ref. 7) has derived equations which relate the maximum attainable pressure, or burst pressure, of thin-walled spheres and cylinders to vessel geometry and material properties. These equations are based upon the deformation energy theory. Cooper (Ref. 8) shows derivations which result in burst pressure equations identical to those obtained by Svensson. The basic steps in deriving these equations will be summarized for both the sphere and the cylinder.

D.4.1 Burst Pressure Analysis of Thin-Walled Spheres

It is obvious, by taking cuts through the center of the sphere and making a summation of the existing forces, that at any instant during deformation,

$$\left.\begin{aligned}
\sigma_1 &= \sigma_2 = \frac{pR}{2t} \\
\text{and} \quad \sigma_3 &= -\frac{p}{2} \cong 0
\end{aligned}\right] \qquad (56)$$

as long as the vessel remains perfectly spherical. If the initial (unstrained) dimensions of the vessel are defined as R_i and t_i, and their values at any instant during radial expansion as R and t, and defining the following:

$$X = \frac{R}{R_i} \qquad (57)$$

$$Y = \frac{t}{t_i} \qquad (58)$$

Then the following expression can be written:

$$\frac{R}{t} = \frac{R_i}{t_i}\ \frac{R}{R_i}\ \frac{t_i}{t} = \frac{R_i}{t_i}\ \frac{x}{y} \tag{59}$$

and substituting this in equation (56):

$$\sigma_1 = \sigma_2 = \frac{P R_i}{2 t_i}\ \frac{x}{y} \tag{60}$$

Since $\sigma_1 = \sigma_2$, it is obvious from symmetry of loading that

$$\epsilon_1 = \epsilon_2 \tag{61}$$

and from the constancy of volume relation,

$$\epsilon_3 = -2\epsilon_1 = -2\epsilon_2 \tag{62}$$

By substituting equation (56) into equation (46) and equations (61) and (62) into equation (47), it is found that

$$\sigma_e = \sigma_1 = \sigma_2 \tag{63}$$

and

$$\epsilon_e = 2\epsilon_1 = 2\epsilon_2 \tag{64}$$

Considering that the circumference of the vessel at any time is proportional to the instantaneous radius, the following expression for the nominal strain can be written:

$$\epsilon_1' = \epsilon_2' = \frac{R}{R_i} - 1 \tag{65}$$

From equations (25) and (62) the following relationship is obtained:

$$\ln(1 + \epsilon_3') = -2 \ln(1 + \epsilon_2') \tag{66}$$

Since the nominal radial strain is $\epsilon_3' = t/t_i - 1$, equations (57), (59), (65), and (66) can be combined to yield,

$$\frac{X}{Y} = X^3 \tag{67}$$

By inserting this into equation (60), and observing equation (63), it can be shown that

$$\sigma_e = p\left(\frac{R_i}{2t_i}\right) X^3 \tag{68}$$

If it is assumed that the effective stress and strain relation coincides with the uniaxial true σ-ϵ relation, equation (68) can be expressed in terms of the plastic portion of the uniaxial true stress-strain curve. By observing this theory and substituting the Ludwik law of equation (26) into equation (68), one form of the pressure-plastic deformation equation can be written as,

$$p = 2\sigma_0 \epsilon^n \frac{t_i}{R_i} \frac{1}{X^3} \tag{69}$$

In order to eliminate the unwanted variable ϵ, use can be made of equations (25), (57), (64), and (65). Hence,

$$\epsilon = 2 \ln X \tag{70}$$

Inserting this value for ϵ into equation (69), the desired expression for the pressure-plastic radial deformation relationship is found for the thin-walled sphere:

$$p = (2)^{n+1} \sigma_0 \frac{t_i}{R_i} \frac{(\ln X)^n}{X^3} \tag{71}$$

The maximum attainable pressure or burst pressure is obtained from $dp/dX = 0$. This results in the following value of X at burst, which will be denoted $\bar{X}$:

$$\bar{X} = e^{n/3} \tag{72}$$

In the derivations up to this point, it has been stipulated that the effective stress-strain relationship must coincide with the true stress-strain relationship in uniaxial tension. If (70) and (72) are combined the effective strain at maximum pressure in a thin-walled sphere is

$$\bar{\epsilon}_e = \frac{2}{3} n \tag{73}$$

This says that the effective strain at maximum pressure is equal to 2/3n. However, equation (41) for the uniaxial true stress-strain relation says that the true strain at maximum load is equal to n. From this it can be surmised that maximum load for the sphere does not occur at an effective strain value equal to the uniaxial true strain at maximum load. If it is assumed that the relation between ϵ_u and n as obtained in equation (41) is approximately correct, then the effective strain at maximum pressure in terms of ϵ_u is:

$$\bar{\epsilon}_e = \frac{2}{3} n \cong \frac{2}{3} \epsilon_u \tag{74}$$

Since the value of σ_0 as given by equation (43) is based on the slope of the true stress-strain curve at ϵ_u, it is apparent that equation (43) will not be compatible with equation (74). A relationship for σ_0 which is compatible with equation (74) would have to contain a stress value of unknown magnitude, somewhat less than σ_u'. For this reason the value of σ_0 as given by equation (43) must be considered approximate for burst pressure calculations.

By substituting equation (72) in equation (71), the maximum attainable pressure $\bar{p}$ is found to be

$$\frac{\bar{p}}{\sigma_0} = \frac{2^{n+1}}{3^n} \frac{t_i}{R_i} \left(\frac{n}{e}\right)^n \tag{75}$$

This formula, like equation (71), is completely general, and makes no restrictions on σ_0 or n. These constants may be determined in any manner desired in order to obtain maximum accuracy of fit to the Ludwik law. Equation (75) may be simplified by use of the approximate value of σ_0 as given by equation (43). Hence,

$$\frac{\bar{p}}{\sigma_u'} = \frac{2^{n+1}}{3^n} \frac{t_i}{R_i} \tag{76}$$

This formula gives an approximate value for the burst pressure $\bar{p}$ of a thin-walled spherical vessel in terms of its unstressed dimensions, the nominal ultimate tensile strength of the material, and the shape n of the uniaxial true stress-strain curve.

D.4.2 Burst Pressure Analysis of Thin-Walled Cylinders

All assumptions used in the spherical vessel analysis will be used for thin-walled cylinders, with one addition. The cylinder must have the equivalent of perfectly free ends, which means that it must have end closures approaching the shape of full hemispheres, with perfectly smooth transitions from end closures to the cylindrical portion of the vessel. The reason for this assumption lies in the fact that in the following analysis no effect of stresses due to discontinuity loads will be considered. For any type of end closure other than hemispherical, these discontinuity forces could be significant, although they exist only locally in the region of the head-cylinder junction. For this type of end closures, the following analysis is not valid except at a finite distance from the head junction, and the vessel may actually be critical in the region of the discontinuity loads.

By a summation of internal forces in the pressurized cylinder, the following well known relationships can be written:

$$\sigma_1 = \frac{pR}{t} \tag{77}$$

$$\sigma_2 = \frac{pR}{2t} \tag{78}$$

$$\sigma_3 = -\frac{p}{2} \cong 0 \tag{79}$$

where σ_2 is the true stress in the axial direction, σ_1 is the true stress in the circumferential direction, and σ_3 is the true stress in the radial direction.

It is obvious that, with the hoop stress σ_1 being twice the axial stress σ_2, ϵ_2 will be very small in comparison with ϵ_1 in the plastic range. If fact, equation (45) shows that the plastic value of ϵ_2 is zero, and test results have shown that this theory is substantially correct. Hence, in the subsequent analysis it will be assumed that:

$$\epsilon_2 = 0 \tag{80}$$

From the equation of no volume change, $\epsilon_1 + \epsilon_2 + \epsilon_3 = 0$, it is obvious that

$$\epsilon_1 = -\epsilon_3 \tag{81}$$

Inserting equations (77), (78), and (79) into equation (47) yields:

$$\sigma_e = \frac{\sqrt{3}}{2}\sigma_1 \tag{82}$$

and substitution of equations (80) and (81) into equation (46) gives:

$$\epsilon_e = \frac{2}{\sqrt{3}} \epsilon_1 \tag{83}$$

By combining equations (82), (77), and (59) it is found that:

$$\sigma_e = \frac{\sqrt{3}}{2} \frac{p R_i}{t_i} \frac{X}{Y} \tag{84}$$

Since equation (65) is perfectly general and applies to a cylinder as well as a sphere, equations (81) and (25) may be combined to yield:

$$\ln (1 + \epsilon_1') = -\ln(1 + \epsilon_3') \tag{85}$$

and by using the expression $\epsilon_3' = (t/t_i - 1)$ with equations (65) and (85), the following expression is obtained:

$$\frac{X}{Y} = X^2 \tag{86}$$

and hence, by equation (84),

$$\sigma_e = \frac{\sqrt{3}}{2} \frac{p R_i}{t_i} X^2 \tag{87}$$

If it is assumed that the effective stress-strain relationship coincides with the stress-strain relationship in simple tension, equation (87) can be written in terms of the uniaxial stress-strain curve by use of the Ludwik law, equation (26). Hence, the following expression is obtained:

$$p = \frac{2}{\sqrt{3}} \sigma_0 \epsilon^n \frac{t_i}{R_i} \frac{1}{X^2} \tag{88}$$

The unwanted variable ϵ may be eliminated by use of equations (25), (57), (65), and (83). Thus,

$$\epsilon = \frac{2}{\sqrt{3}} \ln X \tag{89}$$

By inserting this value of ϵ into equation (88), the pressure-plastic deformation relationship for a thin-walled cylinder is found to be

$$p = \left(\frac{2}{\sqrt{3}}\right)^{n+1} \sigma_0 \frac{t_i}{R_i} \frac{(\ln X)^n}{X^2} \tag{90}$$

This compares with equation (71) for a thin-walled sphere. The maximum attainable pressure, or burst pressure, is obtained by setting the derivative dp / dX = 0. This results in the following value of X at burst, which will be denoted $\bar{X}$:

$$\bar{X} = e^{n/2} \tag{91}$$

and substitution of equation (91) into equation (90) yields:

$$\frac{\bar{p}}{\sigma_o} = \frac{2}{(\sqrt{3})^{n+1}} \frac{t_i}{R_i} \left(\frac{n}{e}\right)^n \tag{92}$$

This is the general burst pressure formula for a thin-walled cylinder, which corresponds to equation (75) for a sphere. To derive the simplified approximate formula, comparable to equation (76) for a sphere, the value of σ_o given by equation (43) is inserted in equation (92).

$$\frac{\bar{p}}{\sigma_u} = \frac{2}{(\sqrt{3})^{n+1}} \frac{t_i}{R_i} \tag{93}$$

This equation is subject to the same discussion that was given in connection with equation (76) for a thin-walled sphere. By combining equations (89) and (91) the effective strain at maximum pressure becomes,

$$\bar{\epsilon}_e = \frac{n}{\sqrt{3}} \tag{94}$$

and if it is assumed $n \cong \epsilon_u$ at $\bar{\epsilon}_e$,

$$\bar{\epsilon}_e = \frac{n}{\sqrt{3}} = \frac{\epsilon_u}{\sqrt{3}} \tag{95}$$

D.5 Stress and Strain at Maximum Load as a Function of Strain Hardening for 1:1 and 2:1 Loading Conditions

In arriving at the burst pressure equations, equations are derived which can be used to obtain the principal strains at instability; i.e., the strains at the maximum attainable pressure. The equations which were developed will be used to derive principal stress and strain relations at maximum load as a function of strain hardening for internally pressurized spheres and cylinders. The principal stress ratio is, of course, 1:1 for spheres and 2:1 for cylinders.

D.5.1 1:1 Stress Ratio

The following discussion is based on the assumption that the effective stress-strain relationship, equations (46) and (47), coincides with the true stress-strain relationship as obtained from a simple tension test. It was pointed out earlier that

the theoretical value of σ_o as given by equation (43) may not cause the Ludwik law to fit the effective stress-strain curve with good accuracy at the point of maximum load. However, this value of σ_o will be used in the analyses for the time being.

The burst pressure of a thin-walled sphere can be related to the initial vessel dimensions and nominal principal stress in the following manner:

$$\bar{P} = \frac{2t_i}{R_i}\sigma_1' = \frac{2t_i}{R_i}\sigma_2' = \frac{2t_i}{R_i}\sigma_R' \qquad (96)$$

where t_i and R_i are the initial unstrained vessel dimensions, σ_1' and σ_2' are the nominal principal stresses at maximum load, and σ_R' is the nominal stress at maximum load. From this relationship it is obvious that

$$\sigma_1' = \sigma_2' = \sigma_R' \qquad (97)$$

The ratio of nominal stress at burst pressure σ_R' to nominal ultimate tensile stress may be obtained by equating equation (96) to equation (76). This ratio is,

$$\frac{\sigma_R'}{\sigma_u'} = \left(\frac{2}{3}\right)^n \qquad (98)$$

For a perfectly elastic-plastic material (n = 0), this ratio would be unity and is equal to the value that results from equation (47) when $\sigma_e = \sigma_u$.

Equation (74) shows that instability under 1:1 tension loading occurs at an effective strain less than the true strain at instability in uniaxial tension. For this reason the value of σ_o used in equation (98) is approximate. However, an expression similar to equation (98) can be obtained which is independent of the approximate value of σ_o as given by equation (43). By combining equations (96) and (75), the following relationship between σ_R' and σ_o is obtained:

$$\frac{\sigma_R'}{\sigma_o} = \left(\frac{2n}{3e}\right)^n \qquad (99)$$

In using equation (99), σ_o should be determined in such a manner that the Ludwik law exactly fits the true uniaxial stress-strain curve in the region of maximum load.

As for the case of simple tension, the beginning of necking for combined loading is the point where the rate of strain hardening is exactly balanced by the decrease in load resistance caused by the decrease in cross section. At this point of instability a maximum load is reached which is followed by a decrease in load to rupture. However, this situation exists only if necking

occurs. If necking does not occur maximum load and rupture occur simultaneously. Whether necking occurs or not, the following equations define the principal strain at maximum load for the case of 1:1 tension loading. By combining equations (64), (70), and (72), the true principal strain at maximum load in a thin-walled sphere at instability becomes,

$$\epsilon_1 = \epsilon_2 = \frac{n}{3} \tag{100}$$

By employing the true strain relationship as expressed by equation (25), equation (100) may be expressed as,

$$\epsilon_1 = \frac{n}{3} = \ln(1+\epsilon_1') \tag{101}$$

or

$$\epsilon_1' = e^{n/3} - 1 \tag{102}$$

and from equation (41) the nominal uniaxial strain at instability is,

$$\epsilon_u' = e^{n} - 1 \tag{103}$$

By dividing equation (102) by equation (103), the ratio ϵ_1'/ϵ_u' becomes,

$$\frac{\epsilon_1'}{\epsilon_u'} = \frac{e^{n/3} - 1}{e^{n} - 1} \tag{104}$$

D.5.2 2:1 Stress Ratio

As was the case for 1:1 loading, the derivations will be based upon the assumption that the effective stress-strain relationship coincides with the true stress-strain relationship in simple tension. Equations are given in D.4 which show that the value of σ_o as expressed by equation (43) may not cause the Ludwik law to fit the effective stress-strain curve with good accuracy at the point of maximum load. The following analyses will deal with both the approximate and exact values of σ_o.

The burst pressure of a thin-walled cylinder can be related to the initial vessel dimensions and nominal principal stress as follows:

$$\bar{p} = \frac{t_i}{R_i}\sigma_1' = \frac{t_i}{R_i}\sigma_R' \tag{105}$$

where t_i and R_i are the initial unstrained vessel dimensions, σ_1' is the nominal principal stress at maximum load, and σ_R' is the nominal stress at maximum load.

Equation (105) considers that failure is due to pure membrane loading. From equation (105) it is obvious that,

$$\sigma_1' = \sigma_R' \tag{106}$$

The ratio of nominal stress at burst pressure σ_R' to nominal ultimate tensile stress may be obtained by equating equation (105) to equation (93). Thus, for a thin-walled cylinder,

$$\frac{\sigma_R'}{\sigma_u'} = \left(\frac{2}{\sqrt{3}}\right)^{n+1} \tag{107}$$

For a perfectly elastic-plastic material (n = 0), this ratio is 1.155 and is equal to the value that results from equation (47) when $\sigma_e = \sigma_u$.

Equation (95) shows that instability under 2:1 tension loading occurs at an effective strain less than the true strain at instability in uniaxial tension. For this reason the value of σ_o used in equation (107) is approximate. However, an expression similar to equation (107) can be obtained which is independent of the approximate value of σ_o as given by equation (43). By combining equations (105) and (92), the following relationship between σ_R' and σ_o is obtained:

$$\frac{\sigma_R'}{\sigma_o} = \left(\frac{2}{\sqrt{3}}\right)^{n+1}\left(\frac{n}{e}\right)^n \tag{108}$$

As was explained for the case of 1:1 tension loading, the beginning of necking for 2:1 tension loading is the point where the rate of strain hardening is exactly balanced by the decrease in load resistance caused by the decrease in cross section. Also, the discussion concerning necking under 1:1 tension loading holds true for the case of 2:1 tension loading. However, whether necking occurs or not, the following equations define the principal strain at maximum load for the case of 2:1 tension loading. By combining equations (83), (89), and (91), the true hoop strain in a thin-walled cylinder at instability becomes,

$$\epsilon_1 = \frac{n}{2} \tag{109}$$

By employing the true strain relationship as expressed by equation (25), equation (109) may be expressed as,

$$\epsilon_1 = \frac{n}{2} = \ln(1 + \epsilon_1') \tag{110}$$

or

$$\epsilon_1' = e^{n/2} - 1 \tag{111}$$

By dividing equation (111) by equation (103), the ratio $\epsilon_1' / \epsilon_u'$ for 2:1 tension loading becomes,

$$\frac{\epsilon_1'}{\epsilon_u'} = \frac{e^{\gamma/2} - 1}{e^{\pi} - 1} \qquad (112)$$

D.6 Theories of Failure for Combined Loading

The deformation energy theory is only one of many theories of failure which have been proposed. The more commonly used and best known theories assume the material to be homogeneous and isotropic; i.e., the material displays the same mechanical properties in all loading directions. Not unlike the deformation energy theory, most theories also assume that fracture under combined loading can be related to some uniaxial property of the material.

It is convenient to analyze combined axial stresses by considering that the stresses act at a point in a solid body. From conditions of equilibrium, the principal stresses σ_1, σ_2, and σ_3 are related to the principal shear stresses τ_1, τ_2, and τ_3 as follows:

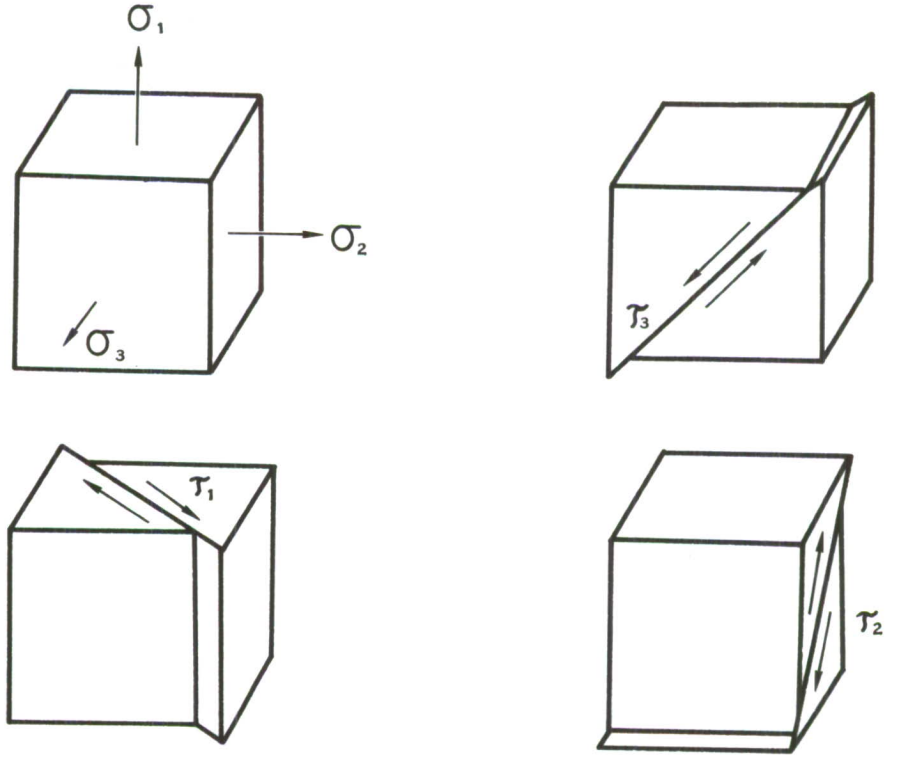

$$\tau_1 = \frac{\sigma_2 - \sigma_3}{2} \; ; \quad \tau_2 = \frac{\sigma_3 - \sigma_1}{2} \; ; \quad \tau_3 = \frac{\sigma_1 - \sigma_2}{2} \qquad (113)$$

Theories of failure are formulated in terms of principal stresses, and by selecting appropriate coordinates the locus of failure points can be shown. In this discussion the stress quadrants and coordinate axes for biaxial loading will be as follows:

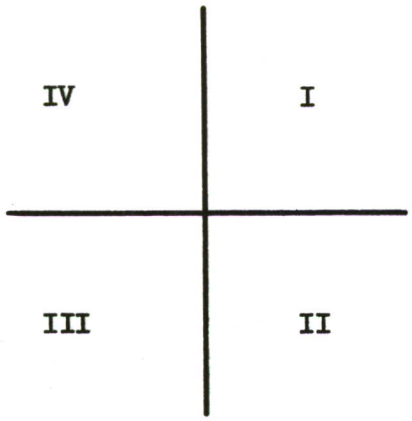

Stress Quadrants

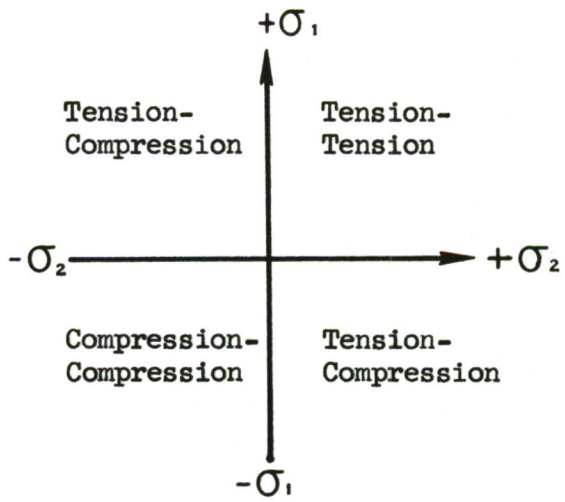

Coordinate Axes

D.6.1 Maximum Shear Stress Theory

The maximum shear stress theory predicts failure will occur at a point under any condition of loading when the maximum shear stress at the point reaches the critical value, as determined from the uniaxial tension or compression test regardless of what the stresses may be on other planes. This criterion can be expressed as

$$\tau_{CR} = \frac{\sigma_1 - \sigma_2}{2} = \text{constant} \qquad (114)$$

If σ_u is the uniaxial tensile ultimate stress, then $2\tau_{CR} = \sigma_u$. From this relationship it is apparent that the shear stress at failure is one-half of the value of the tensile ultimate stress. The locus of failure points can be represented by an irregular hexagon as shown in the following sketch:

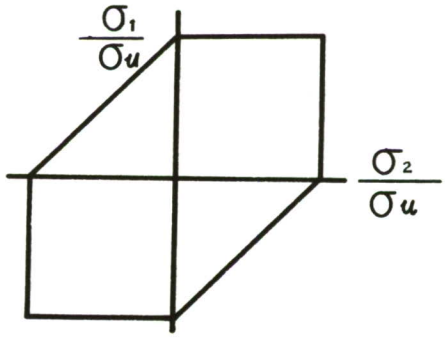

D.6.2 Maximum Normal Stress Theory

The maximum normal stress theory predicts failure will occur at a point under any condition of loading when the maximum normal stress at the point reaches the value of the critical stress, as determined from the uniaxial tension or compression test, regardless of what the stresses may be on other planes. The locus of failure points can be represented by a square, with the sides parallel to the principal stress axes as shown in the following sketch:

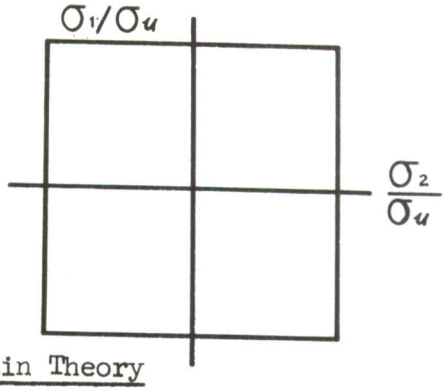

D.6.3 Maximum Normal Strain Theory

The maximum normal strain theory predicts failure will occur at a point under any condition of loading when the maximum normal strain at the point reaches the value of the limiting strain, as determined from a uniaxial tension or compression test, regardless of what the stresses may be on other planes. According to this theory the limiting condition is

$$\epsilon_1 = \epsilon_u \tag{115}$$

where ϵ_1 is the maximum principal strain at the point and ϵ_u is the critical strain as determined from a uniaxial test. Equation (115) can be written in terms of principal stresses as

$$\sigma_1 - \mu \sigma_2 = \pm \sigma_u \tag{116}$$

if σ_1 is greater than the absolute value of σ_2. If σ_2 is greater than the absolute value of σ_1, equation (116) becomes,

$$\sigma_2 - \mu \sigma_1 = \pm \sigma_u \tag{117}$$

where σ_u is the critical stress in uniaxial tension or compression.

Equations (116) and (117) show that if σ_1 and σ_2 are of like sign the maximum normal strain theory will permit a higher failure stress than σ_u. However, if σ_1 and σ_2 are of unlike sign, the reverse is true. The locus of

failure points can be represented by a rhombus as shown by the following sketch:

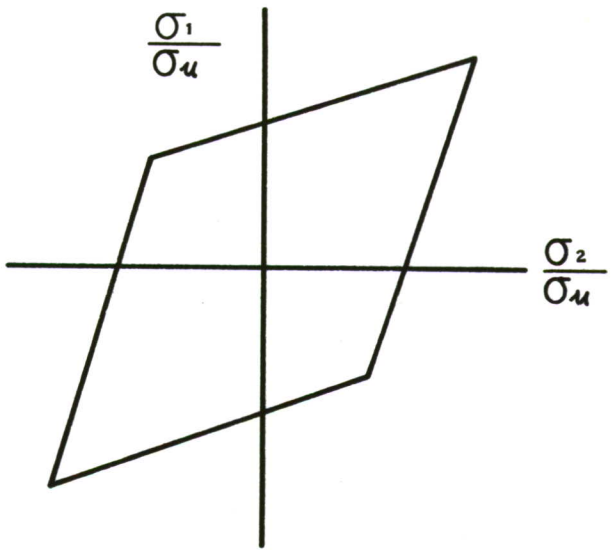

D.6.4 Maximum Strain Energy Theory

The maximum strain energy theory predicts failure will occur at a point when the value of the strain energy per unit volume in the material at the point equals the maximum value of the strain energy per unit volume that the material is capable of absorbing under simple tension. This theory may be expressed as

$$\sigma_1^2 + \sigma_2^2 - 2\mu\sigma_1\sigma_2 = \sigma_u^2 \qquad (118)$$

The locus of failure points can be represented by an ellipse as shown in the following sketch:

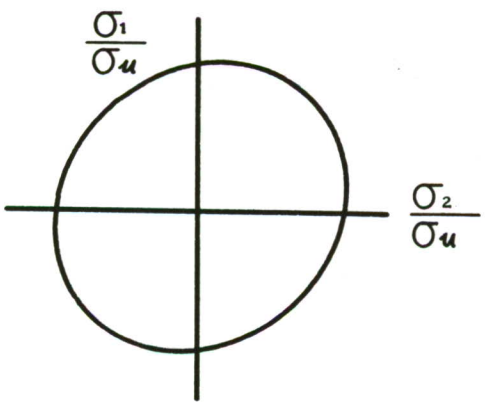

D.6.5 Maximum Distortion Energy Theory (Hencky - von Mises Theory)

The maximum distortion energy theory predicts failure will occur at a point when the energy of distortion equals the energy of distortion that the material is capable of absorbing under simple tension. This theory is expressed as,

$$\sigma_1^2 - \sigma_1 \sigma_2 + \sigma_2^2 = \sigma_u^2 \qquad (119)$$

The locus of failure points can be represented by an ellipse as shown in the following sketch:

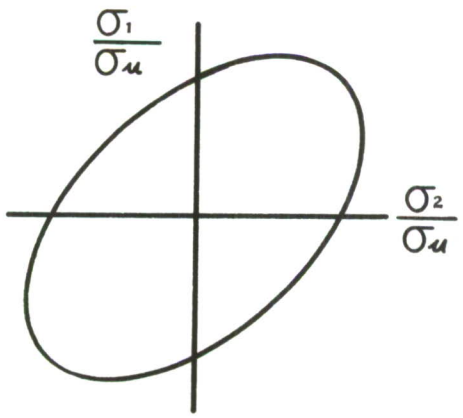

D.6.6 Octahedral Shear Stress Theory

The octahedral shear stress theory predicts failure will occur at a point by shear when a stress invariant related to the intensity of shearing stress reaches some maximum value. According to this theory the octahedral shearing stress is related to the principal stresses as,

$$\tau_{oct.} = \frac{1}{3}\sqrt{(\sigma_1-\sigma_3)^2 + (\sigma_3-\sigma_2)^2 + (\sigma_2-\sigma_1)^2} \qquad (120)$$

For biaxial loading ($\sigma_3 = 0$) this relationship reduces to,

$$\tau_{oct.}^2 = \frac{2}{9}\left(\sigma_1^2 - \sigma_1 \sigma_2 + \sigma_2^2\right) \qquad (121)$$

Nadai (Ref. 6) has shown that at the plastic limit the octahedral shearing stress is related to the uniaxial yield stress as,

$$\tau_{oct.} = \frac{\sqrt{2}}{3}\sigma_y \qquad (122)$$

and if it is assumed that this relationship is true at fracture, then

$$\tau_{oct.} = \frac{\sqrt{2}}{3}\sigma_u \qquad (123)$$

By combining equations (121) and (123), the octahedral shear stress theory becomes,

$$\sigma_1^2 - \sigma_1\sigma_2 + \sigma_2^2 = \sigma_u^2 \qquad (124)$$

A comparison of equations (119) and (124) shows that the distortion energy and the octahedral shear stress theories are expressed identically. The locus of failure points is an ellipse, identical with that of the distortion energy theory.

D.6.7 Griffith Theory

When metallic materials are tested to failure under ordinary conditions of tensile loading, the measured failure strangth is always found to be less than the theoretical value by a factor ranging from 100 to 1000. Griffith (Ref. 9) postulated that microcracks were responsible for the discrepancy between measured and calculated strengths. According to Griffith's theory, microcracks are present in all real materials and these microcracks will grow when the free energy of the system is reduced by the growth of the cracks. Griffith considered two types of energy, the surface energy of the crack and the elastic strain energy of the system. The surface energy increases and the strain energy decreases as the crack grows. The Griffith theory is expressed as,

$$\sigma = \sqrt{\frac{E\omega}{C}} \qquad (125)$$

where σ is the gross normal stress, E is the elastic modulus, ω is the surface energy per unit of area, and C is the crack length. Equation (125) shows that the stress required to cause the crack to become unstable is inversely proportional to the square root of the crack length. Griffith conducted tests on glass plates in which he introduced cracks and found that the results were in agreement with equation (125).

Orowan (Ref. 10) pointed out that mild steel, even in its most brittle state, undergoes some plastic deformation prior to fracture. Orowan also showed that the plastic energy of deformation is much greater than the energy

required to create two new surfaces. Thus, the Griffith theory permits prediction of unstable crack propagation for very brittle materials only.

Orowan (Ref.10) and Irwin (Ref. 11) modified Griffith's theory in order that this concept could be applied to ductile engineering metals. Tests on many metallic materials have shown that if a sharp notch exists in a sheet, crack extension usually starts at tensile loads below the maximum load of the test. Furthermore, the initial crack grows slowly because the plastic strain zones associated with crack toughness increase in size with crack length. Since the size of the plastic strain zones is limited due to the crack toughness of the material, the intensity of the local stress field at the crack-tip soon outweighs the effect of the plastic strain zones. At this point of maximum load unstable crack propagation commences.

APPENDIX E

UNIAXIAL STRESS-STRAIN CURVES

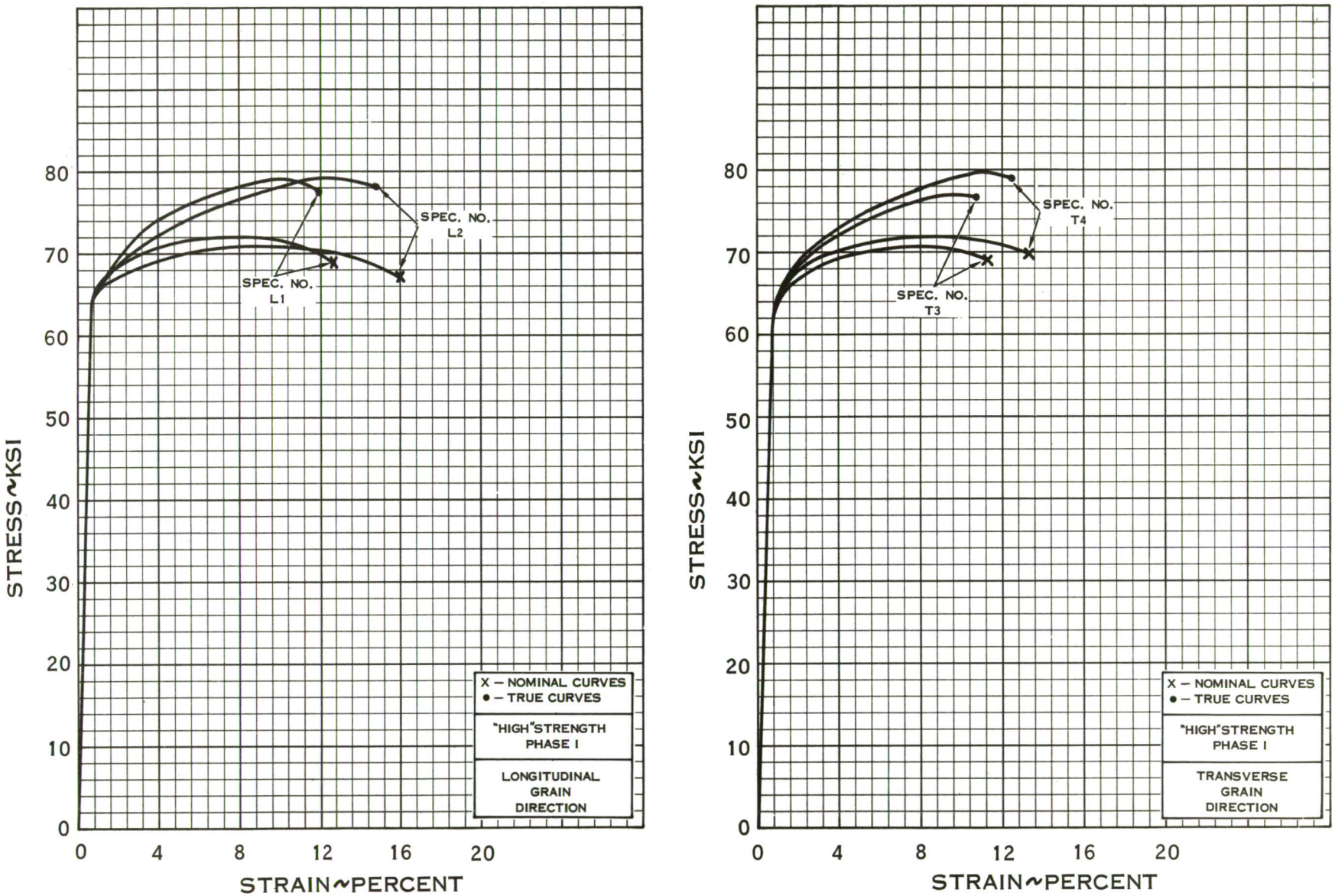

FIGURE 48 – 2014 – T6 ALUMINUM ALLOY UNIAXIAL STRESS – STRAIN CURVES

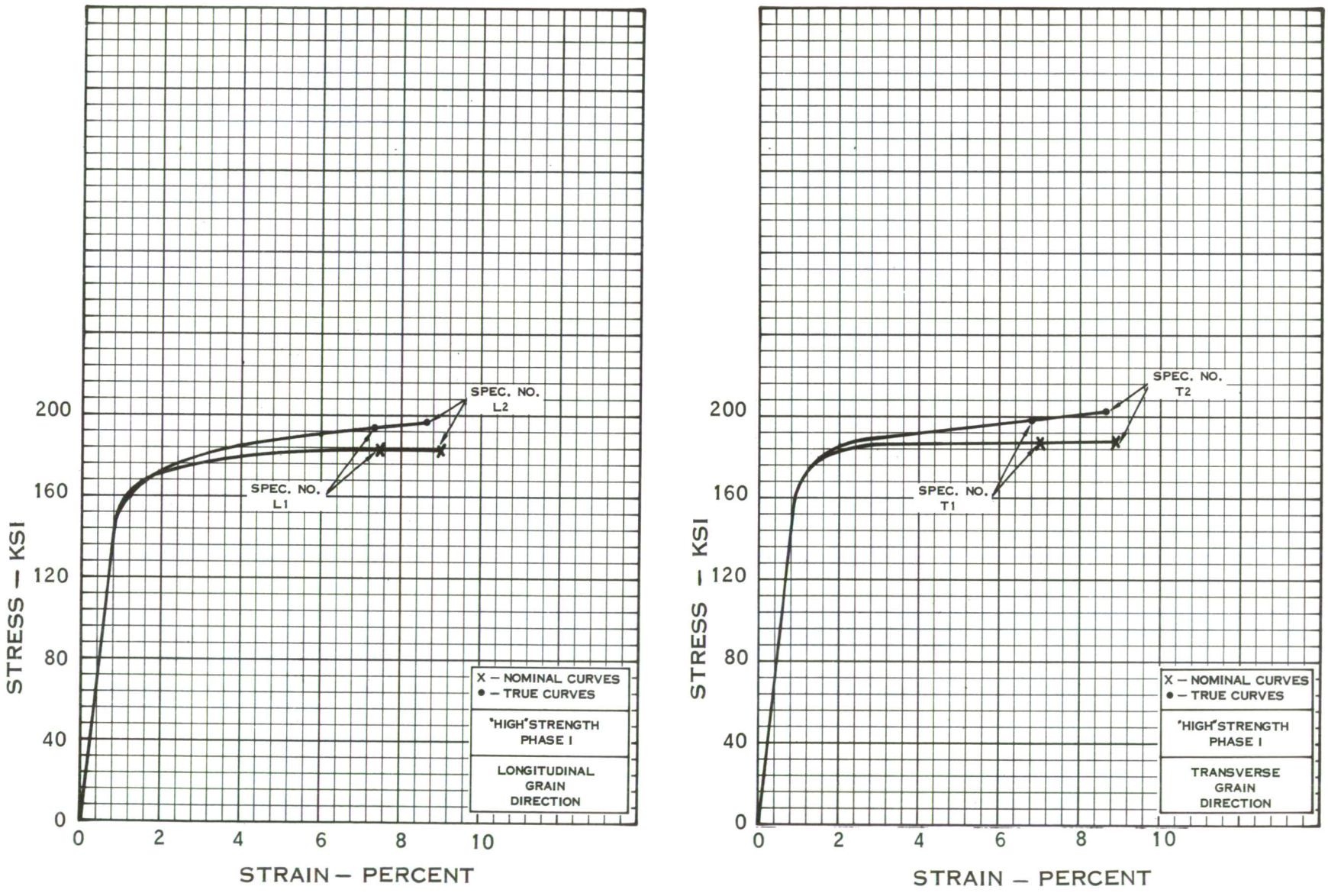

FIGURE 49 – B–120VCA TITANIUM ALLOY UNIAXIAL STRESS – STRAIN CURVES

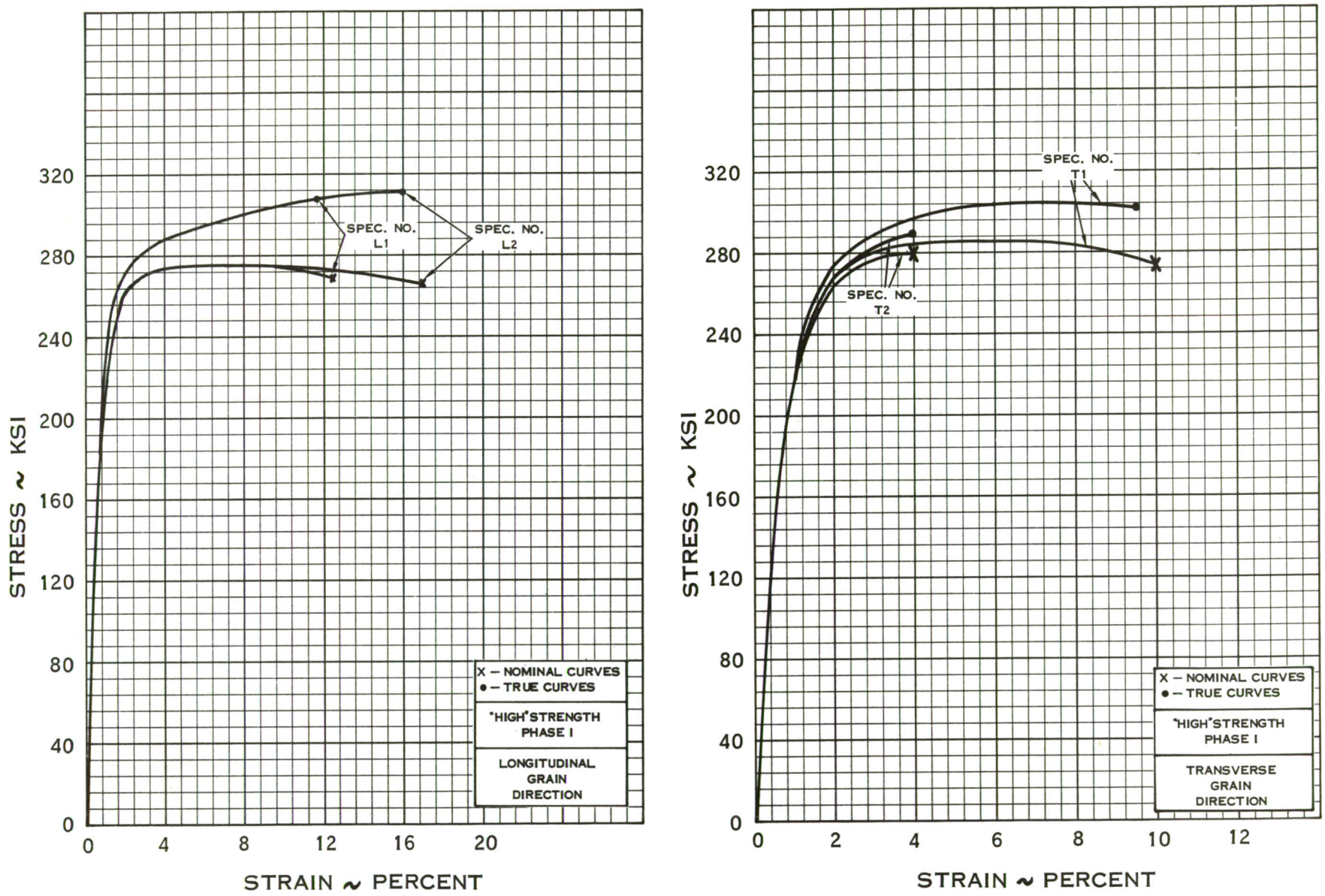

FIGURE 50 – 5CrMoV STEEL ALLOY UNIAXIAL STRESS – STRAIN CURVES

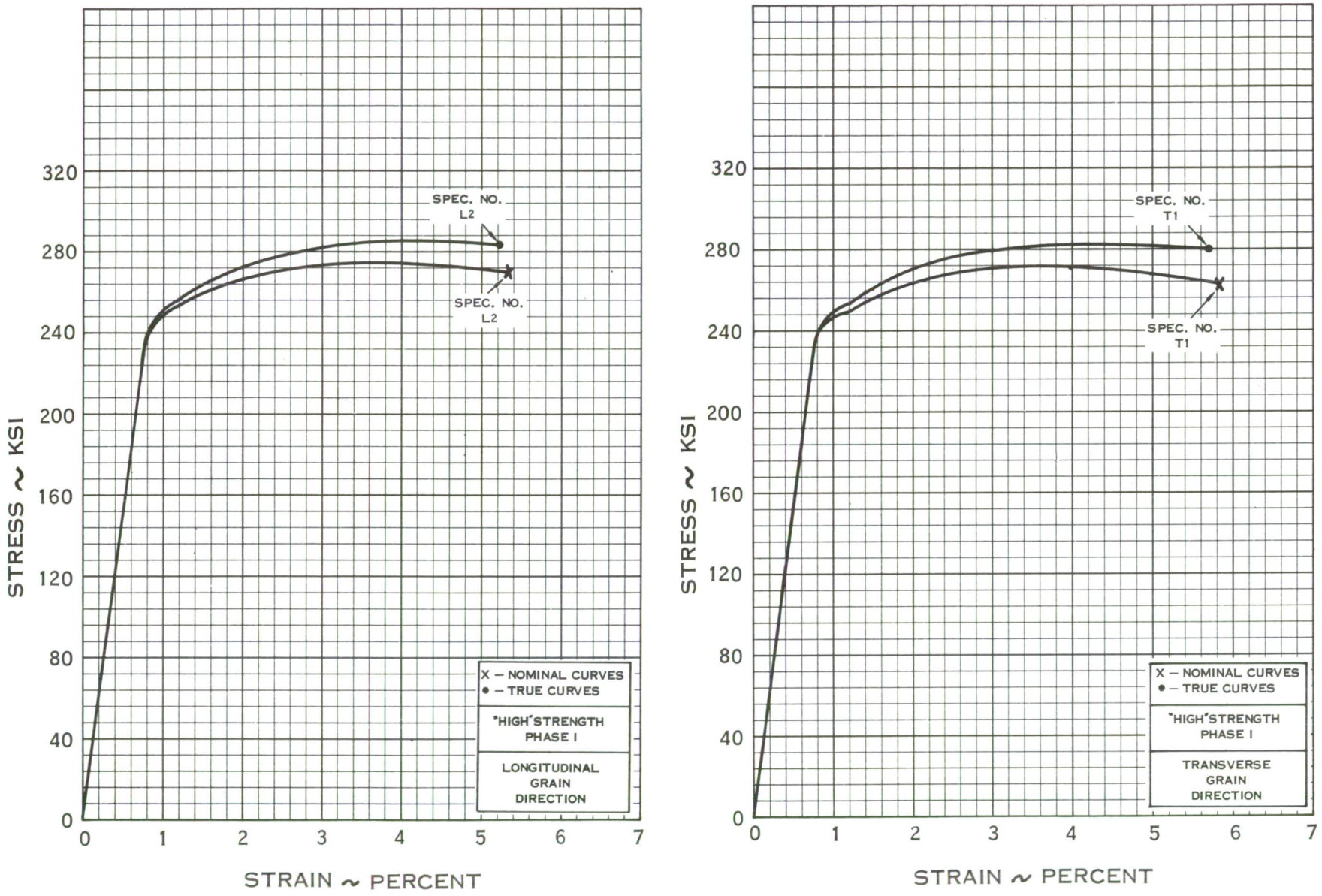

FIGURE 51 – D6A–C STEEL ALLOY UNIAXIAL STRESS – STRAIN CURVES

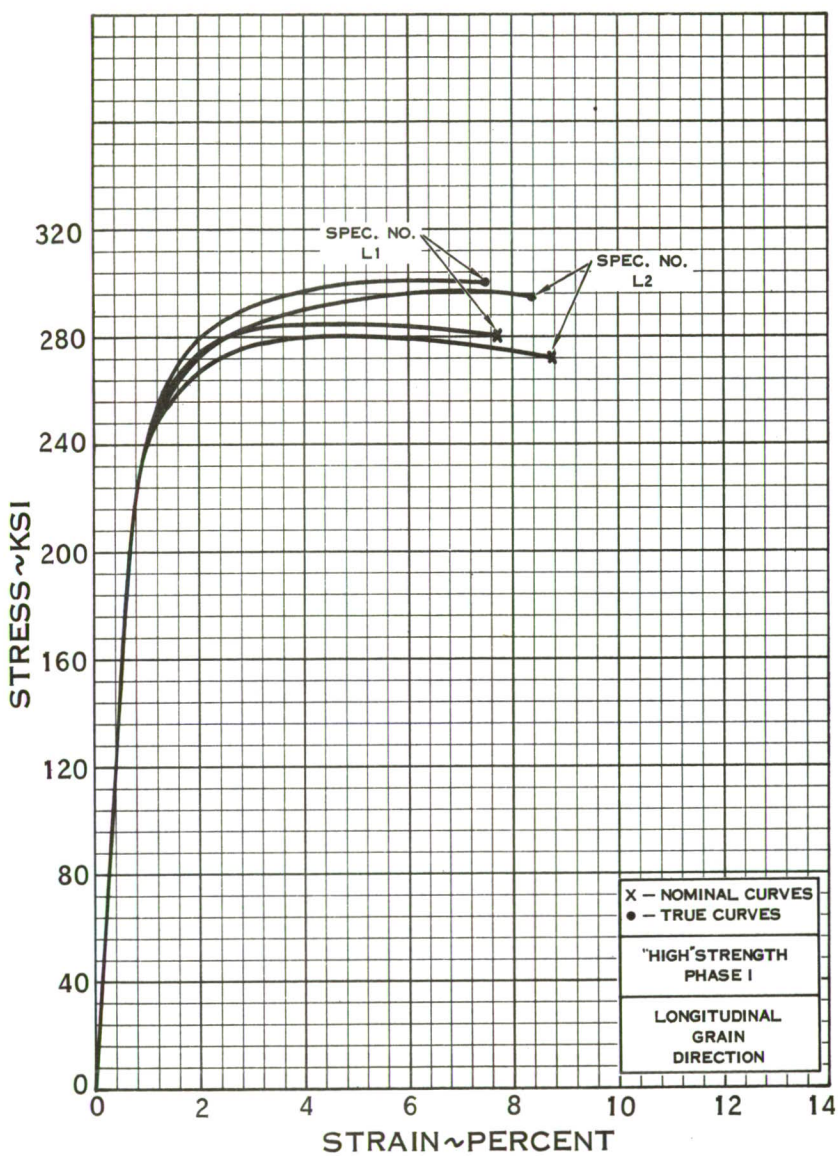

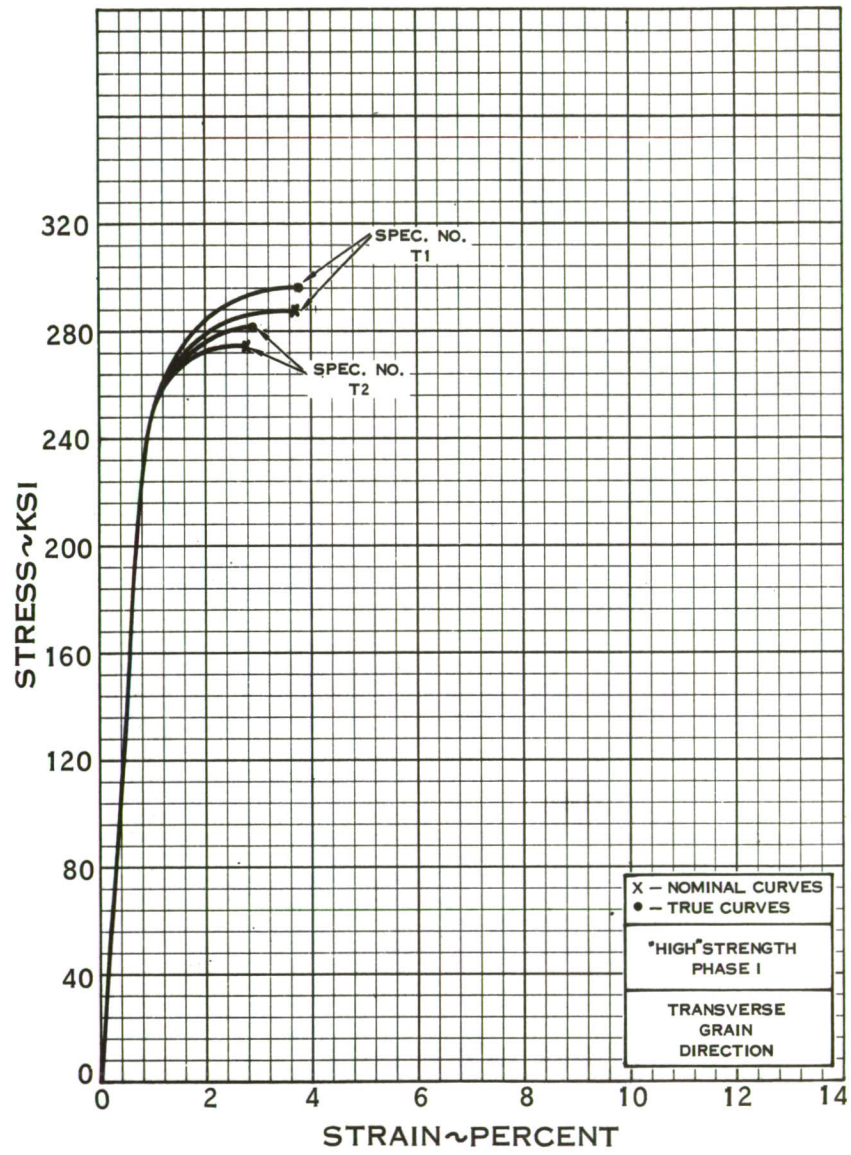

FIGURE 52 — AIRSTEEL X—200 UNIAXIAL STRESS — STRAIN CURVES

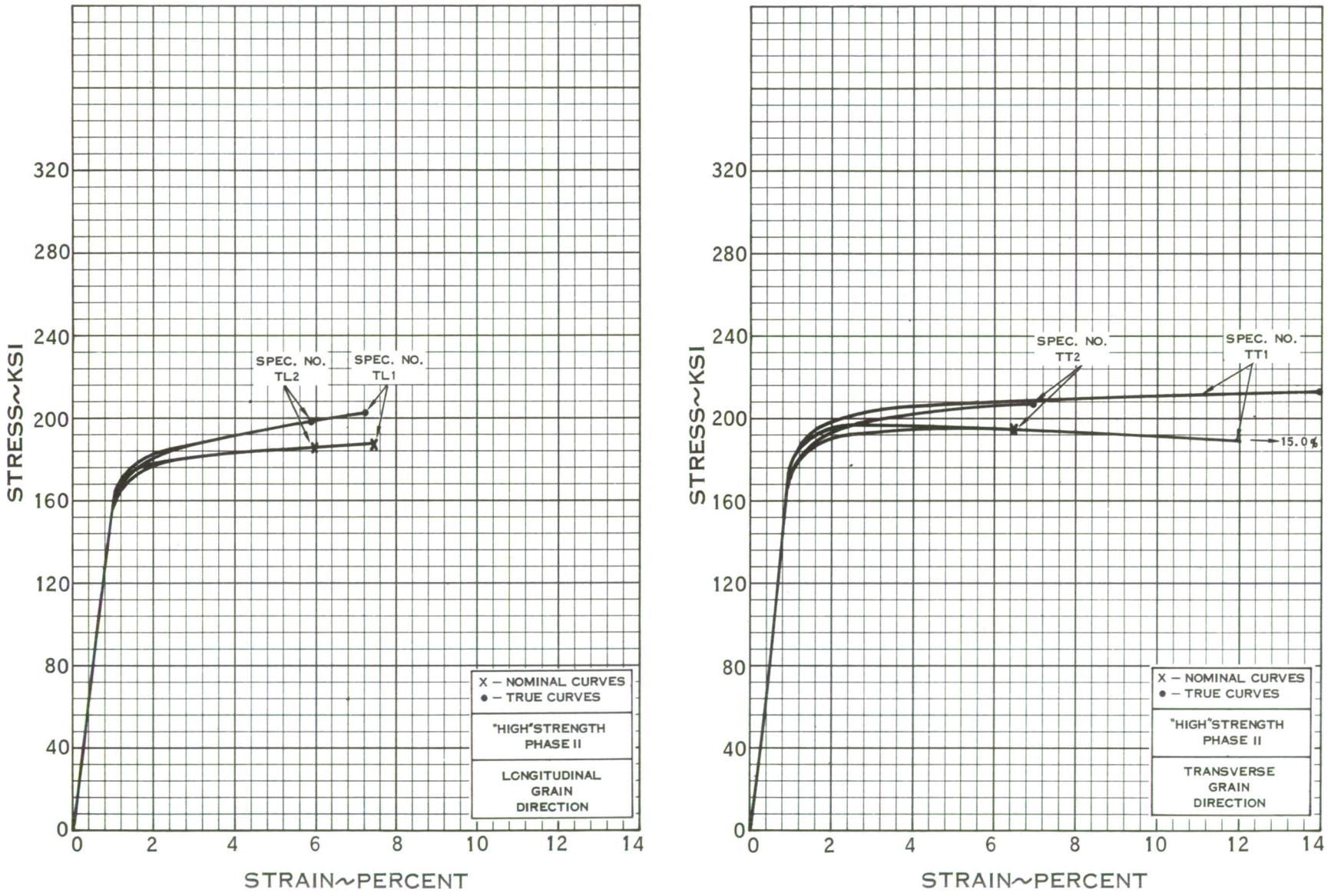

FIGURE 53 – B–120VCA TITANIUM ALLOY UNIAXIAL STRESS – STRAIN CURVES

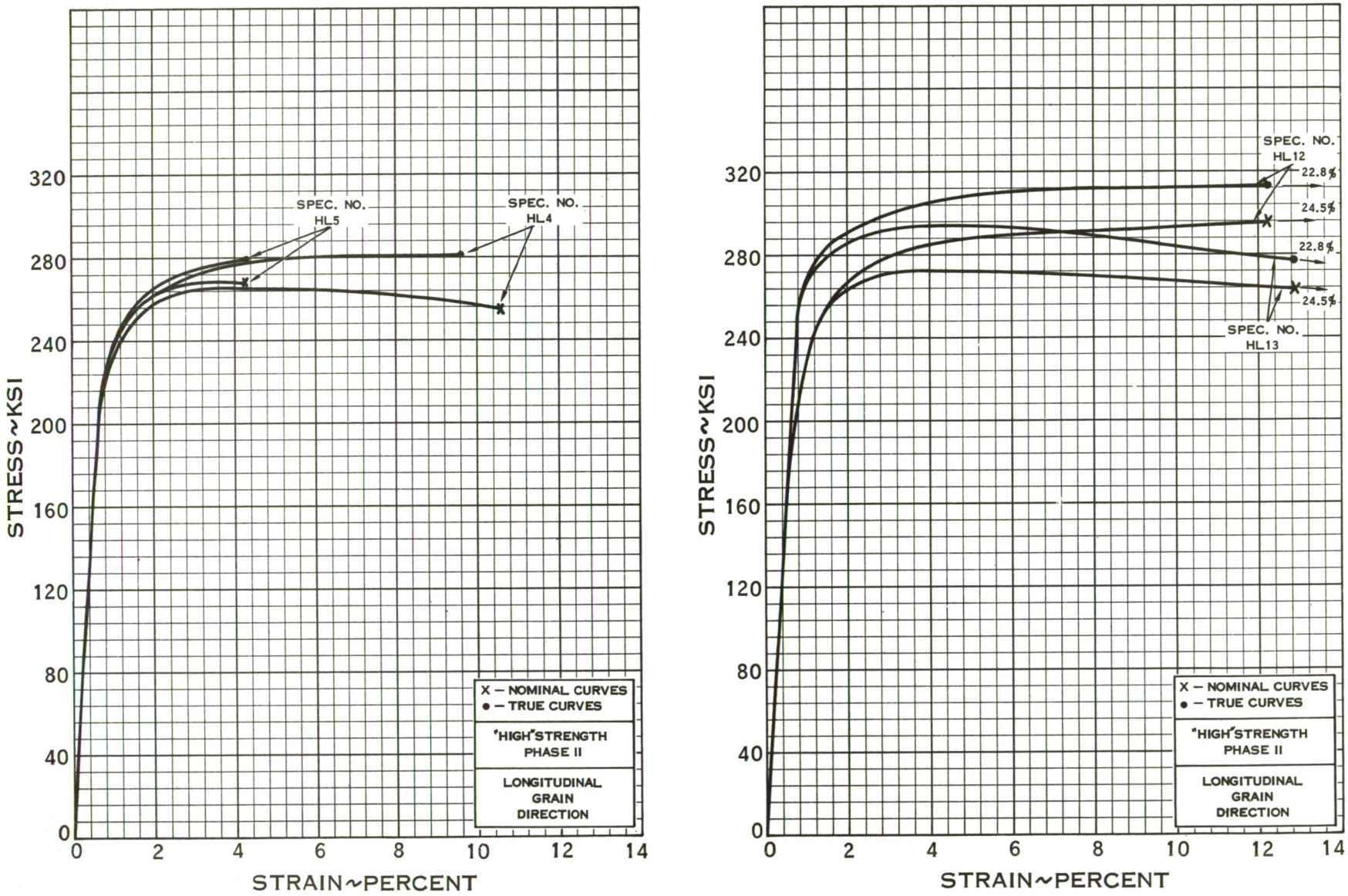

FIGURE 54 – 5CrMoV STEEL ALLOY UNIAXIAL STRESS – STRAIN CURVES

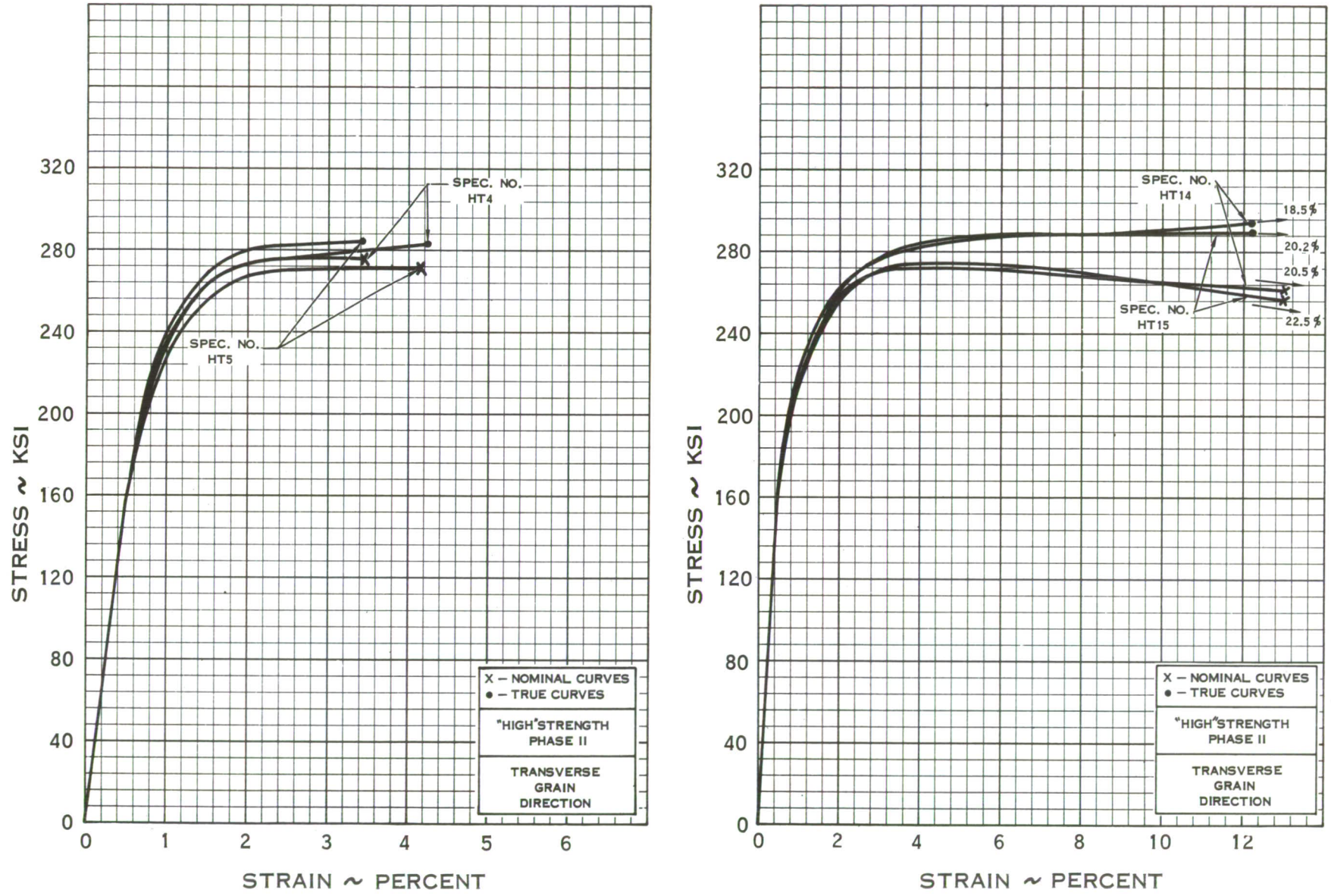

FIGURE 55 – 5CRMOV STEEL ALLOY UNIAXIAL STRESS – STRAIN CURVES

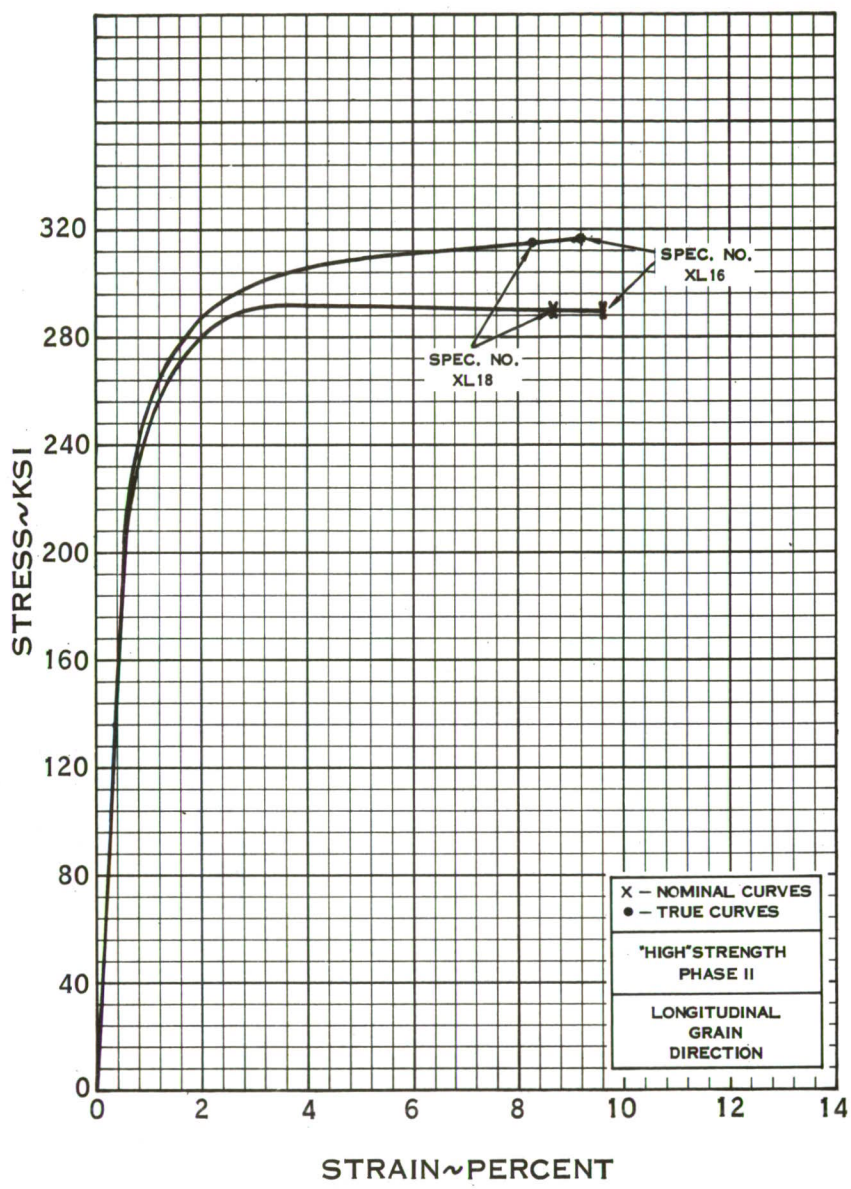

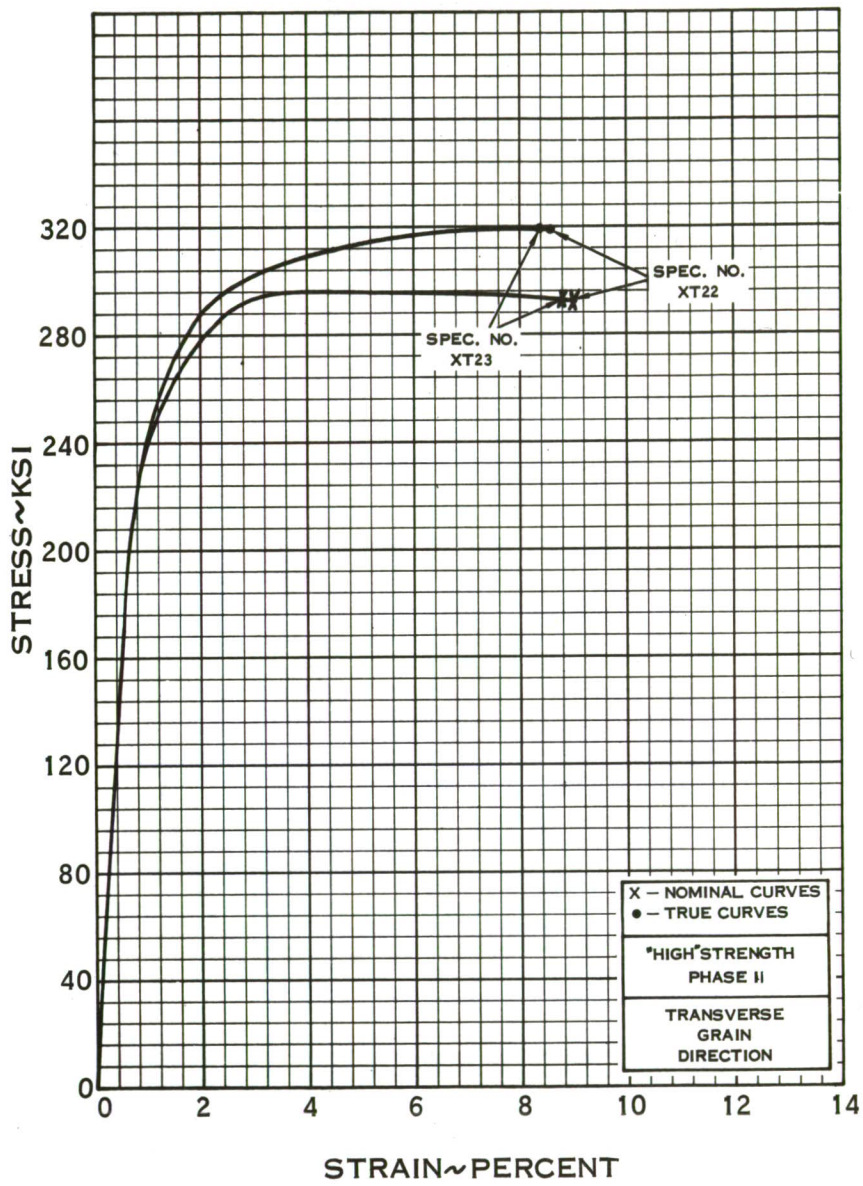

FIGURE 56 – AIRSTEEL X–200 UNIAXIAL STRESS – STRAIN CURVES

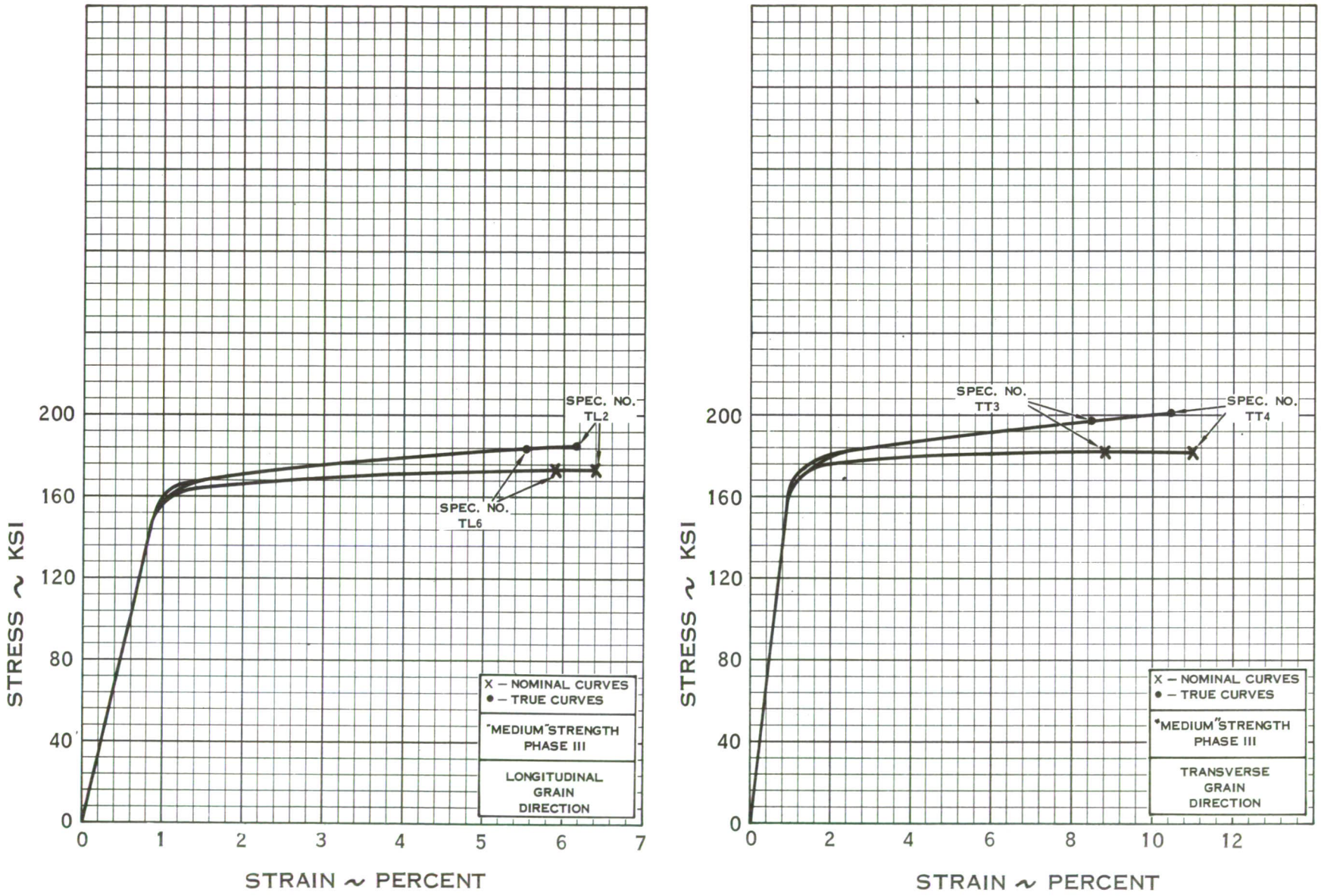

FIGURE 57 —B—120VCA TITANIUM ALLOY UNIAXIAL STRESS — STRAIN CURVES

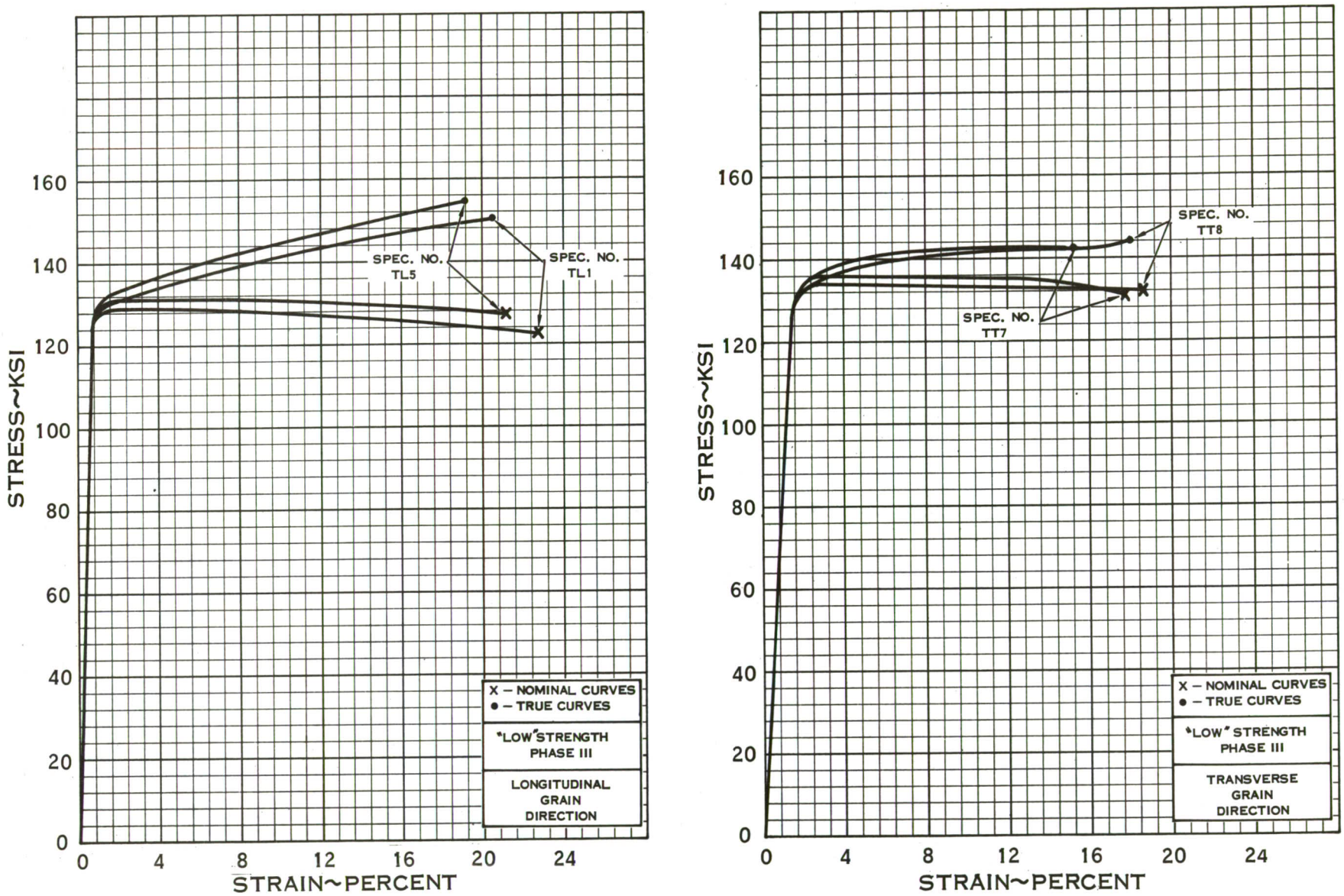

FIGURE 58 – B–120 VCA TITANIUM ALLOY UNIAXIAL STRESS – STRAIN CURVES

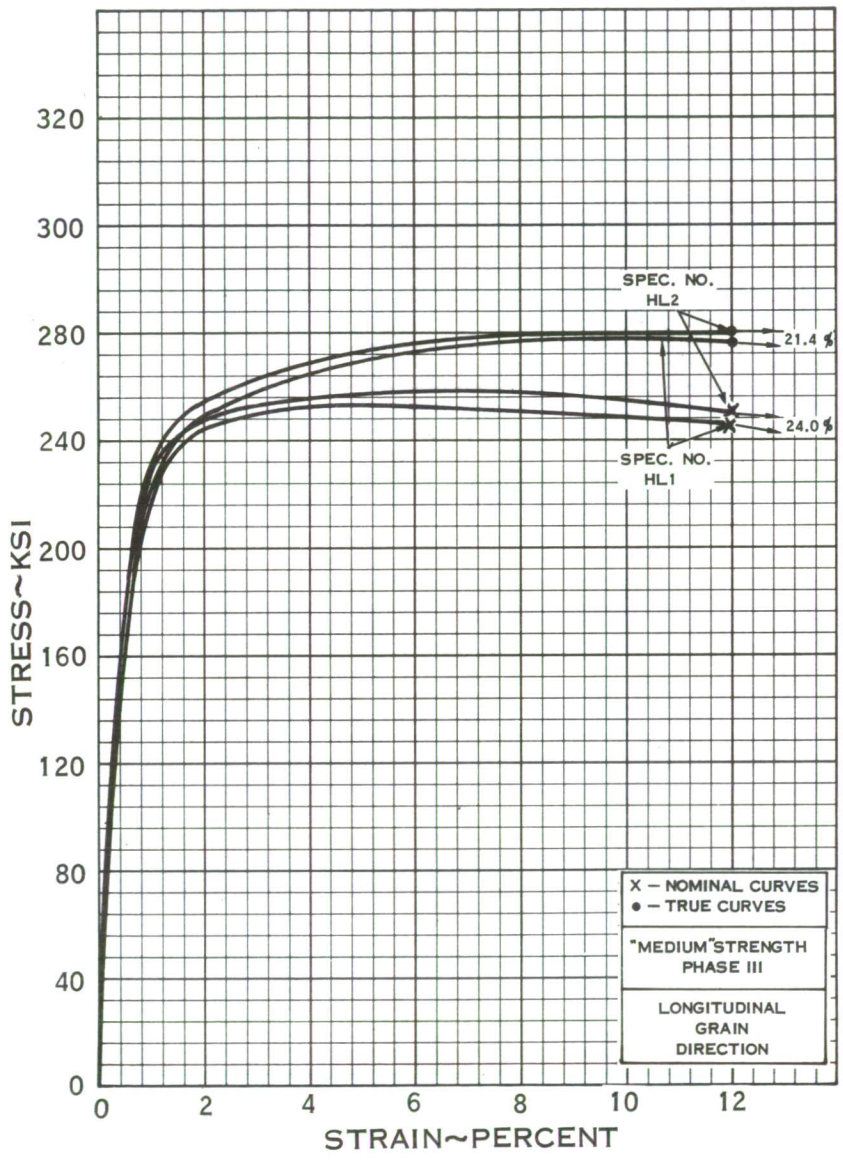

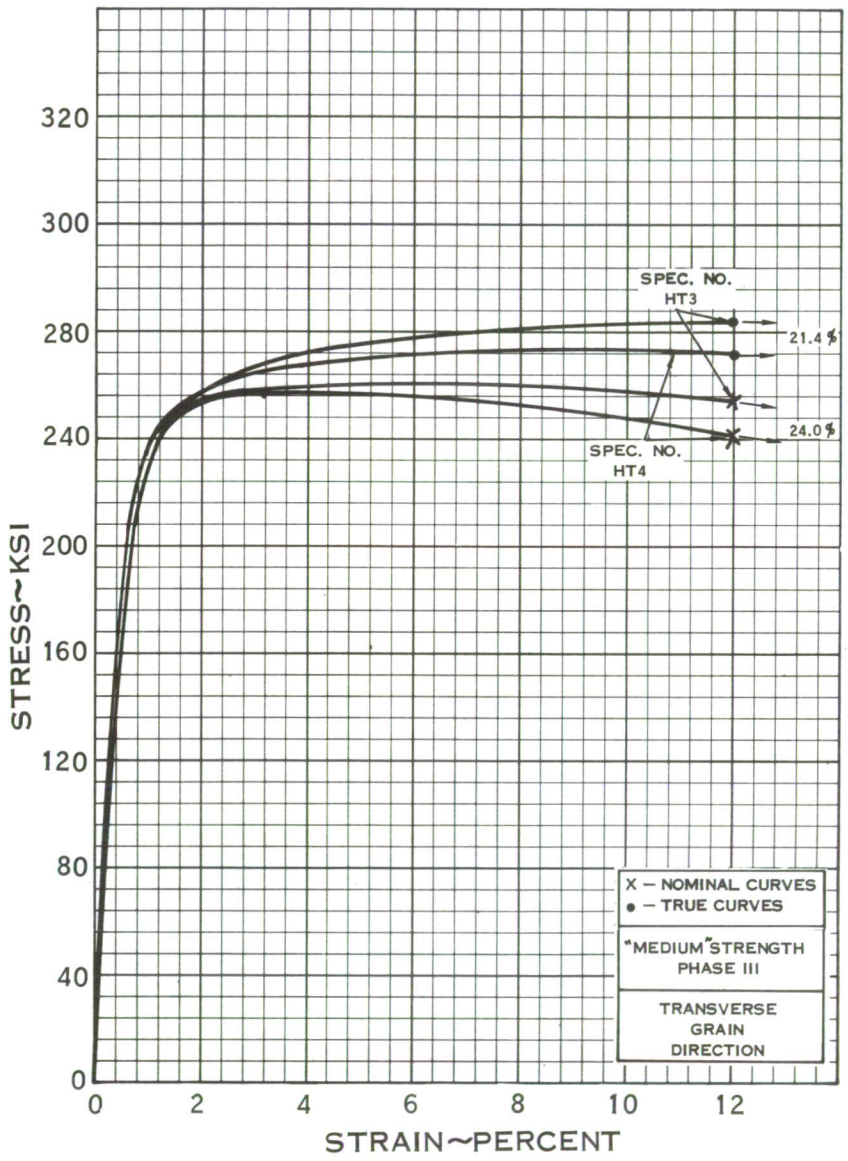

FIGURE 59 – 5CrMoV STEEL ALLOY UNIAXIAL STRESS – STRAIN CURVES

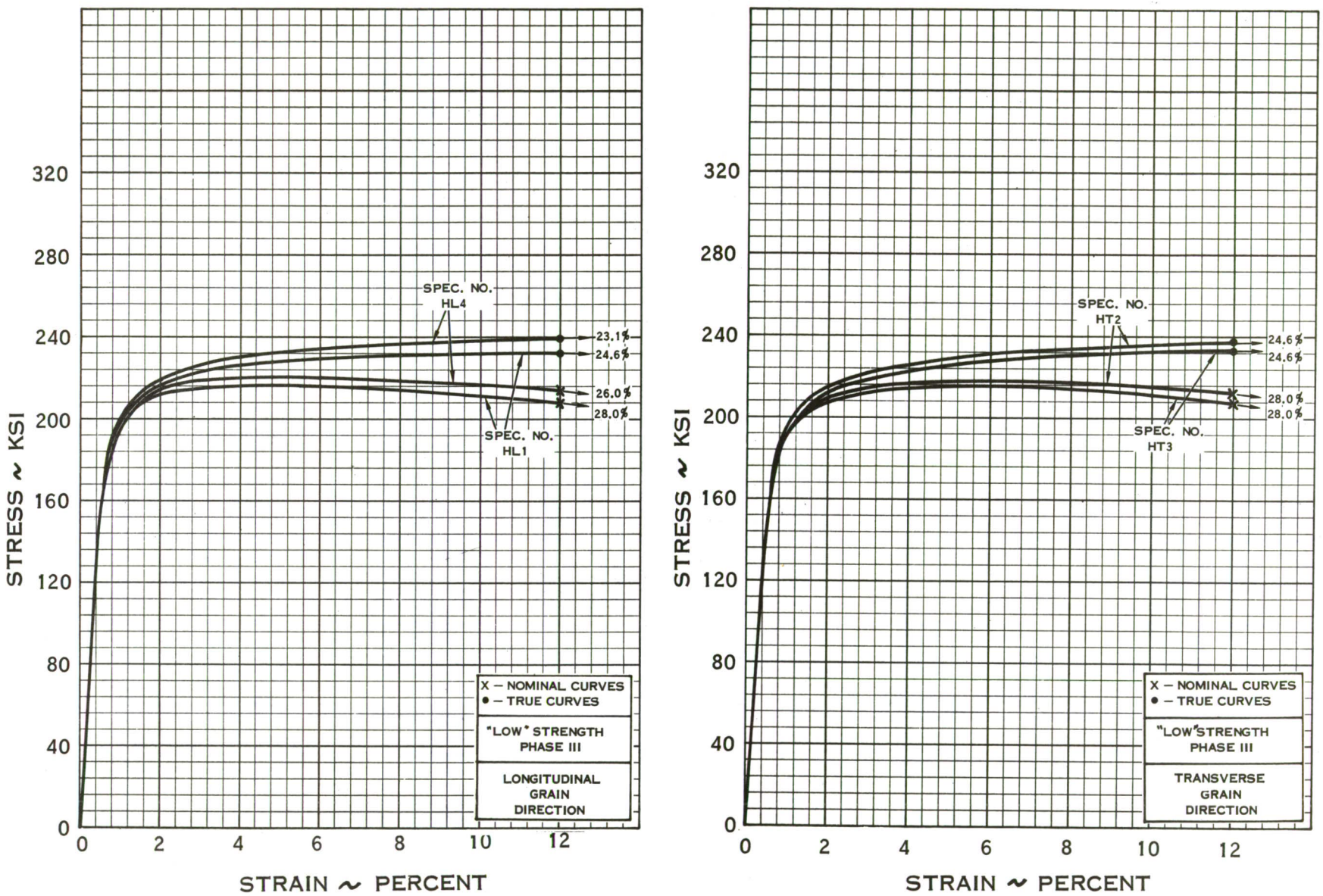

FIGURE 60 – 5CrMoV STEEL ALLOY UNIAXIAL STRESS – STRAIN CURVES

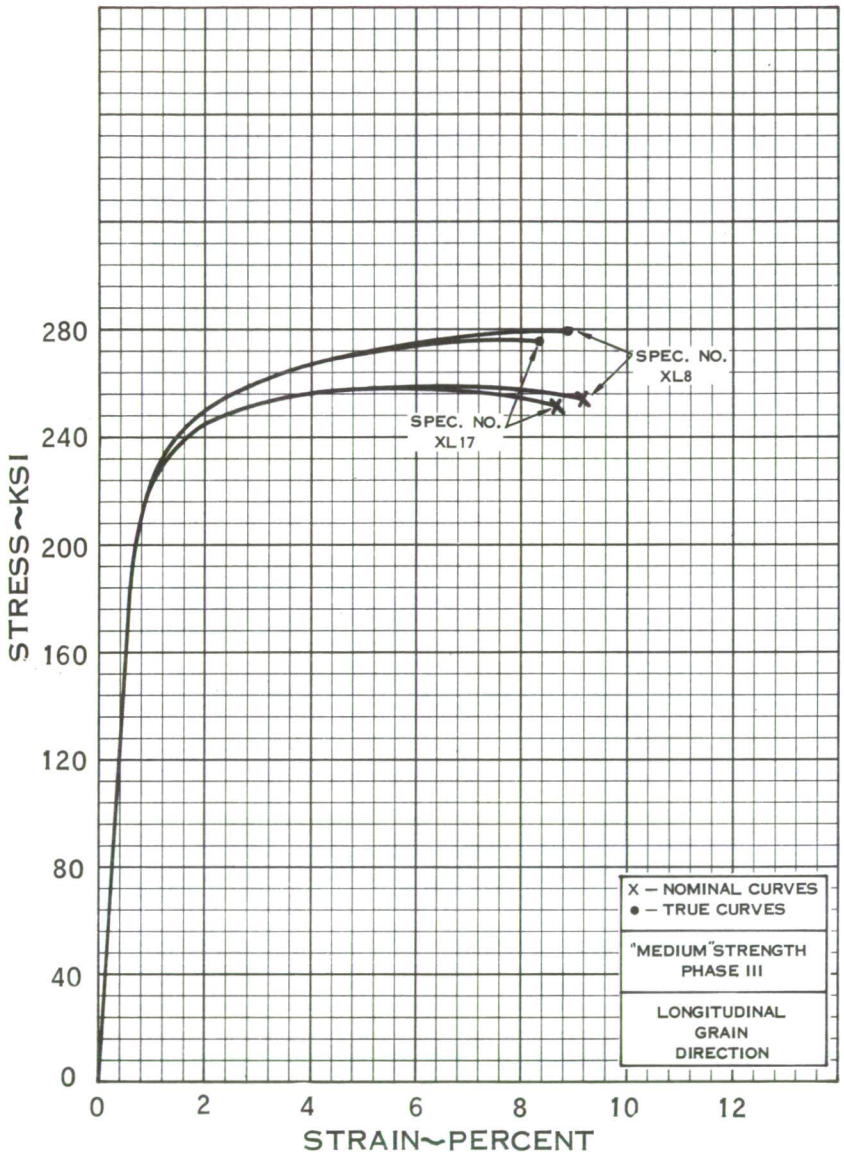

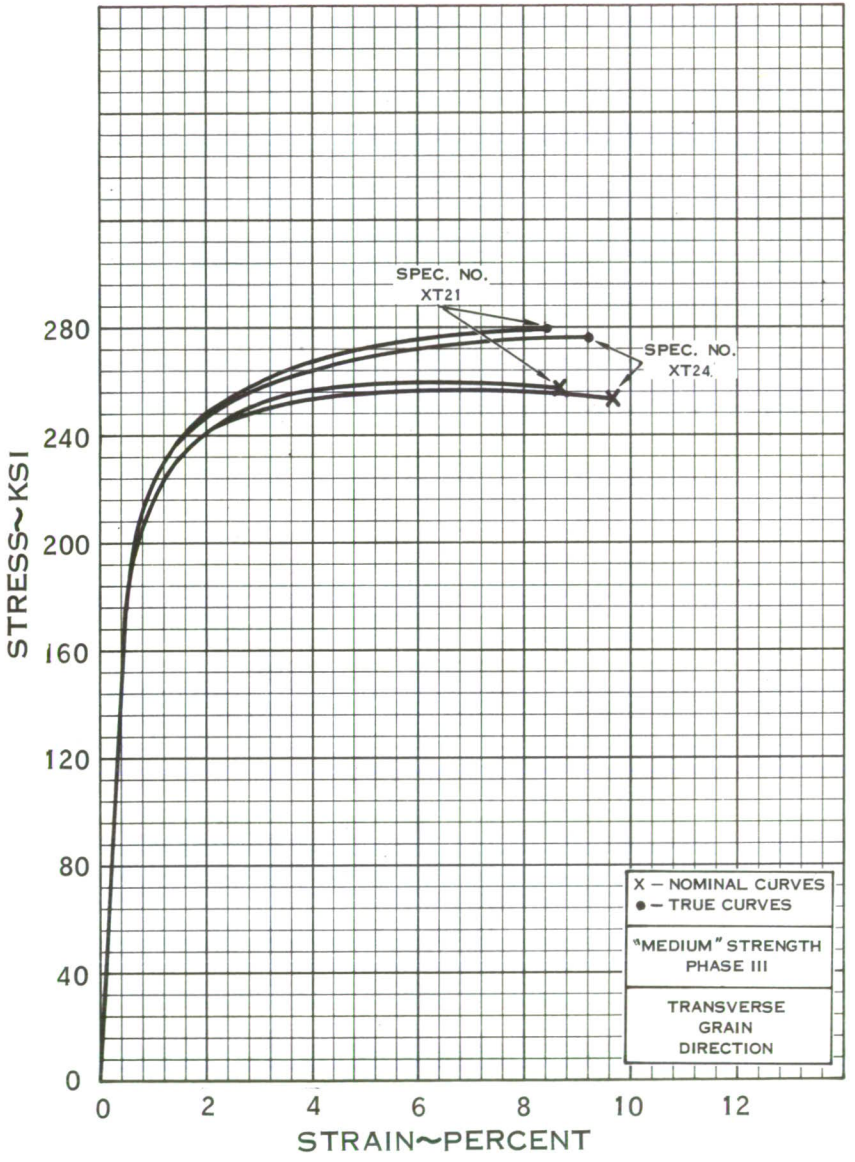

FIGURE 61 – AIRSTEEL X–200 UNIAXIAL STRESS – STRAIN CURVES

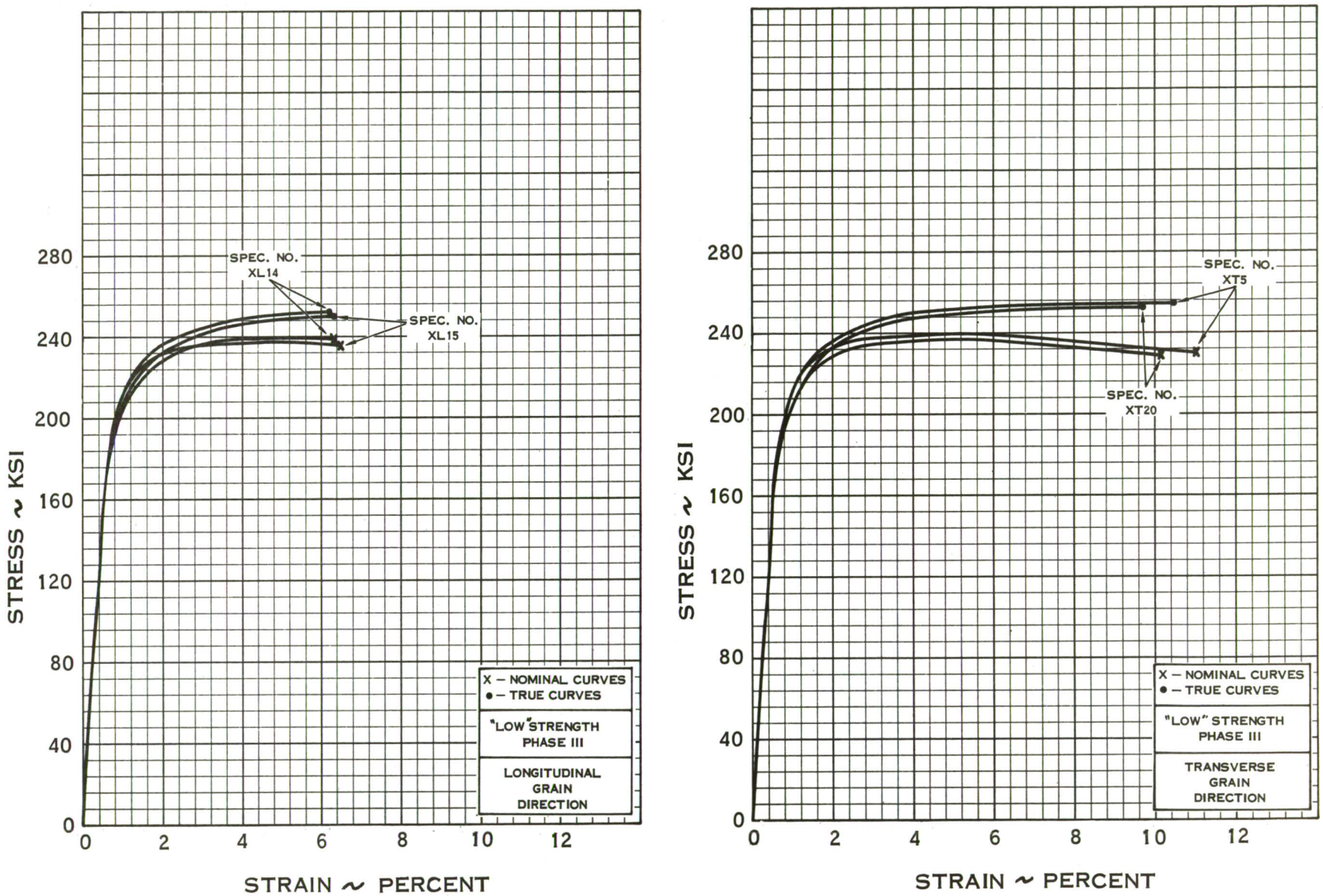

FIGURE 62 – AIRSTEEL X–200 UNIAXIAL STRESS – STRAIN CURVES

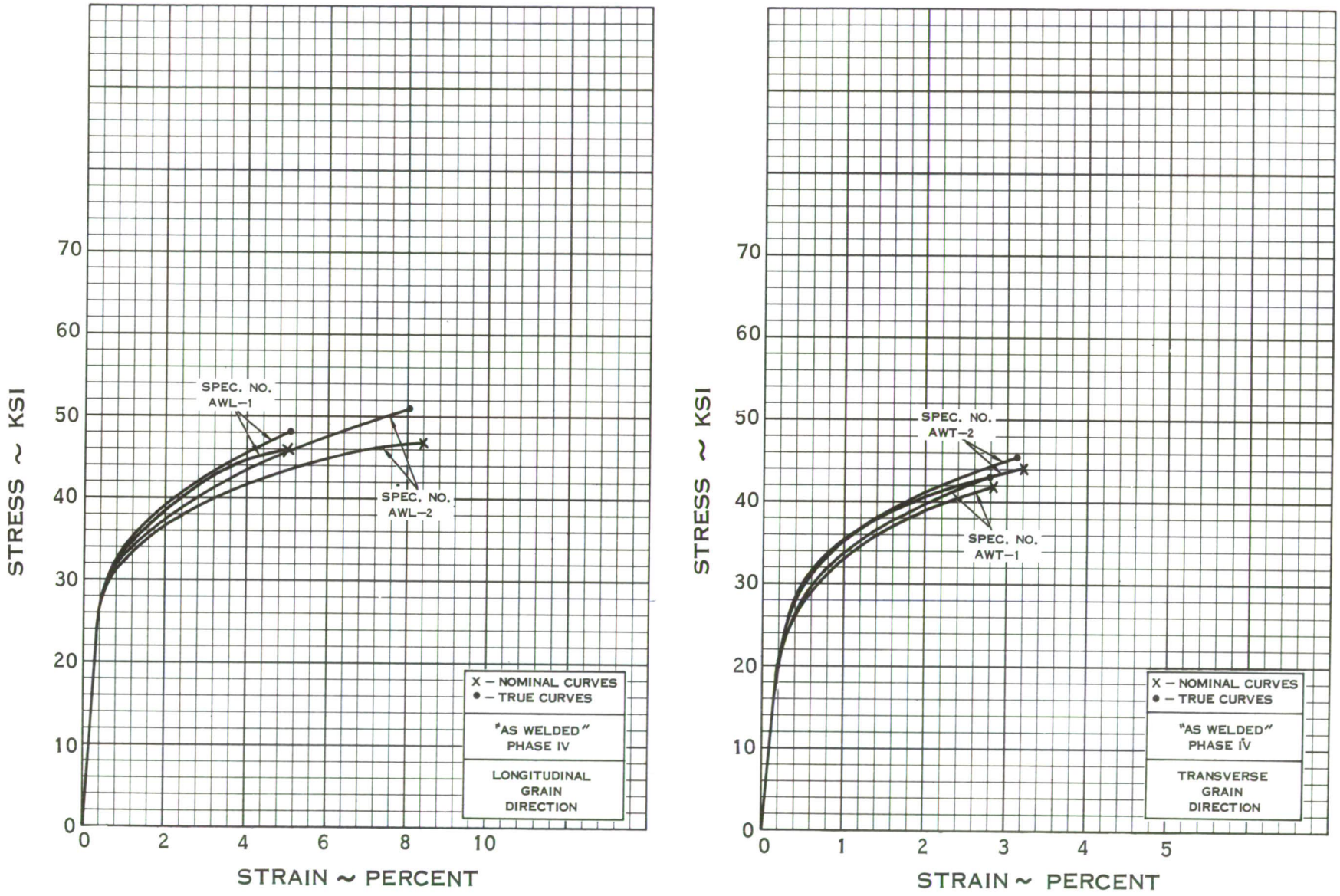

FIGURE 63 – BARE 2014–T6 ALUMINUM ALLOY UNIAXIAL STRESS – STRAIN CURVES WELDED SPECIMENS

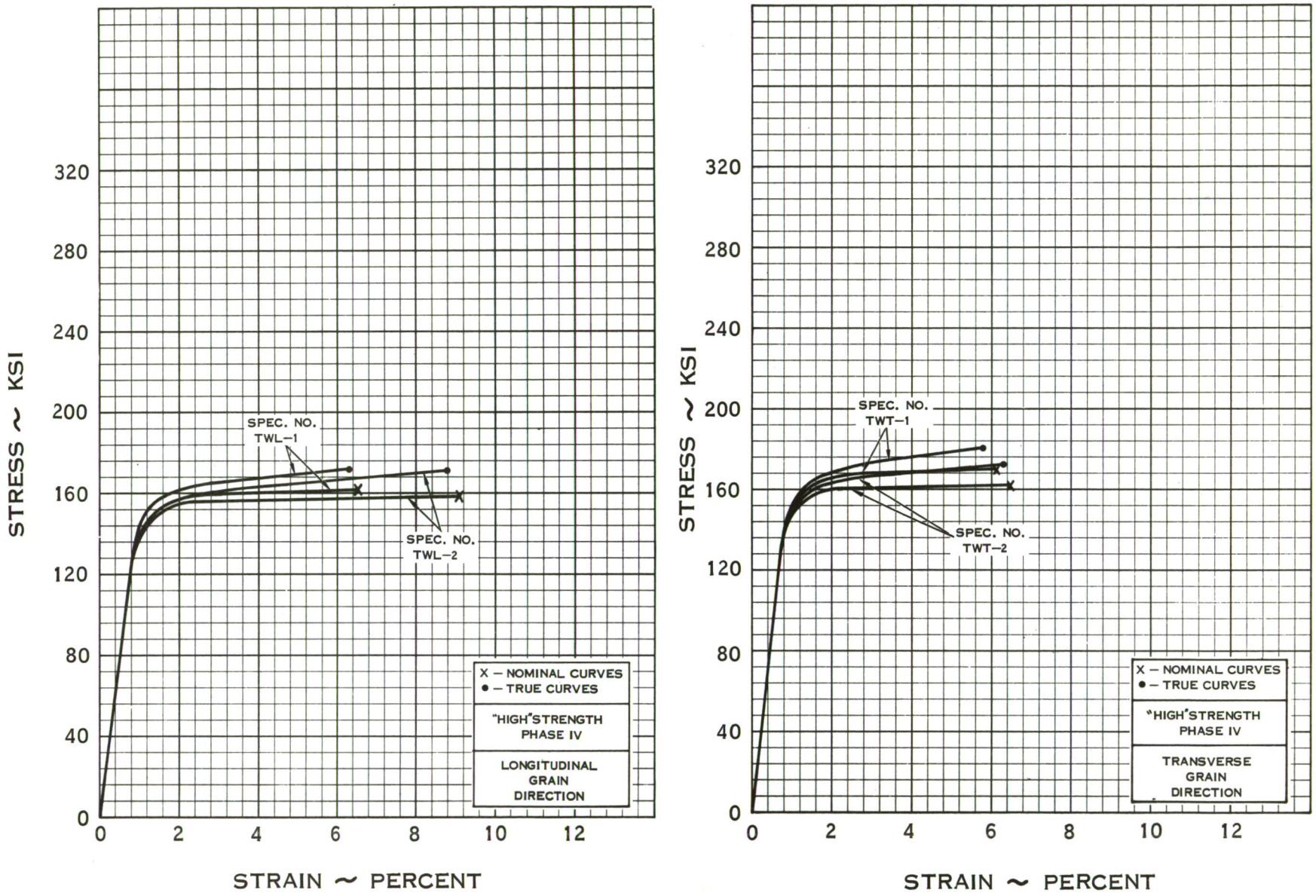

FIGURE 64 –B–120VCA TITANIUM ALLOY UNIAXIAL STRESS – STRAIN CURVES WELDED SPECIMENS

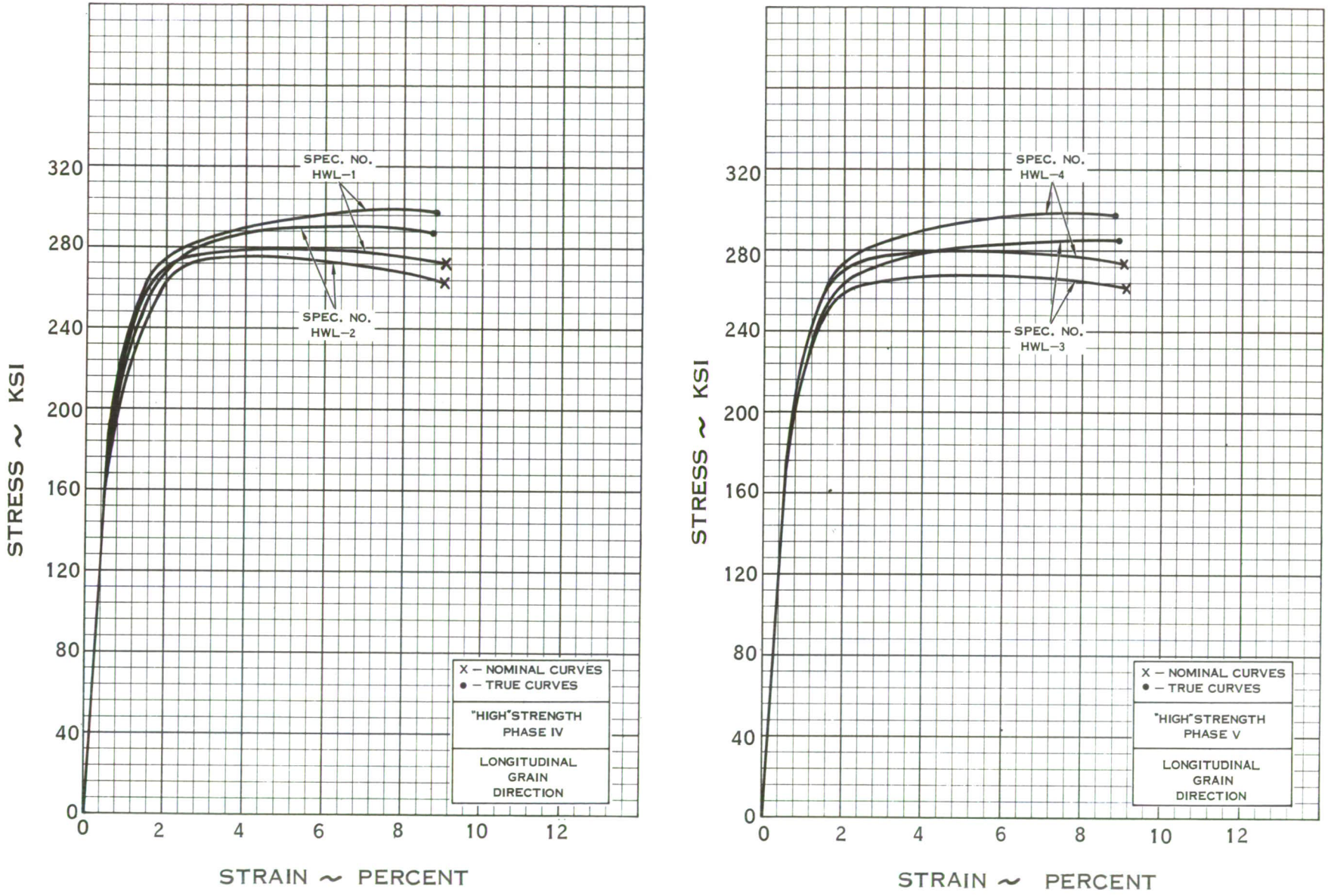

FIGURE 65 – 5CrMoV STEEL ALLOY UNIAXIAL STRESS – STRAIN CURVES WELDED SPECIMENS

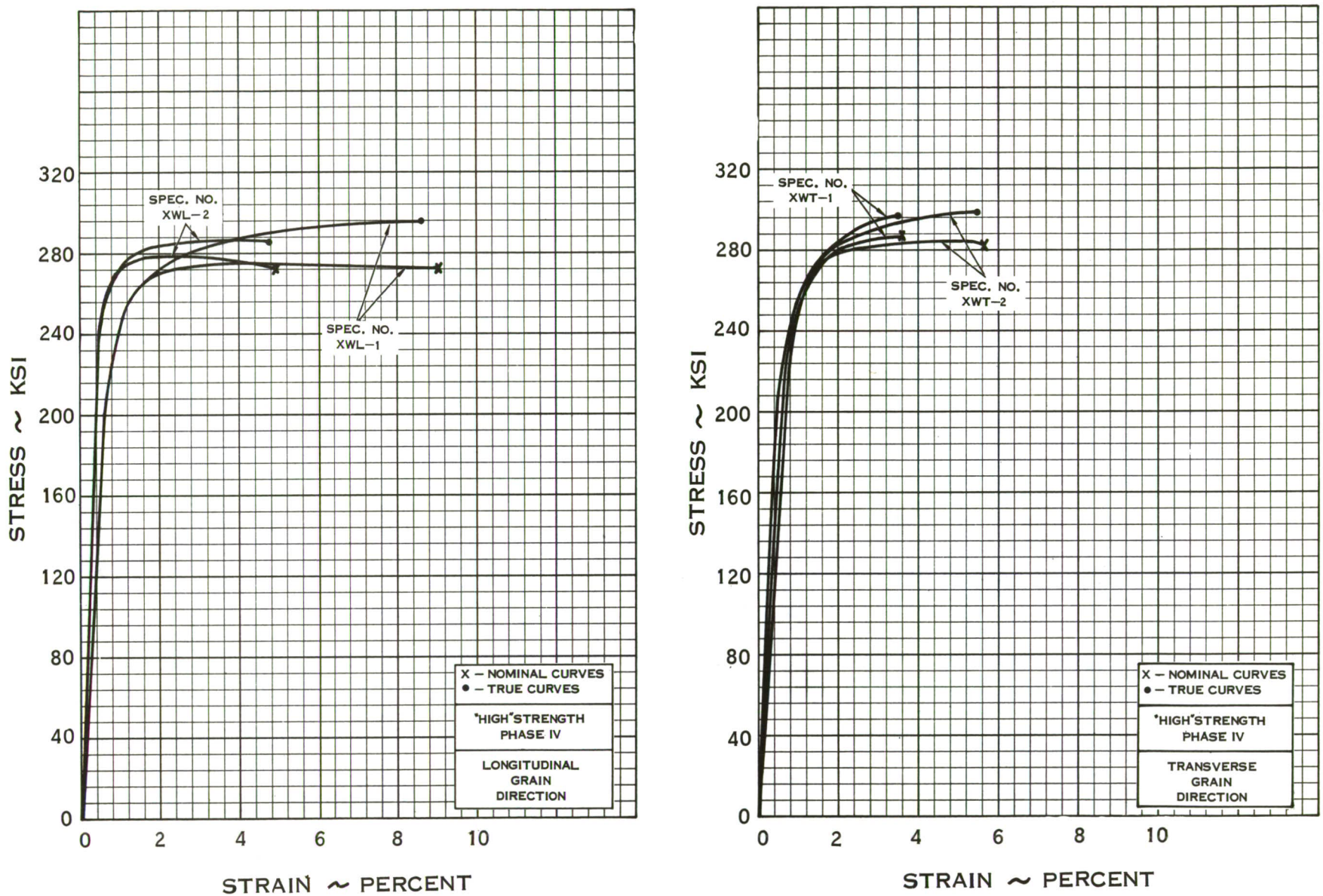

FIGURE 66 – AIRSTEEL X-200 UNIAXIAL STRESS – STRAIN CURVES WELDED SPECIMENS

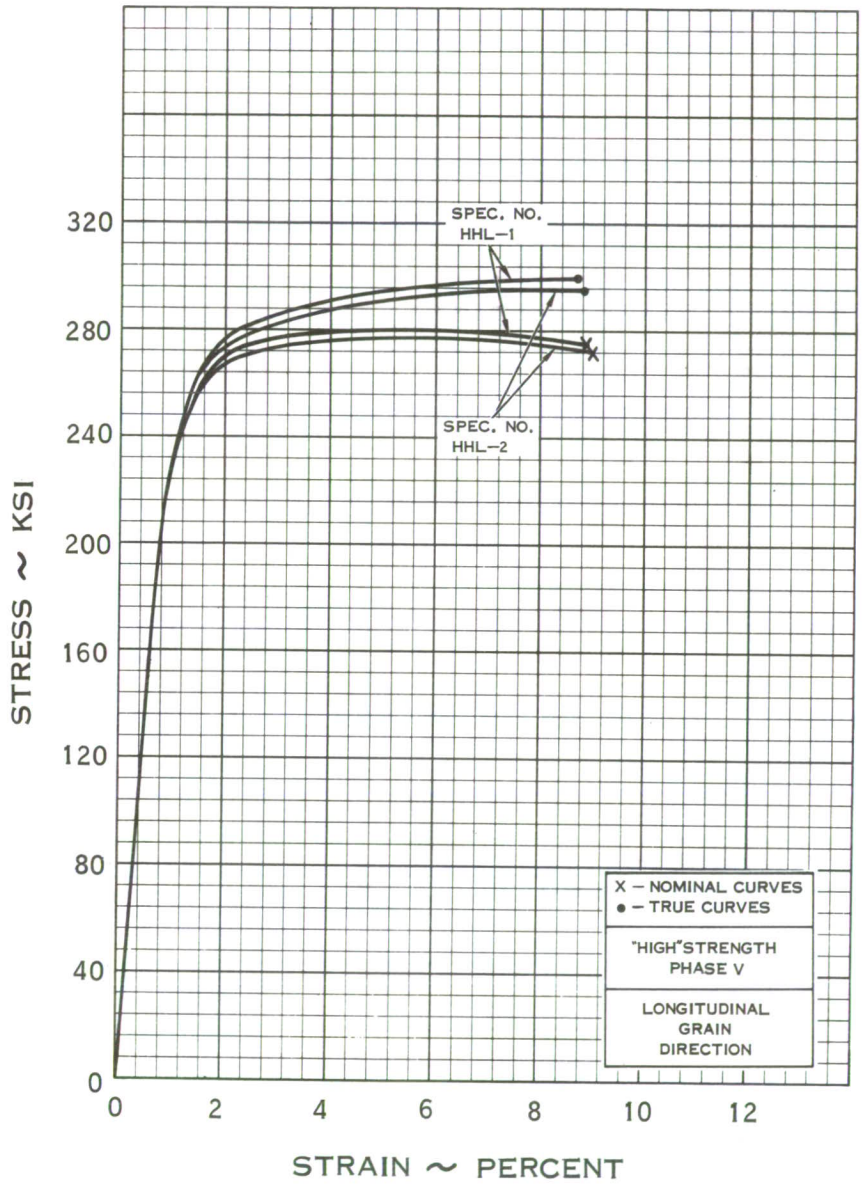

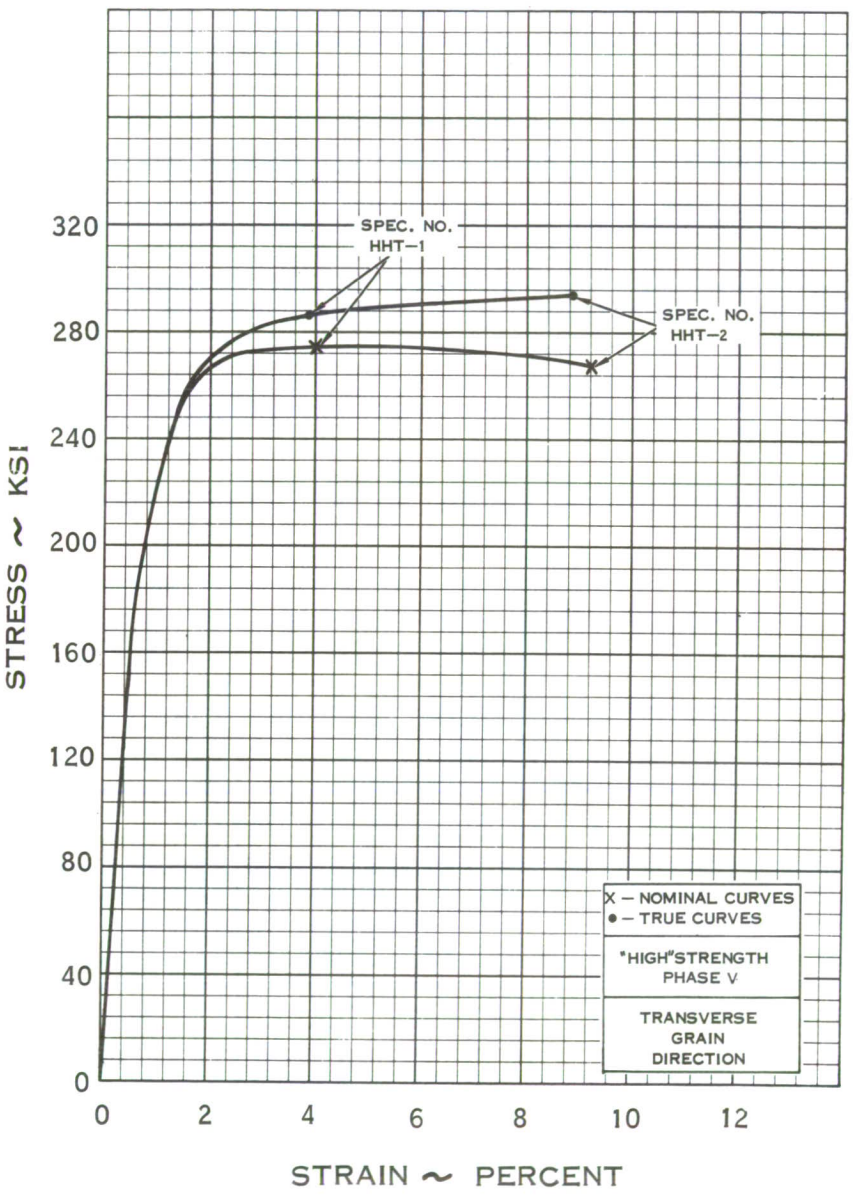

FIGURE 67 – 5CrMoV STEEL ALLOY UNIAXIAL STRESS – STRAIN CURVES

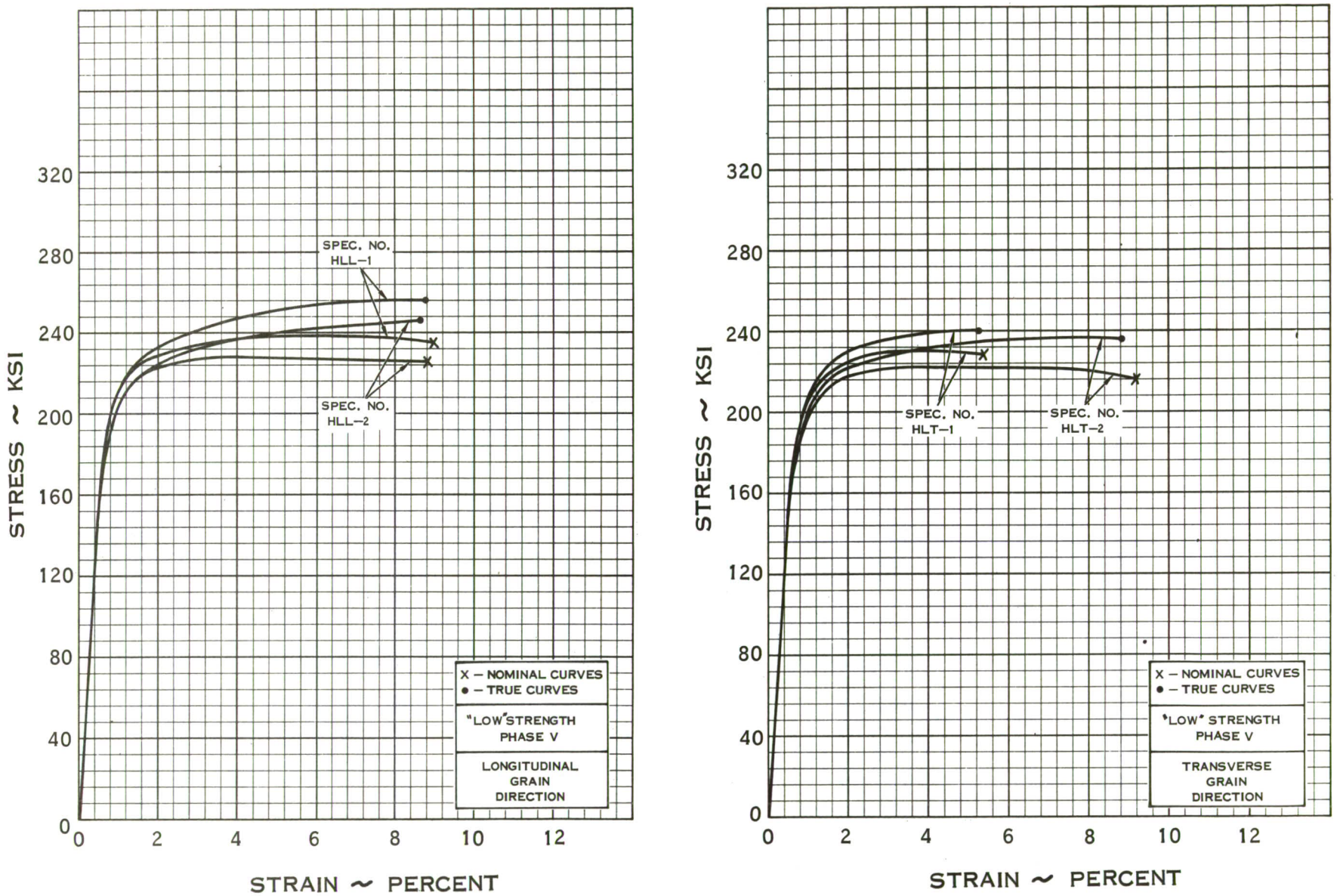

FIGURE 68 – 5CrMoV STEEL ALLOY UNIAXIAL STRESS – STRAIN CURVES

APPENDIX F

METHOD OF CONVERTING BIAXIAL LOAD-STRAIN CURVES TO BIAXIAL STRESS-STRAIN CURVES

1:1 Biaxial Stress Ratio

During each test a continuous record of jack loads applied at the ends of the specimen versus principal strains measured at the center of the specimen was made. This resulted in a load-strain plot similar in shape to a stress-strain curve. As long as the center of the specimen remained in the elastic range, principal stresses could be calculated from the recorded strains, the elastic uniaxial modulus and Poisson's ratio. However, as soon as the center strained into the plastic range, stresses could not be calculated from the strains because the shape of the plastic portion of the biaxial stress-strain curve was not known. In addition, the stresses could not be calculated by a simple load/area relation because the amount of load fed across the center changed as different portions around and near the center of the specimen strained into the plastic region.

Several specimens were photo stressed in an attempt to determine the principal plastic stresses at the center by use of fringes, isoclinics and stress trajectories as suggested by Frocht (Ref. 12). However, these methods give stresses based on an elastic modulus. Therefore, the calculated stresses are approximate except at a free boundary. Boundary stresses can be calculated accurately since the state of stress is uniaxial. The state of stress in the depression of the biaxial specimens is not uniaxial and it is at these points where the shape of the stress-strain curve is not known.

A close study of the manner in which the biaxial specimen loads and strains led to a suitable method for calculating the principal plastic stresses in the center of the depression. Photo-stress studies revealed that the two inch corner radii yield first and at a higher load the center begins to yield. After the corners yield the stresses in the center increase at a higher rate than the corner stresses. However, after all elements across the diagonal A-A shown in Figure 69 have yielded, the stress distribution becomes more uniform. The fracture will initiate in the center because the allowable strain at this point is the lowest due to the state of 1:1 tensile stress. Based on these observations, it is evident that after the center yields the slope of the unload-strain curve will be steeper than the slope of the initial elastic load-strain curve. This situation exists because of the difference in the stress distribution across the diagonal when the center is elastic and when the center has yielded. The steeper slope reflects the higher ratio of center to corner stresses and loads. Tests showed that this behavior occurs in all of the materials that were tested. The following discussion outlines the procedure which was used to calculate the center stresses by use of the unload-strain curves.

Several specimens were loaded until the center had yielded by various amounts and then were unloaded to determine the slope of the unload-strain curve. An earlier test had shown that the specimen could not be completely unloaded without inducing residual compressive stresses into the center. However, the specimens were unloaded far enough to extrapolate the unload-strain curve to determine the permanent strain. The total strain at the point of maximum load and the permanent strain at zero load provide enough information to calculate the stress in the center at the instant unloading commences. The procedure which was followed in obtaining the principal stress-strain curves is illustrated by Figure 70.

The straight line portion of the 1:1 biaxial stress-strain curve was plotted first. The slope of this line, or the effective modulus, was obtained from the following well known relation:

$$\frac{\sigma_1}{\epsilon_1} = \frac{\sigma_2}{\epsilon_2} = \frac{E}{1 - \mu_2} \qquad (126)$$

The modulus of elasticity E and Poisson's ratio μ_2 are obtained from the uniaxial tension test. A line was drawn parallel to the effective modulus line through the permanent set strain at zero stress. The intersection of this line and the value of the total strain at the point when unloading started is the principal stress. It was observed that the unload-strain curve had a constant slope once the center yielded considerably. For this reason, the same slope could be used to obtain principal stresses over a wide strain range up to failure.

It is significant to note that principal stresses at failure calculated by the above method and calculated by dividing the resultant jack loads by the area across the diagonal were within a few percent. There was no definite trend which would show that the latter method always resulted in a higher or lower stress. The resultant jack load P_R is simply $P_1 \times 1.414 = P_2 \times 1.414$.

The reason that this method resulted in the correct failing stress was because all elements across the diagonal had reached maximum load just prior to failure. This type of loading behavior may not occur in materials which do not have a relatively flat plastic stress-strain curve.

2:1 Biaxial Stress Ratio

As discussed previously, principal stresses in the biaxial specimen under 1:1 loading could be calculated from equations of elasticity as long as the test area remained elastic. However, other means had to be used for determining the plastic portion of the biaxial stress-strain curves. This was not the case for 2:1 biaxial loading since use could be made of the fact that no plastic flow occurs in the minimum principal stress direction under 2:1 loading if Poisson's ratio is 0.50 in the plastic range. As shown in Table 9, the plastic value of Poisson's ratio is very close to 0.50 for all of the test materials. The following discussion outlines the procedure which was used to convert the load-strain curves to biaxial stress-strain curves.

During each test, the load-strain curves which were recorded in the minimum and maximum principal stress directions were tick marked at periodic intervals in order to provide a link between the recorded principal strains. Through the use of equation (4) values of σ_1' were determined at each of the ticked marked points on the load-strain curve obtained in the minimum principal stress direction. In this case σ_1' is the maximum principal stress and σ_2' is the minimum principal stress. With these calculated values of σ_1' and the corresponding strain values taken from the load-strain curve in the maximum principal stress direction it was possible to plot the maximum principal stress-strain curve. The stress-strain curve in the minimum principal stress direction was obtained in a similar manner. The minimum principal stress values, σ_2', are simply one-half of the calculated σ_1' stresses. With these values of σ_2' and the corresponding strain values taken from the load-strain curve in the minimum principal stress direction, the stress-strain curve was plotted.

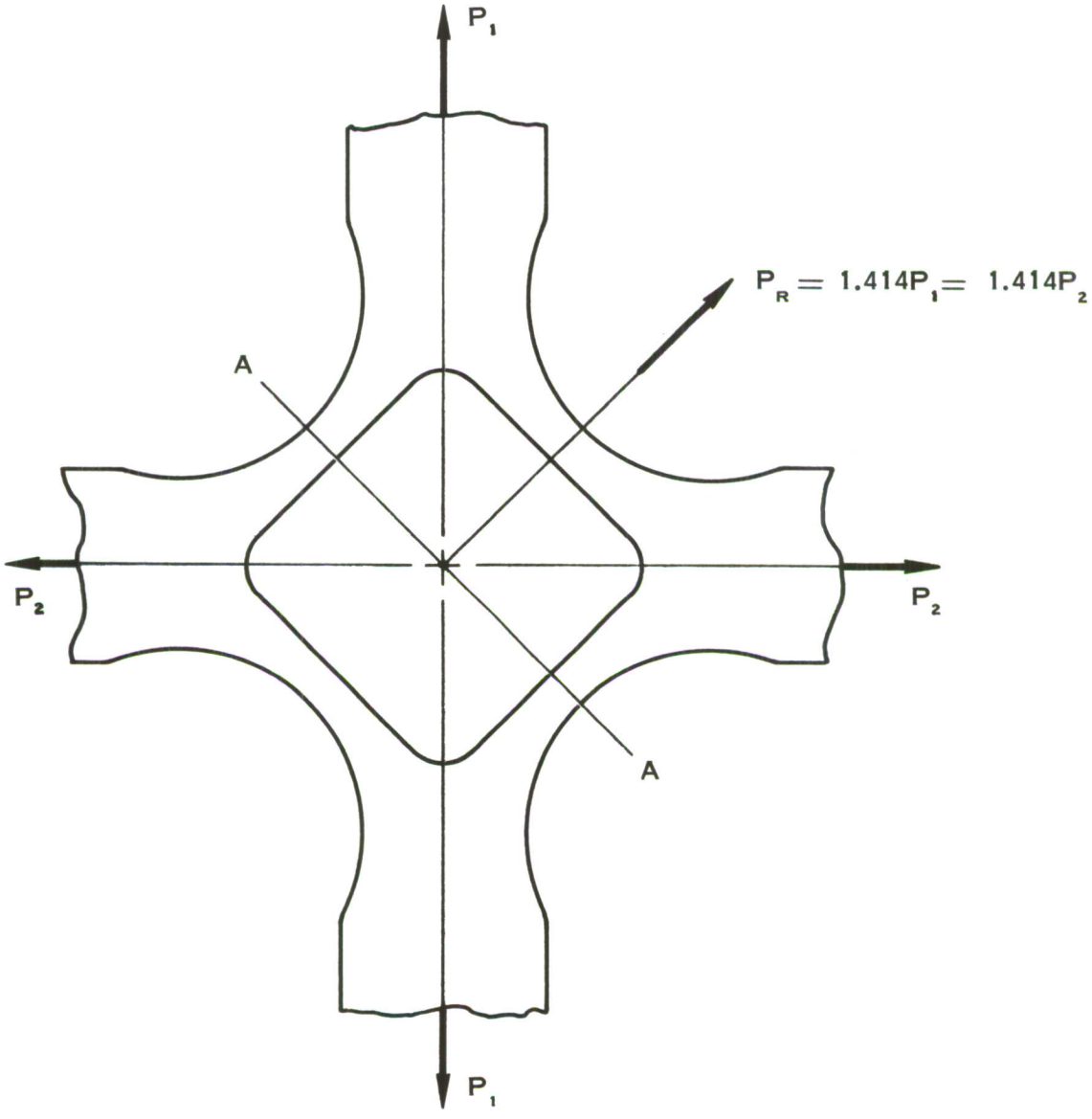

FIGURE 69 – BIAXIAL SPECIMEN UNDER 1:1 LOADING

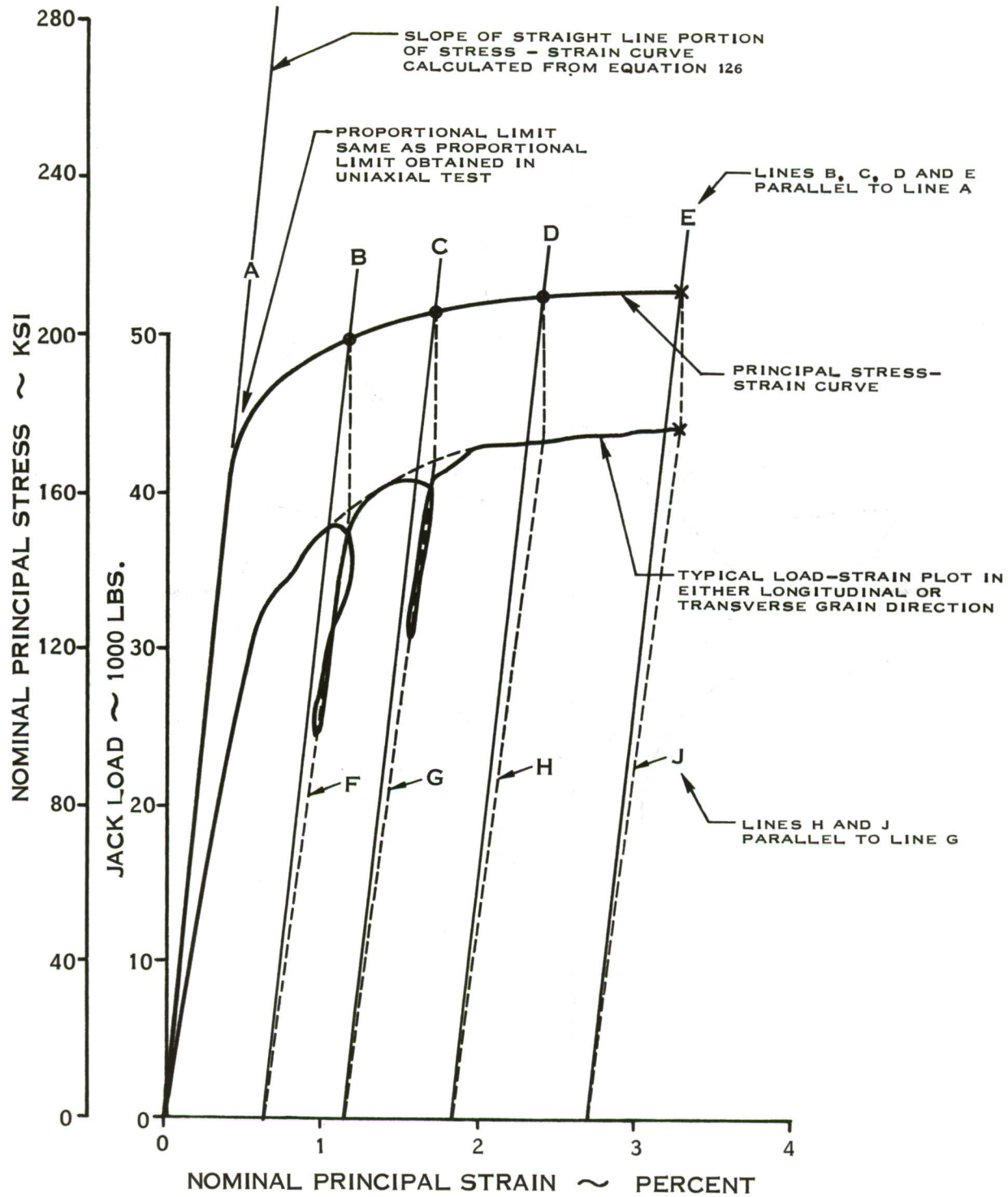

FIGURE 70 — ILLUSTRATION OF METHOD FOR CONVERTING LOAD—STRAIN CURVE TO STRESS — STRAIN CURVE FOR 1:1 LOADING

APPENDIX G

BIAXIAL STRESS-STRAIN CURVES

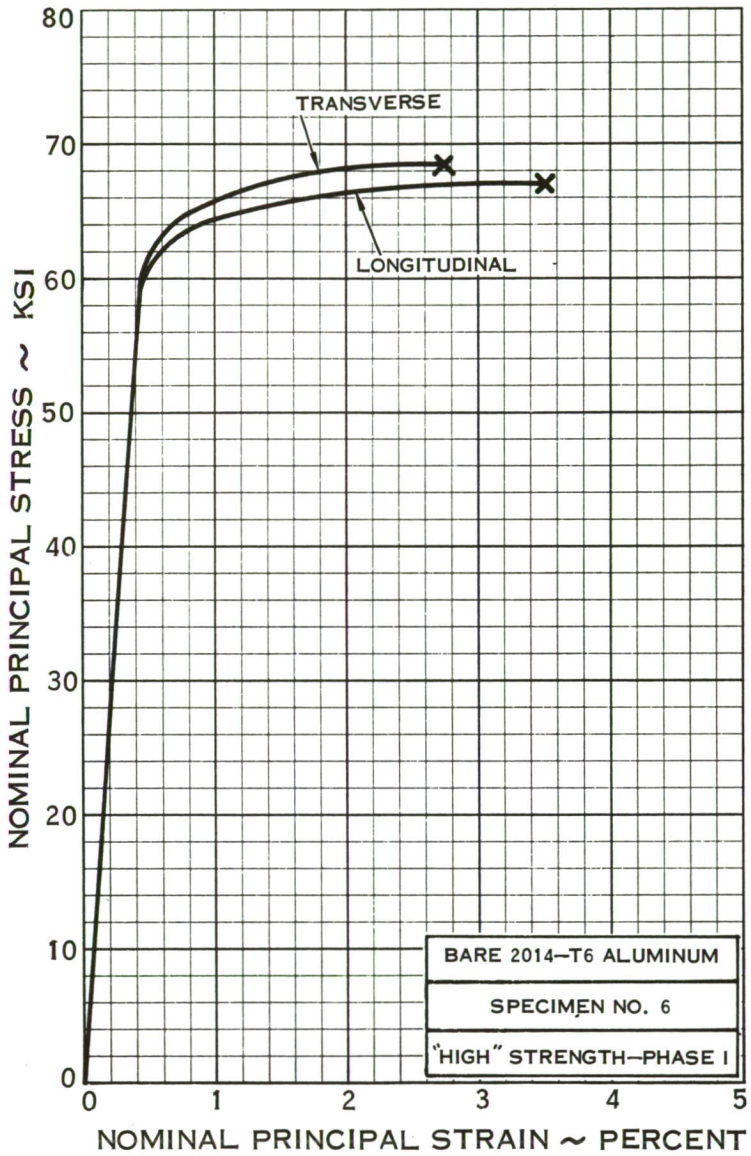

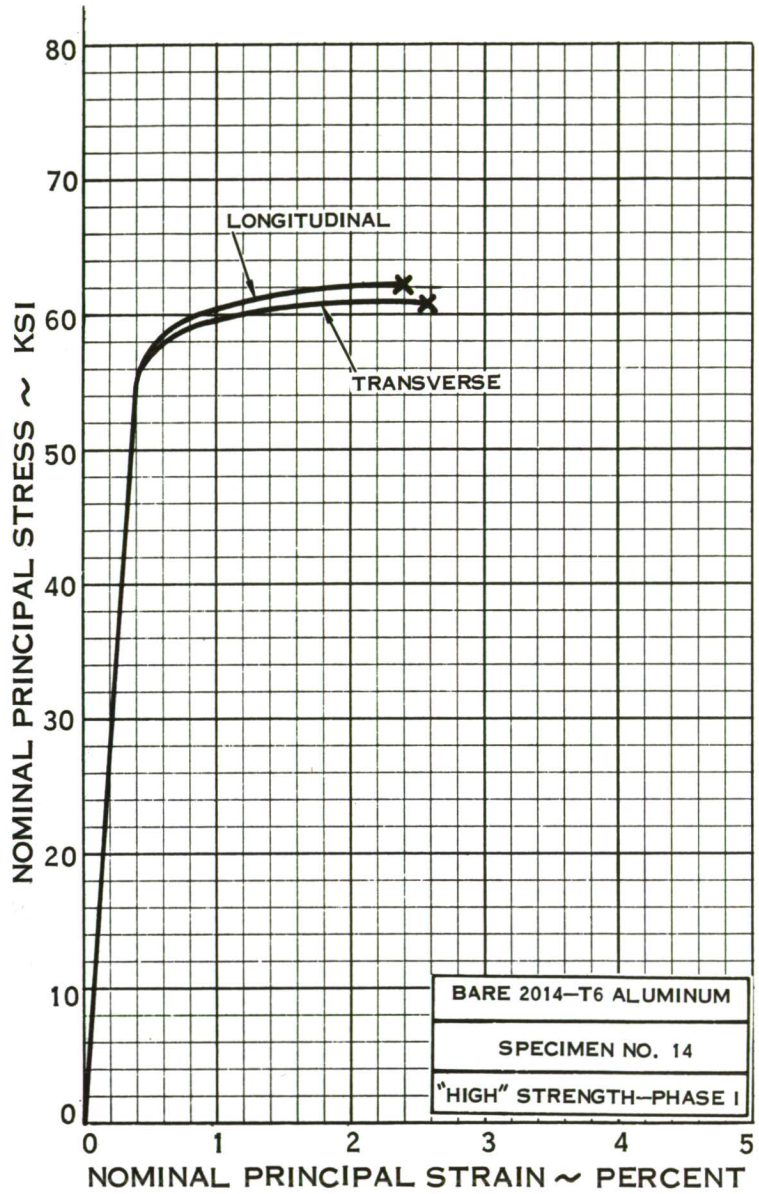

FIGURE 71 –1:1 STRESS RATIO BIAXIAL STRESS – STRAIN CURVES ,
BARE 2014–T6 ALUMINUM ALLOY

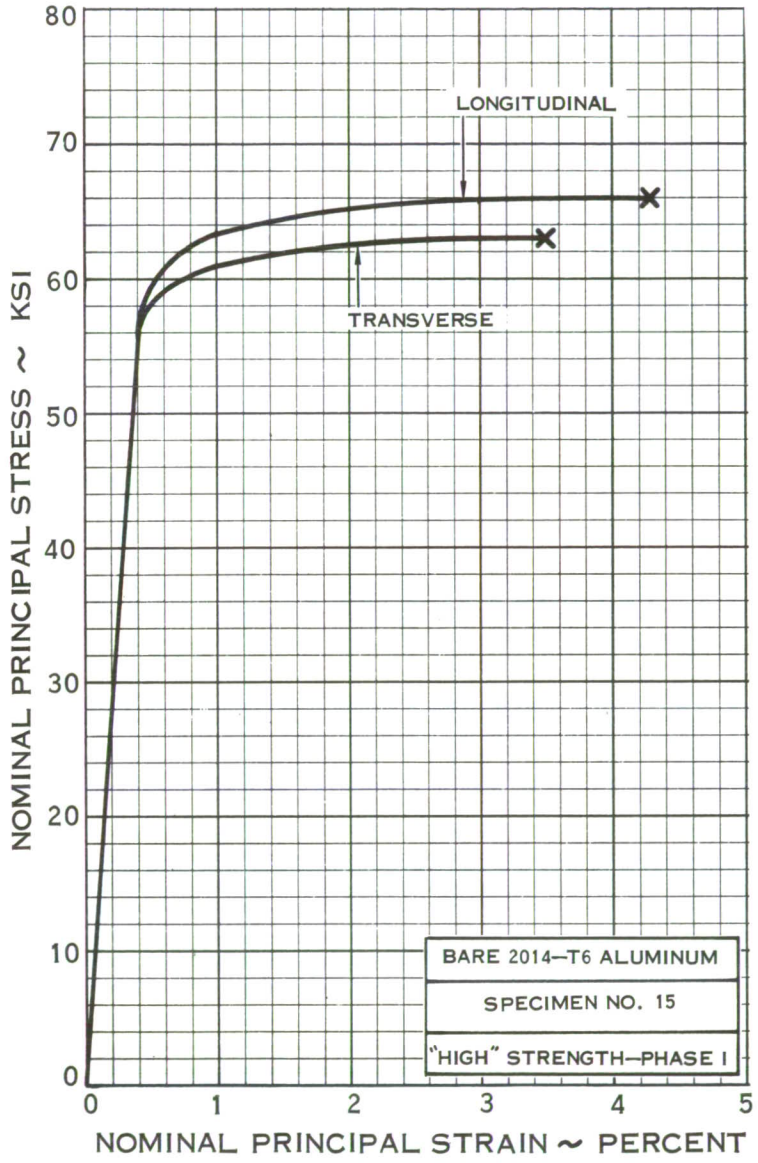

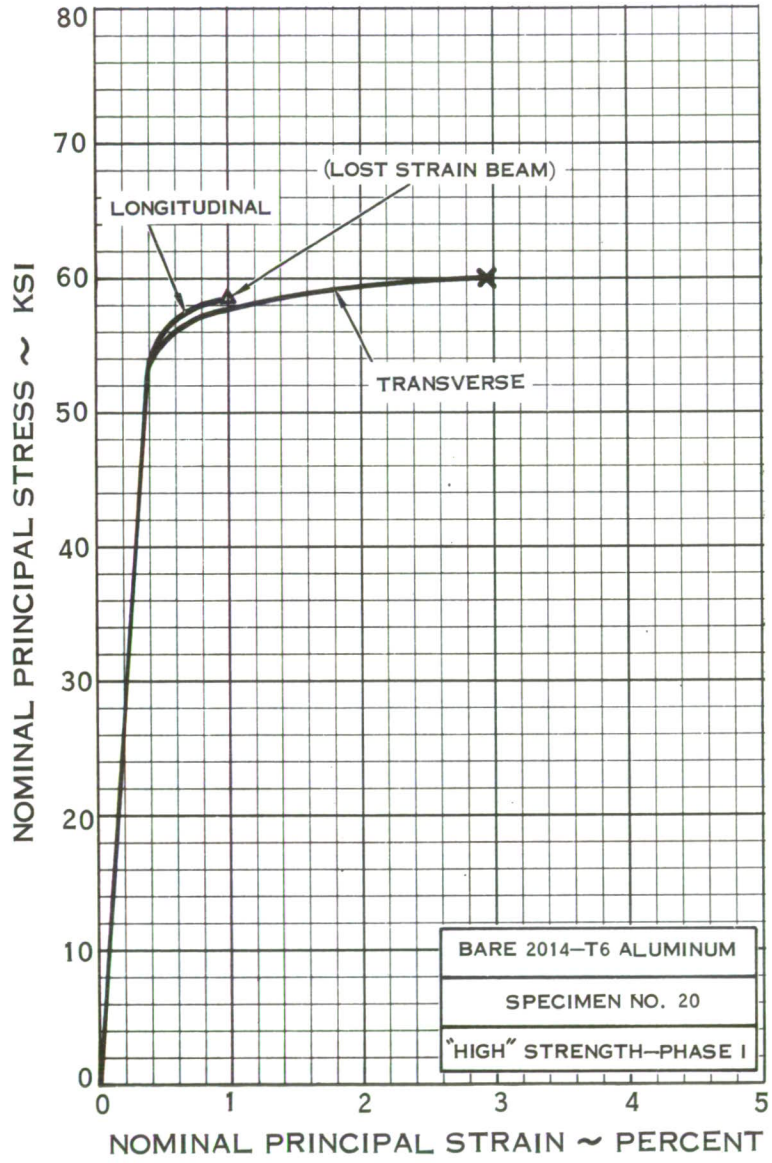

FIGURE 71 – 1:1 STRESS RATIO BIAXIAL STRESS – STRAIN CURVES,
BARE 2014–T6 ALUMINUM ALLOY (CONTINUED)

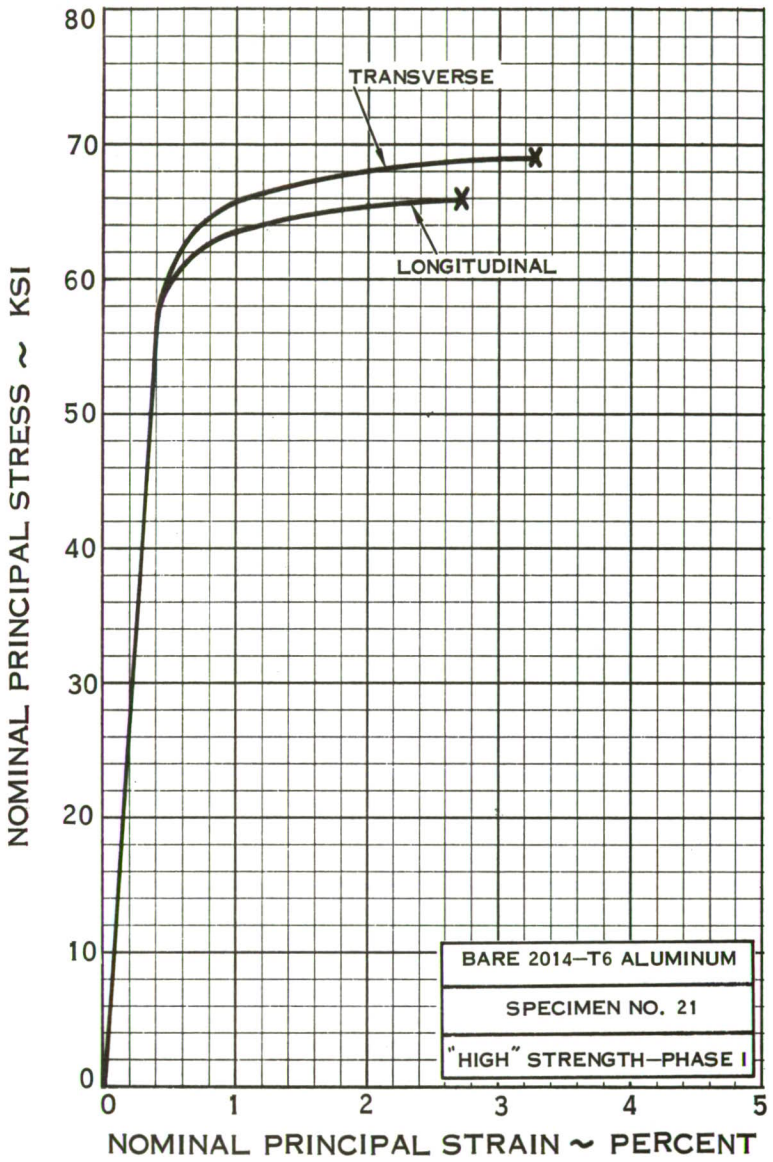

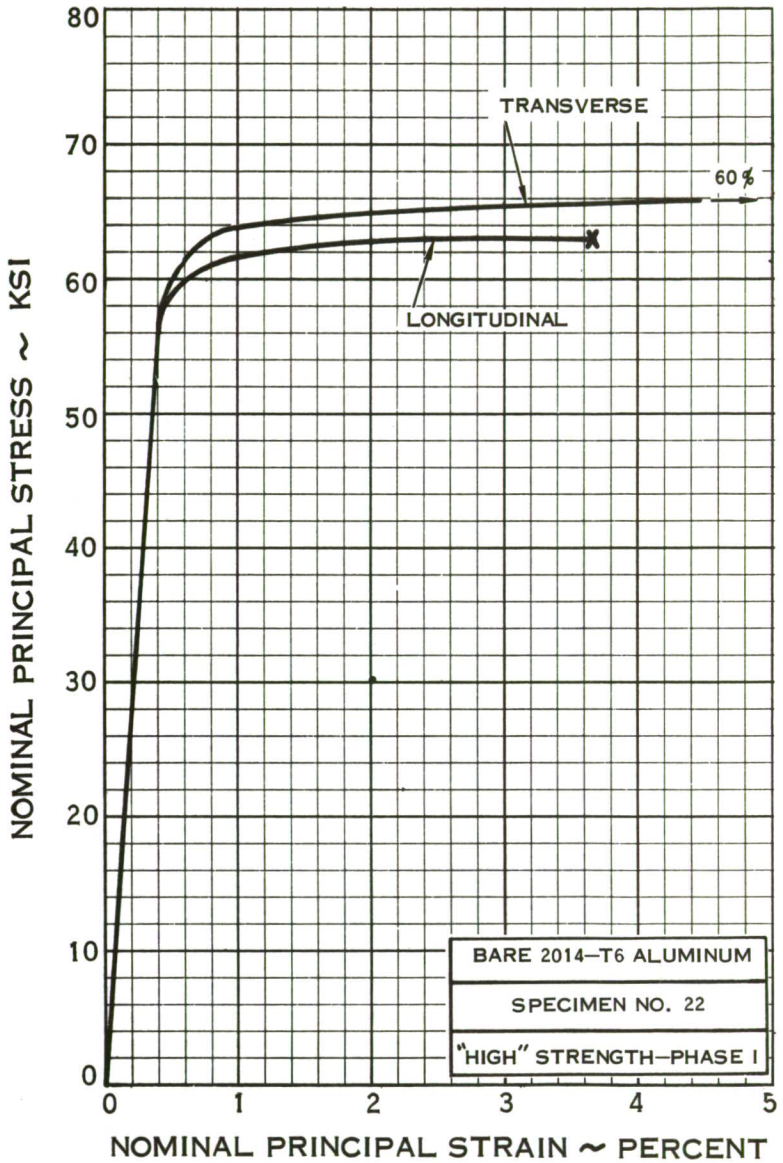

FIGURE 71 – 1:1 STRESS RATIO BIAXIAL STRESS – STRAIN CURVES,
BARE 2014–T6 ALUMINUM ALLOY (CONTINUED)

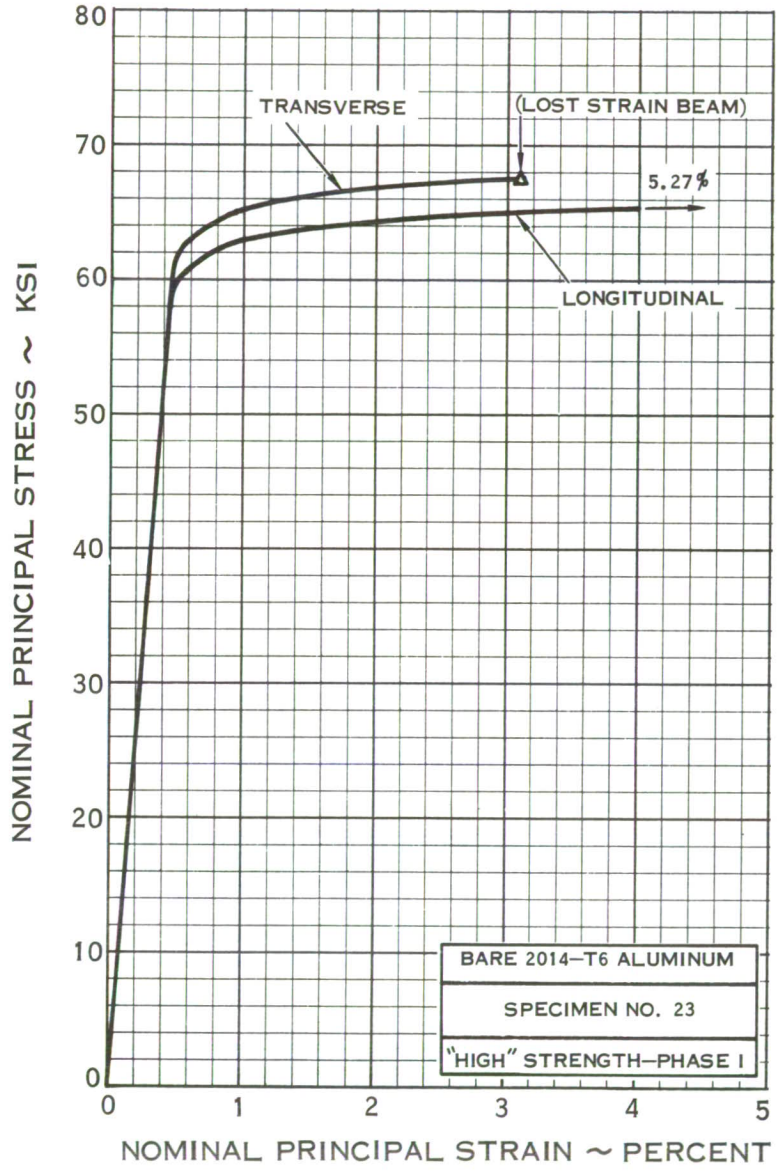

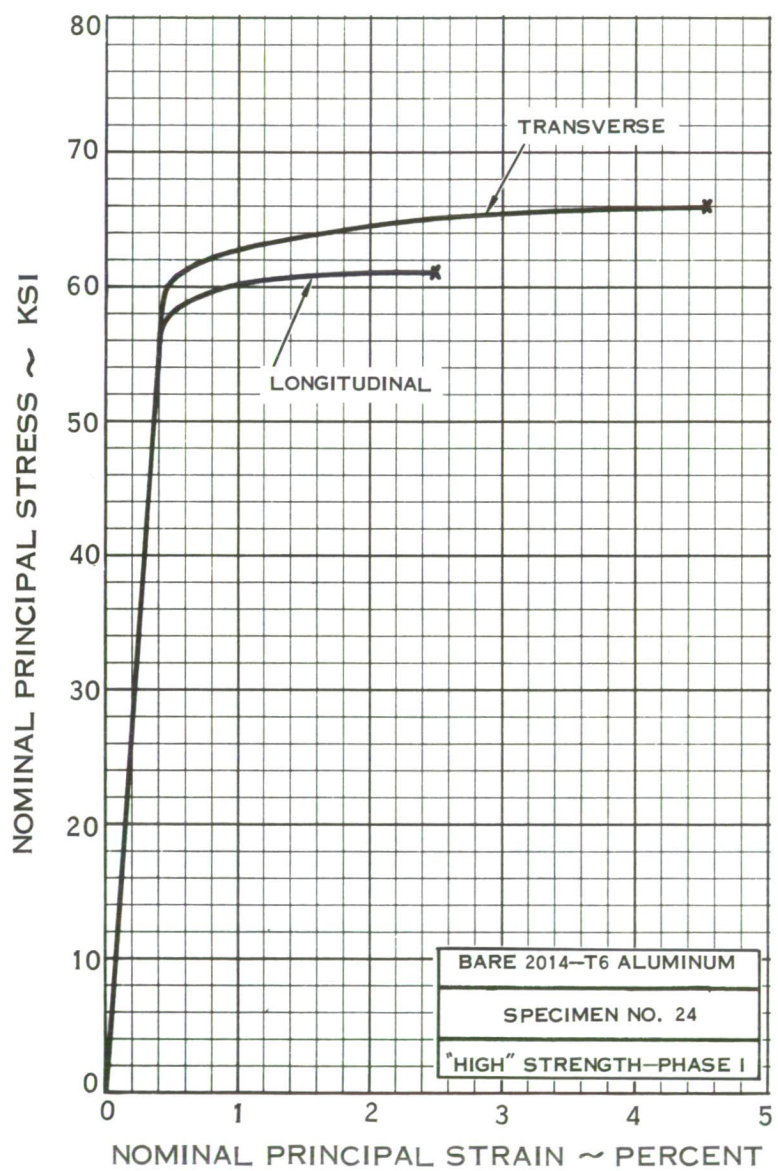

FIGURE 71 –1:1 STRESS RATIO BIAXIAL STRESS – STRAIN CURVES,
BARE 2014–T6 ALUMINUM ALLOY (CONTINUED)

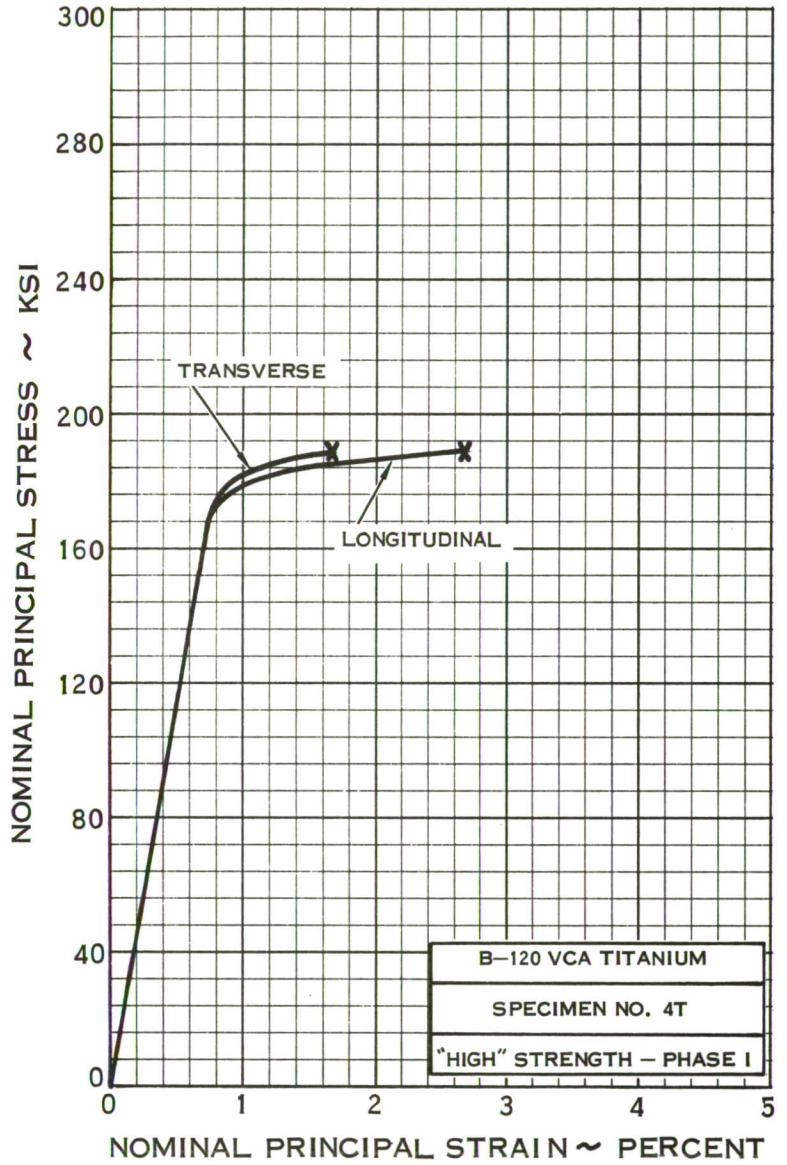

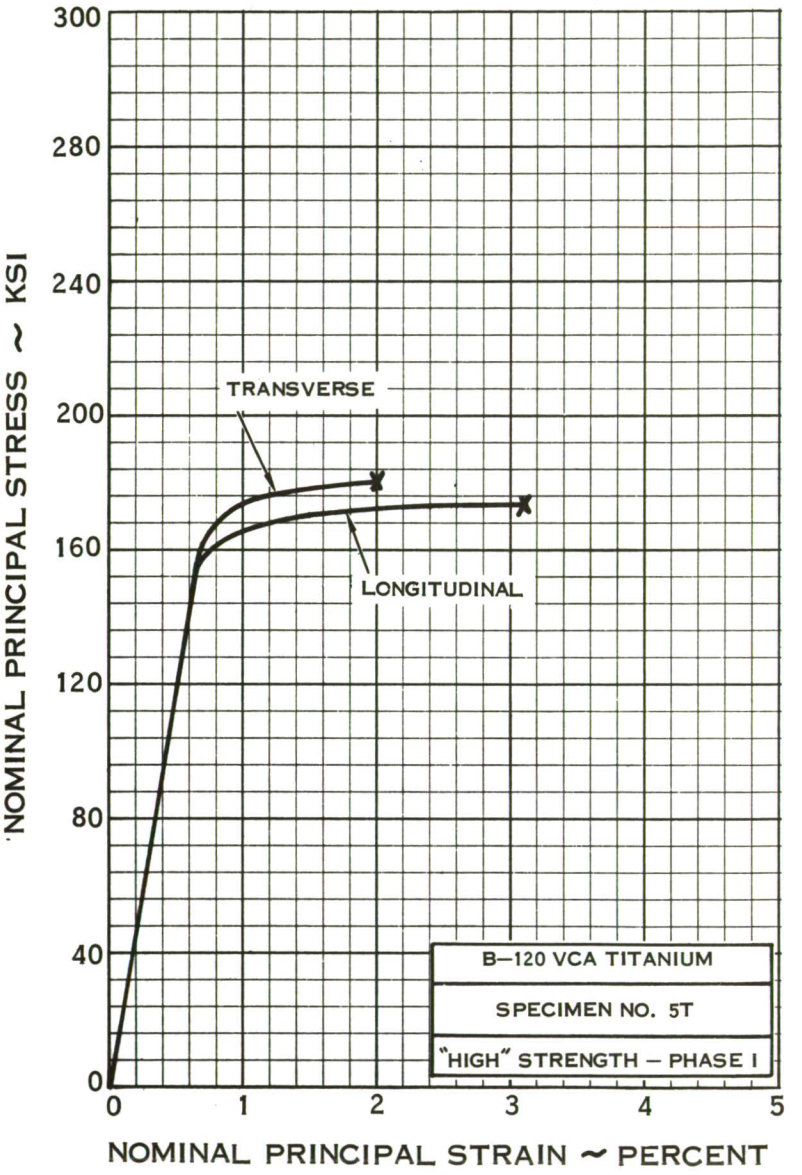

FIGURE 72 – 1:1 STRESS RATIO BIAXIAL STRESS – STRAIN CURVES, B–120VCA TITANIUM ALLOY

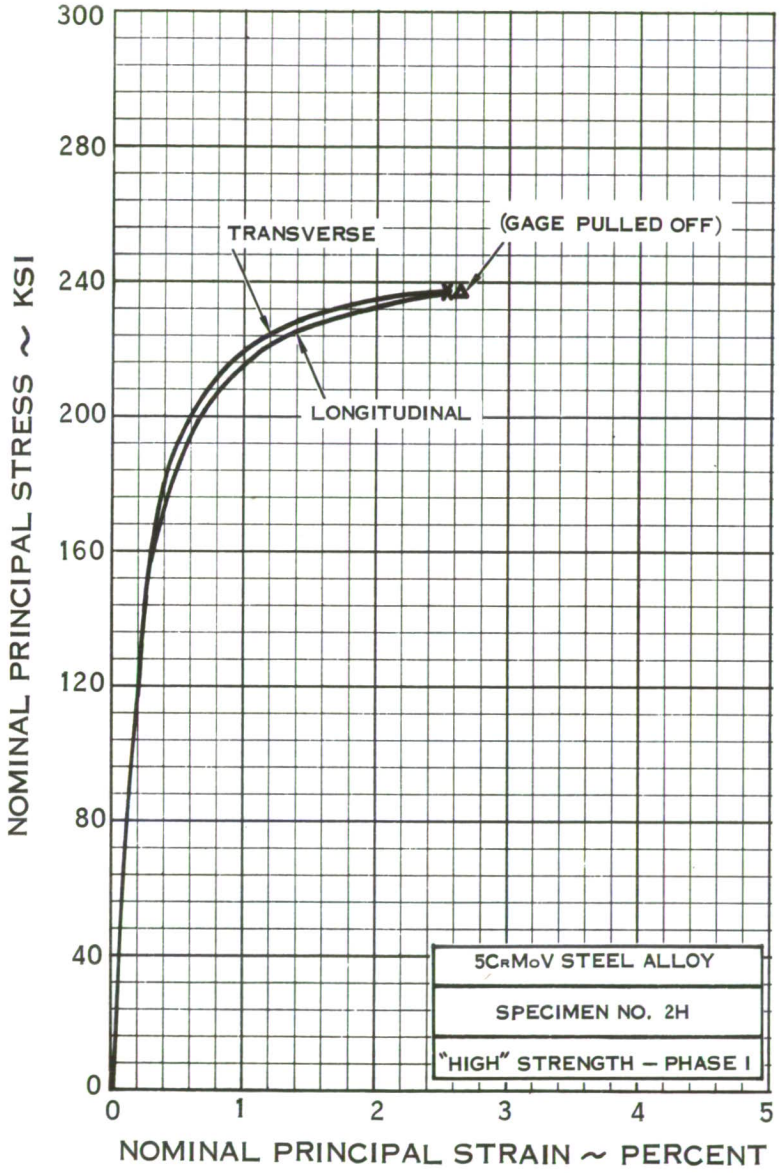

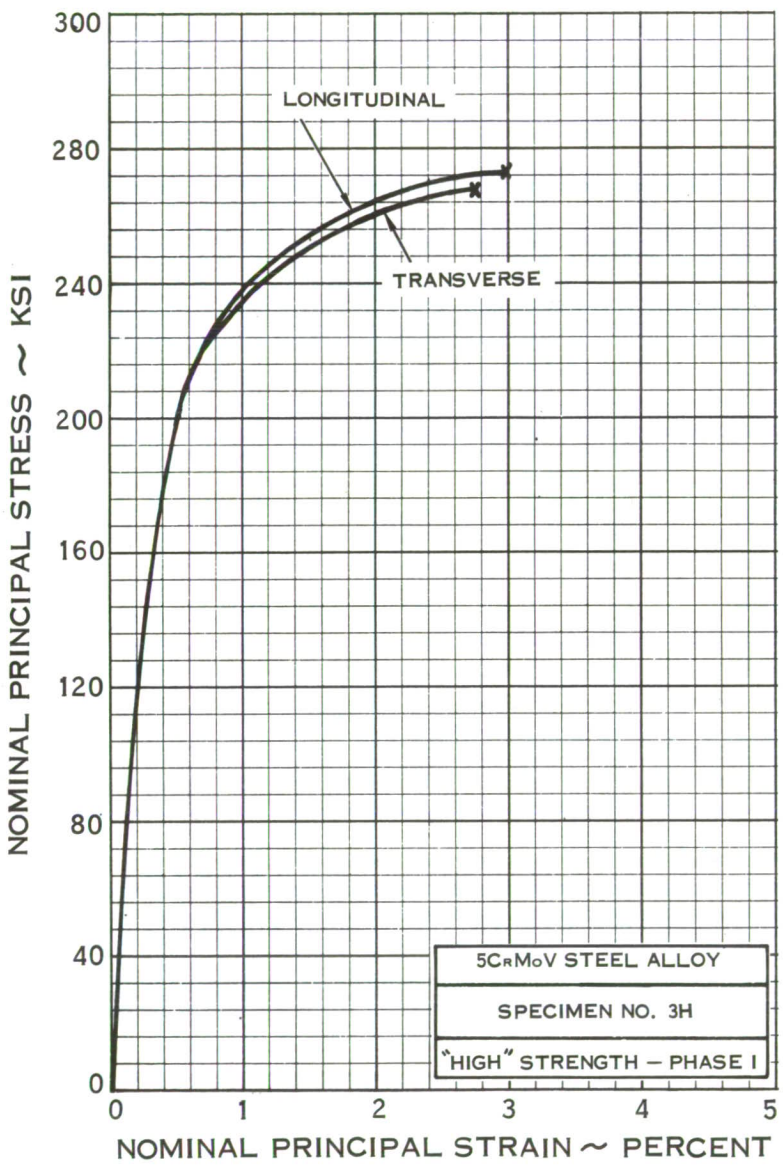

FIGURE 73 – 1:1 STRESS RATIO BIAXIAL STRESS – STRAIN CURVES, 5CrMoV STEEL ALLOY

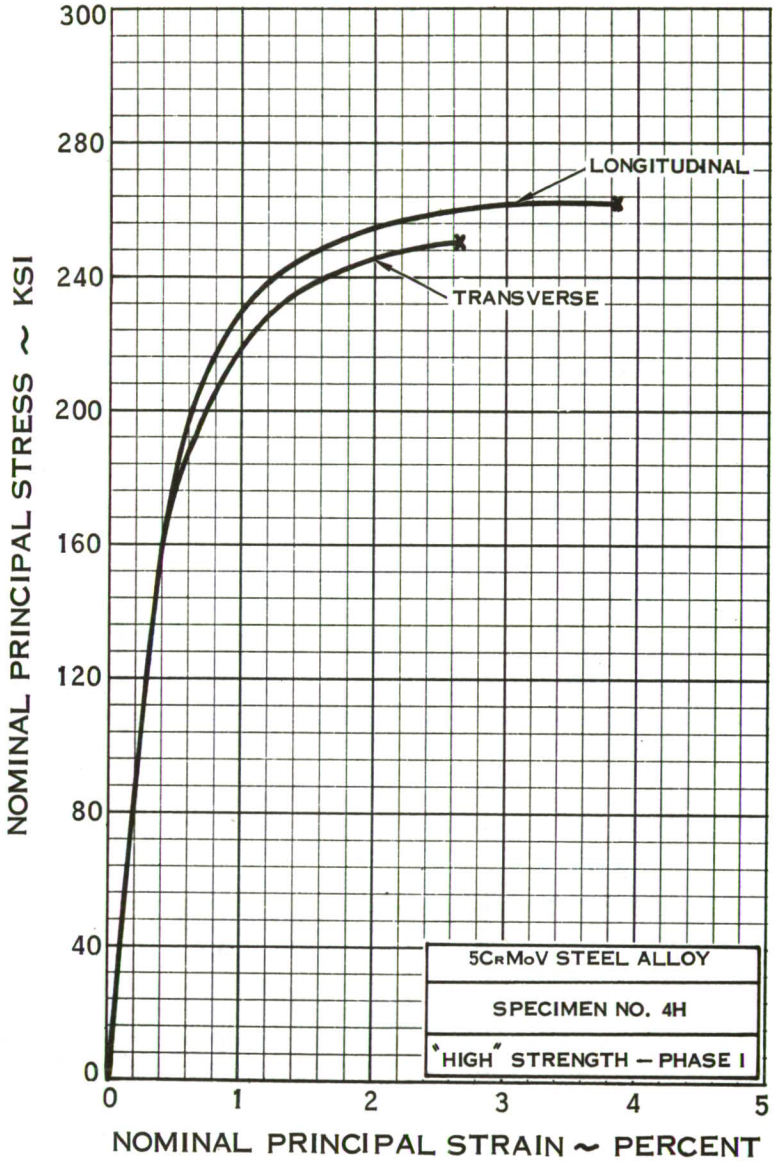

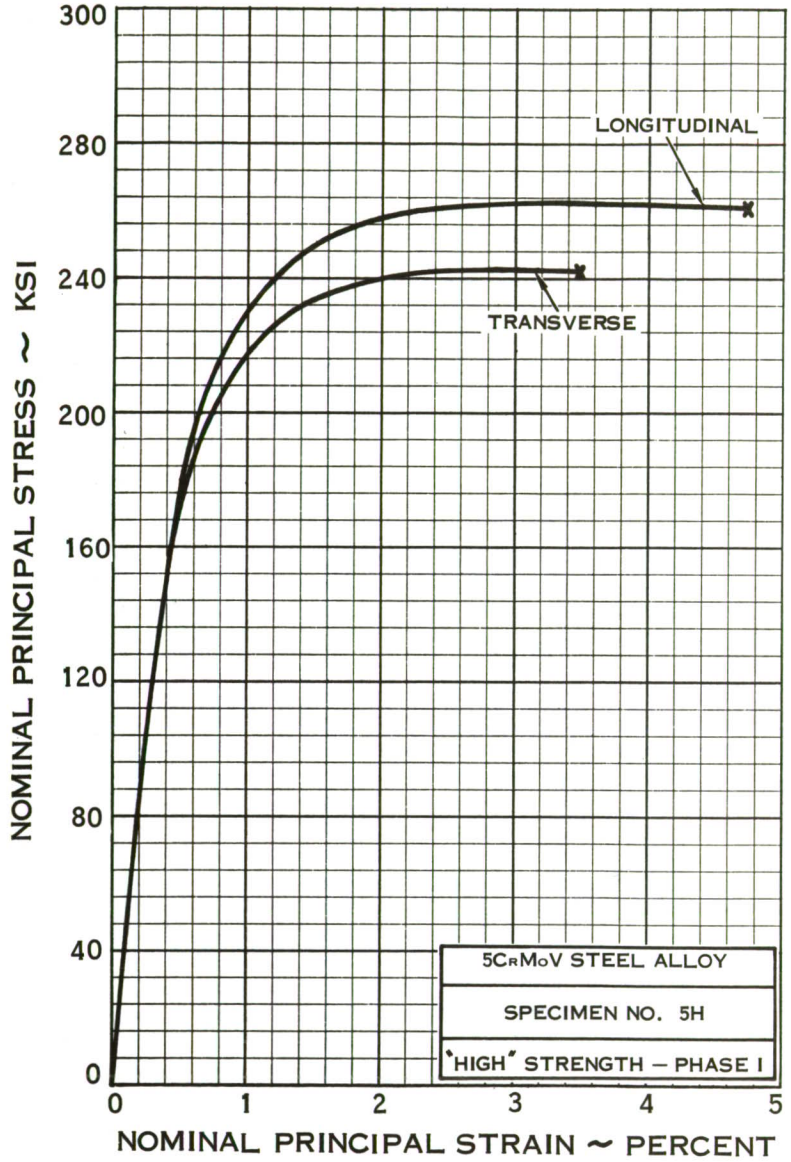

FIGURE 73 – 1:1 STRESS RATIO BIAXIAL STRESS – STRAIN CURVES,
5CrMoV STEEL ALLOY (CONTINUED)

FIGURE 73 – 1:1 STRESS RATIO BIAXIAL STRESS – STRAIN CURVES, 5CrMoV STEEL ALLOY (CONTINUED)

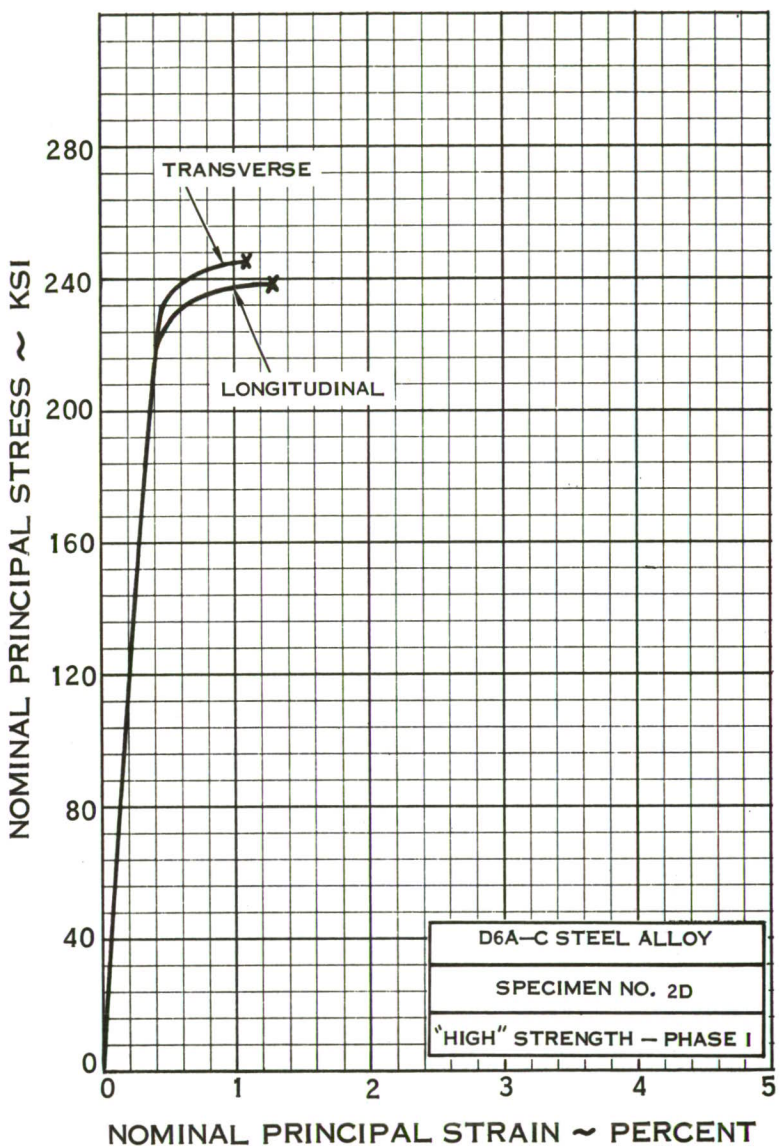

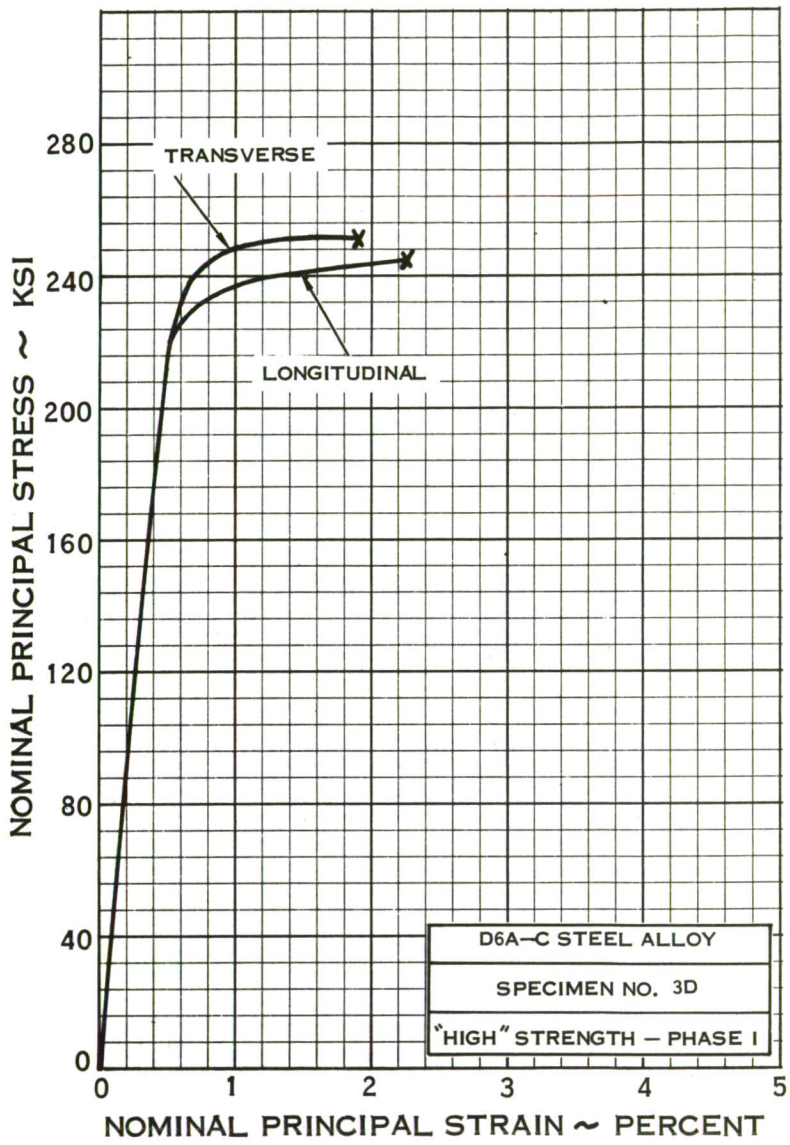

FIGURE 74 – 1:1 STRESS RATIO BIAXIAL STRESS – STRAIN CURVES,
D6A–C STEEL ALLOY

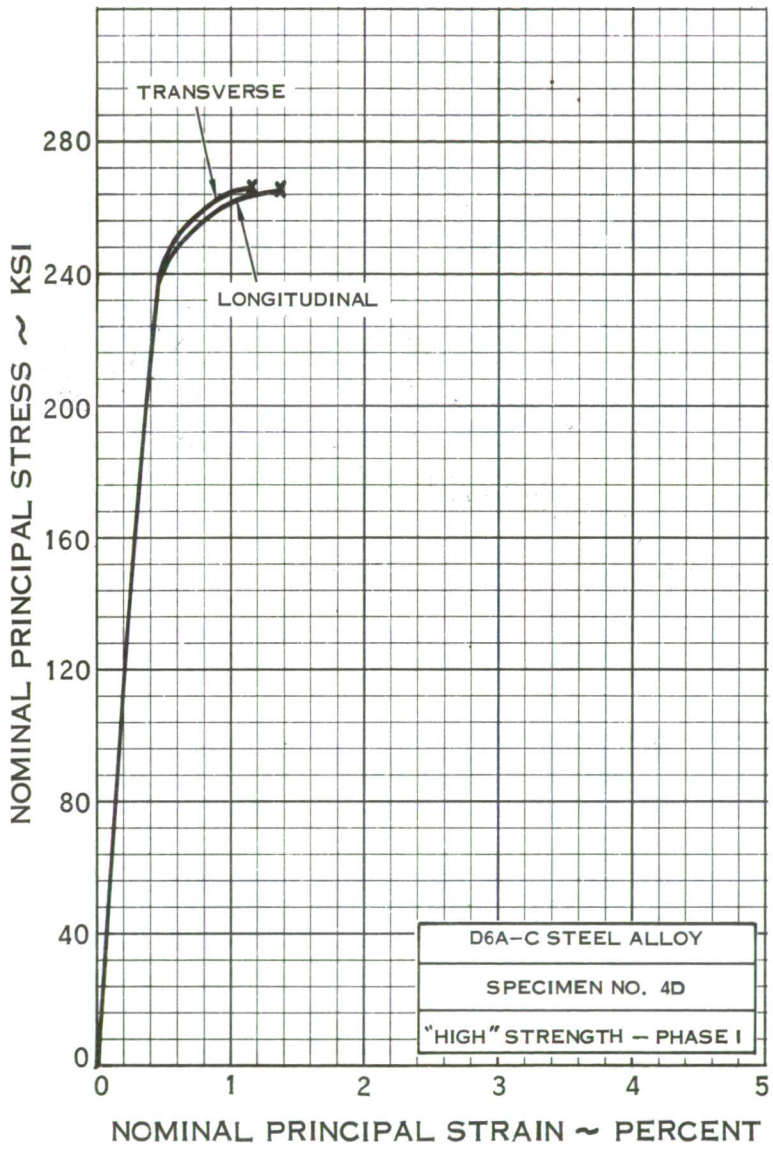

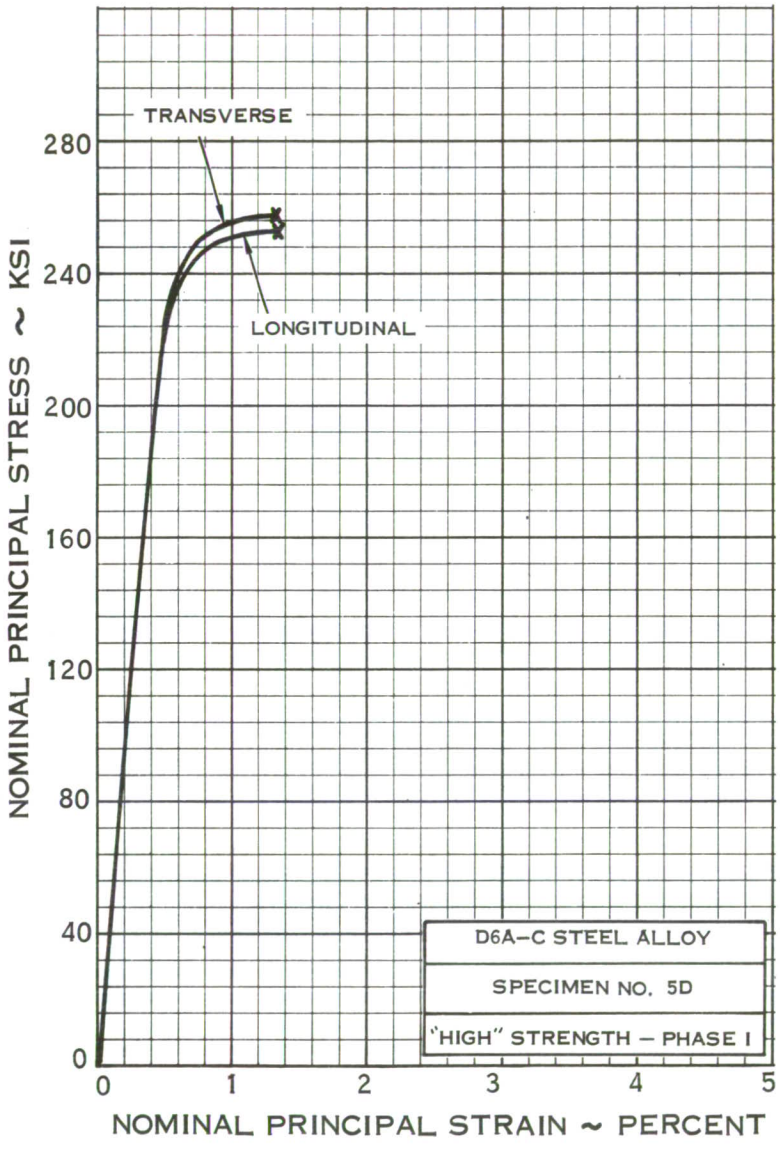

FIGURE 74 – 1:1 STRESS RATIO BIAXIAL STRESS – STRAIN CURVES,
D6A–C STEEL ALLOY (CONTINUED)

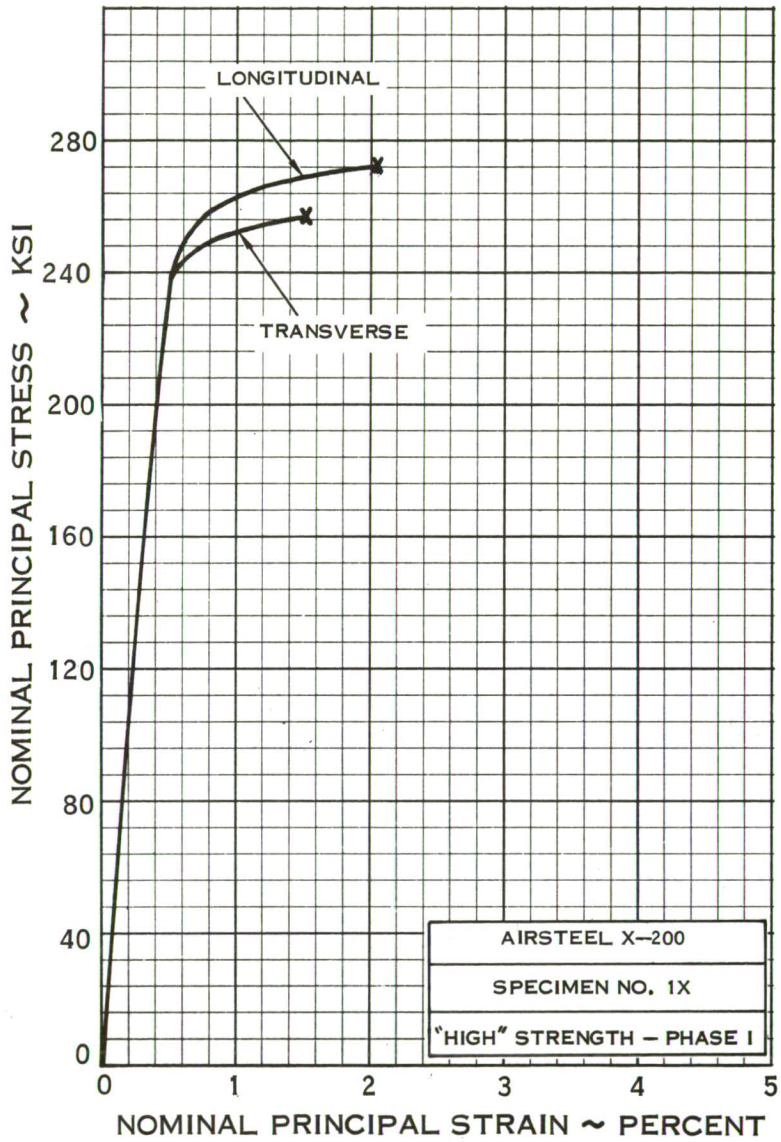

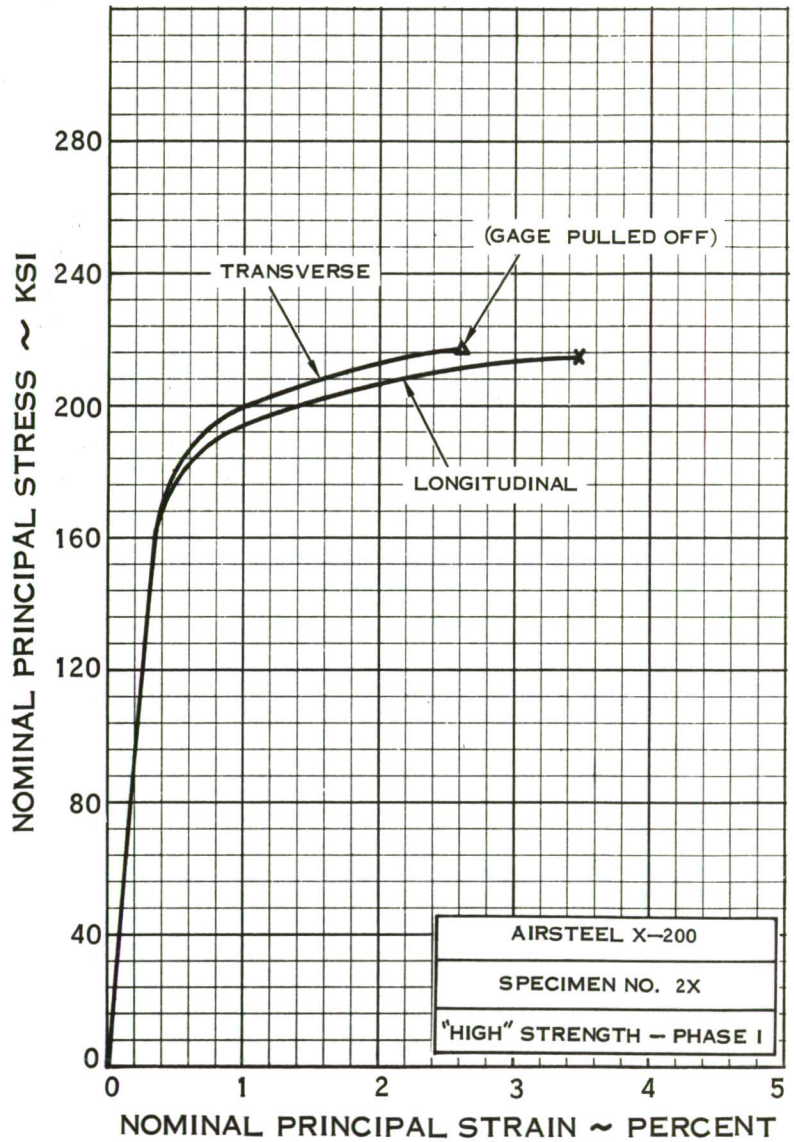

FIGURE 75 — 1:1 STRESS RATIO BIAXIAL STRESS — STRAIN CURVES, AIRSTEEL X-200

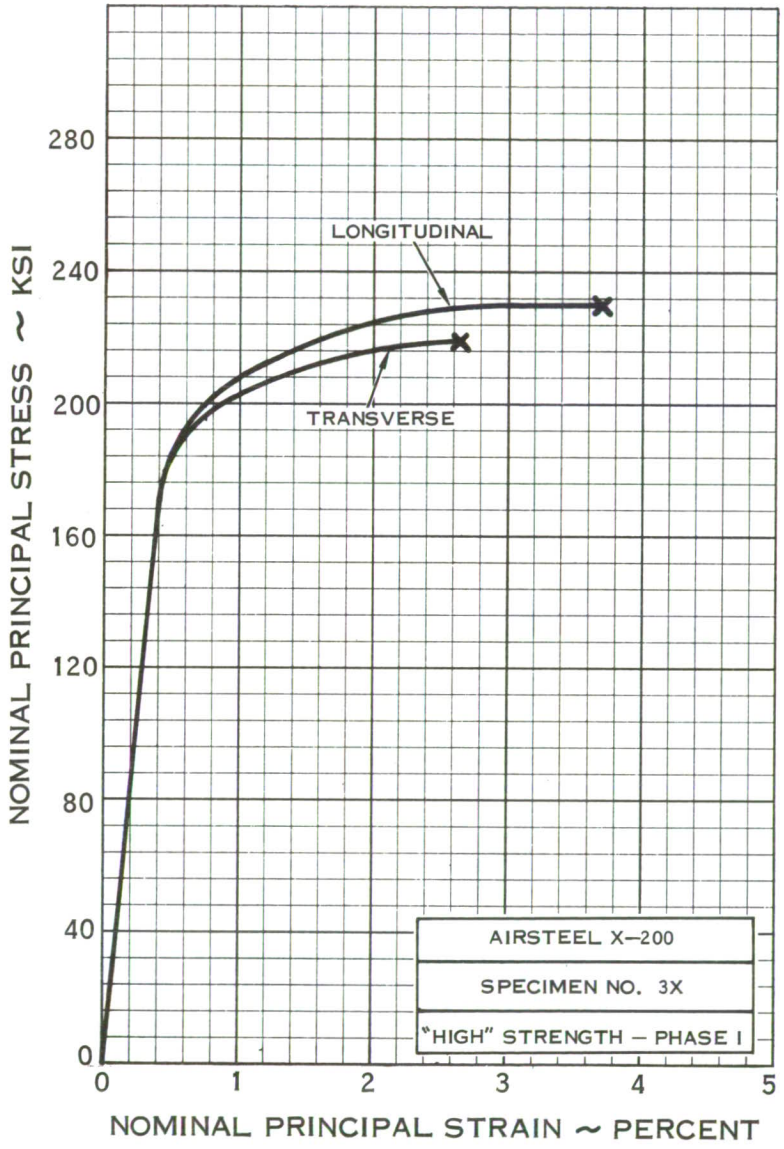

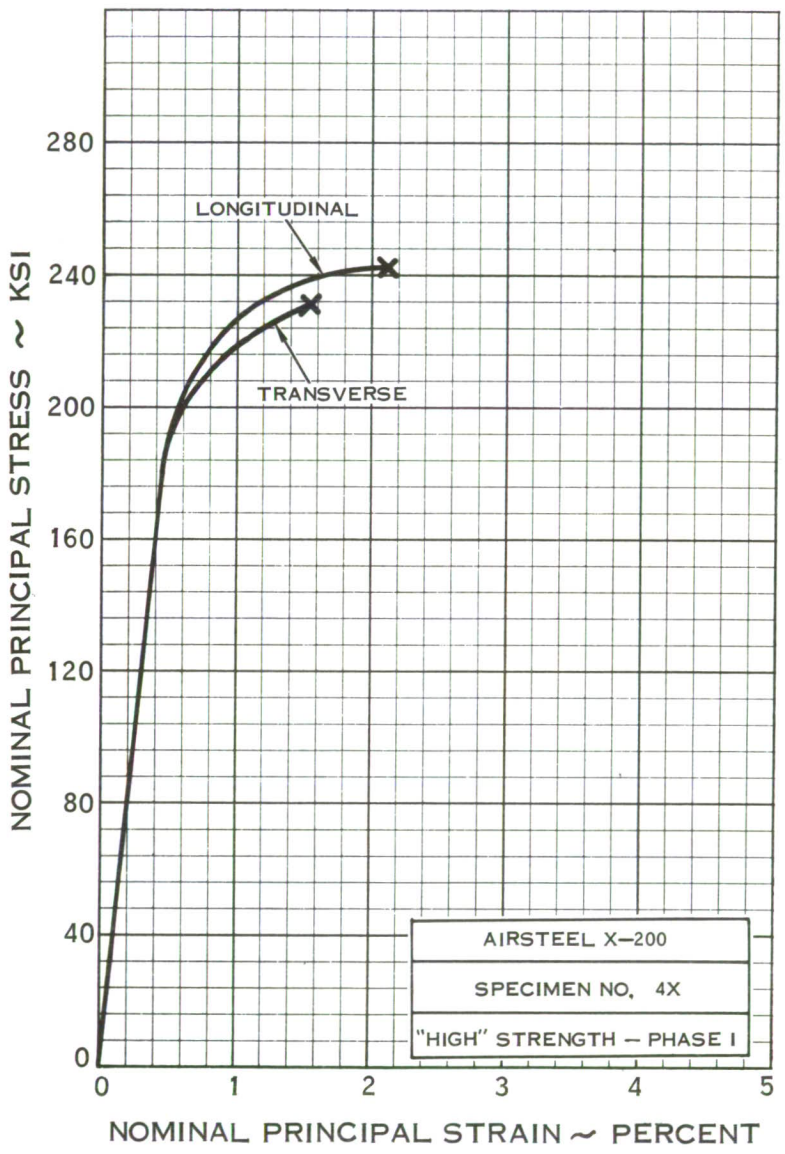

FIGURE 75 – 1:1 STRESS RATIO BIAXIAL STRESS – STRAIN CURVES, AIRSTEEL X–200 (CONTINUED)

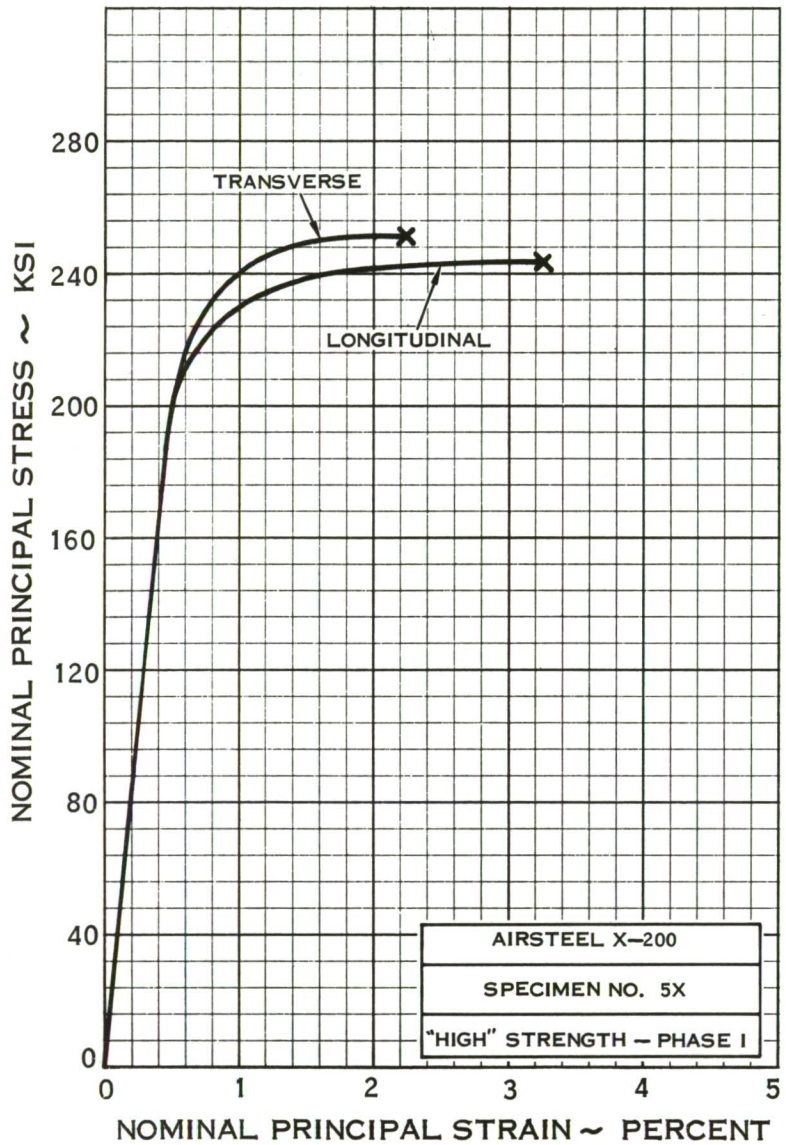

FIGURE 75 – 1:1 STRESS RATIO BIAXIAL STRESS – STRAIN CURVES, AIRSTEEL X-200 (CONTINUED)

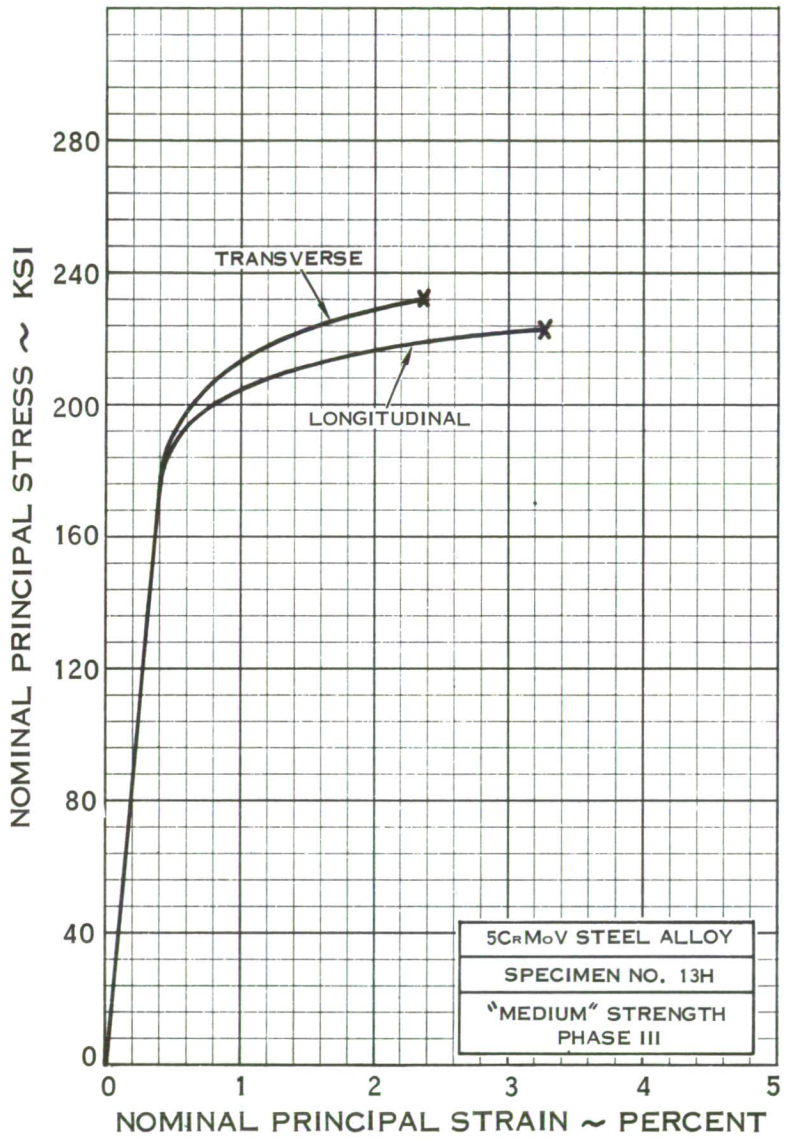

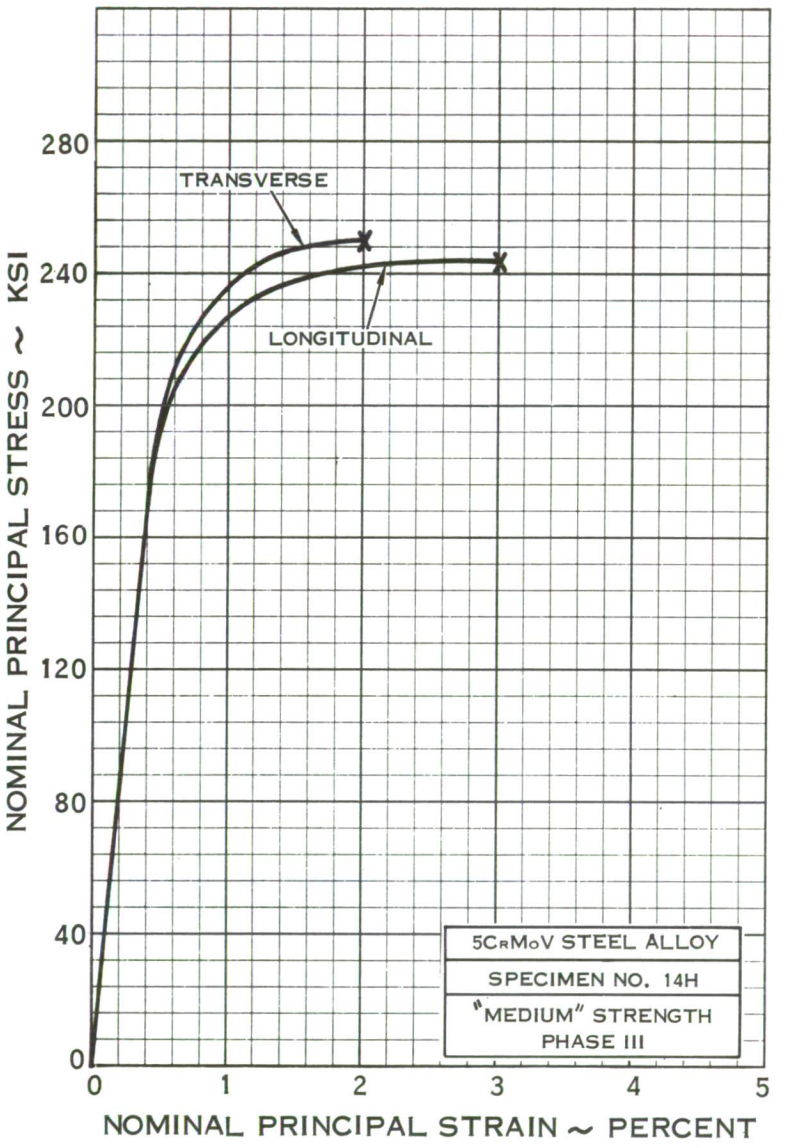

FIGURE 76 – 1:1 STRESS RATIO BIAXIAL STRESS – STRAIN CURVES,
5CrMoV STEEL ALLOY

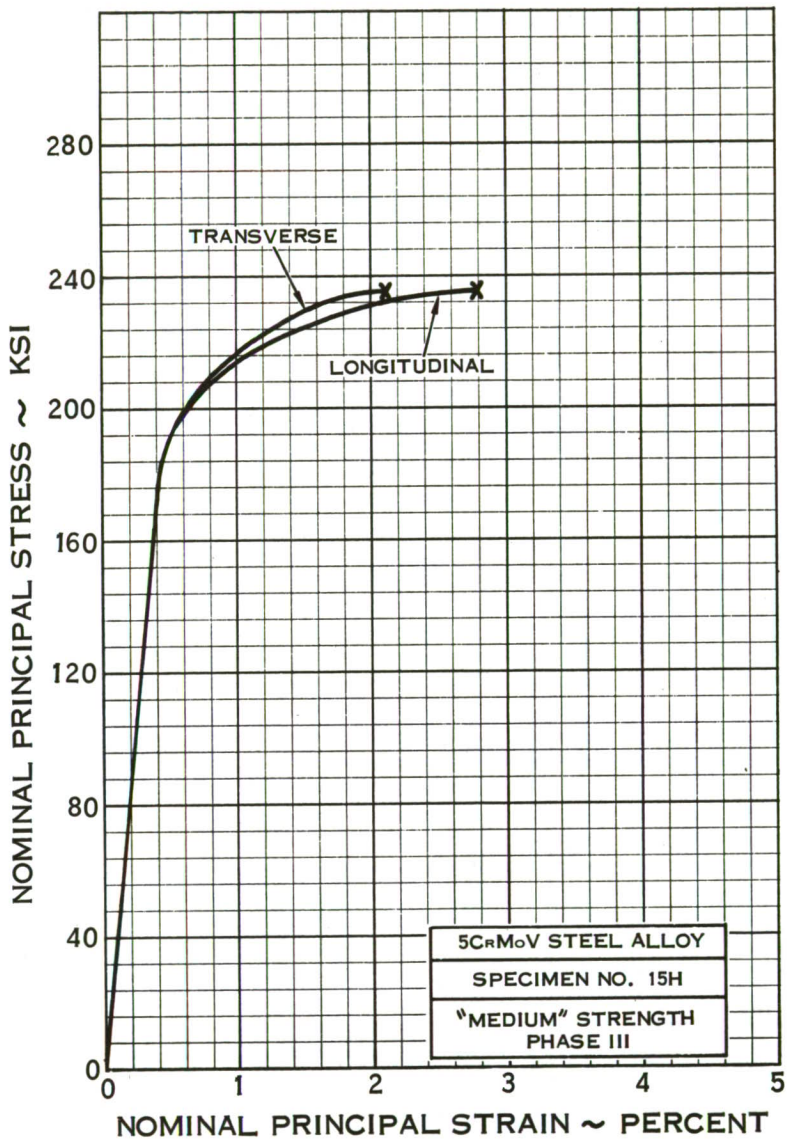

FIGURE 76 — 1:1 STRESS RATIO BIAXIAL STRESS — STRAIN CURVES, 5CrMoV STEEL ALLOY (CONTINUED)

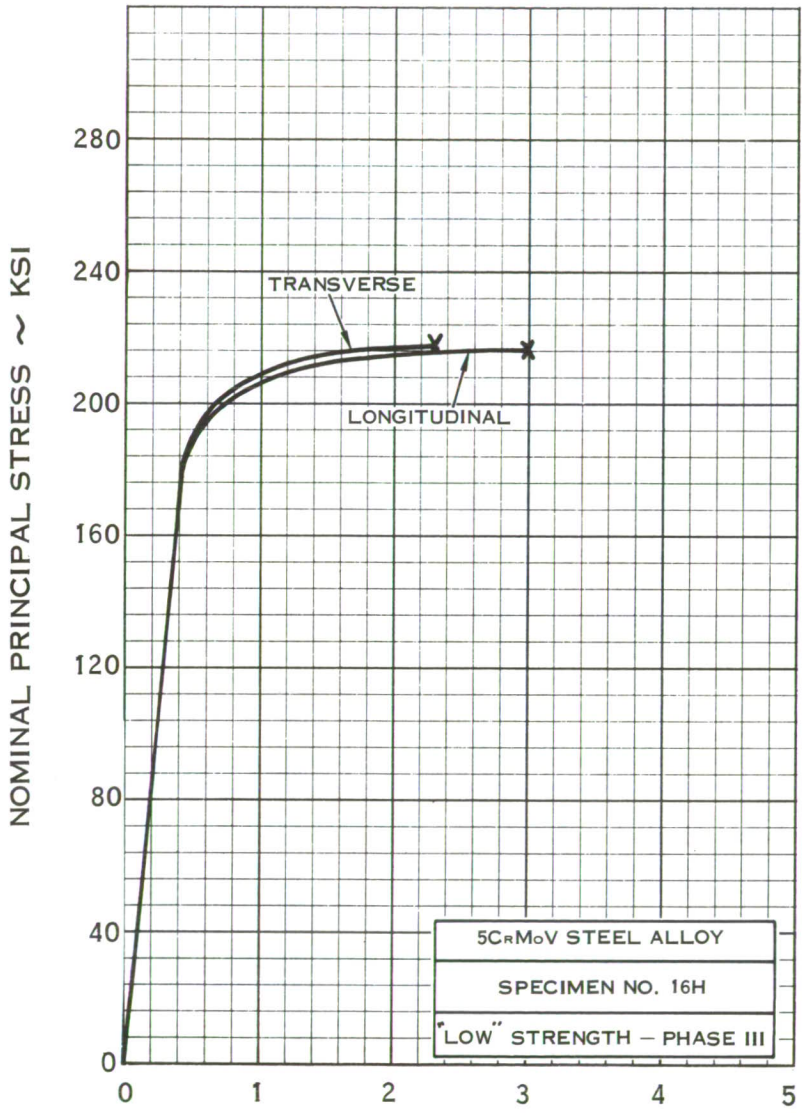

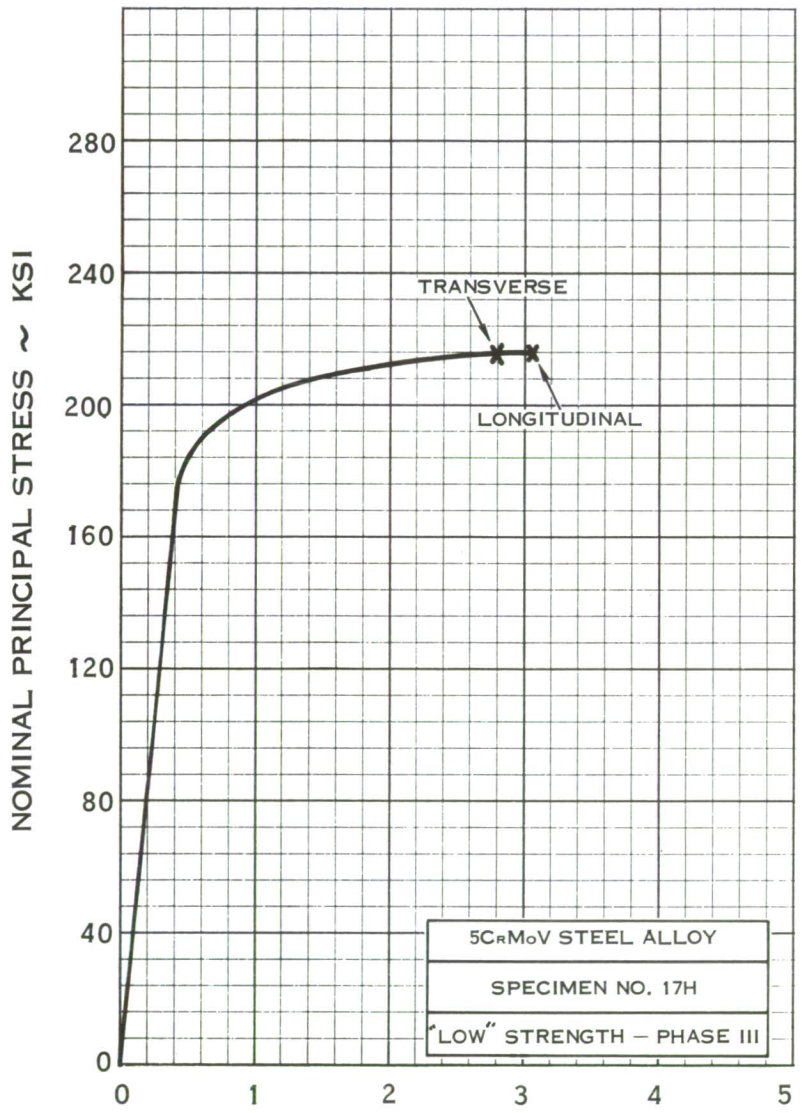

FIGURE 77 – 1:1 STRESS RATIO BIAXIAL STRESS – STRAIN CURVES, 5CrMoV STEEL ALLOY

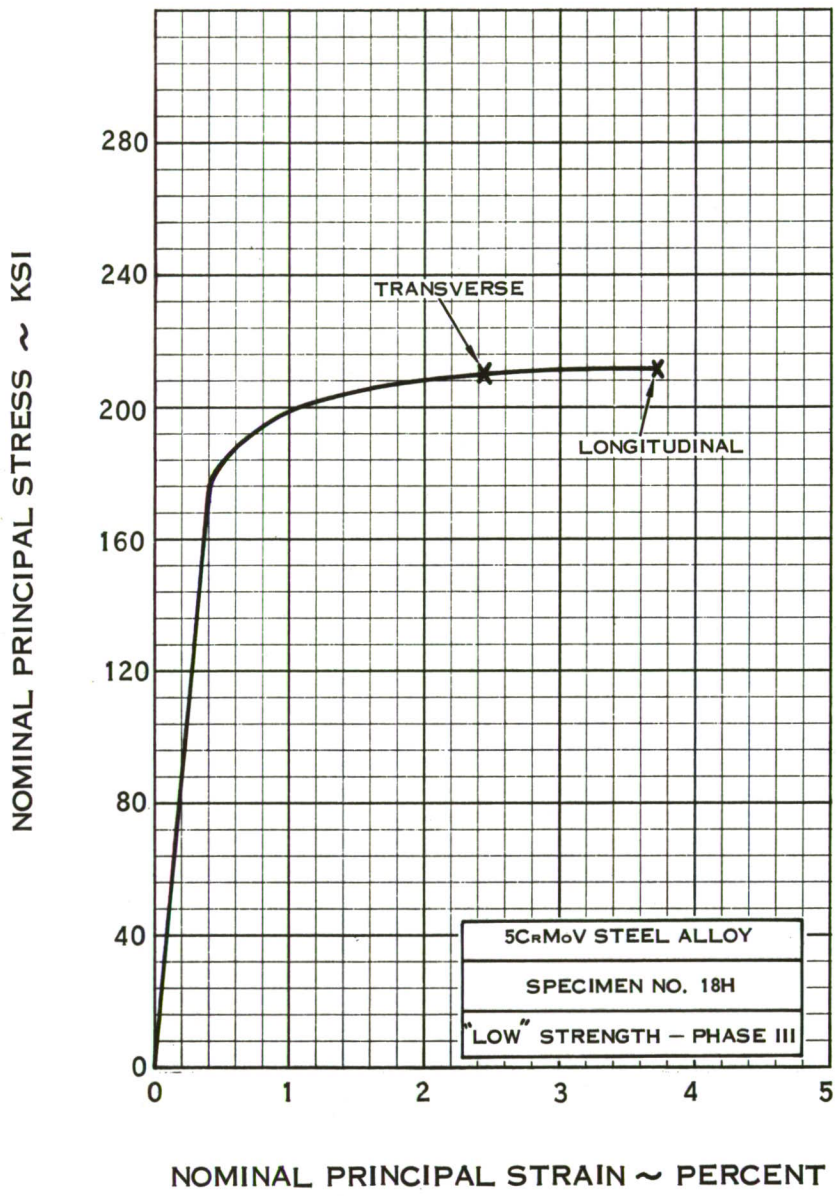

FIGURE 77 – 1:1 STRESS RATIO BIAXIAL STRESS – STRAIN CURVES, 5CrMoV STEEL ALLOY (CONTINUED)

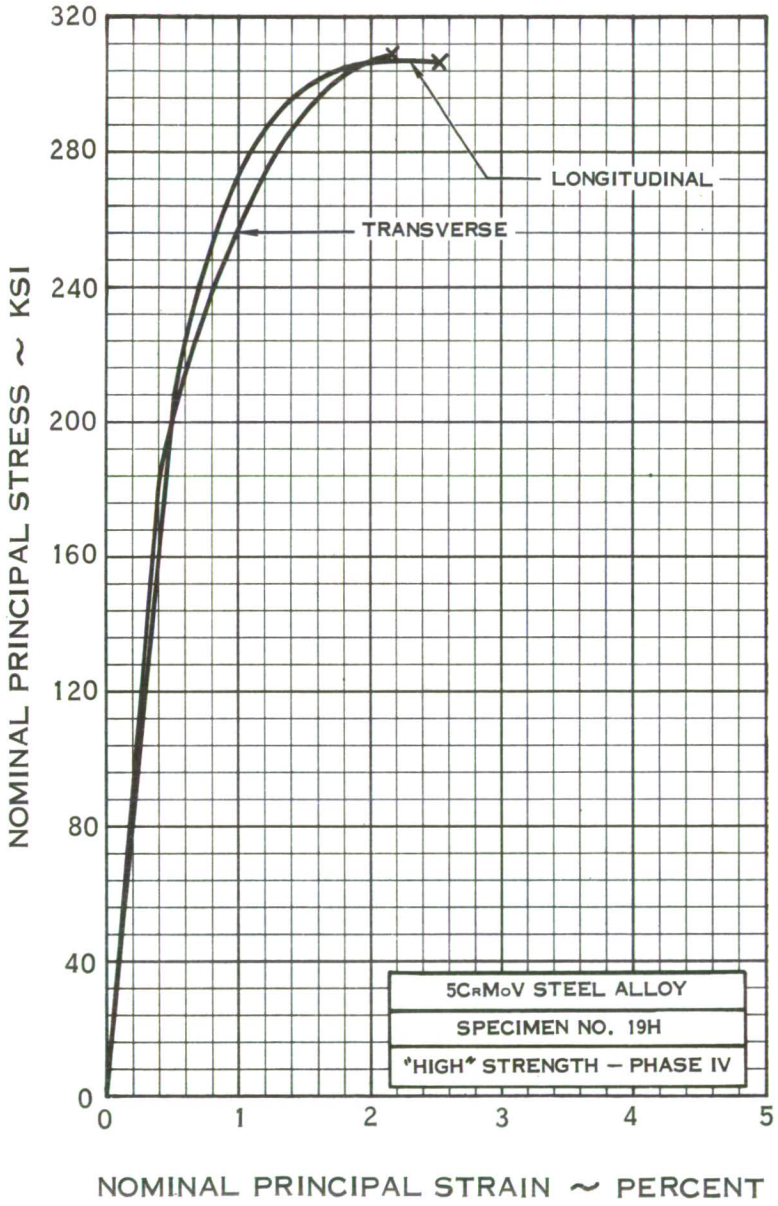

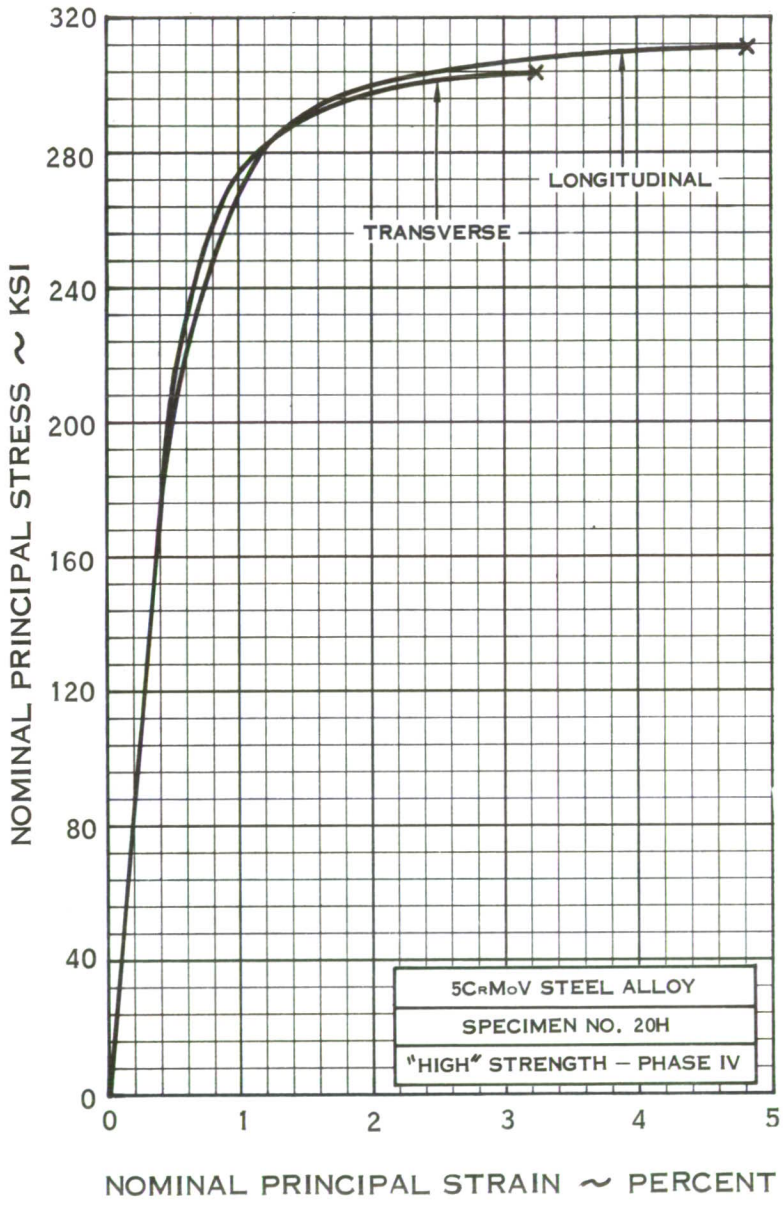

FIGURE 78 – 1:1 STRESS RATIO BIAXIAL STRESS – STRAIN CURVES, WELDED SPECIMENS 5CrMoV STEEL ALLOY

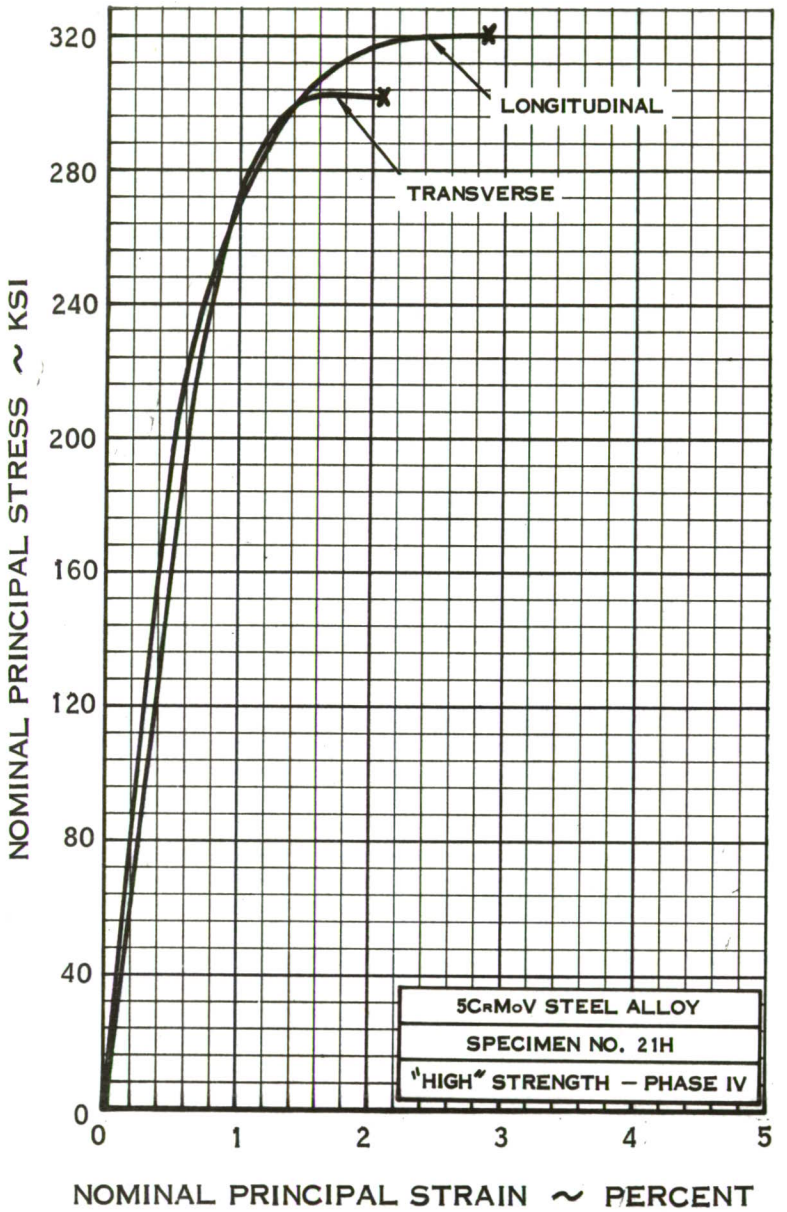

FIGURE 78 – 1:1 STRESS RATIO BIAXIAL STRESS – STRAIN CURVES, WELDED SPECIMEN 5CrMoV STEEL ALLOY (CONTINUED)

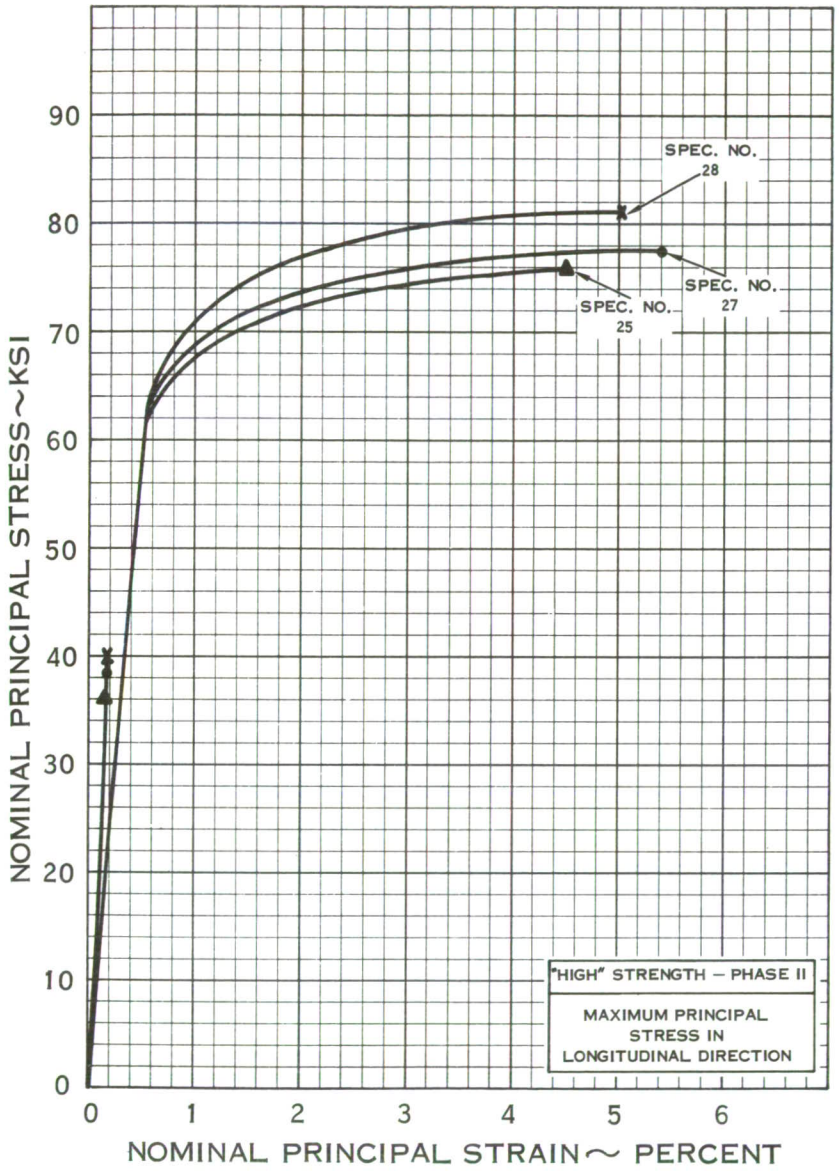

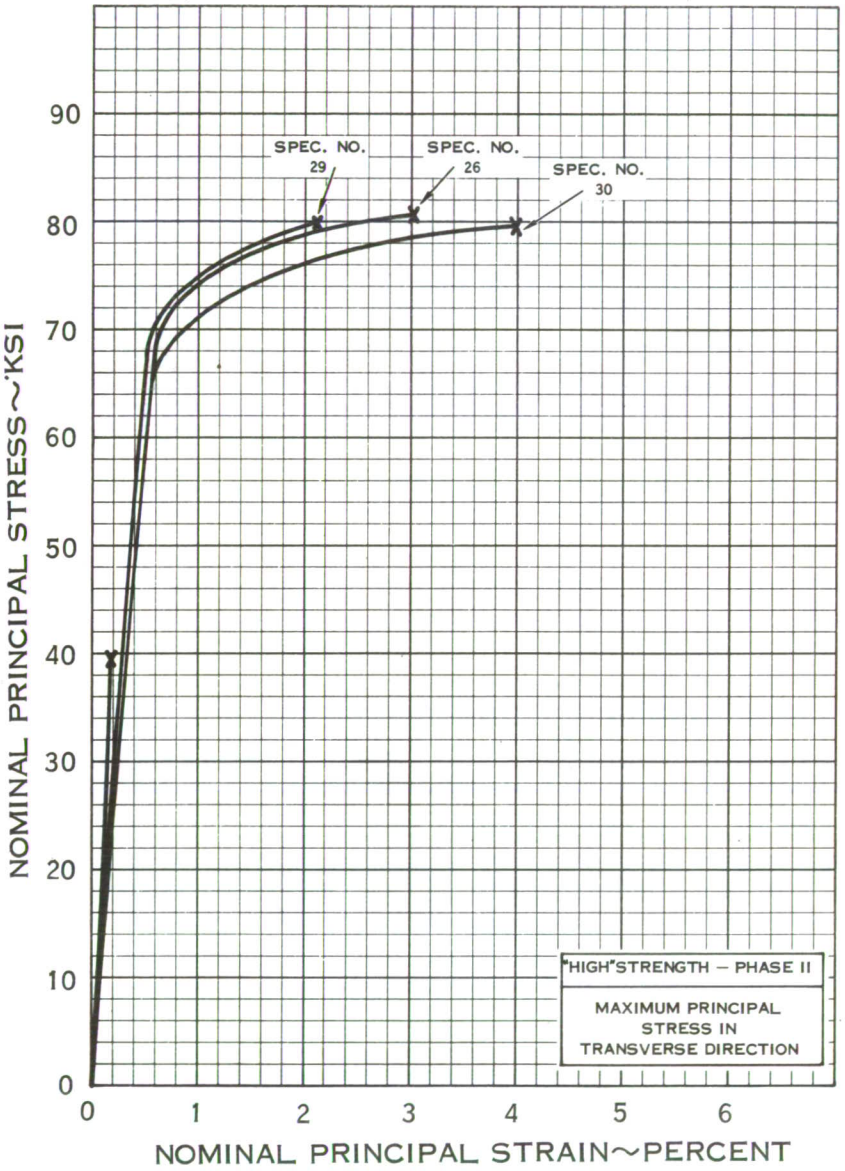

FIGURE 79 – 2:1 STRESS RATIO BIAXIAL STRESS – STRAIN CURVES, BARE 2014 – T6 ALUMINUM ALLOY

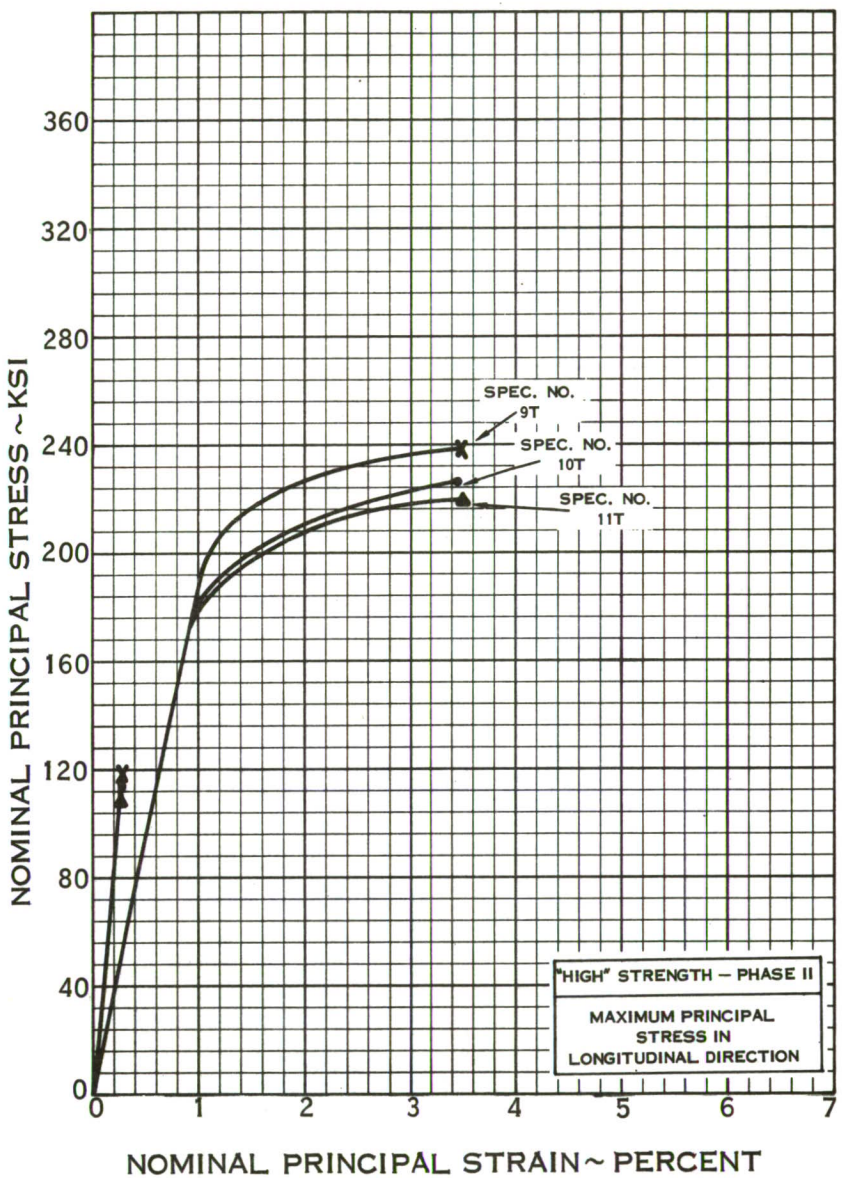

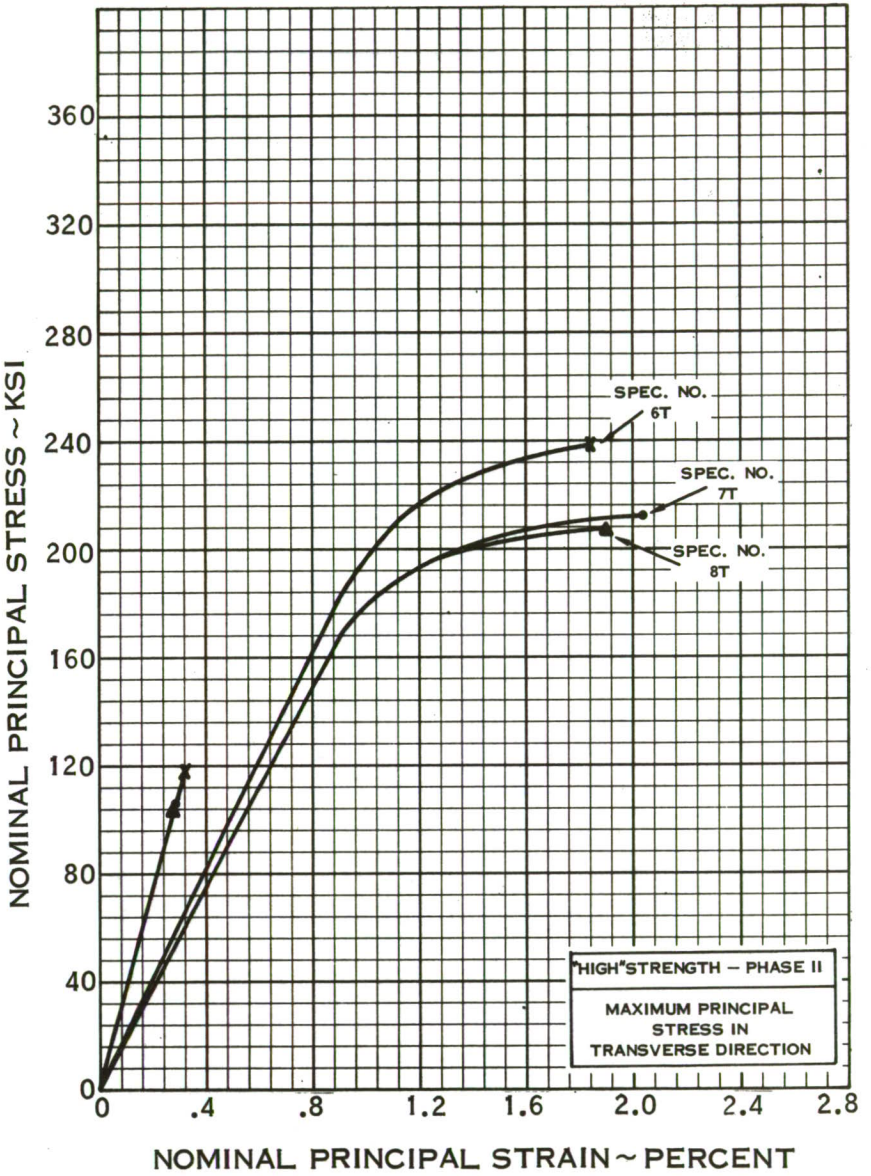

FIGURE 80 – 2:1 STRESS RATIO BIAXIAL STRESS – STRAIN CURVES, B–120 VCA TITANIUM ALLOY

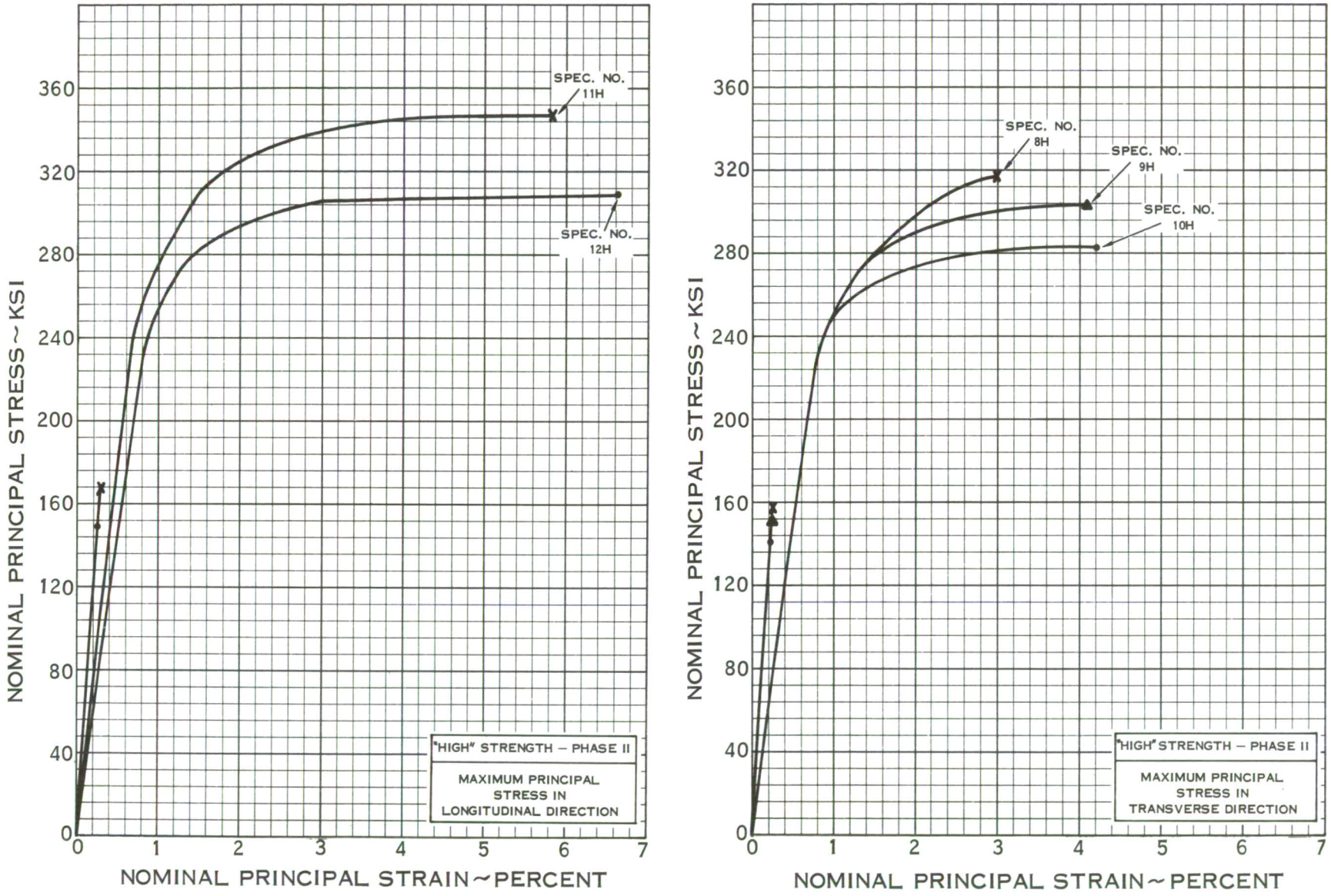

FIGURE 81 – 2:1 STRESS RATIO BIAXIAL STRESS – STRAIN CURVES, 5CRMOV STEEL ALLOY

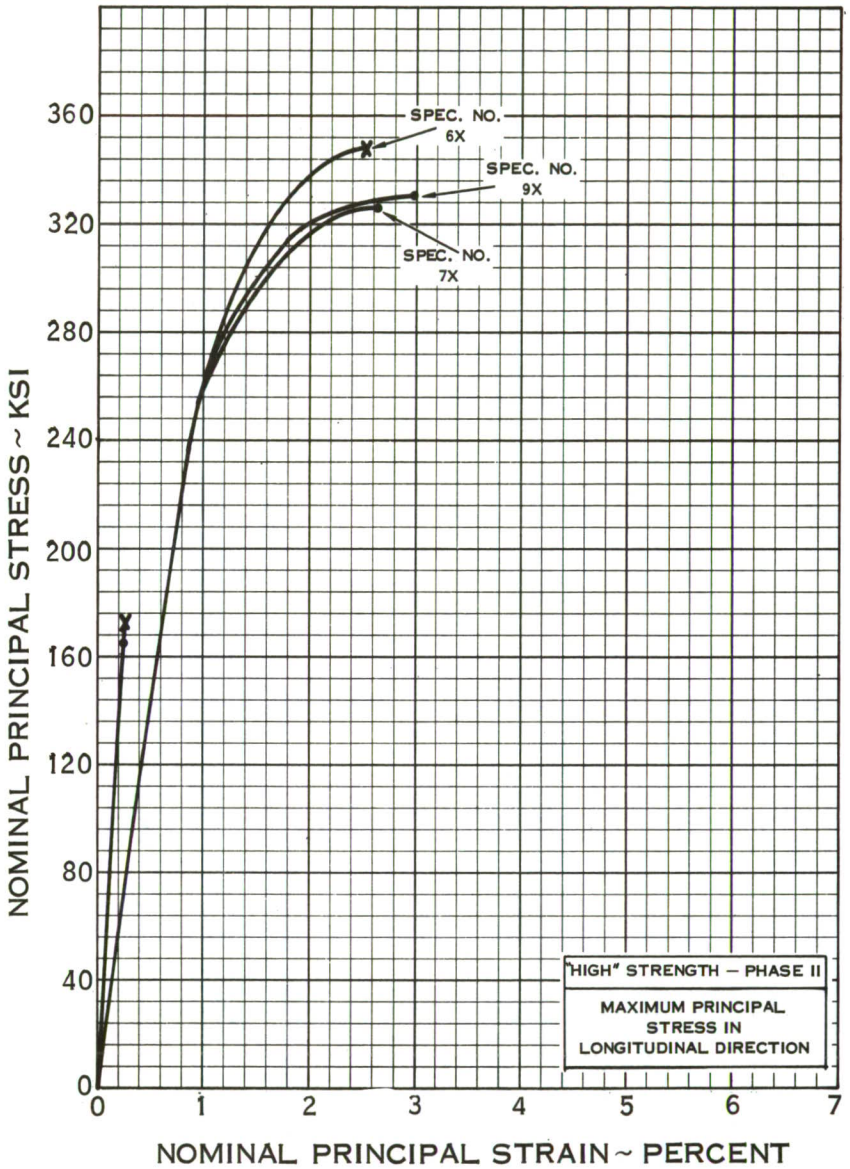

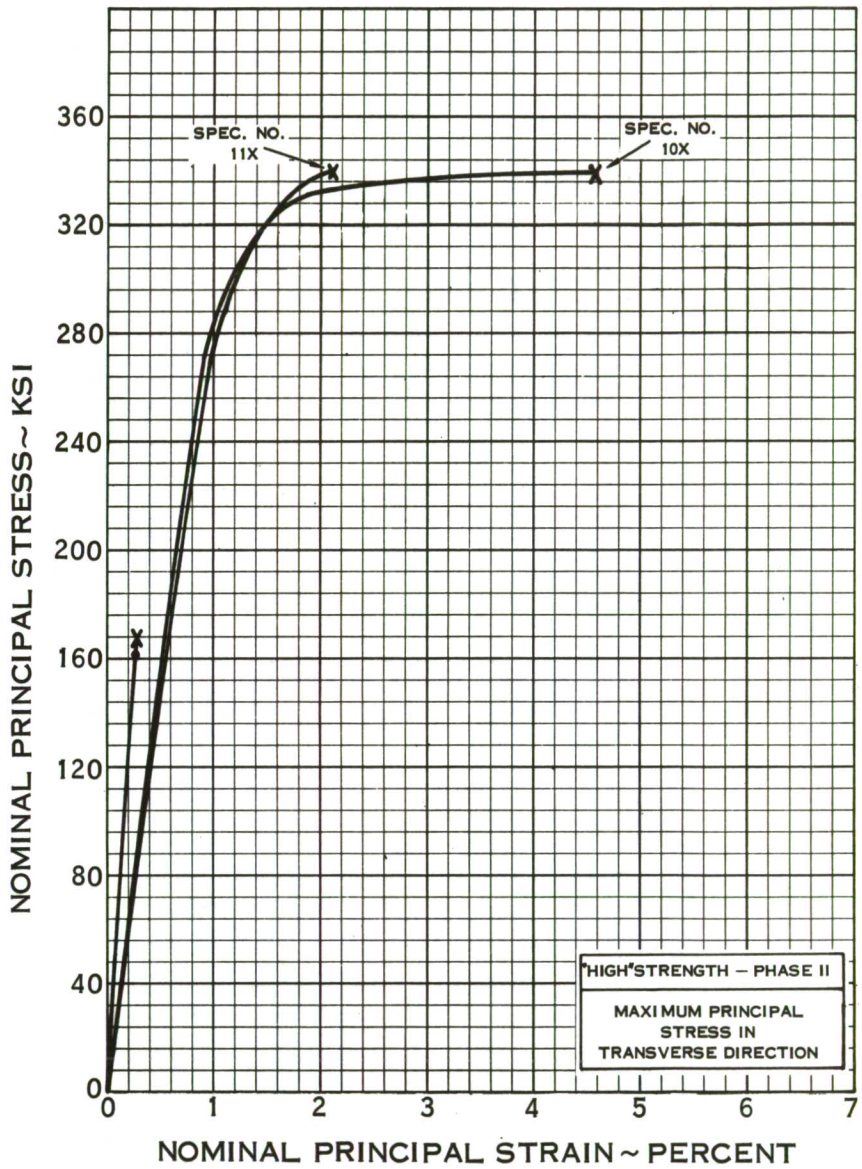

FIGURE 82 – 2:1 STRESS RATIO BIAXIAL STRESS – STRAIN CURVES, AIRSTEEL X–200

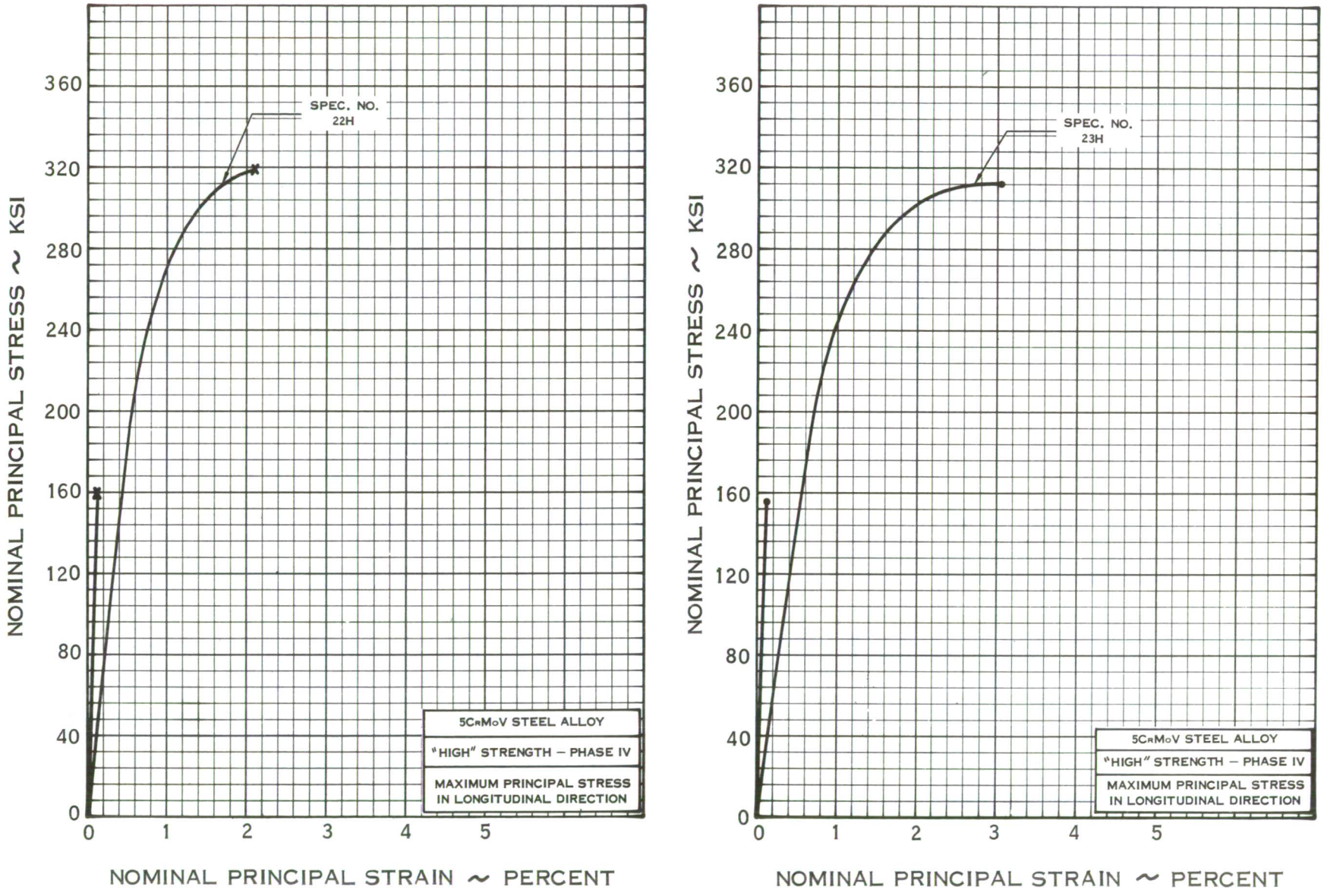

FIGURE 83 – 2:1 STRESS RATIO BIAXIAL STRESS – STRAIN CURVES
WELDED SPECIMENS

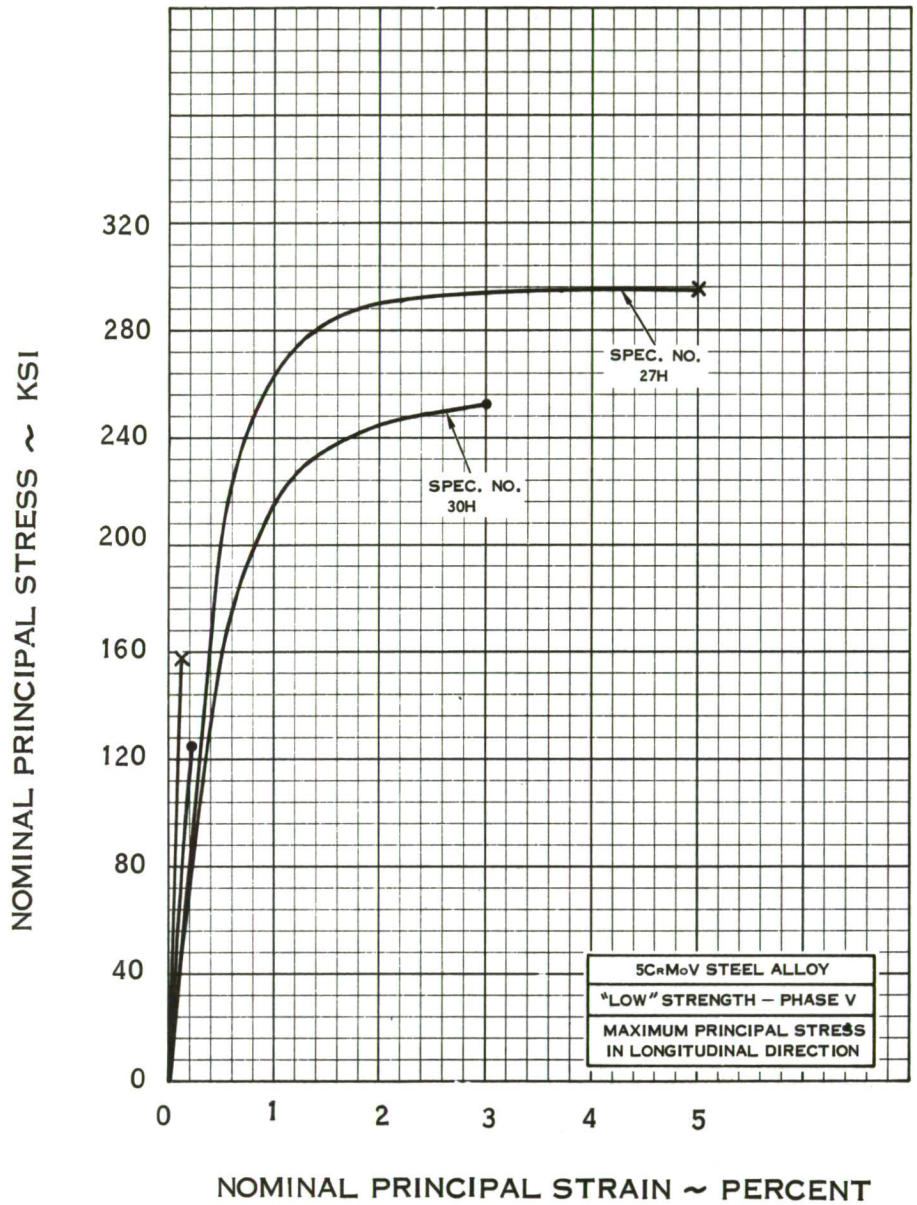

FIGURE 84 – 2:1 STRESS RATIO BIAXIAL STRESS – STRAIN CURVES, 5CrMoV STEEL ALLOY

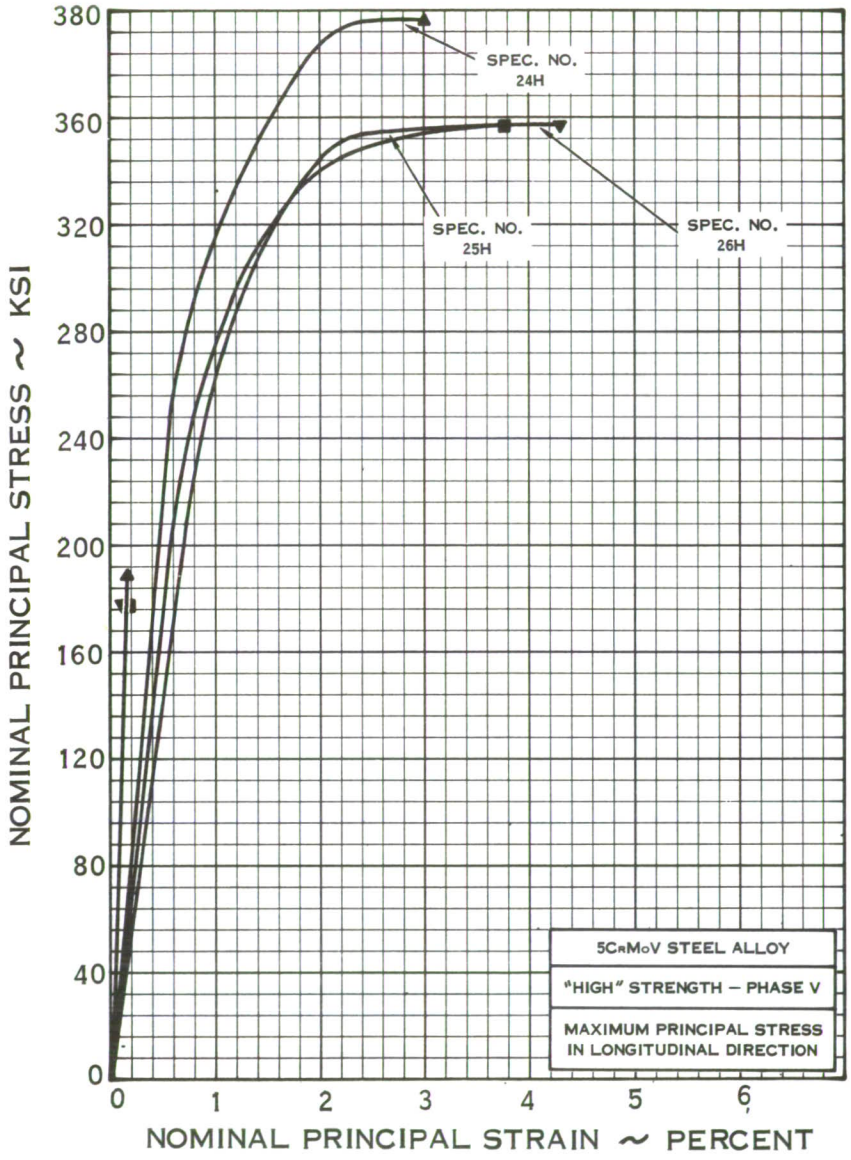

FIGURE 85 – 2:1 STRESS RATIO BIAXIAL STRESS – STRAIN CURVES, 5CrMoV STEEL ALLOY (CONTINUED)

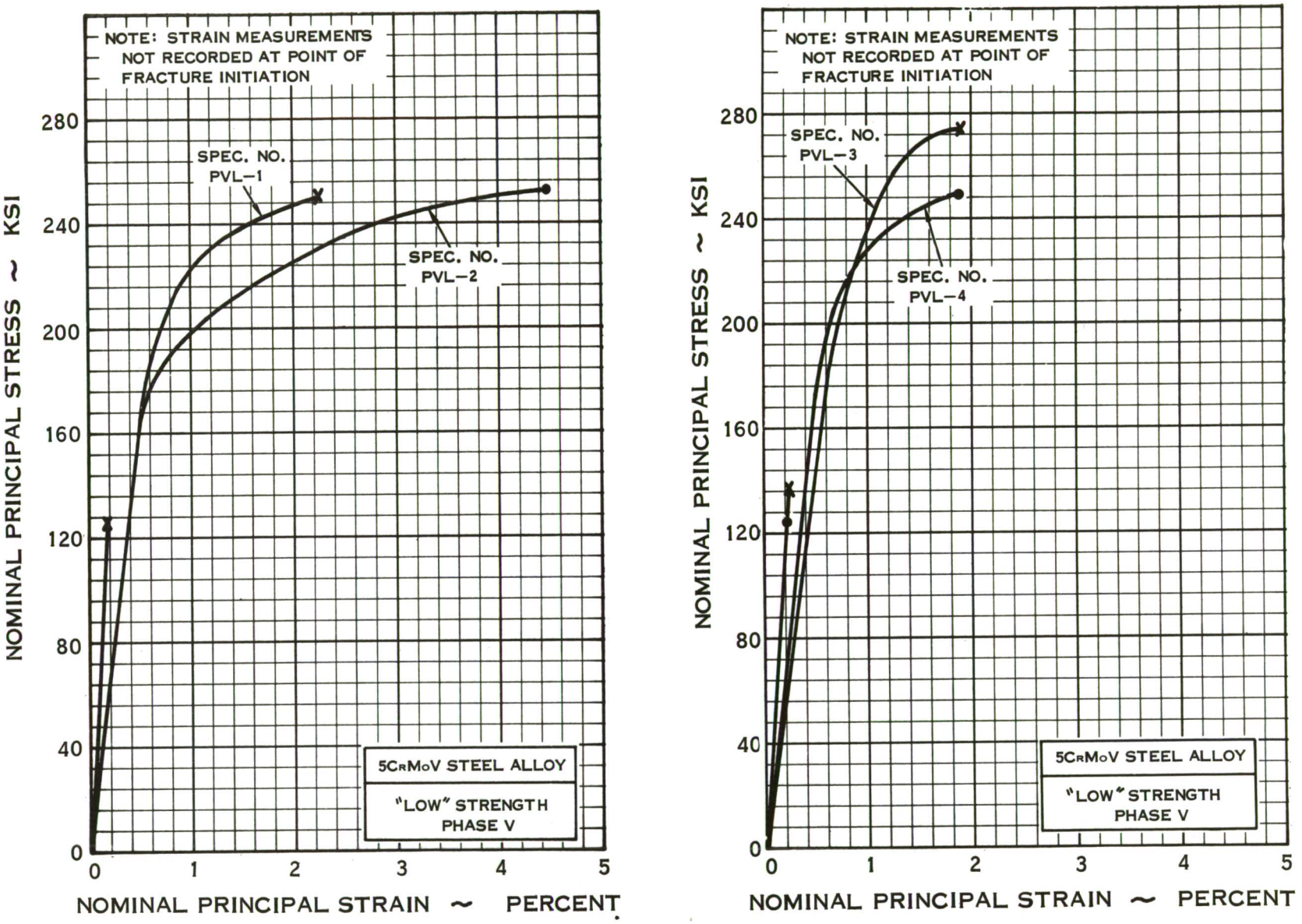

FIGURE 86 — 2:1 BIAXIAL STRESS — STRAIN CURVES OBTAINED FROM CYLINDRICAL PRESSURE VESSEL TESTS

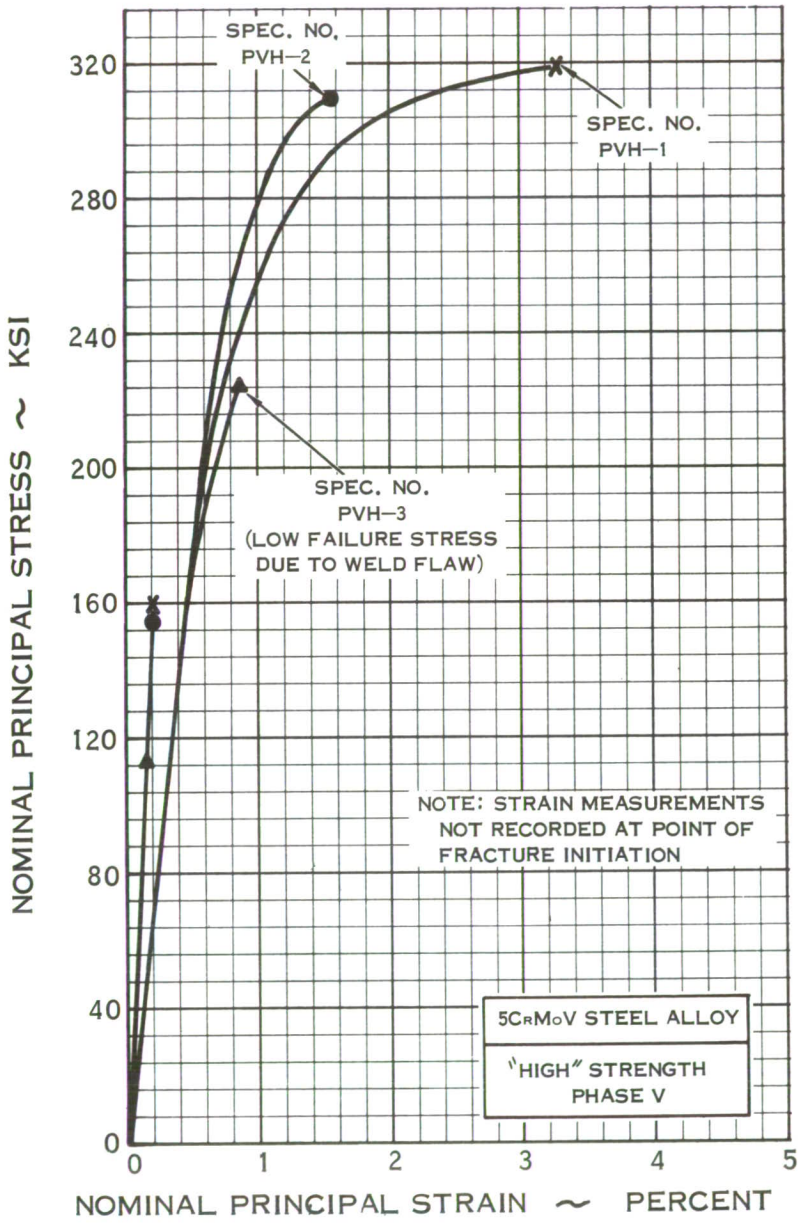

FIGURE 87 — 2:1 BIAXIAL STRESS — STRAIN CURVES OBTAINED FROM CYLINDRICAL PRESSURE VESSEL TESTS

Aeronautical Systems Division, Dir/Materials and Processes, Applications Lab, Wright-Patterson AFB, Ohio.
Rpt Nr ASD-TDR-62-401. BIAXIAL STRESS AND STRAIN DATA ON HIGH STRENGTH ALLOYS FOR DESIGN OF PRESSURIZED COMPONENTS. Final report, Jul 62, 207p. incl illus., tables, 12 refs.

Unclassified Report

A cross shaped specimen was developed for generating complete biaxial stress-strain curves under 1:1 and 2:1 biaxial tension stress ratio loading. Tests on several materials have shown that the specimen has good reliability.

The influence of strength level on the behavior of the 5CrMoV steel under biaxial loading was

(over)

1. Stress-strain test sample
2. Biaxial stress data
3. Biaxial strain data
I. AFSC Project 7381, Task 738103
II. Contract AF 33(616)-7720
III. Change Vought Corp., Dallas, Texas
IV. E. L. Terry, S. W. McClaren
V. Aval fr OTS
VI. In ASTIA collection

Aeronautical Systems Division, Dir/Materials and Processes, Applications Lab, Wright-Patterson AFB Ohio.
Rpt Nr ASD-TDR-62-401. BIAXIAL STRESS AND STRAIN DATA ON HIGH STRENGTH ALLOYS FOR DESIGN OF PRESSURIZED COMPONENTS. Final report, Jul 62, 207p. incl illus., tables, 12 refs.

Unclassified Report

A cross shaped specimen was developed for generating complete biaxial stress-strain curves under 1:1 and 2:1 biaxial tension stress ratio loading. Tests on several materials have shown that the specimen has good reliability.

The influence of strength level on the behavior of the 5CrMoV steel under biaxial loading was

(over)

1. Stress-strain test sample
2. Biaxial stress data
3. Biaxial strain data
I. AFSC Project 7381, Task 738103
II. Contract AF 33(616)-7720
III. Change Vought Corp., Dallas, Texas
IV. E. L. Terry, S. W. McClaren
V. Aval fr OTS
VI. In ASTIA collection

investigated. These tests showed that by lowering the uniaxial strength level from 280 to 260 ksi, the shattering type failure observed at the 280 ksi level ceased to exist. However, the biaxial failure strains did not increase as the strength level was decreased.

Good correlation was obtained between the failure stresses from the pressure vessels and the biaxial specimens.

The data is presented in a form which can be used directly in the design of biaxially loaded components. The test materials are ranked according to the efficiency parameters "biaxially ductility rating", "resistance to crack-like flaws", and "biaxial strength weight".

investigated. These tests showed that by lowering the uniaxial strength level from 280 to 260 ksi, the shattering type failure observed at the 280 ksi level ceased to exist. However, the biaxial failure strains did not increase as the strength level was decreased.

Good correlation was obtained between the failure stresses from the pressure vessels and the biaxial specimens.

The data is presented in a form which can be used directly in the design of biaxially loaded components. The test materials are ranked according to the efficiency parameters "biaxially ductility rating", "resistance to crack-like flaws", and "biaxial strength weight".

Aeronautical Systems Division, Dir/Materials and Processes, Applications Lab, Wright-Patterson AFB, Ohio.
Rpt Nr ASD-TDR-62-401. BIAXIAL STRESS AND STRAIN DATA ON HIGH STRENGTH ALLOYS FOR DESIGN OF PRESSURIZED COMPONENTS. Final report, Jul 62, 207p. incl illus., tables, 12 refs.

Unclassified Report

A cross shaped specimen was developed for generating complete biaxial stress-strain curves under 1:1 and 2:1 biaxial tension stress ratio loading. Tests on several materials have shown that the specimen has good reliability.

The influence of strength level on the behavior of the 5CrMoV steel under biaxial loading was

(over)

investigated. These tests showed that by lowering the uniaxial strength level from 280 to 260 ksi, the shattering type failure observed at the 280 ksi level ceased to exist. However, the biaxial failure strains did not increase as the strength level was decreased.

Good correlation was obtained between the failure stresses from the pressure vessels and the biaxial specimens.

The data is presented in a form which can be used directly in the design of biaxially loaded components. The test materials are ranked according to the efficiency parameters "biaxially ductility rating", "resistance to crack-like flaws", and "biaxial strength weight".

1. Stress-strain test sample
2. Biaxial stress data
3. Biaxial strain data

I. AFSC Project 7381, Task 738103
II. Contract AF 33(616)-7720
III. Change Vought Corp., Dallas, Texas
IV. E. L. Terry, S. W. McClaren
V. Aval fr OTS
VI. In ASTIA collection

Aeronautical Systems Division, Dir/Materials and Processes, Applications Lab, Wright-Patterson AFB Ohio.
Rpt Nr ASD-TDR-62-401. BIAXIAL STRESS AND STRAIN DATA ON HIGH STRENGTH ALLOYS FOR DESIGN OF PRESSURIZED COMPONENTS. Final report, Jul 62, 207p. incl illus., tables, 12 refs.

Unclassified Report

A cross shaped specimen was developed for generating complete biaxial stress-strain curves under 1:1 and 2:1 biaxial tension stress ratio loading. Tests on several materials have shown that the specimen has good reliability.

The influence of strength level on the behavior of the 5CrMoV steel under biaxial loading was

(over)

investigated. These tests showed that by lowering the uniaxial strength level from 280 to 260 ksi, the shattering type failure observed at the 280 ksi level ceased to exist. However, the biaxial failure strains did not increase as the strength level was decreased.

Good correlation was obtained between the failure stresses from the pressure vessels and the biaxial specimens.

The data is presented in a form which can be used directly in the design of biaxially loaded components. The test materials are ranked according to the efficiency parameters "biaxially ductility rating", "resistance to crack-like flaws", and "biaxial strength weight".

1. Stress-strain test sample
2. Biaxial stress data
3. Biaxial strain data

I. AFSC Project 7381, Task 738103
II. Contract AF 33(616)-7720
III. Change Vought Corp., Dallas, Texas
IV. E. L. Terry, S. W. McClaren
V. Aval fr OTS
VI. In ASTIA collection